DEFORMATION AND BREAKUP OF FINITE-SIZED BUBBLES IN INTENSE TURBULENCE

by

Ashik Ullah Mohammad Masuk

A dissertation submitted to The Johns Hopkins University in conformity with the requirements for the degree of Doctor of Philosophy.

Baltimore, Maryland

July, 2020

Abstract

From rain droplets in clouds to entrained gas bubbles in oceans, the majority of fluid mechanics problems in nature and industry are turbulent and consist of multiple phases. In such flows, bubbles and droplets experience complex deformation. Though this deformation occurs at small-scale interfaces, it plays important roles in many large-scale processes e.g. the overall heat and mass transfer in two-phase energy systems. To understand the fundamental physics behind the interaction between turbulence and deformable bubbles, simultaneous 3D measurements of both phases are essential. However, obtaining such measurements is a very challenging task. To address this problem, a unique vertical water tunnel (V-ONSET) capable of generating energetic turbulence is designed. V-ONSET is equipped with six high-speed cameras uniformly distributed around its test section to obtain high-resolution images of both bubbles and the turbulent carrier phase simultaneously. To reconstruct the 3D shapes of bubbles, a new algorithm addressing the limited-angle reconstruction problem by using the physical constraint of minimum surface energy is developed.

ABSTRACT

Moreover, to quantify turbulence, tracer particles in the surrounding flow are tracked with an in-house OpenLPT code. Leveraging such unique simultaneous measurements of bubbles and their surrounding turbulent flow, we investigate the mechanisms in turbulence responsible for the deformation and breakup of bubbles. We identify and evaluate two key mechanisms namely, the coarse-grained turbulent strains and the slip velocity between the two phases. Interestingly, two Weber numbers based on these two mechanisms show that in strong turbulence, the rather ignored mechanism of the slip velocity has a comparable magnitude to the other mechanism of turbulent strains. The distributions of these two Weber numbers are modeled based on turbulent flow characteristics. This also helps to estimate bubble breakup probability in turbulence. Furthermore, we investigate the orientation dynamics of bubbles with respect to the aforementioned deformation mechanisms. It elucidates that bubbles exhibit the strongest alignment with the slip velocity direction indicating the dominant role played by the compression induced by the slip velocity. Finally, a Lagrangian model including both deformation mechanisms is proposed to predict bubble deformation and orientation in turbulence.

Primary Reader and Advisor: Dr. Rui Ni

Secondary Readers: Dr. Gretar Tryggvason & Dr. Charles Meneveau

Acknowledgments

I am surely going to miss this time. The journey has been very exciting and fulfilling both academically and socially. It would not be possible without a great advisor, very helpful colleagues, amazing friends, and an unconditionally supporting family. I am grateful to everyone and for everything.

First, I want to acknowledge that I feel extremely fortunate to have an advisor, Dr. Rui Ni, who truly cares about the professional and personal development of his students. I admire his dedication and commitment toward science, the general well-being of his students, and of course his way of addressing problems be it scientific or general. Rui has always been very encouraging, at the same time he would always point out what I am doing wrong and provide very constructive suggestions. I want to share one story from earlier this year when I was searching for jobs. Rui really pushed me to prioritize the process and secure a position; otherwise, I would probably get stuck in the current hiring freeze due to the unfortunate pandemic situation. Thank you Rui for your constant support and guidance through out my entire PhD. I could not ask for a

better mentor.

I would like to express my sincere gratitude to my friend and colleague Ashwanth Salibindla whom I have worked with since the very beginning of my PhD. Ashwanth and I started to work with Rui at the same time and we collaborated with each other in every project since then. Our work approaches has been quite different but complementary to each other which I believe played an important role in the success of our projects. Also, outside work through out my entire PhD journey Ashwanth has been my go-to friend whom I could always count on through thick and thin. I really appreciate our friendship.

The culture in our Fluid Transport Lab has always been very friendly and collaborative thanks to Rui for always promoting such an ambience. I thank all the members of the lab both at Penn State and Johns Hopkins for being such a good sport and for all your help and support which I appreciate very sincerely.

I also want to thank all the amazing friends that I was lucky to have met in State College and Baltimore during my PhD journey. Its only for them that I could have a life outside work which I cherish very much and will always remain a big part of life. To me they have always been like a family far away from home. I don't want to take names as I don't want to miss anyone, its been a long journey. Any of my friends who is reading this, please know that I am talking about you, thank you!

Finally and most importantly, I want to thank my mother Khadija Begum,

ACKNOWLEDGMENTS

my father Abul Bashar Mohammad Sanaullah, and my brother Mohammad Amimul Ehsan for always being such a strong support system. I cannot thank them enough for their unconditional love, support, and encouragement which has always been the strongest driving force for me. I wish good health and all the happiness for them.

Contents

List of Tables

List of Figures

Chapter 1

Introduction

1.1 Motivation

Turbulent multi-phase flow is a very common phenomenon in both nature and industry. Some examples from nature include bubble generation in oceanic wave breaking (Deane and Stokes, 2002), ocean-atmosphere gas exchange (Wanninkhof and McGillis, 1999), volcanic eruptions (Wilson, 1976), snow drifts (JDoorschot, Lehning, and Vrouwe, 2004), dust storms (Lu and Shao, 2001), and rain droplets in turbulent clouds. Also, human activities such as sneezing, and coughing produce droplet laden turbulent plumes (Bourouiba, Dehandschoewercker, and Bush, 2014) which has indisputable implications in epidemiology; for instance, the spread of COVID-19 and such airborne diseases. To name industrial systems and processes involving turbulent multiphase flow, bio-reactors (Kantarci, Borak, and Ulgen, 2005), pharmaceutical

processes (Minale, 2010), polymer blends in plastic technology (Maffettone and Minale, 1998), chemical process reactors (Degaleesan, Dudukovic, and Pan, 2001), liquid-liquid stirred vessels (Afshar Ghotli et al., 2013), fluidized bed reactors (Foka et al., 1996), and heat exchangers (Ishii and Hibiki, 2010) are just a few examples. The ubiquitous nature of turbulent multiphase flow has motivated research in the fields of turbulence and multi-phase flow for over a century so far. However, due to the inherent complexity of the flow, even today there are many open questions to be investigated in order to understand the fundamental nature of the interaction between turbulence and the other phase e.g. bubbles, droplets or solid particles. Indeed there is a consensus in the scientific community that the existing capabilities to study turbulent multiphase flows as well as our understanding on such flows are far less mature compared single-phase turbulent flows (Balachandar and Eaton, 2010; Elghobashi, 2019). One of the most significant challenges in turbulent multiphase flow is the complexity associated with defining the couplings between different phases. Therefore, to better describe and predict the behavior of such flow phenomena, fundamental understanding on the mechanisms of interaction between different phases is imperative and will be the primary focus of this study.

1.2 Introduction to Turbulent Multi-phase Flow

1.2.1 Turbulence

Turbulence is a seemingly irregular and random flow phenomenon that exhibits spatio-temporal velocity, vorticity,and pressure fluctuations often arising from instability of laminar flows. Such flows are always associated with high Reynolds number that characterizes the complex interactions between inertial and viscous forces in turbulence. This, however, is by no means a formal definition of turbulence. In fact, when talking about turbulence, it is customary to describe its characteristics rather than providing a formal definition as a precise definition of turbulence is very difficult to formulate. Some of the other well known characteristics of turbulence along with the aforementioned ones include (i) diffusivity which promotes effective mixing and enhanced mass, momentum, and heat transfer; and (ii) dissipation of kinetic energy into heat by viscous shear forces. All of these characteristics of turbulence occurs at length scales far larger than the molecular length scales which makes turbulence a continuum phenomenon (Tennekes and Lumley, 1972; Pope, 2000; Kundu and Cohen, 2008).

Another important feature of turbulence is its multi-scale nature. The length scale in turbulence ranges from the largest energy injection scale to the smallest Kolmogorov length scale. These different length scales appear as

some swirling structures which are often referred to as eddies. Most of energy in a turbulent flow field is contained in the large scales and most of it is dissipated at the smallest length scale where viscous forces dominate inertia. On average, there persists a continuous flow of energy from the largest to smallest scales via the intermediate inertial subrange scales where flow is inviscid and the spectrum of energy cascade follows the Kolmogorov's 5/3 law; and the process of this energy flow is called energy cascade as first introduced by Richardson (1922). Therefore, turbulence is a dissipative process that needs consistent supply of energy to sustain itself.

1.2.2 Multi-phase Flow

When there are more than one fundamental phases present in a flow, it is named as multi-phase flow the simplest of which has only two phases e.g. bubbles in a water flow. Depending on the types of phases, volume fraction of each phase, topographical distribution of the phases, surface structures and the boundary conditions, Ishii (1975) classified multi-phase flow phenomenon into different regimes such as separated flows, mixed or transitional flows, and dispersed flows. The focus of this study will primarily be in the dispersed flow regime for bubbles in water.

1.2.3 Turbulent Multi-phase Flow

Turbulent multiphase flows, as the name suggests, are flows where at least one more phase e.g. droplets, bubbles, or dust particles is present in addition to the background turbulent flow. The dynamics of the single-phase turbulence alone is quite complex; the problem becomes much more challenging when some other phases are introduced e.g. gas bubbles in liquid phase turbulent flow (Balachandar and Eaton, 2010). The complexity of the problem again depends on the properties of the second phase in terms of their length scale D. When the length scale of the dispersed phase D is in the range of $\eta \ll D \ll L$ (η is the Kolmogorov length scale, and L is the integral length scale of turbulence), we refer to their length scale as finite-size in contrast to the point particles with $D \ll \eta$. The other properties of the dispersed phase particles that govern the extent of complications in a turbulence multiphase flow are the density ratio, and viscosity ratio between the two phases, shape of the particles (isotropic or anisotropic (Voth and Soldati, 2017)), and whether the interface is deformable or not. In cases where $D > \eta$, the second phase is often deformable exhibiting spatially and temporally varying aspect ratios, and surface curvatures, which introduces more length and time scales to a already multi-scale turbulent flow complicating the problem even further. The presence of a whole range of length scales in a turbulent multi-phase flow has a direct impact on the size evolution of the dispersed particles in the flow field (Deane and Stokes, 2002).

The interaction between two phases in a turbulent flow field is also affected by their relative concentration. Depending on the volume and mass fraction of the dispersed phase, the flow phenomenon can vary in complexity - from a one-way coupled problem to a four-way coupled problem (Elghobashi, 1991). The order of coupling depends on the volume fraction of dispersed phase present in the flow. For the case of low volume fraction, the modification of the turbulent flow induced by the dispersed phase in negligible. In such flows, the dynamics of the dispersed particles is determined by the turbulent flow field and they are referred to as one-way coupled flows. When the volume fraction increases to a moderate level, the dispersed phase also affects the nearby turbulent flow which is referred to as a two-way coupled process. At a very high concentration of dispersed particles, the collisions among particles increase and consequently become important. Such a flow condition is referred to as four-way coupled. In this study, for simplicity we concentrate on dilute suspension of finite-sized air bubbles in a strong turbulent water medium so that we can neglect the feed-back of these bubbles in the overall characteristics of our turbulent multiphase flow and assume the flow to be one-way coupled.

1.3 Numerical Techniques: Multiphase Flows

1.3.1 Multi-phase Turbulence Models

Modeling is an integral part of multiphase flow studies in order to formulate the flow mathematically and to develop expressions for the extra terms that appear in the averaged equations to make the numerical solution of the problem computationally less expensive. For complex turbulent flow problems there exists no analytic solution to the instantaneous governing equations due to the non-linearity of turbulence. In principal, the instantaneous microscopic governing equations can be solved using numerical direct numerical simulation (DNS) techniques such front tracking method (Unverdi and Tryggvason, 1992; Tryggvason et al., 2001), volume of fluid method (VOF) (Scardovelli and Zaleski, 1999; Dodd and Ferrante, 2016), and Level-set method (Sussman, Smereka, and Osher, 1994; Osher and Fedkiw, 2001). However, owing to the highly multi-scale nature of turbulence, such analysis for the real scale problems can quickly become very time demanding because computationally fully resolving the flow would require a grid size and time resolution comparable to the smallest length and time scales of the flow (Enwald, Peirano, and Almstedt, 1996). Therefore, the governing equations are often averaged (over time, space or ensemble) to formulate a numerically more affordable problem. In two-phase turbulence modeling these issues become even more challenging as

the interaction between the two phases, fluid properties like viscosity, and relative distribution of the phases have to be modeled as well.

Modeling turbulent multi-phase flows can broadly be categorized into Euler-Euler models and Euler-Lagrange models. This classification is based on how the dispersed phase is formulated – in an Eulerian frame or as Lagrangian trajectories. Often for simplification, the Eulerian equations are averaged and such averaging procedure certainly results in loss of information about the scales in between which are valuable especially regarding the dynamics of the dispersed particle phase (Fox, 2012). Therefore, in some cases mesoscopic models are formulated for the dispersed phases dynamics (Fox, 2012; Chen and Doolen, 1998). Different models of turbulent multi-phase flow will be explored in more details in the following sections; and the discussion henceforth will be focused on the dispersed flow regime.

1.3.1.1 Euler-Euler Models

Euler-Euler modeling of two phase turbulent flow uses Eulerian description for both phases and attempts to capture the development of the flow phenomenon at fixed locations in the flow field over time. The Eulerian modeling approach can broadly be classified in two major categories, namely, diffusion models and two-fluid models (Ishii and Hibiki, 2010). Diffusion models (also known as mixture models) approximate the two phases by one mixture-fluid;

and the properties of the mixture-fluid is modeled by some sort of weighted averaging of both fluids (Manninen, Taivassalo, Kallio, et al., 1996). The mixture-fluid can then be modeled as a single phase using one continuity equation, one energy equation, one diffusion equation (to take concentration gradient into account), and one momentum equation in each principle direction of the lab frame of reference (Enwald, Peirano, and Almstedt, 1996). The diffusion equation is derived from the continuity equation for a single phase and using the definition for diffusion velocity (Ishii and Hibiki, 2010; Manninen, Taivassalo, Kallio, et al., 1996).

On the other hand, two-fluid models treat the two phases as separate entities with interfacial exchanges. In this approach, at a given instant in time, any infinitesimal volume in the flow field can contain either one of the two phases or the interface in between (Fox, 2012). Such possibilities are taken into account by formulating a continuity equation (Eqn. 1.1), three momentum equations (Eqn. 1.3), and an energy equation for each phase in the instantaneous form; where, ρ is the density, $\mathbf{u}$ is the velocity vector, $\mathbf{b}$ is the body force, $\overline{\overline{\mathbf{T}}}$ is the stress tensor, and k represents either of the phases. Also, each of these equations are accompanied by a jump condition equation (Eqn. 1.2, 1.4) that describes the interaction between the phases. In (Eqn. 1.2 and 1.4), $\dot{m}$ is the mass transfer rate, and $\mathbf{n}_k$ represents the unit normal vector at the interface pointing outward from the phase k. These conservation equations

mentioned can give local balance of the fundamental quantities (e.g. mass, momentum, energy) in any of the pure phases but on a location at the surface of discontinuity (the interface). For such surfaces of discontinuity, jump conditions are needed to relate the quantities on both sides of an interface (Delhaye, 1974). The instantaneous equations are then averaged in order to obtain the macroscopic equations (Eqn. 1.5,1.6) where α_k is the averaged phase indicator function, X_k is the phase indicator function, $\mathbf{U}_k$ is the mass-weighted average velocity of phase k, $\overline{\overline{\mathbf{T}}}_k^{X_k}$ is the phasic averaged stress tensor, $\overline{\overline{\mathbf{T}}}_k^{Re}$ is the fluctuating stress tensor, and $\mathbf{M}_{k\mathbf{I}}$ represents the interfacial momentum transfer. The averaged momentum equations in a two-fluid model include unclosed interfacial exchange terms (Eqn. 1.7) and calls for additional closure laws to be modeled in order to mathematically close the problem. Most of such closure laws are developed based on empirical inputs; therefore, high fidelity experimental measurements are essential to formulate physically significant closure models (Enwald, Peirano, and Almstedt, 1996).

Instantaneous conservation equations

mass conservation:

$$\frac{\partial}{\partial t}(\rho_k) + \nabla \cdot (\rho_k \mathbf{u_k}) = 0 \tag{1.1}$$

jump condition for mass conservation:

$$\sum_{k=1}^{2} \dot{m}_k = 0 \tag{1.2}$$

momentum conservation:

$$\frac{\partial}{\partial t}(\rho_k \mathbf{u_k}) + \nabla \cdot (\rho_k \mathbf{u_k} \mathbf{u_k}) + \nabla \cdot \overline{\overline{\mathbf{T}}}_k - \rho_k \mathbf{b} = 0 \tag{1.3}$$

jump condition for momentum conservation:

$$\sum_{k=1}^{2} (\dot{m} \mathbf{u_k} - \overline{\overline{\mathbf{T}}}_k \cdot \mathbf{n_k}) = 0 \tag{1.4}$$

Averaged conservation equations

mass conservation:

$$\frac{\partial}{\partial t}(\alpha_k \rho_k^{X_k}) + \nabla \cdot (\alpha_k \rho_k^{X_k} \mathbf{U_k}) = 0 \tag{1.5}$$

momentum conservation:

$$\frac{\partial}{\partial t}(\alpha_k \rho_k^{X_k} \mathbf{U_k}) + \nabla \cdot (\alpha_k \rho_k^{X_k} \mathbf{U_k} \mathbf{U_k}) = \nabla \cdot (\alpha_k (\overline{\overline{\mathbf{T}}}_k^{X_k} + \overline{\overline{\mathbf{T}}}_k^{Re})) + \alpha_k \rho_k^{X_k} \mathbf{g} + \mathbf{M_{kI}} \tag{1.6}$$

interfacial momentum transfer:

$$\mathbf{M_{kI}} = - < \overline{\overline{\mathbf{T}}} \cdot \nabla X_k > \tag{1.7}$$

The conservation equations presented in this discussion is obtained from the derivation given by Enwald (1996) (Enwald, Peirano, and Almstedt, 1996) following the work of Delhaye (1981) (Delhaye, Giot, and Riethmuller, 1981) and of Bouré and Delhaye (1982) (Boure and Delhaye, 1982). In the formulation of these equations surface tension term was neglected because, the main objective was to model gas-solid particle flows. Such elimination of the surface tension term was made in the general integral balance equation for any scalar or vector quantity, written as the first step. A more complete form of integral balance equations for both linear and angular momentum can be found in the work of Delhaye (1974) (Enwald, Peirano, and Almstedt, 1996; Delhaye, 1974) where the surface tension terms is included as cyclic line integrals of the boundary of interfacial area between the phases (boxed terms in Eqn. 1.8, and Eqn. 1.9).

$$\begin{aligned}\frac{d}{dt}\int_{\mathcal{V}_1(t)}\rho_1\mathbf{u}_1 d\mathcal{V}+\frac{d}{dt}\int_{\mathcal{V}_2(t)}\rho_2\mathbf{u}_2 d\mathcal{V}+\frac{d}{dt}\int_{\mathcal{A}_i(t)}\rho_i\mathbf{u}_i d\mathcal{V}=\\ \int_{\mathcal{V}_1(t)}\rho_1\mathbf{F}_1 d\mathcal{V}+\int_{\mathcal{V}_2(t)}\rho_2\mathbf{F}_2 d\mathcal{V}+\int_{\mathcal{A}_i(t)}\rho_i\mathbf{F}_i d\mathcal{A}+\\ \int_{\mathcal{A}_1(t)}\mathbf{n}_1\cdot\tau_1 d\mathcal{A}+\int_{\mathcal{A}_2(t)}\mathbf{n}_2\cdot\tau_2 d\mathcal{A}+\boxed{\oint_{\mathcal{C}(t)}\sigma\mathbf{N}d\mathcal{C}}\end{aligned} \tag{1.8}$$

$$\frac{d}{dt}\int_{\mathcal{V}_1(t)} \mathbf{r}\times\rho_1\mathbf{u}_1 d\mathcal{V} + \frac{d}{dt}\int_{\mathcal{V}_2(t)} \mathbf{r}\times\rho_2\mathbf{u}_2 d\mathcal{V} + \frac{d}{dt}\int_{\mathcal{A}_i(t)} \mathbf{r}\times\rho_i\mathbf{u}_i d\mathcal{V} = \int_{\mathcal{V}_1(t)} \mathbf{r}\times\rho_1\mathbf{F}_1 d\mathcal{V} + \int_{\mathcal{V}_2(t)} \mathbf{r}\times\rho_2\mathbf{F}_2 d\mathcal{V} + \int_{\mathcal{A}_i(t)} \mathbf{r}\times\rho_i\mathbf{F}_i d\mathcal{A} + \int_{\mathcal{A}_1(t)} \mathbf{r}\times(\mathbf{n}_1\cdot\tau_1) d\mathcal{A} + \int_{\mathcal{A}_2(t)} \mathbf{r}\times(\mathbf{n}_2\cdot\tau_2) d\mathcal{A} + \boxed{\oint_{\mathcal{C}(t)} \mathbf{r}\times\sigma\mathbf{N} d\mathcal{C}} \tag{1.9}$$

Surface tension (σ) can play a significant role when the two fluid phases have different densities, viscosities and the dispersed particles are finite-sized. In a numerical simulation using a level set method, as surface tension was added to the momentum equation as a body force using smoothed delta function, it showed that for a bubble rising in water, presence of surface tensions causes thinning of bubble skirts (Sussman, Smereka, and Osher, 1994). Another similar simulation for bubbles having lower density than the continuous phase demonstrated that coalescence of bubbles gets delayed in presence of surface tension; and also the regularizing effect near the interface is more (Chang et al., 1996). In a front tracking numerical study of head-on collision of two viscous drops, surface tension was also found to be appearing in the average momentum equation and they showed the importance of surface tension in such collision dynamics of droplets (Nobari, Jan, and Tryggvason, 1996). However, including surface tension in numerical simulations is not a trivial task.

The averaged continuity [Eqn. 1.5] and momentum [Eqn. 1.6,1.7] equations

require to be assisted by closure laws to become solvable (i.e., to close the set of PDEs). The closure laws can be classified according to the type of physical relations they model: constitutive laws, transfer laws, and topological laws. Constitutive laws describe physical properties of the phases; transfer laws are predictive of the interaction between phases; and, topological laws model the spatial distribution of phases and their properties. It should also be noted that different closure laws are sometimes referred to as constitutive laws in general (Enwald, Peirano, and Almstedt, 1996). Developing realistic closure laws is the key challenge in modeling of turbulent multi-phase flows.

1.3.1.2 Euler-Lagrange Models

Euler-Lagrange models are generally formulated with a large-scale model and a medium scale model (Lapin and Lübbert, 1994). The large-scale, and medium-scale here are suggestive of the size of volumetric elements used to simulate the models. The large-scale model considers both phases as a quasi-single-phase with variable density (ρ) (Lapin and Lübbert, 1994; Sokolichin and Eigenberger, 1994). The variable density is modeled from experimental gas hold-up data or from a continuous treatment of the dispersed phase. On the other hand, the small-scale model is formed in order to track the dispersed particle in the Lagrangian manner. Dispersed particles can either be treated as individuals or as a cluster.

In order to have a model for quasi-single-phase treatment of the two phase mixture, single phase continuity and momentum equation can be used with a variable density (ρ) and an effective mixture viscosity (η_{eff}) defined [Eqn. 1.10, 1.11, 1.12] (Lapin and Lübbert, 1994). There appears no interfacial exchange term in this case as the whole mixture is considered as a pseudo-continuum (Jakobsen et al., 1997). The variable density expression, and an expression for effective viscosity in the large scale model has to be obtained from a separate continuous model of the dispersed phase. In this model the dispersed phase is characterized by some density function, W, in the phase space; and the density function can be defined as a function of position vector (r) and particle mass (m) [Eqn. 1.13]. In this Eqn. 1.13, the terms on the left hand side of the equation accounts for the total time rate of change of W, the changes in W due to particles crossing control volume, and the mass transfer effect, respectively (Lapin and Lübbert, 1994). The terms a_{eff} and a_d are included in order to account for the breakup and coalescence of particles, which need to be estimated using models or experimental data (ibid.). In cases, the variable density is modeled as an weighted average of the densities of the phases as well (Jakobsen et al., 1997).

$$\frac{\partial}{\partial t}\rho + \nabla \cdot (\rho \mathbf{u}) = 0 \tag{1.10}$$

$$\rho[\frac{\partial}{\partial t}\mathbf{u}_i + \mathbf{u}_j\frac{\partial}{\partial x_j}\mathbf{u}_i] = -\frac{\partial}{\partial x_i}p + \frac{\partial}{\partial x_j}\mathbf{T}_{ij} + \rho\mathbf{g} \tag{1.11}$$

$$\mathbf{T}_{ij} = \eta_{eff}(\frac{\partial \mathbf{u}_i}{\partial x_j} + \frac{\partial \mathbf{u}_j}{\partial x_i} - \frac{2}{3}\delta_{ij}\frac{\partial \mathbf{u}_n}{\partial x_n}) \tag{1.12}$$

$$\frac{\partial W}{\partial t} + \nabla\cdot(\mathbf{u}_b, W) + \frac{\partial}{\partial m}(\frac{dm}{dt}W) = \nabla\cdot(a_{eff}\nabla W) + \frac{\partial}{\partial m}(a_d\frac{\partial W}{\partial m}) \tag{1.13}$$

$$\rho = f(T, W) \tag{1.14}$$

$$\frac{d}{dt}(m\mathbf{u}) = \mathbf{F}_D + \mathbf{F}_P + \mathbf{F}_V + \mathbf{F}_G + \mathbf{F}_B + \mathbf{F}_L + \mathbf{F}_E \tag{1.15}$$

The discrete medium-scale model track the center of each dispersed phase particle or the center of a considered cluster at a higher resolution as compared to the numerical grid used for calculating the pseudo-continuum field. A Monte-Carlo method can be used to track the particles. The motion of particles can be given by [Eqn. 1.15] (Jakobsen et al., 1997; Johansen, 1990). In order to track individual particles, each particle need one equation of motion [Eqn. 1.15] (Jakobsen et al., 1997) where $\mathbf{F}_D$ is the drag force, $\mathbf{F}_P$ is the global pressure force, $\mathbf{F}_V$ is the virtual mass force, $\mathbf{F}_G$ is the gravity force, $\mathbf{F}_B$ is the Basset

force, $\mathbf{F}_L$ is the transverse lift force, and $\mathbf{F}_E$ represents the external field force other than gravity. Depending on the flow phenomenon being studied some of the force terms are usually neglected.

The solution for a two-phase flow using Euler-Lagrange model is obtained through numerical iterations. First, an estimation of the velocity field from the large scale model for one time step is made. Second, using the velocity field from first step the motion of each bubble and consequently their their new positions are obtained for the same numerical time step. The distribution of dispersed particles gives new density distribution of the flow field. Then the first step is repeated again using the new flow field density distribution; and the process goes on a loop until convergence is attained (Lapin and Lübbert, 1994; Sokolichin and Eigenberger, 1994).

In the Euler-Lagrangian framework, a very popular approach for dispersed bubbles/droplets with $D \ll \eta$ is to treat them as rigid point particles that are advected by the carrier phase as passive tracers. Such a framework in usually one-way coupled for dilute suspension of particles and often the carrier phase flow is obtained by DNS disregarding the dispersed particles in the flow (Elghobashi, 1991; Squires and Eaton, 1991). Recently, such framework has been extended to take deformability into account (Biferale, Meneveau, and Verzicco, 2014; Spandan, Lohse, and Verzicco, 2016) where the deformation is calculated based on some phenomenological model (Maffettone and Minale, 1998) as long

as $D \ll \eta$. As most of such phenomenological models are only applicable for $D \ll \eta$, it is challenging to extend this framework further for $D \gg \eta$. Therefore, developing appropriate phenomenological models capable of predicting deformation of finite-sized bubbles/droplets in turbulence could be extremely valuable for turbulent multiphase flow simulations.

1.4 Experiments on bubbles in turbulence

In the previous section we discussed state of the art numerical techniques to study turbulent multiphase flows. From the discussion it is evident that except for the DNS methods all other faster numerical techniques are heavily dependent on models that can capture the interfacial exchanges between the dispersed particles and turbulence. Therefore, physical understanding of the mechanisms involved in the dispersed particle dynamics in turbulence is essential to develop such models with high fidelity which naturally demands careful experimental investigations on this subject. However, currently the experimental investigations on finite-sized bubble dynamics are quite limited in the literature as it is more tractable to study neutrally buoyant and heavy particles either experimentally or numerically (Mathai, Lohse, and Sun, 2020b; Lohse, 2018).

The main objective of this work is to unveil important mechanisms of finite-

sized bubble dynamics in homogeneous isotropic turbulence. Homogeneous isotropic turbulence (HIT) is a special case of turbulent flow which contains all the fundamental characteristics of turbulence. Since for homogeneous isotropic turbulence the Reynolds stress term in Navier-Stokes equation is mathematically much simpler, it is more convenient to formulate mathematical models for such flow conditions. Moreover, the universality of the inertial range of homogeneous isotropic turbulence makes the problem more lucrative and also provides extremely valuable understanding on the real world turbulent flows (Pope, 2000; Mathai, Lohse, and Sun, 2020b). Therefore, studying the couplings between dispersed phase and such statistically homogeneous and isotropic turbulent flow should provide significant fundamental insights into problem which is the primary motivation for this study.

1.4.1 Laboratory scale homogeneous isotropic turbulent flow

The experimental techniques used to generate homogeneous isotropic turbulence along with a brief discussion on the requirements for experimental setups to generate homogeneous isotropic turbulence in laboratory scale is presented in this section. A detailed discussion on this topic is provided in later in this dissertation (chapter 2).

To create homogeneous turbulence, a well-known method is to set up a

mesh at a cross-section of the flow which induces turbulence to the flow as the fluid flows past the grid (Lance and Bataille, 1991; Kurian and Fransson, 2009). The structure of the mesh and the mean flow velocity through the mesh control the properties of the turbulence generated and gets advected downstream. Typically a high mean flow is required to attain intense turbulence with this method. To attain further control over the intensity of the generated turbulence flapping wings are added to the grid (Poorte and Biesheuvel, 2002; Rensen, Luther, and Lohse, 2005) – commonly known as active grid – and they are often actuated randomly to modulate the generated turbulence properties. Turbulence created by grids is homogeneous but lacks isotropy. For isotropic turbulence, the root-mean-square velocity fluctuations in all directions should be equal without having any directional preference. As the turbulence generated by grids depends on the flow passing through the grid, the velocity fluctuation along the flow direction is always larger than the other two lateral components. Also, due to energy dissipation in the flow the turbulence intensity keeps decreasing along the flow direction. Therefore, grid turbulence cannot produce a large three dimensional region of homogeneous turbulence.

Another popular method for creating laboratory turbulence is agitating an otherwise stationary fluid by imposing symmetric forcing (Goepfert et al., 2010; Zimmermann et al., 2010). Because energy is continuously added to the flow in this technique, turbulence can sustain over a three dimensional region without

decaying in intensity. Such three dimensional region of turbulence can extend up to a few integral length scales (Bellani and Variano, 2014) for forcing from two opposing planes. Also, the turbulence created by such symmetric forcing is homogeneous and isotropic in nature, having less than 10% variation in the velocity fluctuation components. It has also been reported in literature that if the forcing is randomized, planar HIT region can be generated even with unidirectional forcing with negligible mean flow (Variano, Bodenschatz, and Cowen, 2004).

The dynamics of the interfacial evolution of the dispersed particles is affected by history effects (Loewenberg, 1993; Albråten, 1981). Therefore, to obtain the full dynamics of the particles, it requires collecting data for the same particles over multiple time scales present in the experiment. For deformable particles like air bubbles, as they try to flow upward due to buoyancy force therefore, introducing an opposing mean flow to stabilize or slow down the particle in the experimental section. Therefore, an ideal experimental facility would be one in which both the turbulence properties and the mean flow can be controlled individually. This is one of the key ideas behind the experimental rigs built for this study which is discussed in chapter 2.

1.4.2 Finite-sized bubble dynamics in homogeneous isotropic turbulence

Regarding bubbly turbulent flows, turbulence induced by swarm of bubbles in an otherwise quiescent liquid has been studied quite extensively and the turbulence created in this way is called bubble induced turbulence (BIT). The primary reason for such turbulence generation is agitation of the liquid phase by the swarm of bubbles due to their wake induced path instability. Interested readers may refer to a recent review by Risso (2018) where this topic of BIT has been discussed in great detail. On the other hand, the literature on experimental investigation of finite-sized bubble dynamics in a background homogeneous isotropic turbulence is so far very limited (Mathai, Lohse, and Sun, 2020b) owing to challenges associated with experimental and measurement techniques. Lance and Bataille (1991) in their pioneering experimental work on the effect of bubbles in grid generated turbulence observed modulation of the turbulent power spectrum scaling. They found that the power spectrum scaling changes to -3 from $-5/3$ which was later confirmed both experimentally (Prakash et al., 2016) and through numerical investigations. Another important question in turbulent bubbly flows is that how the background turbulent flow effect the dynamics of bubble with regard to their deformation and breakup in turbulence which is also as mentioned before the primary interest of this study. In order to answer these questions, the foundation was laid by the

seminal works of Kolmogorov (1949), and Hinze (1955) where they introduced the concept of bubble-eddy collision. In light of this picture of bubble turbulence interaction several experimental investigations followed. Sevik and Park (1973) studied breakup of air bubbles in turbulent water jet and updated the value for critical Weber number provided by Hinze (1955). Phenomenological models on bubble breakup frequency were also developed based on concept of bubble-eddy collision and these models were compared with two dimensional (2D) measurements of bubble breakup in bubble column (Prince and Blanch, 1990), and turbulent water jet (Martínez-Bazán, 1999). Risso and Fabre (1998) studied bubble deformation and breakup in turbulence generated by a axisymmetric water jet experimentally in micro-gravity condition to avoid the effect of buoyancy in bubble deformation. They measured bubble deformation in 2D and also performed measurement of turbulent fluctuation at a fixed location which was used to estimate eddies at bubble scale. Such measurements of turbulent flow was then used to estimate bubble deformation in time using their spring oscillator model for bubble deformation. Again, the key concept was to understand the interaction between bubbles and turbulent eddies. However, there might be other mechanisms in turbulence such as the slip velocity between two phases that has significant effect on deformation and breakup of finite-sized bubbles in homogeneous isotropic turbulence. For instance, the average shape of a bubble rising in a turbulent water medium was shown to be domi-

nated by the mean slip velocity between bubble and the water phase whereas the turbulent fluctuations contributed to the random deformation of the bubble (Ravelet, Colin, and Risso, 2011). In the current study, taking advantage of our unique experiments on bubble dynamics in homogeneous isotropic turbulence we make an attempt to identify and evaluate all the key mechanisms that govern deformation and breakup of bubbles in turbulence.

1.5 Dissertation Outline

In this dissertation, four aspects of our experimental investigation on the dynamics of bubble deformation and breakup in homogeneous isotropic turbulence are presented:

(i) Design of experiments and building a vertical water tunnel capable of generating a strong homogeneous isotropic turbulent flow. The tunnel also facilitates simultaneous 3D measurements of both the bubbles and the turbulent flow (Chapter 2).

(ii) A new algorithm for 3D reconstruction of the complex surface geometries of bubbles deforming in turbulence combining images from six high-speed cameras (Chapter 3).

(iii) Evaluation of the key mechanisms in turbulence responsible for bubble deformation and breakup (Charter 4, and 5).

(iv) A new Lagrangian phenomenological model to predict bubble deformation in turbulence (Chapter 6).

Finally, the summary of this dissertation and the outlook for future research are discussed in Chapter 7.

Chapter 2

V-ONSET (Vertical Octagonal Noncorrosive Stirred Energetic Turbulence): a vertical water tunnel with a large energy dissipation rate to study bubble/droplet deformation and breakup in turbulence

A novel vertical water tunnel facility has been constructed to study the dynamics of turbulent multiphase flow. The new system features several unique designs that allow us to study bubble deformation and breakup in strong turbulence: (i) The mean flow can be adjusted to balance the rising velocity of

buoyant bubbles/droplets so that they can stay in the view area for an extended period of time; (ii) Turbulence is generated and controlled using a 3D-printed jet array that can generate 88 random high-speed momentum jets with velocity up to 12 m/s. This component allows us to attain turbulence with a high energy dissipation rate ($\geq$0.1 m^2/s^3), which is orders-of-magnitude higher than most of the existing turbulent multiphase flow facilities. (iii) Turbulence generated in the test section is nearly homogeneous and isotropic, and the turbulent fluctuations is also decoupled from the mean flow. The resulting turbulence intensity can be varied between 11 – 80 % with a mean flow at around 0.2 m/s. (iv) This system has an octagonal test section that allows multiple views to reconstruct deformable bubbles/droplets in turbulence. Six high-speed cameras were used to simultaneously measure bubble deformation as well as their surrounding turbulence. Both the reconstruction and particle tracking were completed using our in-house codes that are parallelized to run on high-performance computering clusters efficiently.

2.1 Introduction

From dust storms to breaking waves, flows in nature are often turbulent and concentrated with objects in a different phase, such as gas bubbles, oil droplets, or solid aggregates. In these environmental flows, because of the ex-

tremely large length scale and abundant energy, both the Reynolds number (Re) and the energy dissipation rate $\epsilon = 2\nu\langle S_{ij}S_{ij}\rangle$ (ν is the kinematic viscosity and S_{ij} represents the rate-of-strain tensor) are large. Numerous facilities have been built to target high-Reynolds-number turbulence, including classical wind tunnel and water tunnel, large-scale pipe flow facility (König et al., 2014), coaxial counter-rotating disks system (La Porta et al., 2001), and Taylor-Couette setups (Gils et al., 2011; Lathrop, Fineberg, and Swinney, 1992; Ravelet, Delfos, and Westerweel, 2010) as well as other systems that use different working fluid, such as the variable pressure facilities (Hultmark et al., 2012; Bodenschatz et al., 2014), liquid metal experiments (King and Aurnou, 2013), and cryogenic liquid studies (White, Karpetis, and Sreenivasan, 2002). Compared with this decades-long effort to push to high Reynolds number, the effect of high energy dissipation rate has not been paid much attention, even though it is more important than Re in multiphase flows. In multiphase flows, the dispersed phase is typically very small in size, and it only senses the local flow around it, which is controlled by ϵ. Although ϵ is not a dimensionless number, it can be converted to the particle Stokes number St or Weber number We.

We measures the ratio between the turbulent stress acting on bubbles and the surface-tension restoring stress σ/l_b. The turbulent stress on finite-sized bubbles of size l_b ($l_b \gg \eta$) can be related to the energy dissipation rate following the second-order structure function as $\tau = C_2\rho(\epsilon l_b)^{2/3}$ (Hinze, 1955;

Kolmogorov, 1941). C_2, ρ, and η are the Kolmogorov constant, density of the carrier phase, and the Kolmogorov scale, respectively. As the result, $We = C_2\rho(\epsilon l_b)^{2/3}l_b/\sigma$.

In addition to We, bubble deformation can also be affected by its buoyancy force, which is determined by the Eötvös number, i.e. $Eo = \Delta\rho g l_b^2/\sigma$. To make sure that the turbulence-induced deformation outweighs the buoyancy-induced one, one would want to have $We \geq Eo \geq 1$, which provides two equations for two unknowns ϵ and l_b assuming other fluid-related parameters are constant. Based on the calculation, the minimum requirement is that the mean energy dissipation rate $\epsilon \geq 0.57$ m^2/s^3 for bubbles with size in a small range near 2.7 mm. For ϵ much smaller than $O(0.1)$ m^2/s^3, bubbles of all sizes will be dominated either by surface tension (small sizes) or buoyancy (large sizes), never by turbulence–even with the help of the extremely-large energy dissipation due to turbulence intermittency. If one can afford a larger mean energy dissipation rate, the size range of bubbles that is controlled by turbulence will become wider. Note that this calculation is to provide an order-of-magnitude estimation rather than a specific number, as the critical Weber number for bubble deformation is of order unity rather than the value of one. So the goal of the designed facility is to reach $\epsilon \approx O(0.1)$ m^2/s^3.

Using the second-order structure function to estimate turbulent stress on bubbles is a standard practice in the chemical engineering community to study

steady-state emulsion droplet size distribution (Maaß et al., 2010). However, strictly speaking, this formulation only works for homogeneous and isotropic turbulence (HIT). The flow in a stirred vessel is highly inhomogeneous and anisotropic, and bubbles/drops tend to shatter into tiny pieces if encountering strong shear region near the surface or tip of the impeller. The bubble breakup frequency and dynamics are not the same everywhere in the system, and they are sensitive to the design of the impeller and tank geometry (Zhou and Kresta, 1996).

To overcome this problem, vertical water tunnels have been constructed in at least two research groups (Ravelet, Colin, and Risso, 2011; Mercado et al., 2012) before to study bubble dynamics in turbulence. Both these tunnels have some interesting design features. One system has a rotating grid that was used not only to generate turbulence but also to create a large-scale vortex to trap bubbles near the centerline of the test section. In spite of this rotating mean flow, flow exhibits a clear inertial range and seems to be homogeneous in the axial direction. ϵ in this system was not reported but can be estimated based on the fluctuation velocity u' and the integral length scale L, $\epsilon \approx u'^3/L = 7 \times 10^{-3}$ m^2/s^3, which is much smaller than 0.1 m^2/s^3 that is needed. Although bubbles can still be deformed by turbulence when the local energy dissipation rate of the flow is significantly higher than its mean, the probability of bubbles encountering such strong local turbulence is rather low. The Twente Water Tun-

nel is another signature vertical water tunnel facility that has been used to study light particles. The system features an active grid that is used to generate turbulence. The active grid can increase the turbulence intensity and energy dissipation rate, but to a limit. In this system, as the mean flow increases from 0.22 m/s to 0.67 m/s, ϵ grows from 3.9×10^{-5} m^2/s^3 to 7.86×10^{-4} m^2/s^3. For the upper limit of ϵ, assuming bubble size varies from 1 mm to 10 mm, We is from 2.4×10^{-3} to 0.11, whereas Eo ranges from 0.13 to 13.6, nearly two orders-of-magnitude larger than We. This calculation suggests that, for deformable bubbles, the buoyancy-induced deformation (measured by Eo) dominates over the turbulence-induced deformation (measured by We). This difference only increases for larger bubble size as $Eo \propto l_b^2$, which grows faster than $We \propto l_b^{5/3}$ for a constant ϵ.

In addition to these two water tunnels, bubbles have also been studied in other facilities, e.g. the Twente Taylor-Couette system (Gils et al., 2013) to study drag reduction. Bubbles in this system are clearly deformed (ibid.). Although the global-averaged energy dissipation rate is large (ibid.), $\epsilon = 1.96$–13.5 m^2/s^3 (may even reach more than 180 m^2/s^3)(Gils et al., 2011), most of it comes from the shear within two thin boundary layers. The bulk region that is closer to HIT condition has a much smaller energy dissipation rate from 10^{-4} to 1 (Ezeta et al., 2018). Bubble deformation in this system is affected both by the mean shear and by the local turbulent fluctuations. So one of the design

goals for V-ONSET is to isolate the effect of turbulent fluctuations on bubble deformation and breakup by removing the mean shear.

The passive grid or active grid method, although standard for producing turbulence in water tunnels, are not adequate to create turbulence with a large energy dissipation rate ($\epsilon \geq 0.1$). These methods rely on siphoning energy from the mean flow to drive turbulence, and only an extremely-large mean flow can supply sufficient energy dissipation rate. A large mean flow is always problematic for optical diagnostics because bubbles often travel with the mean flow quickly in and out of the view area, creating a large statistical bias. To overcome this problem, we seek design inspirations from other turbulence facilities. In recent years, different mechanisms have been successfully used to generate HIT in a closed box. These mechanisms include oscillating grids (De Silva and Fernando, 1994; Villermaux, Sixou, and Gagne, 1995; Srdic, Fernando, and Montenegro, 1996), propellers (Zimmermann et al., 2010), loudspeakers (Birouk, Sarh, and Gökalp, 2003; Hwang and Eaton, 2004), or jets (Bellani and Variano, 2014; Carter et al., 2016). Momentum is injected into the system from multiple symmetrical locations. The symmetry includes two facing planes (Bellani and Variano, 2014; Carter et al., 2016), eight corners of a cube (Birouk, Sarh, and Gökalp, 2003; Hwang and Eaton, 2004) or polyhedrons (Zimmermann et al., 2010). It has been shown that planar injection produces HIT in a region that covers almost the entire cross section of the system (Bellani and

Variano, 2014). The facing jet array design used in closed systems adopts a random forcing scheme by actuating jets randomly in space and in time (Bellani and Variano, 2014). The random forcing is designed to prevent the development of any persistent secondary flows in the system (Variano, Bodenschatz, and Cowen, 2004).

The symmetric forcing using injections from multiple corners produces HIT confined in a small region at the center, and outside of this region the flow recovers the characteristics specific to the way that the momentum is injected. Since turbulence decays as it moves away from the nozzle or loudspeaker, ϵ at the center is typically orders of magnitude lower than that near the injection point. As a result, the system features a low-ϵ core that is HIT but covered with a large shell of non-HIT with a much larger ϵ. If bubbles or droplets are introduced near the boundaries, they will be severely deformed or broken before even entering the HIT region. As a result, the only option is to inject bubbles or droplets directly into this region, but then the memory of injection could bias the statistics of bubble deformation and breakup as it is known that bubbles could experience a series of oscillation after detaching from a submerged needle even in a quiescent medium and it could be more complicated when there is a flow present or the needle is not perfectly aligned vertically (Oguz and Prosperetti, 1993).

For our system, turbulence is driven by the momentum jets coming from a

plane. After some developing length, flow starts to become HIT within a thick slab that covers a large cross-sectional area. In a vertical water tunnel, the momentum injection plane should be placed at the top of the test section where ϵ is the strongest at about 4×10^4 m^2/s^3. As flow moves away from the injection plane into the test section, turbulence quickly decays and ϵ gets smaller and smaller. Bubble injection is at the bottom of the test section where ϵ is the smallest. As bubbles rise, they experience flow with a growing ϵ, and their breakup probability starts to increase. The view area is set at a location where $\epsilon >$0.1 m^2/s^3 and bubbles with a few millimeters in size will undergo strong deformation and breakup. This location is far away from the injection point, and any memory of the injection will be lost by the time bubbles entering the view area. The ϵ mentioned above was calculated from compensated second- and third-order structure functions; the details of structure function calculations along with other flow characteristics will be discussed later in chapter 2.

2.2 Experimental apparatus

The new facility is constructed to meet three goals: (i) the system should be able to slow down the bubble rising velocity; (ii) the system can generate turbulence that is nearly HIT over a large region; (iii) generated turbulence should have a large energy dissipation rate.

The experimental facility, V-ONSET (Vertical Octagonal Noncorrosive Stirred Energetic Turbulence), is designed to meet these goals. The system is essentially a vertical water tunnel with an octagonal test section coupled with a jet array on the top of the test section. The system contains several subsystems: main flow loop, turbulence generator and controller, bubble injector, contraction section, filtration and other components. Each subsystem and their respective control mechanisms will be discussed and introduced in the following sections.

2.2.1 Main Flow Loop

V-ONSET is made of noncorrosive materials such as fiberglass, acrylic, and PVC for hosting purified and deionized water as well as salt water. In contrast to most water tunnel designs, mean flow and turbulence can be controlled independently in V-ONSET. The main flow loop of the tunnel adopted a modular design such that each section can be swapped and connected in a different order to switch the mean flow direction between top-down or bottom-up configurations. This tunnel is designed for studying different types of multiphase flows, including light and heavy particles with different densities.

Driven by buoyancy, the terminal rising velocity of bubbles u_s roughly scales with the size of the bubbles as $u_s \propto \sqrt{l_b}$ (Wu and Gharib, 2002). For light or heavy particles with diameter of a few millimeters in quiescent water, u_s is

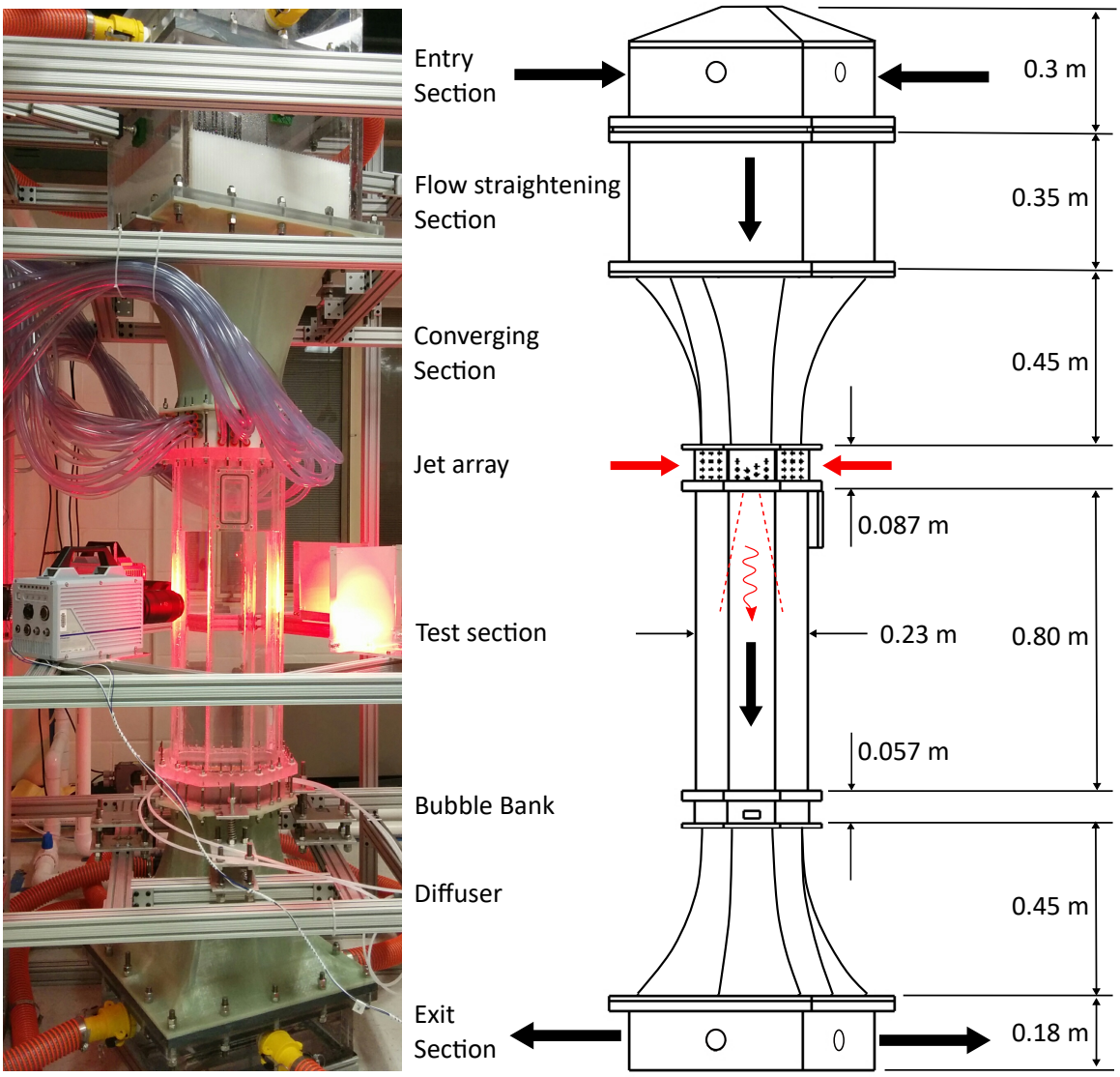

Figure 2.1: Picture and different components of V-ONSET with the total height of the facility being 2.67 m.

about 0.08 – 0.32 m/s (Wu and Gharib, 2002; Talaia, 2007). In comparison, the fluctuation velocity $u' = \sqrt{(u_1'^2 + u_2'^2 + u_3'^2)/3}$ is about 0.04 – 0.24 m/s, which is of the same order of magnitude as the bubble rising terminal velocity in a quiescent medium. If there is no mean flow, bubbles or particles may exit the

view area in the vertical direction faster than it will from other two directions, which may lead to biased statistics. To avoid this finite view area effect, the mean flow along the vertical direction $\bar{w}$ is adjusted to u_s but in the opposite direction.

Most traditional wind/water tunnel design takes a large footprint because the return loop has almost the same cross-sectional area as the main section to reduce the pressure drop and maximize the flow rate in the system. In our system, the mean flow is used only to suspend bubbles not to drive turbulence, so it was kept very low. This allows us to reduce the size of the return loop significantly. The return section is made of 5.1 cm-diameter PVC pipe. When the cross-sectional size reduces from 23 cm at the test section to 5.1 cm at the return loop, the flow velocity increases roughly by 20.3 times and the pressure drop increases by 413.6 times. But the pump can still afford such a large pressure drop through the entire system.

When only the mean flow is turned on, bubbles of millimeter in size stop rising up in the test section. Bubbles that are much larger will still be able to rise through the view area, although at a reduced velocity. Much smaller bubbles will be flushed with the mean flow to the bottom of the main loop and back to the top of the tunnel through the return loop. At the top of the tunnel, there is a large mixing tank with a contracting cone-shaped top that is used to trap bubbles, force them to merge, and release them back to air. By relying on

this mechanism, between two experiments, the mean flow will be kept on for about forty minutes to completely remove the fragmented bubbles from the entire system. After running the mean flow for about twenty minutes, the water becomes fully clear and bubbles are gone. The total number of tracer particles can be identified on camera images typically decreases by $<10\%$ between two runs of experiments. This indicates that the remaining micro-bubbles in the system between experiments, if exist at all, are fewer than tracer particles lost between runs .

The mean flow acts as a filter to select bubbles of certain size range depending on their rising velocity. The interesting part is that bubbles staying in the test section do not freeze completely. They jiggle around at a relatively fixed location. This motion is likely driven by their unsteady wake dynamics (Ern et al., 2012). Now the mean flow essentially moves the lab reference frame with the bubble mean rising velocity, so a spiraling or zigzagging rising motion appears to be a local jiggling motion.

2.2.2 Turbulence generator and controller: high-speed jet array

The mean flow loop and the turbulence control loop are divided after the pump, but later reunited in the test section using a jet array, which is the heart of the entire V-ONSET. The jet array looks like a bar grating. 88 circular

nozzles of 5 mm in diameter are positioned in a staggered pattern with 2.1 cm apart from each other on the bottom surface of the jet array, as shown in Fig. 2.2(b). These nozzles are used to inject high-speed water jets into the test section coaxially with the mean flow. The turbulence characteristics are generated and controlled by the switching pattern and speed of these high-speed jets. In addition to these nozzles, 52 square through holes with 2×2 cm^2 in cross-sectional area are left for the mean flow to pass. The length of these through holes is 8.7 cm, same as the thickness of the jet array. After the jet array, the high-speed jets and mean flow merge together and produce turbulence with a low mean flow and high turbulence intensity $\sim$80%.

The mean flow uses most of the flow rate from the pump but only takes 1.12% of the total pressure head when the jet velocity is 10 m/s and the mean velocity through the test section is 0.25 m/s. On the other hand, turbulence generation loop consumes most of the pressure head because the nozzle diameter is much smaller than that of the return loop. Small nozzles also limit the total flow rate in the turbulence generation loop. Since two flow loops have very different but compatible needs, only one pump was used to supply for both loops. Two loops are connected in parallel, and their respective flow rate and pressure head are controlled by two proportional valves and monitored by two flow meters with accuracy of $\pm$1%. This allows us to accurately control and quantify the mean flow velocity and jet velocity.

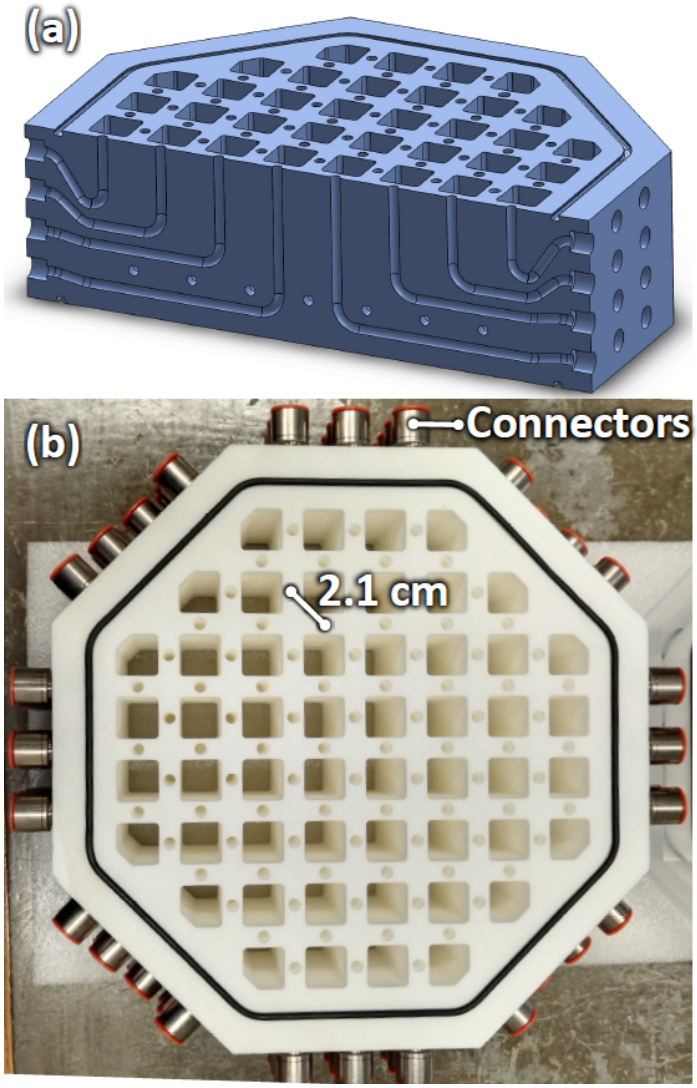

Figure 2.2: (a) A 3D schematic of the jet array showing the holes on side faces which are connected to their respective holes on the top face through internal channels. It also shows grid openings across the structure that allow mean flow to pass through it; (b) A photograph of the 3D printed jet array fitted with an O-ring at the top and push-to-connect fittings on the side

The jet nozzles are connected to the side openings through internal channels, as shown in the cutaway view in Fig. 2.2(a). Note that there are seven holes near the bottom of the cutaway plane, which indicates another seven in-

ternal channels going perpendicular to this plane. The arrangements of all internal channels are designed based on three principles: (a) There has to be a sufficiently-long (six nozzle diameter) vertical channel before the nozzle exit to ensure straight coaxial jet with similar jet profile; (b) Inlets are distributed evenly on eight walls, shown as the red connectors in Fig. 2.2(b). Every nozzle needs to be connected to one inlet on the closest wall. This design features two key flow isolations: the square through holes for the mean flow and the internal channels for the jets are separated, and the individual channels for the jets are also separated from each other. The wall thickness of each nozzle is set at 2.5 mm to make sure that the high-pressure water jets do not leak through different channels.

Due to the complexity of 88 curved internal channels stretched around 52 squared holes, we decide to use additive manufacturing (so-called 3D printing) method to construct the jet array. Many methods have been tested, and most extrusion-based methods are not water-proof even at a very low material porosity (high material density). Metal powder Selective-Laser-Sintering (SLS) process is too expensive for a structure at this large scale. After several iterations, the best option is to use PA12 polyamide 60 μm size powders fused together through SLS process. The printed structure is water proof with around 48 MPa maximum tensile strength based on the ASTM D638 standard. Note that the material strength is so high that the jet array can handle a much

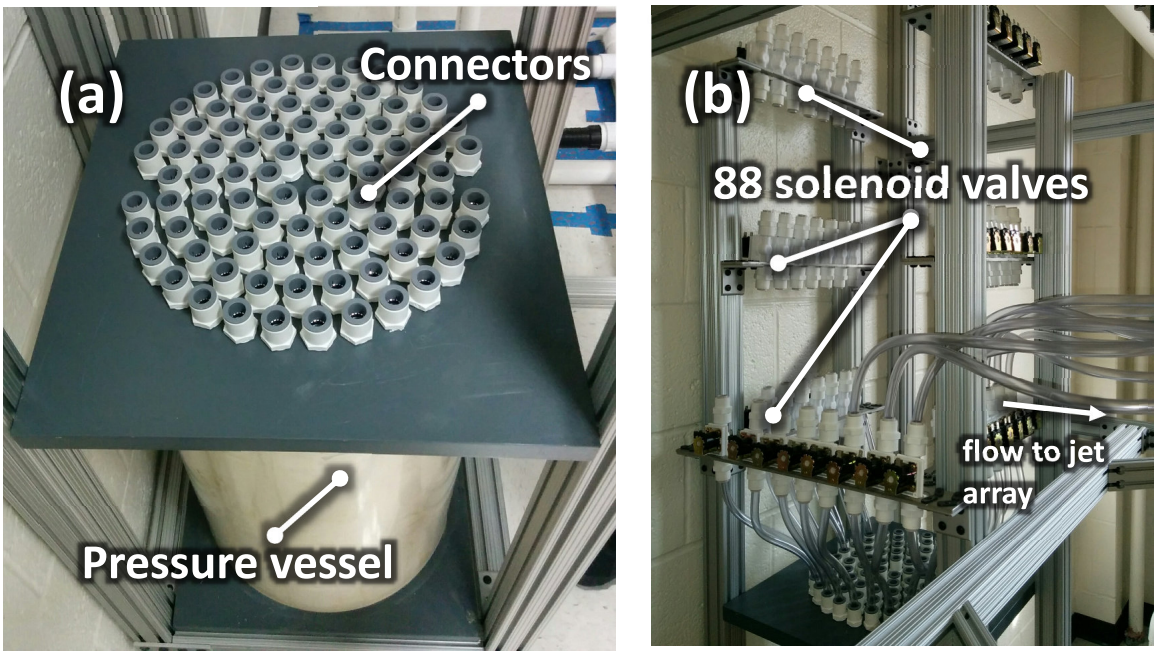

Figure 2.3: Pressure manifold & Solenoid valves used to control the high speed water jets used for generating turbulence in the test section

higher pressure than what the system was operated at.

Each nozzle in the jet array is controlled by a dedicated solenoid valve that opens and closes the jet from a common pressure vessel. The pressure vessel features a cylindrical storage tank with outer diameter of 0.36 m and wall thickness of 9.5 mm. The top end of the vessel is covered with a 0.05 m thick PVC plate and is fitted with 88 outlets. The bottom of the vessel is sealed with the same PVC plate fitted with a 0.051 m diameter pipe as the inlet. Given the large pressure surges caused by the frequent switch on-off of the jets, the inlet is connected to a variable pressure release valve to mitigate the water hammering problem.

The key difference between our jet array design and many previous versions driven by submerged pumps (Bellani and Variano, 2014; Variano, Bodenschatz, and Cowen, 2004; Variano and Cowen, 2008) is that the jet velocity u_j can be much larger. For example, in our current configuration, the record of u_j is 12 m/s from each nozzle, and it can be pushed even higher as long as our pressure vessel can withstand the pressure. For our purpose, at least for now, 10 – 12 m/s jet velocity is sufficient. Another benefit of this jet array design is that the jet is a momentum jet with zero net mass flux. Water supply of these jets comes from the upstream of the jet array. When a jet is fired down into the test section, the incompressible water forces the same amount of water taken away from exactly the same plane through those square through holes. Most other jet array systems that rely on submerged pumps do not necessarily have the suction end and nozzles co-located at the same plane, potentially resulting in some small amount of mass flux. In our system, this zero mass flux is inherent to the design and guaranteed.

Although the net mass flux is zero, each jet does not follow a classical synthetic jet profile (Smith and Glezer, 1998). In our system, the mass is taken away uniformly from these squared holes across the entire jet array cross-sectional plane, which is different from the alternating momentary ejection and suction of fluid across an orifice as used in classical synthetic jets (Glezer and Amitay, 2002). The Reynolds number of each jet produced by our jet array,

based on the jet velocity of 12 m/s, is about $Re = 6 \times 10^4$, which is well into the turbulence regime.

For the turbulent round jet, in the near field, most kinetic energy is contained within the mean flow. In the far field ($x/d > 15$), as the kinetic energy continues to transfer from the mean flow to the turbulent fluctuations, the jet half-width $R_{1/2}$ grows linearly as a function of the streamwise coordinate x as $R_{1/2}(x)/d = K_d(x - x_p)/d$, where x_p is the virtual jet origin and K_d is about 0.1 (Malmstr oem et al., 1997). At this large Reynolds number ($Re > 50,000$), after scaling with the jet width, the jet profile should be self-similar (self-preserve) (Pope, 2000). The energy dissipation rate of the flow can be as large as 2000 m^2/s^3 at $x/d = 15$ away from the nozzle (Martínez-Bazán, Montanes, and Lasheras, 1999). But in this range, the flow is dominated by the jets. As x/d increases, ϵ drops quickly. For the view area resided 38 cm (x/d=76) away from the jet array, the half width of the jet is close to 3.8 cm, which is larger than the jet spacing of 2 cm. This suggests that, at this distance, jets are likely to be fully mixed with each other and also with the background turbulence. Most of the kinetic energy has been converted from the mean flow to the turbulent fluctuations. Even though ϵ reduces to 0.16 m^2/s^3, the view area is still chosen at this location to make sure that any dynamics seen in our system is driven by HIT rather than turbulent jets. Ideally, we would like to vary the distance between the view area and the jet array. But the six-camera

optical configuration that we designed to reconstruct the complex shapes of deformable bubbles in the tunnel becomes too heavy and cumbersome to move up and down. The view-area-to-nozzle distance has been kept constant so far.

Each jet is controlled by a solenoid valve, which can be switched on and off by a relay board. The relay board is controlled by a LabView code that programs the on-off time of each nozzle. The system allows us to open all 88 nozzles if necessary, but so far we have not tried to open all jets because opening only eleven jets is sufficient to provide a large energy dissipation rate.

The spatial-temporal jet driving pattern is similar to what has been used in other jet array systems (Bellani and Variano, 2014; Variano and Cowen, 2008). The probability of each jet being on is 12.5%. The total number of open jets at any given time follows a Gaussian distribution (mean $\mu = 11$, standard deviation $\sigma = 3$). Each random pattern lasts for three seconds. During experiments, pressure surges caused by water hammering is not as dangerous as turning off too many jets suddenly. For most following studies, the control system forbids the number of jets at any time from going below nine, because one pressure vessel broke after turning off too many jets.

2.2.3 Bubble/droplet bank

Bubble bank is an octagonal structure located right below the test section. As shown in Fig. 2.4, it is composed of two structures: (i) a base that is used

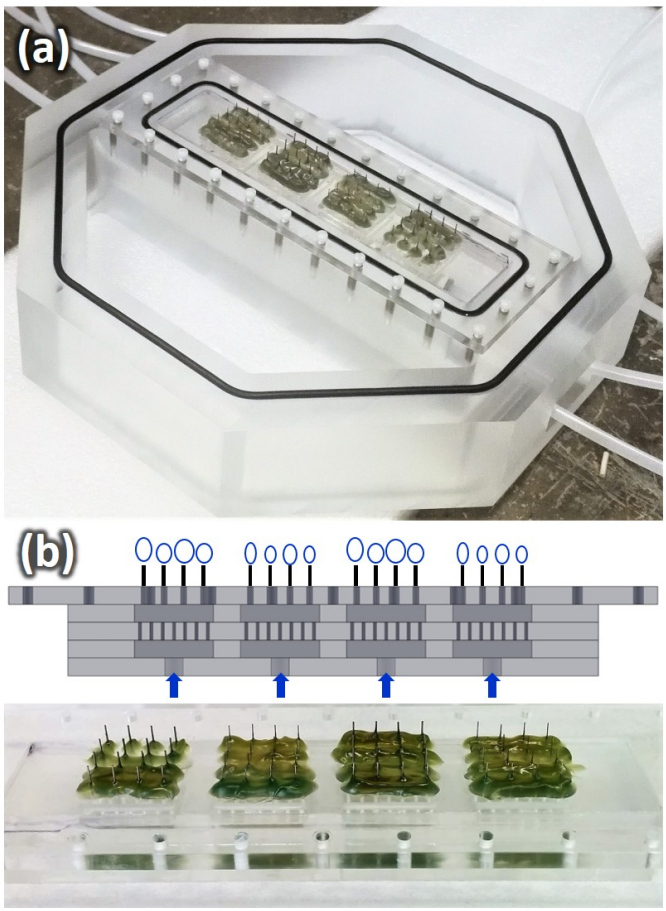

Figure 2.4: (a) Bubble bank base housing the gas flow distributor (b) Closer look at the capillary island fitted with hypodermic needles and showing 5 levels constituting the gas distribution arrangement to ensure uniform gas flow to the capillary island

to connect to the tunnel (Fig. 2.4(a)), (ii) a gas flow distributor that uniformly sends air through independently-controlled islands of hypodermic needles to generate bubbles (Fig. 2.4(b)). These two components are connected and sealed using nylon screws and an O-ring, rather than using permanent glue. This design allows us to easily switch capillary islands for different experiments as the island that is used for oil with surfactants cannot be reused for gas bubble injection.

Another unique part of our design is that the gas flow distributor is designed like a shower head with five layers of structures to distribute flow and pressure head from one inlet to an array of needles uniformly. Out of total four islands, two of them contain gauge 25 (inner diameter: 160 μm, outer diameter: 300 μm) needles, whereas the other two house gauge 30 (inner diameter: 260 μm, outer diameter: 500 μm) needles. These needles are permanently glued to the acrylic plate using plastic-steel glue. The bubble/droplet bank allows us to inject bubbles or oil droplets with a wide size distribution by adjusting the needle gauge and the air flow rate through the needles.

2.2.4 Flow conditioning section

To maintain a relatively-uniform mean flow in the test section, the flow needs to be conditioned to remove as much of the secondary flow generated from other parts of the tunnel as possible. The largest source of uncontrolled

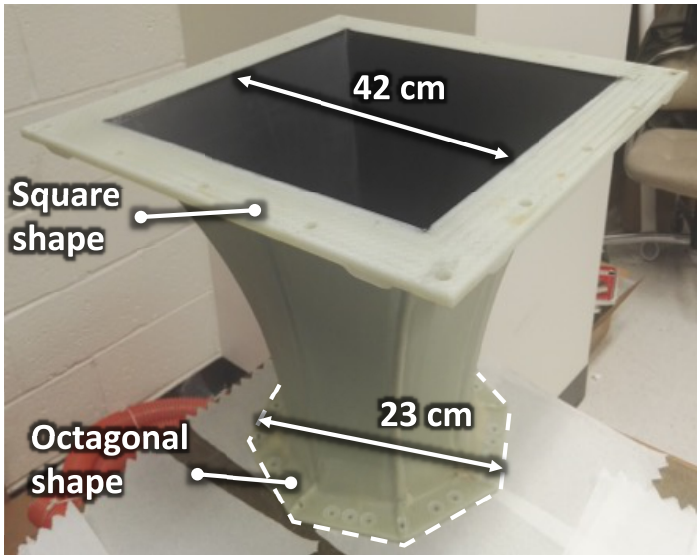

Figure 2.5: Contraction section made of fiber glass

secondary flow is produced in the top mixing tank, where flows coming from four small pipes mix together. Immediately after this mixing tank, a pressure plate with many small holes is used to distribute the pressure uniformly to the entire cross section. The settling chamber that holds a honeycomb structure is connected to the pressure plate to force the flow to become laminar.

Below the settling chamber, the contraction section is a key component in most wind tunnel and water tunnel designs. The contraction accelerates and aligns the flow into the test section, and it also helps to stretch vortices that survived the honeycomb structures to continue to reduce the turbulent fluctuations. If the goal is to reduce the turbulence intensity down to less than 1%, the contraction ratio of this section has to be large than 4:1. For example, the Stanley Corrsin wind tunnel at Johns Hopkins features a contraction ratio of 25:1

(Hak and Corrsin, 1974). For our case, we simply adopted the same design to reduce the uncontrolled turbulence resulting from the large mixing tank at the top of the tunnel. With the help of a pressure plate and a honeycomb structure upstream, this contraction section with contraction ratio 4:1 helps to reduce the upstream turbulence that is not desired in our test section.

The other key purpose of the contraction section is to convert the cross-sectional geometry. The octagonal design of the test section posed many manufacturing challenges. If we have to maintain this geometry throughout the entire water tunnel, the problem escalates and the cost of the tunnel would increase probably by a factor of two. The contraction section is designed to convert the cross section from a squared geometry to an octagonal geometry. A plug for fiberglass molding was made with a CNC machine first, and the fiberglass materials were laid on the plug to make the actual contraction section. The structure also has flanges at both ends to connect to the other side.

2.2.5 Filtration and other components

For bubbles/droplets, the interfacial contamination could change the dynamics significantly. The water purification system has to be very efficient and capable of producing large amount of water overnight. V-ONSET has a dedicated water purification system (Pacific TII by Thermo Scientific). It is a three stage water purification system that can provide Type II purified wa-

ter. The purification system can produce purified water at 7 liters per hour. A customized recreational vehicle (RV) storage tank with volume of 0.57 m^3 was purchased to connect to our purification system. A timer was designed to control the total amount of water produced. One night before experiments, the purified water would be produced and stored in the tank. The water would also be degassed by connecting the tank with a vacuum pump. Although one side of the tank is deformed during degassing, the tank is strong enough to survive the process.

The flow circuit of V-ONSET contains two pumps – a large 7.46 kW three-phase pump, and a smaller 1.12 kW three-phase pump. Both pumps offer some advantages compared to the other. The large one is a high flow rate pump with the maximum flow rate of 0.016 m^3/s and a maximum pressure of 561.8 kPa. This pump is used as the main energy source to create both mean-flow and high-speed water jets. The small pump can provide a maximum flow rate of 3.8×10^{-3} m^3/s and a maximum pressure of 328.4 kPa, which serves as an auxiliary pump that is mainly used for filtration and filling the tunnel. In addition to the water purification system, water in the tunnel also needs to be regularly filtered and sanitized. For example, high-concentration of tracer particles needs to be removed from the system using two 50 micron sedimentation filters (FM50-975 by Flow Max) that can allow flow rates up to 6×10^{-4} m^3/s withstanding a maximum pressure drop of 275.8 kPa. This filter has one of the

largest flow rate that we could find, but it still cannot keep up with the flow rate supplied by the large pump. So the small pump is used to circulate water through the filters. In addition to filters, a UV system was also connected to remove any bacteria growing in the system. In addition, occasionally for some experiments that do not need mean flow, the small pump is sufficient to drive the jet array to create strong turbulence.

2.3 Imaging System

2.3.1 Octagonal test section

Fig. 2.6 shows the test section of the tunnel, which is 80 cm tall and 23 cm in diameter as an inscribed circle. The tank is made of 25.4 mm thick acrylic sheet for optical access. Both ends of the test section are glued with a flange that is made of the same material. The inner side of the test section can be reached from a small window that is about 5×10 cm^2 in size. This window is typically used to provide access to the inner side of the test section. For example, before filling up the entire tank, a calibration target required for the optical diagnostic system is put into the tank through this window. This opening is located near the top flange and the jet array because this portion of the test section is reserved for jets to merge and mix together, so no optical access is needed.

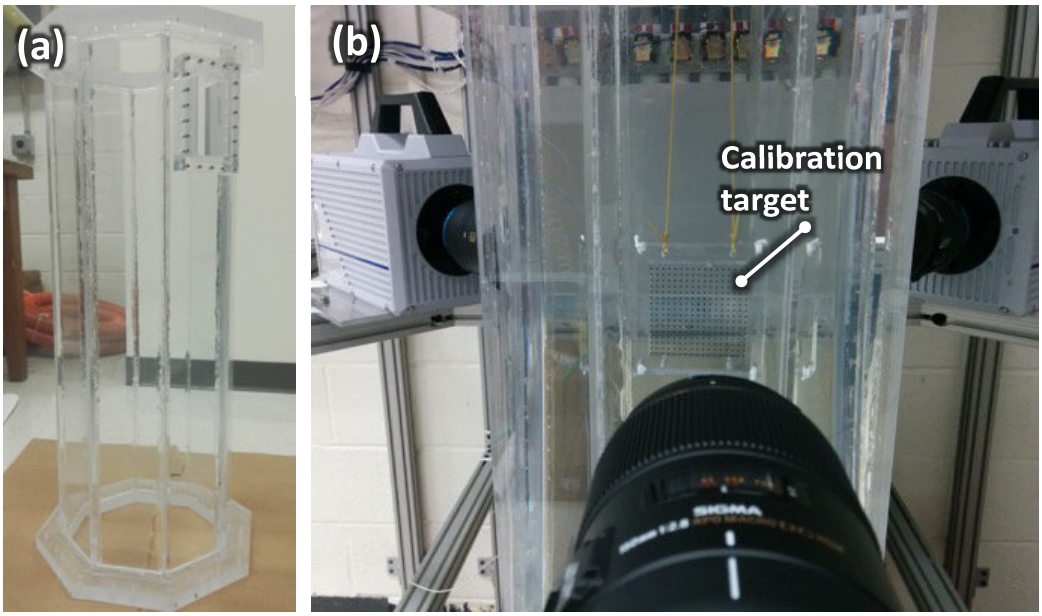

Figure 2.6: (a) Picture of the 80cm long octagonal test section. It also shows a window on one of the faces to insert a calibration target; (b) Three of the total six cameras look at a transparent target with an array of dots with known positions in the center of our view area.

The facility was designed to study 3D complex deformation and breakup dynamics of bubbles or droplets in strong turbulence. The octagonal test section is selected because we would like to have cameras covering the entire perimeter of the test section from multiple different directions. This camera configuration is crucial both for the 3D reconstruction of complex deforming bubbles and for having more than three cameras to simultaneously view many tracer particles close to bubbles without being shadowed. In addition, an octagonal test section helps to avoid using the liquid-filled prisms that typically limit the view area.

These optical benefits outweigh the manufacturing complexity. Most challenging part of manufacturing the test section is to glue all eight walls of the tank together. Two edges along the length direction of the acrylic slab need to be machined to exact 67.5 degree angles. All of the eight walls after precise machining were held together with the help of an octagonal inner supporter and binding straps from the outside. Acrylic solvent was applied at the mating edges using a syringe and spread evenly within the edge thanks to the capillary forces. Additional grooves were machined into the joints near the inner side to add another strengthening thick acrylic-based glue to make the joint stronger and avoid any possible cracks to damage the tank.

To image the dispersed phase, backlighting is selected because it is the best to generate sharp images of bubble/droplet (Jordt et al., 2015) without strong reflection that would occur if using laser diagnostics. The imaging system was

Table 2.1: V-ONSET Controllable Parameters

Controllable Parameters			
$N_{jets,total}$	$\langle N_{jets,on} \rangle$	u_{jet} (m/s)	$\langle u \rangle$ (m/s)
88	11	2.455	0.1965
88	11	11.92	0.2322

Table 2.2: V-ONSET Turbulence Characteristics

Turbulence Characteristics					
u' (m/s)	ϵ (m^2/s^3)	$Re_\lambda = \sqrt{15u'L/\nu}$	$L = u'^3/\epsilon$ (cm)	τ_η (ms)	η (μm)
0.0383	0.00125±0.00023	160±15	4.49±0.8	28.3±2.5	168±7
0.2122	0.16 ± 0.02	435 ± 20	5.97 ± 0.70	2.5 ± 0.15	50±1.5

designed to achieve simultaneous measurements of both phases. The system consists of six high speed cameras. Normally in fluid dynamics community, four-camera setup has been proven to be sufficient to acquire the 3D velocity field. Even though the cost of six cameras is more than the four-camera configuration, it has two significant advantages: (i) visualizing bubble deformation with large degrees of freedom requires shape reconstruction that typically requires more than four views. In general, three orthogonal views are minimum requirement for shape reconstruction. The benefit of having every additional one camera is similar for the fourth to sixth camera. The benefit in terms of the improvement of the reconstruction fidelity starts to decrease for the number of cameras more than six. If one axis cannot be accessed due to flow or laser light, such as the vertical direction occupied by the flow in our case, one

needs more cameras. Six-cameras configuration is chosen to maximize the benefit (reconstruction fidelity) and cost ratio per camera. (ii) In addition to the shape reconstruction, the other goal of the project is to measure the dynamics of flows surrounding these deforming and breaking bubbles. This requires particles around these bubbles to be imaged by at least three to four cameras. One problem for finite-size bubbles is that they block views of particles behind them, leaving a blind spot that can only be accessed from another camera from almost 90 apart. If one wants a reliable reconstruction of particles in these blind corners, more cameras are needed to cover these blind corners.

Fig. 2.7 shows our camera configuration. Cameras need to be positioned to cover as many orthogonal views as possible. In practice, camera views are limited by the tunnel configuration and illumination designs. For example, in our system, cameras cannot be placed in the vertical direction because of the vertical alignment of the tunnel. To mitigate this problem, four cameras are positioned in the horizontal plane to cover at least two orthogonal views, and two cameras (Cam 5 and Cam 3) are tilted to provide some information in the vertical direction. To keep the integrity of the tunnel, no liquid prisms were used for these two cameras, so the tilted angle is very small to avoid refraction-led uncertainty.

The diffused LED are used to image the deformable dispersed particles as they have been shown to be most effective in imaging finite transparent

bubbles and droplets (Jordt et al., 2015). The carrier phase is seeded with polyamide tracer particles for performing Lagrangian Particle Tracking (Ni et al., 2015). These particles have nominal radius a of 30 μm with density close to 1.03 g/cm^3. The particle response time τ_p ($\tau_p = 2a^2\Delta\rho/(9\nu\rho_f)$) is approximately 6 μs; The Kolmogorov time τ_η ($\tau_\eta = \sqrt{\nu/\epsilon}$) is about 2.2 – 3.5 ms. The ratio of these two timescales leads to the Stokes number, which is much smaller than unity for these particles ($St = \tau_p/\tau_\eta \ll 1$) (Raffel et al., 2018), indicating that these particles can be safely treated as tracers. Also, It has been shown that adding tracers has a negligible effect on bubble rising velocity (less than 1%) as compared to that in pure water (Lindken and Merzkirch, 2000, 2002). This helps to justify that adding particles may not alter the interfacial dynamics significantly, but the contamination of the interface is possible and cannot be completely ruled out.

2.4 Example of Flow Measurement

Prior to experiments, tracer particles were injected into the system from the mixing tank at the top. Tracer particles get quickly mixed with water and transported down into the test section. The concentration was kept low in the very beginning of our experiments. A few test images were acquired to estimate the concentration of particles in the view area. Some of the low-concentration

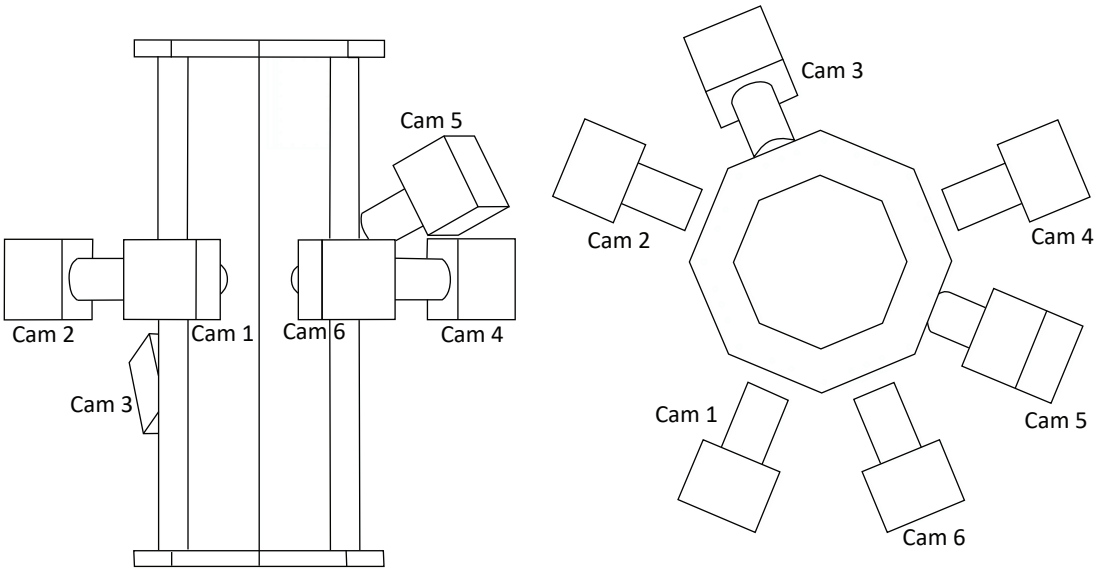

Figure 2.7: Schematic of six high speed cameras positioned around the octagonal test section of V-ONSET including (left) the side view and (right) the top view.

datasets were acquired and used to improve the calibration results. After this procedure, the concentration was gradually increased until the number of particles on 2D images was roughly from 10,000 to 20,000 for our cameras with one mega-pixels resolution. Since particle shadow imaging was used, the shadows of tracer particles in front of the white background were projected onto the imaging planes of all six cameras. The images were then inverted to have bright particles in front of a dark background. Most tracer particles appeared to have three to five pixels in diameter on images. Their positions were triangulated and tracked over time using our in-house shake-the-box code (Tan et al., 2019a). The code was parallelized to run on the Maryland Advanced Research Computing Center (MARCC). For each experiment, the raw images

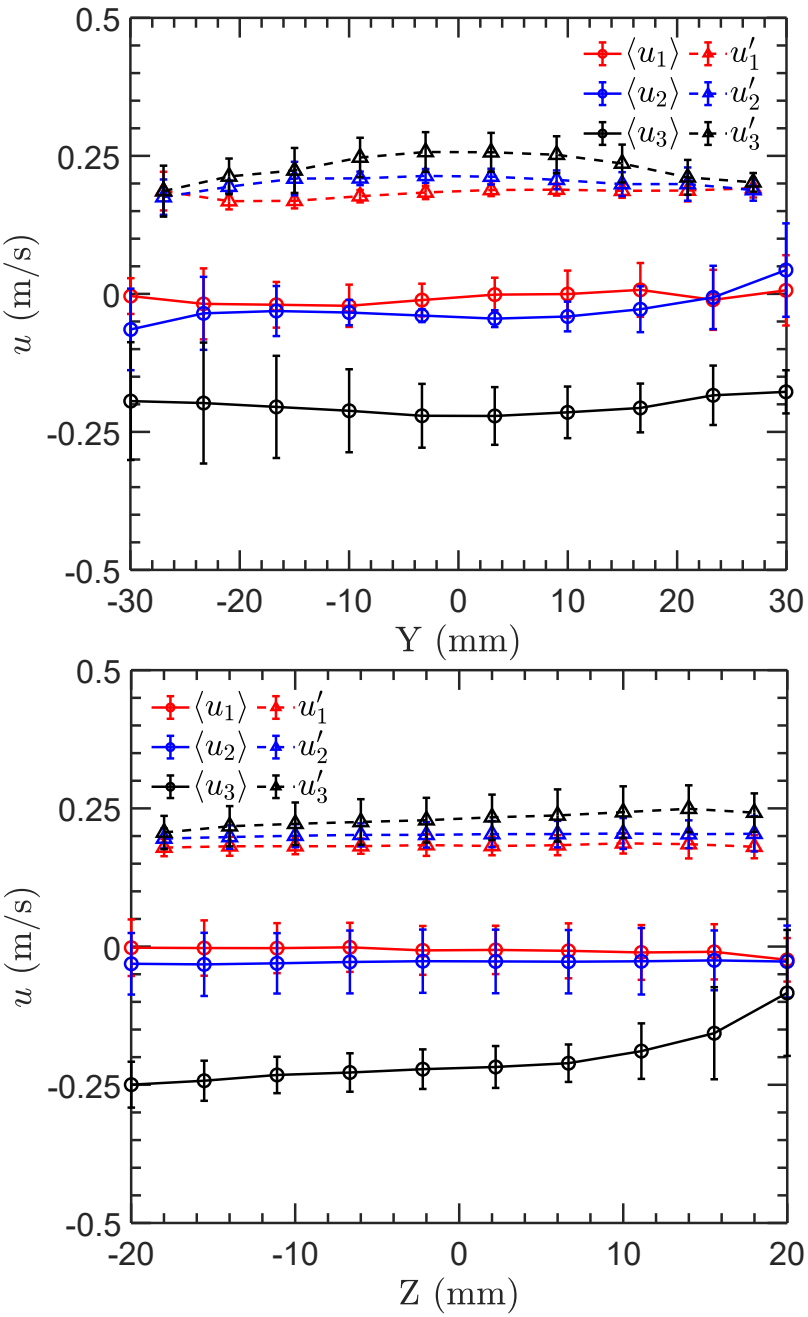

Figure 2.8: The mean and fluctuation velocity ($|\langle u \rangle|$ and u') are plotted as a function of (a) the horizontal axis (X) and (b) the vertical axis (Z). The error bar indicates the standard deviation of the velocity in other directions.

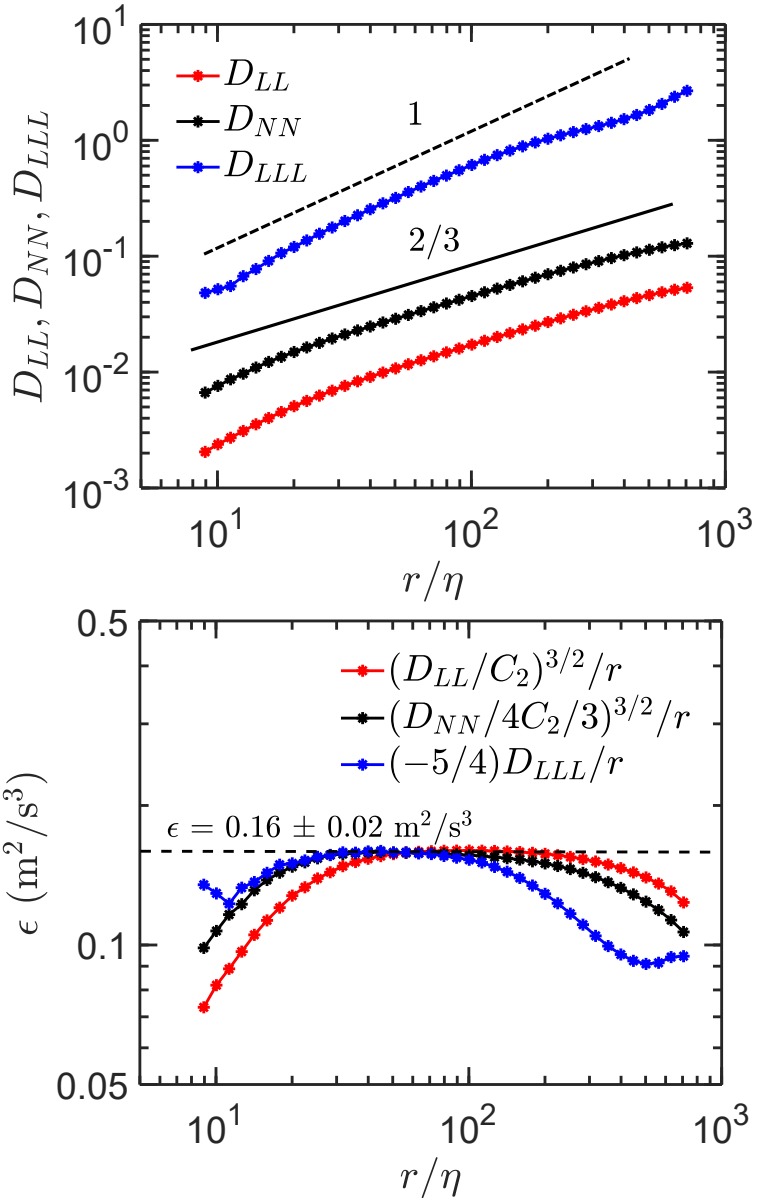

Figure 2.9: (a) The second-order longitudinal (D_{LL}) and transverse (D_{NN}) structure functions as well as the third-order longitudinal structure functions (D_{LLL}) as a function of scale separation r. The dashed line indicates r^1, and the solid line shows $r^{2/3}$. (b) Energy dissipation rate ϵ (m^2/s^3) estimated by structure functions compensated by their respective scaling laws. The plateau height can be used to estimate ϵ.

were uploaded to MARCC and simple image preprocessing was done. Particles were tracked and their trajectories were stored in a binary file. MARCC allows us to run multiple jobs at one time, which significantly improves the speed of our data analysis.

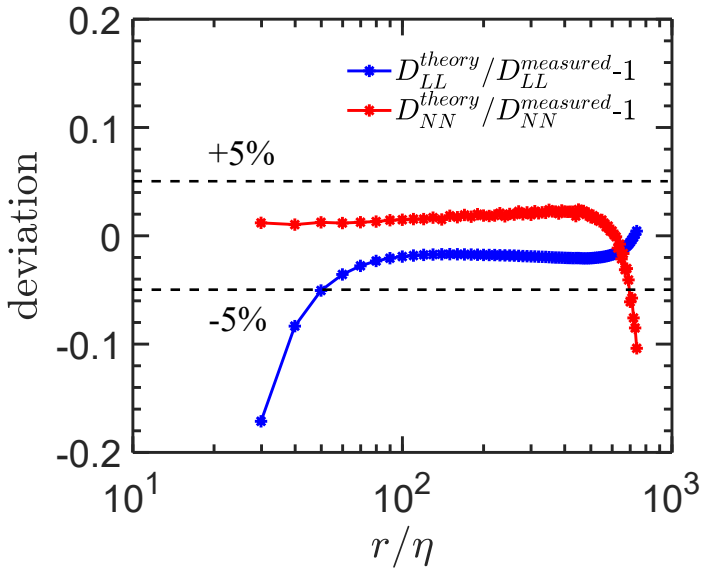

Figure 2.10: The deviation between the measured and calculated second-order longitudinal (D_{LL}) and transverse (D_{NN}) structure functions versus length scale r. The calculated structure functions are obtained from Eqs. 2.1 and 2.2.

Table 2.3.1, and 2.3.1 show two examples of the flow regime that can be achieved in this system, one with the lowest jet velocity and the other one with the highest jet velocity. Both flow configurations have the identical total number of jets $N_{jets,total}$ as well as the averaged number of open jets $\langle N_{jets,on} \rangle$. As one can see, as the jet velocity increases, the fluctuation velocity increases proportionally as well. Since ϵ scales with u' to its third power, it is not surprising that the energy dissipation rate increases two orders of magnitude with the

maximum one larger than 0.1 m^2/s^3. In addition, the Taylor-scale Reynolds number, $Re_\lambda = \sqrt{15u'L/\nu}$, is also seen to grow as the jet velocity increases with the maximum one reaching $Re_\lambda = 435 \pm 20$.

For each experiment, all particle trajectories in the entire view volume of roughly 6 cm $\times$ 6 cm $\times$ 5 cm were used. Figure 2.8 shows the velocity profile, including both the mean $\langle u_i \rangle$ and the fluctuation components u_i', in the horizontal and vertical directions. The error bar shows the standard deviation of these quantities in other directions. $\langle u_i \rangle$ and u_i' are relatively uniform in both directions. In particular, the horizontal fluctuation components are significantly stronger than their mean counterparts which are close to zero. In the vertical direction, the fluctuation velocity does not show a strong trend, but it is not as flat as other two directions. In particular, it shows a weak decay in the vertical direction as it moves away from the jet array (positive Z is closer to the jet array). This is consistent with one would expect that turbulence should decay as it moves away from the energy injection. For this particular configuration, the decay rate seems to be slow.

One important design goal is to have strong turbulence with a large energy dissipation rate $\epsilon \geq 0.1$. This is to assure that the turbulence-induced deformation is stronger than the buoyancy-induced one $We \geq Eo \geq 1$. To estimate the energy dissipation rate in our system, the Eulerian velocity structure function $D(r) = \langle (u(x+r) - u(x))^2 \rangle$ is calculated based on the Lagrangian particle

trajectories (Ni, Huang, and Xia, 2011).

Particle velocity obtained from the Lagrangian trajectories was converted into the Eulerian velocity field. For every frame, a pair of velocity vectors was selected based on their separation r. The difference between these two velocity vectors can projected to the separation direction to separate the longitudinal component from the transverse component, from which both the longitudinal and transverse structure function can then be calculated. In this work, the spatial resolution is not sufficient to resolve the dissipative range ($r \ll \eta$) below the Kolmogorov scale η. But the scales in the inertial range ($\eta \ll r \ll L$, $L \approx 400\eta$) is well resolved. Based on the Kolmogorov theory, in the inertial range, the structure function should only depend on the energy dissipation rate and the scale separation r. The longitudinal D_{LL} and transverse D_{NN} components of the second-order structure function can be related to ϵ and r as $D_{LL} = C_2(\epsilon r)^{2/3}$ and $D_{NN} = 4C_2(\epsilon r)^{2/3}/3$ ($C_2 \approx 2.3$). In Fig. 2.9(a), both D_{LL} and D_{NN} are shown as a function of r, and the solid line indicates the $r^{2/3}$ scaling in the inertial range. In addition, the four-fifth law of the Kolmogorov theory suggests that the third-order structure function in the inertial range is $D_{LLL} = -4\epsilon r/5$. Compensated by their respective inertial range scalings and prefactors, all three structure functions can be used to estimate ϵ. In Fig. 2.9(b), three compensated structure functions are shown together. A perfect collapse between D_{LL} and D_{NN} confirms that: (i) Turbulence in this region is fully-developed and

has a reasonable wide inertial range for our Reynolds number at $R_\lambda \approx 435$; (ii) Flow in this range of scales should be close to the HIT condition. In addition, the compensated third-order structure function is also shown. The uncertainty of ϵ is estimated to cover this difference among three structure functions. The energy dissipation rate in this particular flow configuration can be estimated to be around 0.16 ± 0.02 m^2/s^3, which is in the range that is required to have bubble deformation primarily driven by turbulence.

The statistically-isotropic turbulence follows the Kármán-Howarth equation (De Karman and Howarth, 1938), and it can be expressed as the relationship between the longitudinal and transverse second-order structure functions:

$$D_{NN}(r) = D_{LL}(r) + \frac{r}{2}\frac{\partial D_{LL}(r)}{\partial r} \tag{2.1}$$

and its reverse form

$$D_{LL}(r) = \frac{2}{r^2}\int_0^r x D_{NN}(x) dx \tag{2.2}$$

These two equations help to calculate D_{LL} and D_{NN} from the experimental results of D_{NN} and D_{LL}, respectively. The measured structure functions were shown in figure 2.9. The deviation between the measured structure function and the calculated one can be obtained, and this deviation measures the validity of the isotropic assumption. As shown in Fig. 2.10, the deviation between the calculation and experimental measurements is less than 5% for the length

scales in the range of $[50\eta, 500\eta]$, indicating that the turbulence is close to homogeneous and isotropic within the inertial range.

The statistical isotropy can also be tested by evaluating the coarse-grained velocity gradient tensor. The entire measurement volume was divided into small cubes with 8 mm in size to calculate the local coarse-grained velocity gradient tensor. Each measured tensor was decomposed into vorticity vector and rate-of-strain tensor. For statistically-isotropic turbulence, the orientations of the vorticity vector ω and the eigenvectors of the rate-of-strain tensor λ_i are supposed to be random with respect to the lab frame of reference. Fig. 2.11 show the PDFs of the cosine of the angles between the (a) ω and (b) λ_1 with three principal axes of the lab frame of reference. The uniform distribution in both PDFs implies that the turbulence generated in this facility is close to isotropic. To confirm that this calculation is not an artifact, the PDF of the alignment between vorticity vector and the three eigenvectors of the strain rate tensor is also shown in Fig. 2.11 (c). The results show that the vorticity is preferentially aligned with the intermediate eigenvector of the strain rate tensor. This is due to the delayed alignment between flow stretching and vorticity vector (Ni, Ouellette, and Voth, 2014). This result confirms that our calculation of the coarse-grained velocity gradient tensor is correct, and the flow is indeed close to isotropic.

The single-phase measurement confirms that the flow characteristics sat-

isfy our design goals. Within this flow, bubbles will experience strong turbulence that is close to HIT. This will help us to collect statistics of bubble dynamics and two-phase couplings. In Fig. 2.12, an example of the two-phase flow measurements is shown. The trajectories of tracers around bubbles are shown as lines color-coded with their respective velocity magnitude. These lines are set with certain level of transparency to show bubbles within. The 3D geometry of bubbles are shown as gray blobs. In this particular case, bubble deformation is not very strong, and we can reconstruct bubbles with a range of sizes. With six high-speed cameras coupled with a new reconstruction algorithm, bubble geometry is acquired at an unprecedented accuracy. The center-of-mass of bubbles can also be tracked in a similar way using our particle tracking code. This facility offers us a unique opportunity to study the bubble-turbulence couplings in both Eulerian and Lagrangian framework.

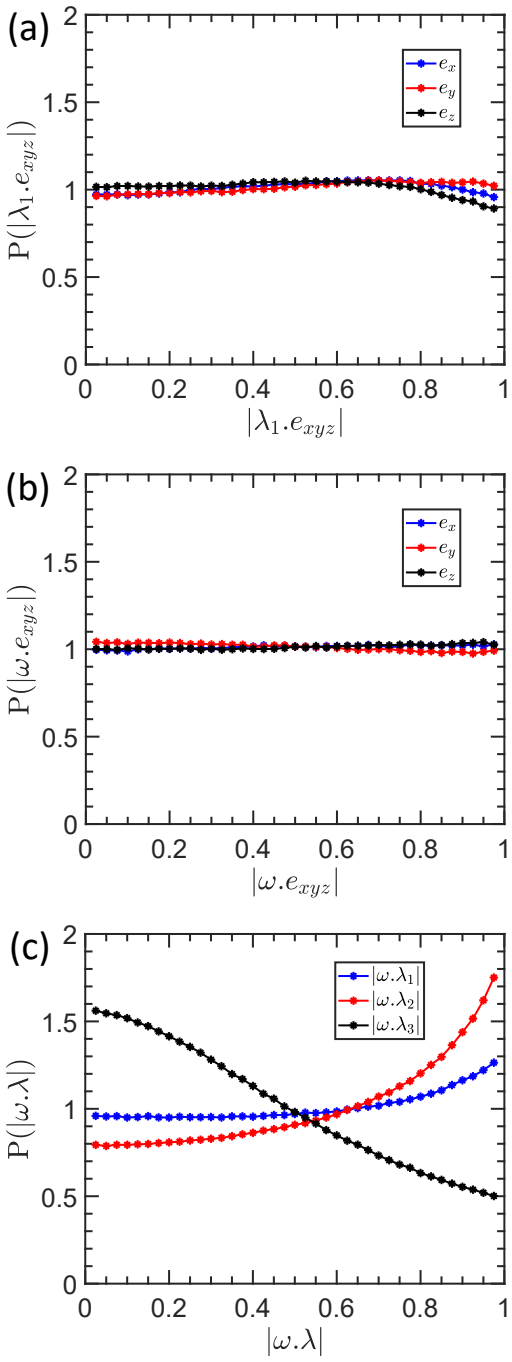

Figure 2.11: (a) Alignment of the largest eigenvalue of the coarse-grained velocity gradient tensor with lab frame of reference (b) Coarse-grained vorticity vector alignment with the lab frame of reference (c) PDF of the alignment between vorticity unit vector and the three eigenvectors of the coarse-grained strain rate tensor showing a preferential alignment between vorticity vector and the intermediate eigenvector of the strain rate tensor which is characteristic of isotropic turbulence.

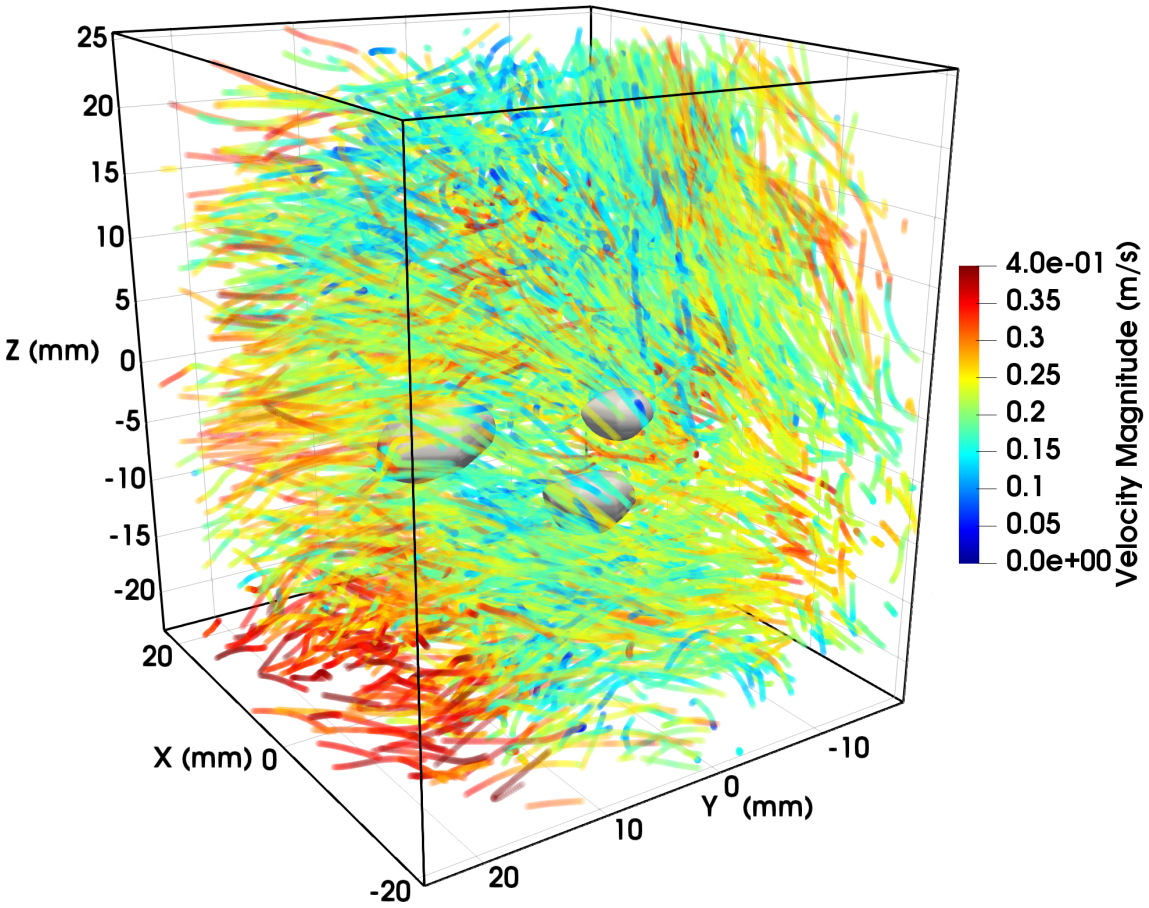

Figure 2.12: Reconstructed bubbles (grey blobs) with surrounding tracer particle trajectories color coded by their velocity magnitude

Chapter 3

A robust virtual-camera 3D shape reconstruction of deforming bubbles/droplets with additional physical constraints

Bubbles and droplets in strong turbulence exhibit non-affine deformation, especially near the breakup when the strong necking and interfacial instability begin to play roles. The virtual-camera (VC) method was designed and implemented to mitigate the limited-angle reconstruction problem for complex bubble/droplet geometry. The VC method incorporates the additional physical constraint of minimum surface area into reconstruction. This framework helps to reduce the reconstruction uncertainty for experiments studying mul-

tiphase flows that use a limited number of cameras, non-ideal camera positions, or the combination of both. The method was tested with three synthetic geometries– sphere, ellipsoid, and dumbbell–that represent the undeformed, gently-deformed, and severely-deformed bubbles. In addition, a DNS dataset of bubbles with a 2% void fraction in turbulent channel flow was also tested, and the volume overestimation was found to decrease from over 20% to about 10% after applying the VC method. Finally, the method was applied to the experimental dataset of bubble-turbulence interaction, and the result shows over 20% improvement in volume estimation. The uncertainty quantification that relies on the bubble aspect ratio and orientation has also been developed so that the reconstruction uncertainty of each bubble in each frame can be estimated. This allows a more selective process to obtain statistics of multiphase flow based on the quality of reconstruction.

3.1 Introduction

Multiphase flows are more common than their single-phase counterpart in many natural and industrial applications, such as solid particles in air during dust storms (White, 1982), bubble-mediated gas transfer in the ocean (Woolf, 1997), two-phase heat transfer in energy systems (Sun et al., 2002), and fermentation in biochemical reactors (Galindo, Pacek, and Nienow, 2000). Out of

all types of multiphase flow, flow that consists of only two phases is the simplest and may serve as a canonical case for understanding the complex interfacial mass, momentum, and energy transfer.

In gas-liquid or liquid-liquid two-phase flows, bubbles and droplets may behave either as rigid or deformable objects depending on their sizes, inner viscosity and surface tension. For some cases, deformation is driven completely by buoyancy, in which the deformation is simple and can be reconstructed even with two cameras. In many other instances, bubbles subjected to strong turbulence may experience extreme stretching and distortion, leading to complicated non-affine deformation. This type of deformation dynamics must be revealed by a robust shape reconstruction method that can deal with complex geometries.

One method that has been attempted is to reconstruct bubble geometry by fitting an ellipse to each projected outline (Ravelet, Colin, and Risso, 2011; Jordt et al., 2015; Besagni and Inzoli, 2016; Giovannettone, Tsai, and Gulliver, 2009; Maldonado et al., 2013), and these ellipses were combined in 3D to get the final ellipsoid. This step removes some key deformation features. The underlying assumption used in the reconstruction is that the bubble deformation is always affine with no bending, surface wave, or any high-order deformation, even though some of these dynamics could be very important in turbulent multiphase flow.

To improve this method, a slicing method has been proposed and used by many groups (Fujiwara et al., 2004; Honkanen, 2009; Fu and Liu, 2018) based on an assumption that the horizontal slice can be smoothed either by fitting with ellipse (Fujiwara et al., 2004; Honkanen, 2009) or spline (Fu and Liu, 2018). Some geometrical information will be preserved in this manner, but slicing along the horizontal plane works the best if the bubble deformation is primarily in this plane. Note that the slicing method was designed primarily for studying bubble rising in a quiescent medium, where the bubble deformation is driven by the buoyancy. If the deformation is chaotic and strongly non-affine, this method may not work so well since it may become necessary to also slice and smooth in other directions. But along which direction to slice is the question.

To broaden the scope of the discussion, it is worth noting that reconstructing of a complex geometry with non-affine deformation is also prevalent in computer vision. In particular, silhouette-based (also known as the visual hull technique) method has been used extensively (Mulayim, Yilmaz, and Atalay, 2003; Matusik et al., 2000; Laurentini, 1994; Kutulakos and Seitz, 2000). The silhouette of an object is projected onto cameras at different angles. To obtain the 3D reconstructed volume of the object, as shown in Fig. 3.1 (top view), cone-like volumes are extruded from the 2D images, and the intersection of these cones from different cameras form the visual hull (VH) of the object. This technique

has also been used in medical instruments such as computerized tomography (CT) (Sidky and Pan, 2008). In order to provide accurate shape reconstruction, a typical VH method requires using either many cameras or rotating one camera to cover more than a hundred of angular positions. (Medoff et al., 1983; Sidky, Kao, and Pan, 2006).

For turbulent multiphase flow, the typical timescale is in milliseconds. The complex dynamics of deformation has to be recorded using high-speed cameras. These fast events cannot be reconstructed using the rotating camera technique. The price of the high-speed camera is often so high that two to four of those already reach the limit of the budget for many experiments. So for turbulent multiphase flow, neither many cameras nor many angles are viable options. In this scenario, the problem becomes the so-called limited-angle or limited-data VH reconstruction. One inherent issue with the limited-angle VH reconstruction is associated with the extra materials shadowed by the object itself, as shown in Fig. 3.1. Nevertheless, the VH method has been used in the literature to study many multiphase flow phenomenon e.g. boiling (Rau, Vlachos, and Garimella, 2016), rising bubbles (Fu and Liu, 2018), and complex-shape rigid objects (Adhikari and Longmire, 2012).

The VH method can be improved if some *a priori* knowledge of the object is available. For example, the shape of a moving insect can be reconstructed based on the known anatomical structure of its body (Ristroph et al., 2009).

The surface texture and color of objects have also been used to improve the reconstruction (Isidoro and Sclaroff, 2003; Furukawa and Ponce, 2009; Kanatani and Chou, 1989). In the context of turbulent multiphase flows with bubbles and droplets, most of these methods to improve VH cannot be implemented directly due to bubbles' high deformability, transparency, interface reflection, and the absence of colored textures.

Bubbles and droplets have their own unique physical constraint, surface tension. Even under extreme stretching, the surface tension still attempts to minimize the surface area and decrease the curvature. On the other hand, most extra materials produced by the limited-angle VH method tend to have sharp corners because of the intersection of two lines-of-sight, as shown in Fig. 3.1. Implementing this physical constraint into the reconstruction is nevertheless nontrivial. Medoff *et. al.* (Medoff et al., 1983) and references within presented a general framework to incorporate all available *a priori* information using the iterative convolution backprojection algorithm. Although this technique is designed for X-ray CT data that deals with streak artifacts that are not relevant to our optical system, this idea can also be applied to our case to account for the surface tension constraint.

In this article, a simple algorithm to improve the 3D reconstruction of deformable bubbles in turbulent flow will be introduced. The idea of this method is to spread the minimum interfacial-area constraint to many angles that are

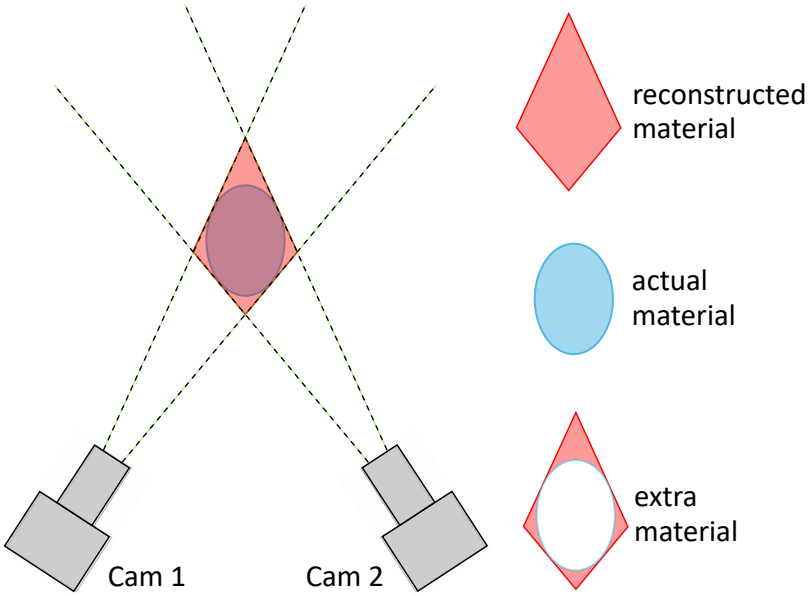

Figure 3.1: Schematic of the limited-angle VH Reconstruction, which tends to result in an overestimation of the volume.

not covered with real cameras, hence the name "virtual camera". The method will be tested on (i) three synthetic geometries with different aspect ratios and orientations, (ii) a DNS dataset of turbulent channel flow, and (iii) our experimental dataset in fully-developed turbulence. In addition, we will introduce a novel way to independently assess the reconstruction uncertainty of the experimental data by using the aspect ratio and orientation information. This allows us to be more selective in the postprocessing step.

3.2 Volume of reconstruction

3.2.1 Challenges and solutions

As shown in Fig. 3.1, for the limited-angle VH reconstruction, there are some important features of the excess materials: (a) As shown in Fig. 3.1, the extra materials are shadowed by the object itself and hidden within a volume bounded by the intersection of lines of sight from cameras. (b) The volume of the extra material drops as the number of real cameras increases. Depending on the geometrical complexity of the object of interest, there is a limit in terms of the number of cameras needed, above which the benefit of adding one extra camera is outweighed by the cost and complexity of the setup. (c) The most efficient way to remove the extra material is to position another camera from a direction that clearly views the shadowed extra material. One example is shown in Fig. 3.1. If the optical axes of two cameras lie on a plane, the third camera should be positioned so that its viewing direction is perpendicular to that plane.

For 3D fluid dynamics measurements, it is a standard to position four cameras on one side next to the test section with a small angle among them facing towards the view volume. There are two reasons for this camera configuration: (i) flow and laser typically take two orthogonal directions, which leave only one direction for cameras. (ii) For 3D Tomographic particle image velocimetry (PIV)

or particle tracking velocimetry (PTV), the only information that is needed for a particle is its center of mass, which only has three degrees of freedom. The angle separation among four cameras, albeit small, is sufficient to extract particle motion (Ouellette, Xu, and Bodenschatz, 2006; Ni, Huang, and Xia, 2012). If particles have finite size and are deformable, the degrees of freedom grow significantly, and one would need much larger angle separation among cameras to resolve the complicated motion.

In Fig. 3.2, a simple finite-size sphere is reconstructed using a 4-real-camera configuration typically used in 3D Tomographic PIV. The reconstructed volume (gray) using the standard VH method has a spindle shape with two tips pointing in the direction towards four cameras. The excess material hid in these two tips represents a volume that is shadowed by the sphere itself and thus cannot be accessed by any of these four cameras. This extra volume constitutes about 30% of the actual sphere volume and leads to an overestimation of the aspect ratio to nearly 2 for a sphere.

3.2.2 Virtual camera method

To address the problem experienced in the limited-angle VH reconstruction, the VC method is designed and implemented. The method incorporates the *a priori* physical constraints, e.g. the minimal surface area in our case, in virtual cameras that are positioned along the directions that were not accessible by

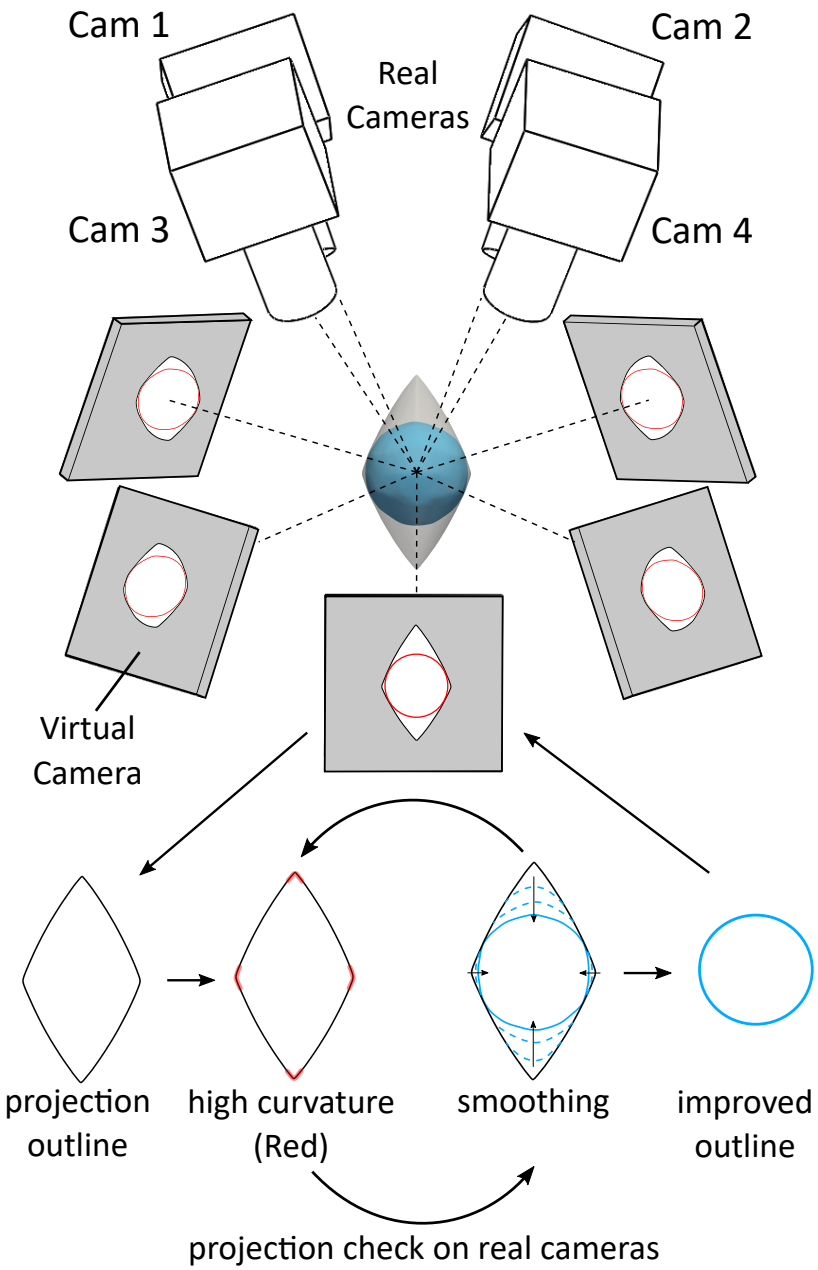

Figure 3.2: Schematic of the classical VH and our VC method with four-real-camera configuration (top). Gray panels indicate the virtual cameras. On each panel, the black outline marks the reprojection from the VH reconstructed geometry (gray spindle shape), and the red outline marks the smoothed ones after several iterations that can be used to obtain the blue sphere.

real cameras.

The steps involved in the VC method are illustrated in Fig. 3.2 and discussed in details as follows:

Step 1: The first step is to process the images acquired from the real cameras to separate bubbles from the background. These processed images are then fed to the classical VH method to achieve the first initial 3D reconstruction of all bubbles in the field of view. As shown in Fig. 3.2, four real cameras are closely packed along the vertical direction, with small angles among them. The initial reconstruction of a sphere looks like a spindle with two pointing tips, as shown by the gray volume in the center.

Step 2: Virtual cameras need to be positioned along the directions that are least covered by all the existing cameras. In practice, a code was designed to achieve this by minimizing the objective function $Z = \max(\theta_i)$, and θ_i represents the obtuse angle between the newly-added virtual camera with the i_{th} existing one, real and virtual. Following this method, the first virtual camera, in the case shown in Fig. 3.2, should be positioned facing towards the reader. The initial reconstructed volume is then projected to this view, which clearly shows the two pointing tips.

Step 3: An iterative process starts in order to remove the sharp corners of the projected outline in this particular virtual camera without affecting bubble images on all real cameras. This process illustrated at the bottom of Fig. 3.2

will be briefly introduced here.

(a) 2D curvature along the entire projected outline is determined.

(b) Locations with high curvature are identified. Outlines near the high-curvature corners are smoothed by averaging the points in the vicinity. The difference between the areas covered by the smoothed and the original outlines is A_{virt}.

(c) The smoothed outline from this virtual camera is added to the reconstruction along with other cameras, and a new 3D volume is generated by using the VH method.

(d) The newly-reconstructed volume is then projected to all the real cameras. If the projected area differs from the actual area by less than 10% of A_{virt}, the smoothing procedure is accepted and the iteration continues. Otherwise, the reconstruction is reverted to the previous iteration, and the entire iteration stops.

This method allows us to remove most reconstruction artifacts with minimum impact on the actual volume. However, this is the most time-consuming step that can be accelerated by GPU or high-performance computing clusters in the future.

Step 4: Virtual cameras are added one by one, and step 2 to 3 are repeated until adding one more virtual camera does not provide much benefit. For our

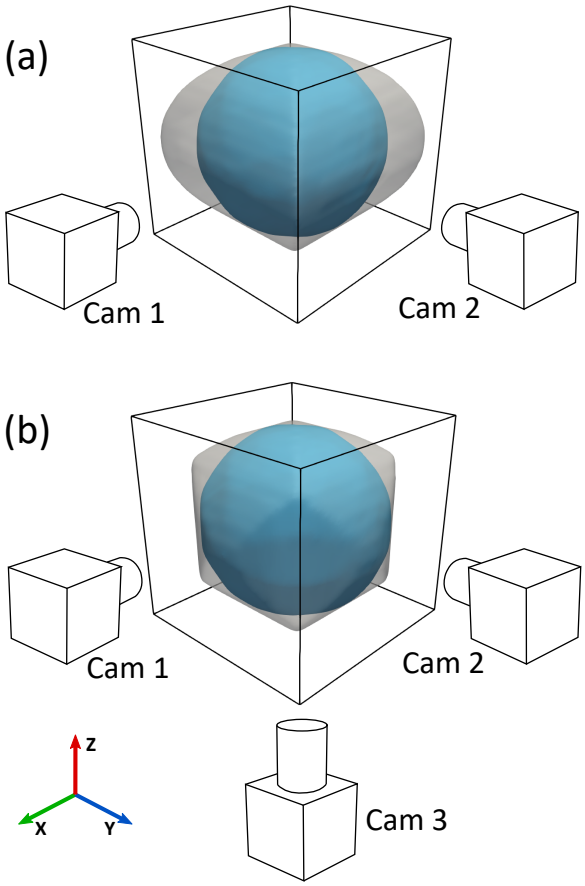

Figure 3.3: Schematic of the 3D reconstruction of a sphere with (a) two real cameras and (b) three real cameras. Gray color represents the geometry reconstructed by the limited-angle VH method, and the blue color represents the geometry reconstructed by the VC method.

experiments, in most cases, 17 virtual cameras are sufficient.

For a convex geometry, this method works for as few as two real cameras. In Fig. 3.3, a sphere was reconstructed using (a) two real cameras and (b) three real cameras. In both cases, cameras are placed orthogonal to each other. With only the VH method, the extra material, indicated by the gray volume, reduces from 31% to 15% as N_{cam} increases from 2 to 3. On the other hand, the volume uncertainty drops below 3% for both 2 and 3 real cameras after implementing

VC. This indicates that the VC method works well for even two real cameras if the geometry is simple and convex. Relatively more benefit is gained from the VC method for two real cameras than that for three real cameras.

3.3 Experimental apparatus

Fig. 3.4(a) shows the experimental setup. Six high-speed cameras were used to cover the perimeter of the test section of a vertical water tunnel (V-ONSET). The azimuthal angles of all the cameras are shown in the top view (Fig. 3.4(b)), and their individual inclination angles are indicated on the side. For the rest of the paper, all the analysis of the synthetic datasets is performed based on this camera configuration. Although the exact uncertainty varies with the camera configurations chosen, the overall principle can still be learned from this example.

The water tunnel used in our experiment is aligned vertically, allowing its mean flow to balance the rising velocity of buoyant bubbles. This flow configuration forbids the optical access into the test section from the top or bottom as these directions are occupied by the mean flow. To mitigate this problem, three cameras (Cam 3, Cam 5, and Cam 6) were tilted away from the horizontal plane to acquire some information from the third axis. No prism was used for inclined cameras; 22 is probably the largest angle that one can use and still

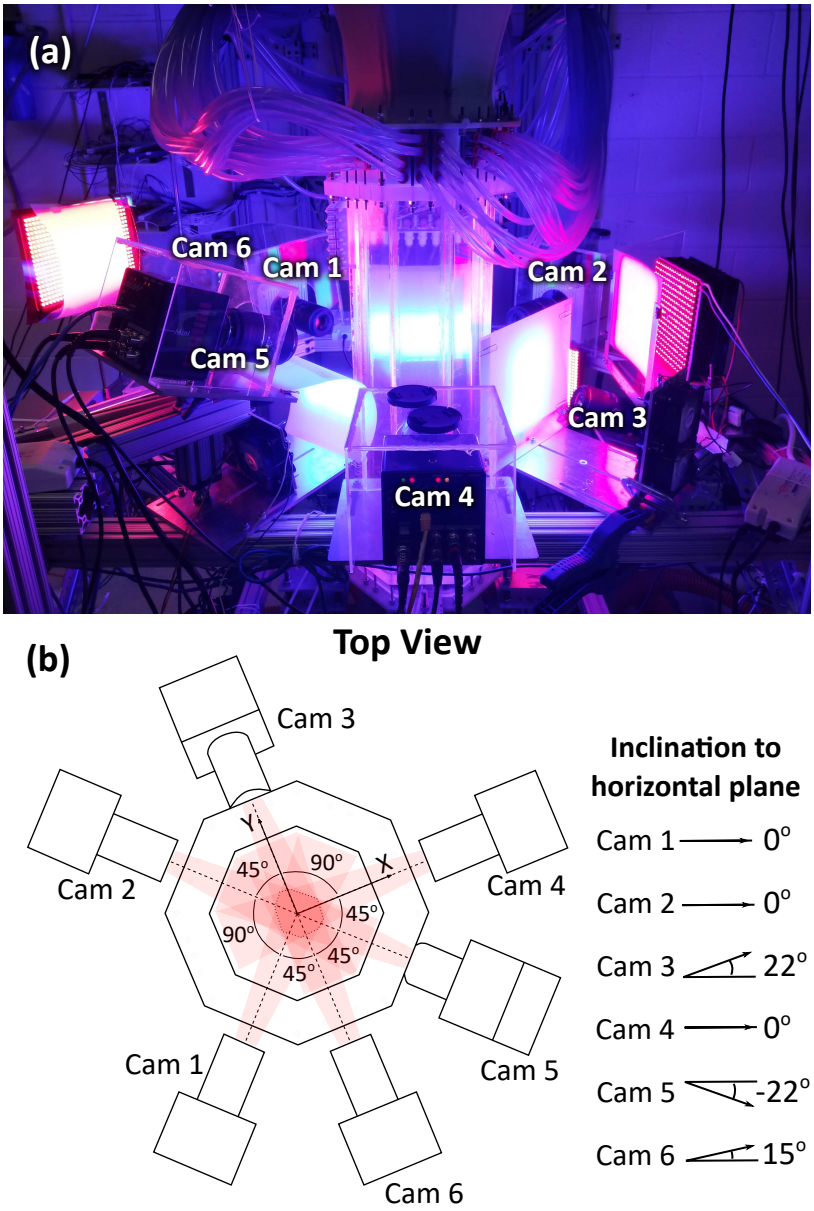

Figure 3.4: (a) Photo of the vertical tunnel V-ONSET with six cameras and their LEDs, (b) The top view of camera configuration with respect to the octagonal test section; the inclination angle of each camera from the horizontal plane is also marked.

be able to reach similar calibration accuracy in our facility without a prism. For each camera, a dedicated high-power LED array was used to illuminate bubbles.

3.3.1 Calibration

Six cameras have to be carefully calibrated to establish a correspondence between points in space and points on the images (Tan et al., 2019a). Such a relationship is acquired by imaging a pattern on a calibration target by all cameras simultaneously. In our setup, since cameras cover the entire perimeter of the test section, some cameras have to view the target from behind. A transparent acrylic target with known thickness and refractive index was used. One side of the target was laser-etched with some dots. These dots can be viewed from both sides. The calibration results of the cameras seeing the dots from behind through the acrylic target has to be corrected for the refractive index mismatch between acrylic and water. The algorithm worked very well with the final nominal calibration uncertainty at about 0.5 pixels.

The initial calibration uses the classical Tsai's model (Tsai, 1986) to recover the camera transfer function in terms of the interior parameters and the exterior parameters. The exterior parameters connect from a 3D scene in the physical space to a camera location. The interior parameters link from the 3D camera location to its 2D image. Additional radial and linear distortion coef-

ficients were also added. The parameters were estimated by performing the least-square fit of all the dots on the target.

After the initial calibration, tracer particles of 50 μm in diameter were injected into the view volume; the number of particles in the view was kept very low ($\sim$100 particles) to ensure that the inter-particle distance is large enough to avoid ambiguity. Water was stirred gently to move these particles, and their positions were triangulated and tracked using our in-house particle tracking code with the initial calibration configuration. The search radius that is used to triangulate particles was set at 0.2 mm to allow finding all possible candidates. Only the tracked particles exceeding 100 frames were selected as positions that we could trust. Their positions were distributed over the entire view volume, but not uniformly. To avoid possible risks of calibration bias, certain sub-volumes that have more particles than others were randomly downsampled to ensure a similar number density of particles throughout the entire volume. Finally, these particles and their corresponding images were used to conduct a non-linear optimization to find an optimal set of camera parameters that would minimize the intersection errors of all epipolar lines, the so-called self calibration method. The uncertainty error was reduced from 0.5 to 0.2 pixels after this step.

The importance of this step has been widely accepted in the tomographic particle image velocimetry (PIV) (Wieneke, 2008). Comparatively less atten-

tion has been paid on bubble shape reconstruction, partly because the requirement of accuracy is different. In PIV, particle size is only two to three pixels in diameter, and tracking them requires an accurate determination of their center to the sub-pixel level. Bubbles are much larger so calibration was conducted typically without the volumetric self-calibration. Nevertheless, it was emphasized before by Wieneke (2008) that, without this step, one is not even aware of how large the calibration errors actually are.

3.4 Results

When a bubble starts to deform and its shape deviates away from a perfect sphere, the reconstruction becomes sensitive to the shape, e.g. concave or convex, which can be represented by a dumbbell or an ellipsoid. These two geometries are simple, yet representative of either the weakly-deformed or severely-deformed states. All tests introduced in the rest of this paper uses the camera configuration adopted in our experiments. For tests that use fewer than six cameras, some real cameras were removed.

Fig. 3.5 shows a dumbbell oriented vertically and visualized by two to six real cameras. This dumbbell geometry is generated by using the spherical harmonics $Y_m^l(\theta, \phi)$, with degree $l = 1$ and order $m = 0$. This particular dumbbell orientation allows all real cameras to see its neck. The blue line shows the

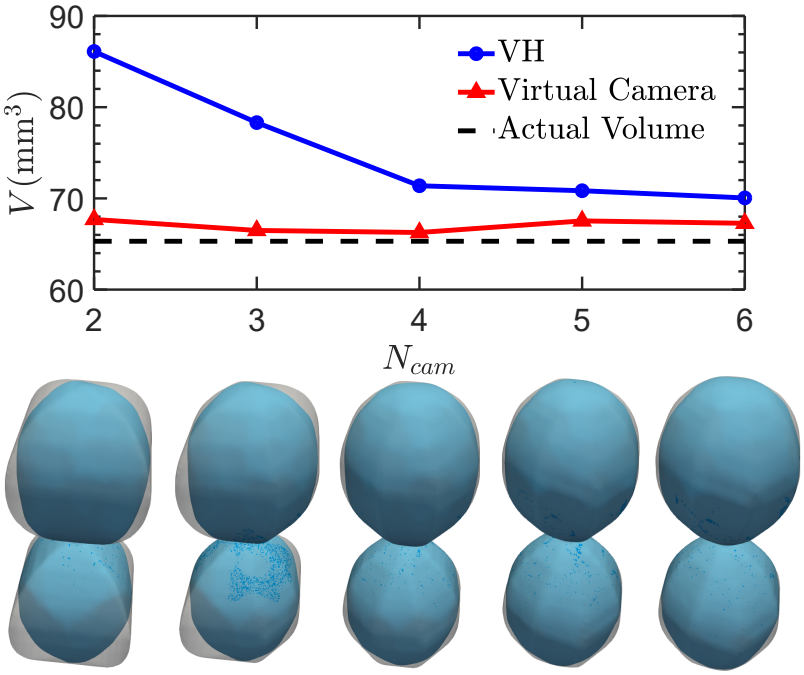

Figure 3.5: The reconstructed volume V of a synthetic dumbbell versus the number of real cameras N_{cam}. Five 3D objects indicate the reconstructed geometry for different N_{cam}. Gray color represents the VH reconstruction and blue color indicates the VC method.

reconstructed volume V as a function of the number of real cameras N_{cam} used in the standard VH reconstruction. As N_{cam} increases, V approaches the actual volume (dashed line) as expected. The volume drops quickly for $N_{cam} < 4$, suggesting that one would ideally need four cameras for this complex shape if only VH is available. The reconstructed volume using the VC method is shown as the red curve. It can be clearly seen that the red curve almost overlaps with the dashed line, indicating that the reconstruction is very accurate and insensitive to N_{cam} for this particular configuration. The comparison of the reconstructed geometry between VH and VC is shown as the gray and blue 3D geometries in the lower panel of the figure. As one can see, the method successfully removed the extra materials, especially for small N_{cam}.

The reconstruction uncertainty is also sensitive to the orientation of the object, which can be represented by the Euler angles (ϕ, θ, ψ). The Euler angle at (0,0,0) is shown in Fig. 3.6(a). For this orientation, the major axis of the dumbbell aligns with the vertical axis. Since the generated dumbbell is symmetrical about the major axis, θ and ϕ are sufficient to represent all the orientations.

In Fig. 3.6(b), the volume reconstruction uncertainty ϵ_V is shown as a function of θ and ϕ. When all six cameras view the neck at $\theta = 0$ (Fig. 3.6(a)), the uncertainty is the smallest at around 5%. When the dumbbell lies down and its major axis falls on the horizontal plane at $\theta = 90$, the view of its neck for some cameras can be shadowed by its two large ends. For this orientation, the

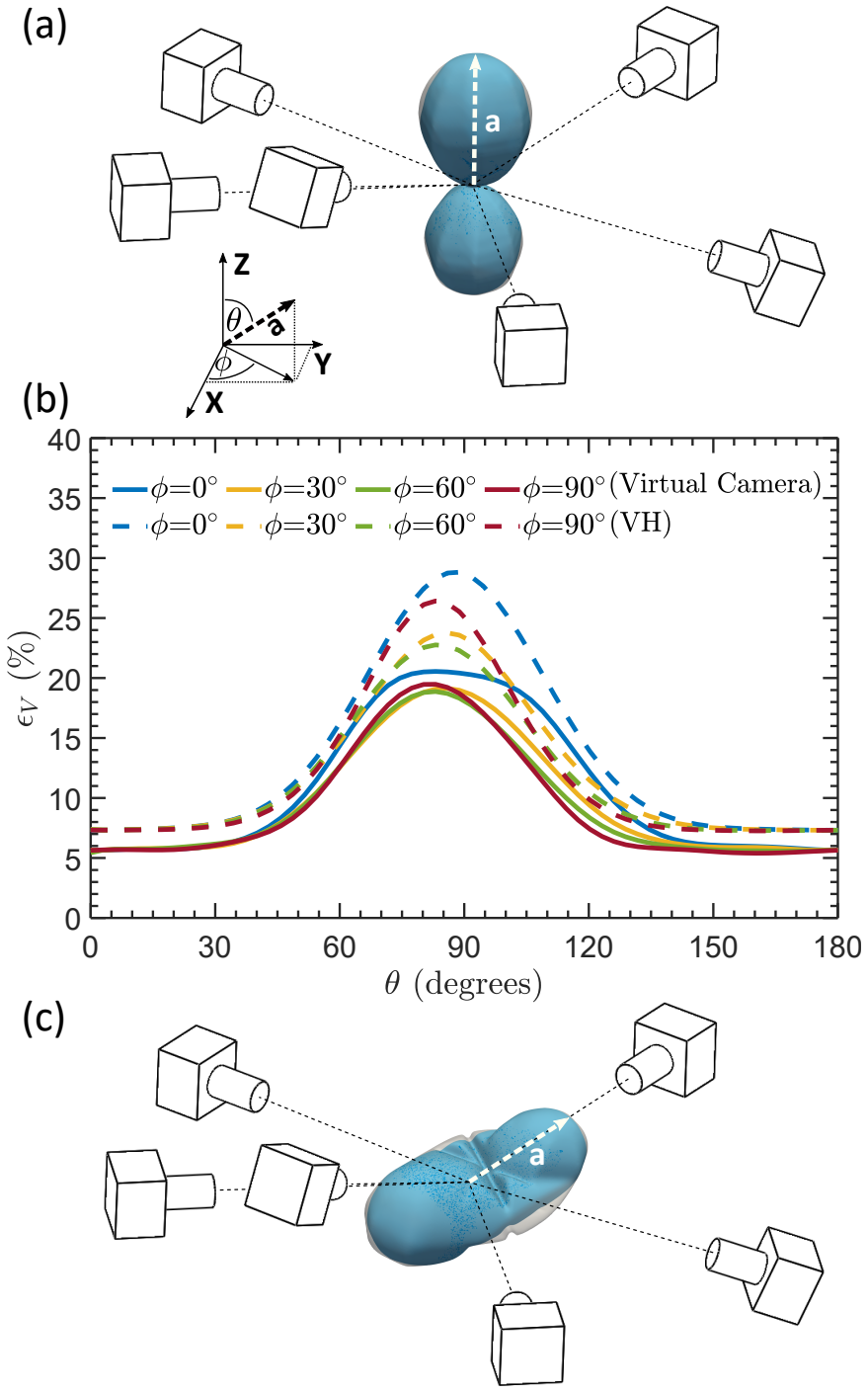

Figure 3.6: (a) A dumbbell with its Euler angle at (0, 0, 0) surrounded by six real cameras. (b) The volume reconstruction uncertainty ϵ_V versus two Euler angles θ and ϕ. Dashed lines and solid lines are for the VH and VC method, respectively. (c) The reconstructed dumbbell geometry with extra mass at the neck when the Euler angle is at (0, 90, 0).

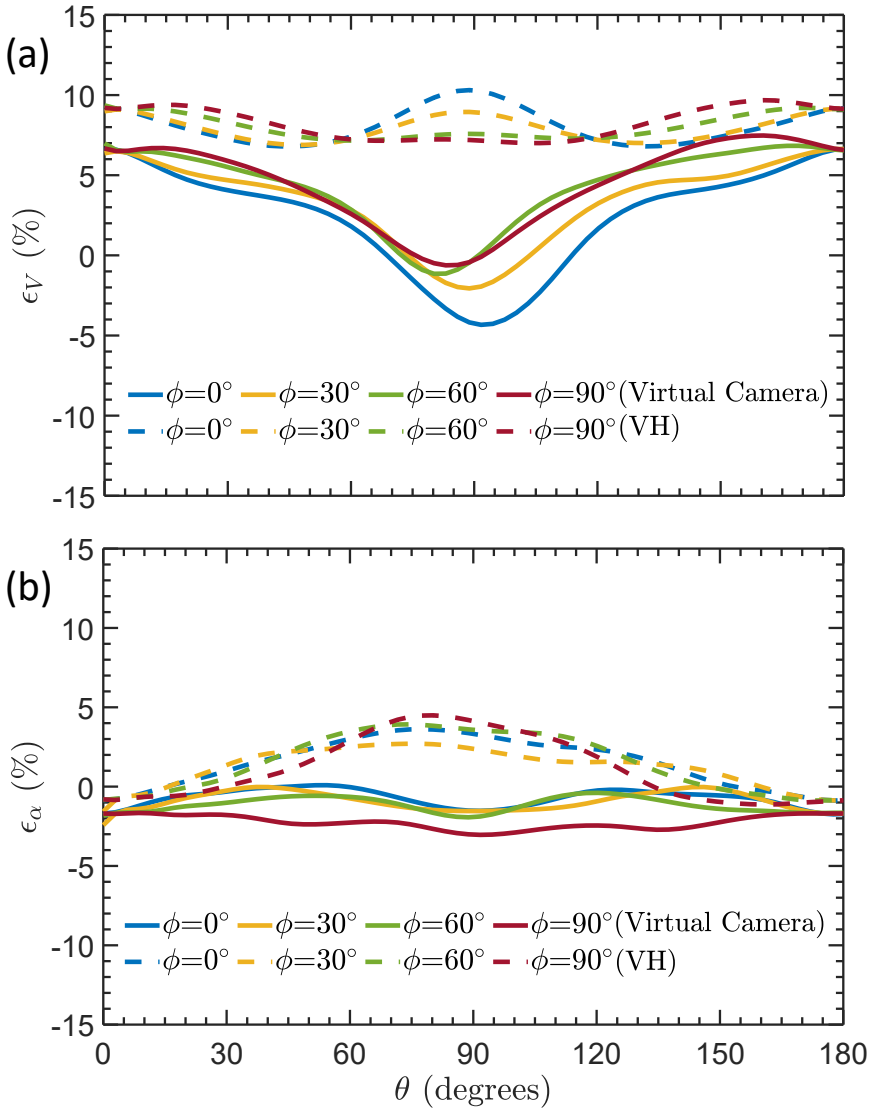

Figure 3.7: The reconstruction uncertainty of the (a) volume ϵ_V and (b) aspect ratio ϵ_α of an ellipsoid as functions of its two Euler angles θ and ψ.

uncertainty really depends on how many real cameras can see the neck. At $\phi = 60$, three cameras still have clear views, resulting in 23% uncertainty. As shown in Fig. 3.6(c), the worst case occurs at $\phi = 0$, where the uncertainty is 28%. In this case, the dumbbell is almost pointing towards three cameras, completely blocking the view of these cameras to see the neck. As the result, the reconstructed volume has significant amount of excess material at the neck. After implementing the VC method, it can be seen that all the uncertainties systematically reduce. At $\theta = 90$, ϵ_V decreases by nearly 10%. However, the remaining extra material is still about 20% because the algorithm cannot refine the neck that cannot be seen.

A dumbbell represents a bubble that is close to breakup, which is an extreme case with a large uncertainty. Most deformed bubbles are probably closer to ellipsoids until the breakup moment. A similar test has also been performed with a synthetic ellipsoid with the length of the major and two minor axes being 4.5 mm, 2.5 mm, and 1.5 mm, respectively. The volume uncertainty ϵ_V is shown as a function of θ and ϕ in Fig. 3.7(a). ϵ_V appears to be low $< 10\%$ for all orientations and does not show strong dependence on either angle. In particular, at $\theta = 90$, the peak ϵ_V is about 11%, which is much smaller than that of the dumbell case, i.e. $\epsilon_V = 28\%$. After using the VC method, ϵ_V reduces to $\sim \pm 5\%$.

In addition to ϵ_V, the aspect ratio uncertainty ϵ_α is also sensitive to the reconstruction accuracy. As shown in Fig. 3.7(b), the classical VH method

systematically overestimates α, and the peak value of ϵ_α is about 5% at $\theta = 90$. After implementing our VC method, ϵ_α becomes very close to zero for all orientations.

3.5 Synthetic test case using a DNS dataset

Although sphere, ellipsoid, and dumbbell respectively represent the undeformed, weakly-deformed, and severely-deformed geometry of a bubble, they cannot reflect the non-affine deformation that bubble will experience in turbulence. A DNS dataset of bubbles in turbulent channel flow was utilized to generate a synthetic test case for non-affine deformation (Lu and Tryggvason, 2008). Only one randomly-picked snapshot was used as the test case. As shown in Fig. 3.8(a), there are 19 bubbles within this frame, and they are representative of the realistic bubble deformation in turbulence. Most of these bubbles cannot be modeled as simple ellipsoids.

The synthetic images, cropped only to the part with bubbles, on all six real cameras are shown in figure 3.8(a). These bubbles occupied only about 1/4 of the total camera resolution, and the full camera image could cover as many as 80 bubbles. In each camera, at least one pair of bubble images appear to be overlapped because the bubble void fraction for this particular dataset is about 2%, which is relatively high for 3D optical reconstruction.

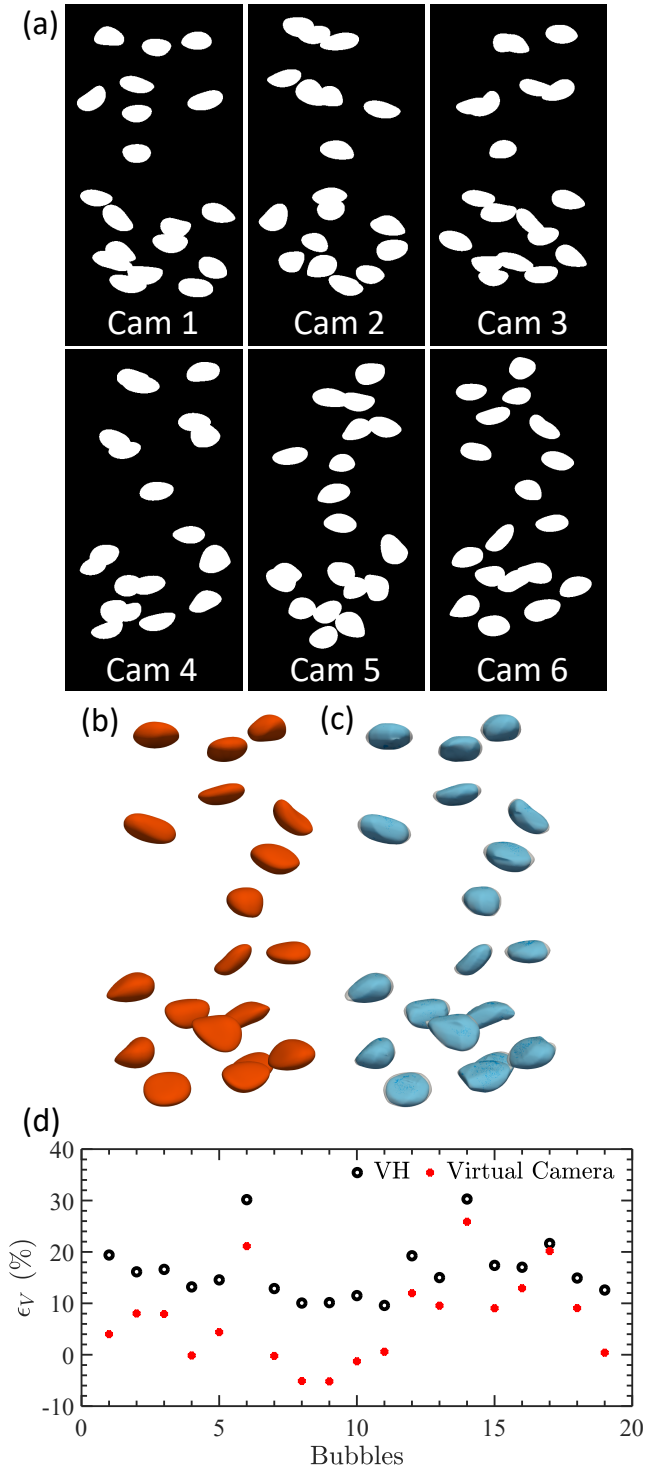

Figure 3.8: (a) Synthetic images of a DNS bubble data on all six real cameras; (b) The geometry of 19 bubbles from the DNS data; (c) The reconstructed geometry (gray, VH; blue, virtual camera); (d) The volume reconstruction uncertainty ϵ_V for all 19 cases with black circles for VH and red dots for VC method.

During the reconstruction, we realize that overlapping bubbles can be automatically segmented as long as at least one camera can view them as two separate bubbles. It is, in fact, safer to allow the reconstruction method to separate bubbles than attempting segmentation in 2D (Fu and Liu, 2016) for all cameras, as a highly-deformed bubble can be easily mistreated as two overlapping bubbles. Another motivation to use six real cameras is therefore to maximize the possibility of having at least one camera viewing the gap between two bubbles.

In Fig. 3.8(a), although there are about two to five pairs of bubbles overlapping with each other in each camera. Fortunately, most overlapping images do not appear on more than two cameras for the same pair of bubbles, which left for more than four cameras to reconstruct the bubble geometry. This explains why the reconstruction results in Fig. 3.8(c) has no discernible difference from the simulation result shown in Fig. 3.8(b).

Figure 3.8(d) shows ϵ_V for all the bubbles in the frame. For most cases, after implementing our VC method, ϵ_V reduces to $\pm$ 10%, which suggests that our method works well even for non-affine bubble deformation in turbulence at a relatively high void fraction. However, there are three bubbles (No. 6, 14, and 17) that have larger ϵ_V than others. For these three cases, bubbles suffer from the overlapping image problem in more than two cameras. Implementing VC does not improve much–ϵ_V is still at around 20%. This suggests

that this method does not work for data at a very high void fraction with many overlapped bubble images.

3.6 Experimental results

The first source of uncertainty starts from the camera calibration. As introduced in Sec. 3.3.1, after two steps, the calibration uncertainty drops to 0.2 pixels. In comparison, a bubble of 2 mm in diameter will appear on images as 40 pixels in size. Therefore, the camera calibration uncertainty is smaller than 0.5% of the total diameter, which is orders of magnitude smaller than the limited-angle reconstruction uncertainty. So the calibration uncertainty can be safely ignored.

Once the calibration was completed, bubbles were released in turbulence and their deformation were recorded by all the six real cameras simultaneously. Fig. 3.9 shows two examples, (a) a weakly-deformed case that remains close to a sphere, and (b) a highly-deformed case. To acquire bubble images at the highest contrast, the dynamics of both bubbles and their surrounding tracer particles were illuminated by LED panels from the back. Six LED panels were used to provide individual lighting for each of the six cameras.

The acquired images were uploaded to Maryland Advanced Research Computing Center to speed up the iterative process that this shape reconstruction

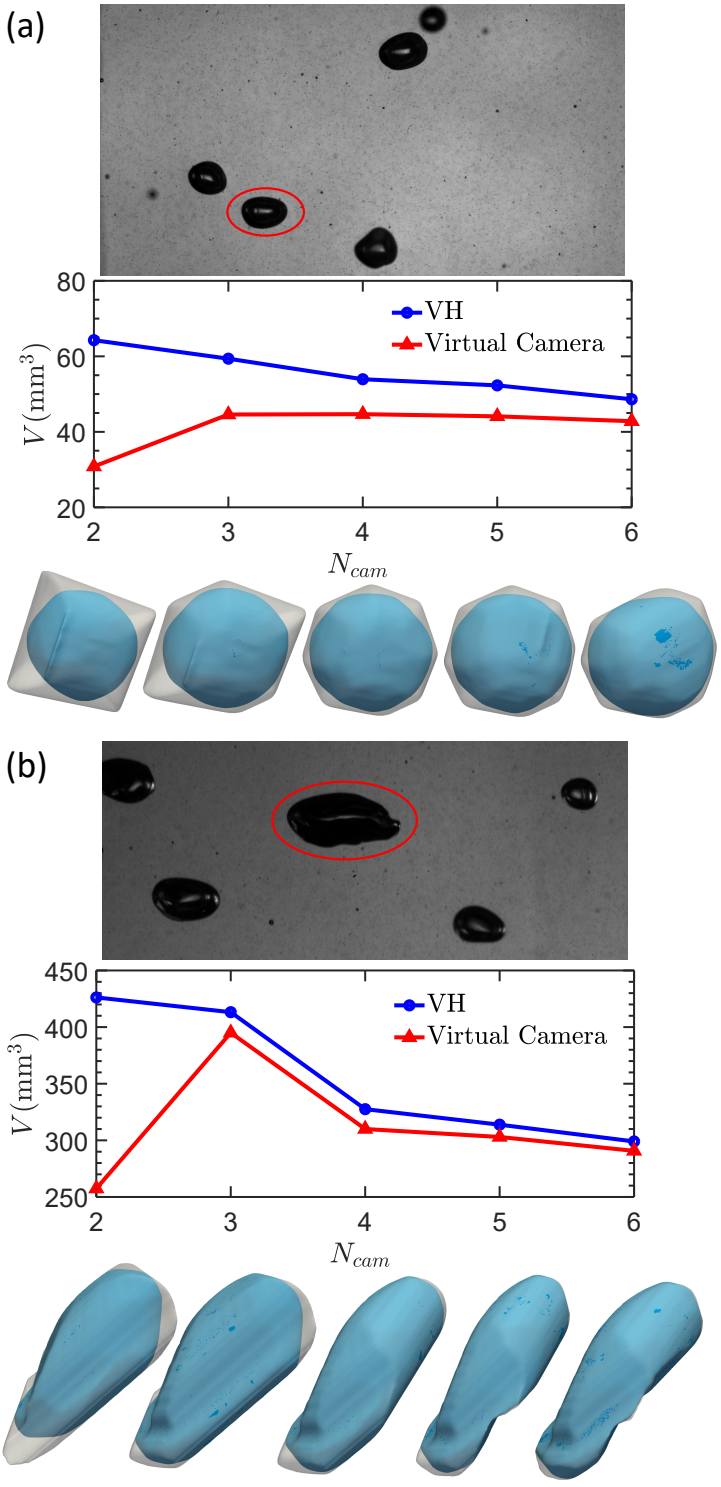

Figure 3.9: A raw experimental image, the reconstructed volume V as a function of the number of real cameras N_{cam} used, and the reconstructed geometry (gray, VH; blue, Virtual Camera) of (a) a bubble that is close to sphere and (b) a bubble that has a large aspect ratio

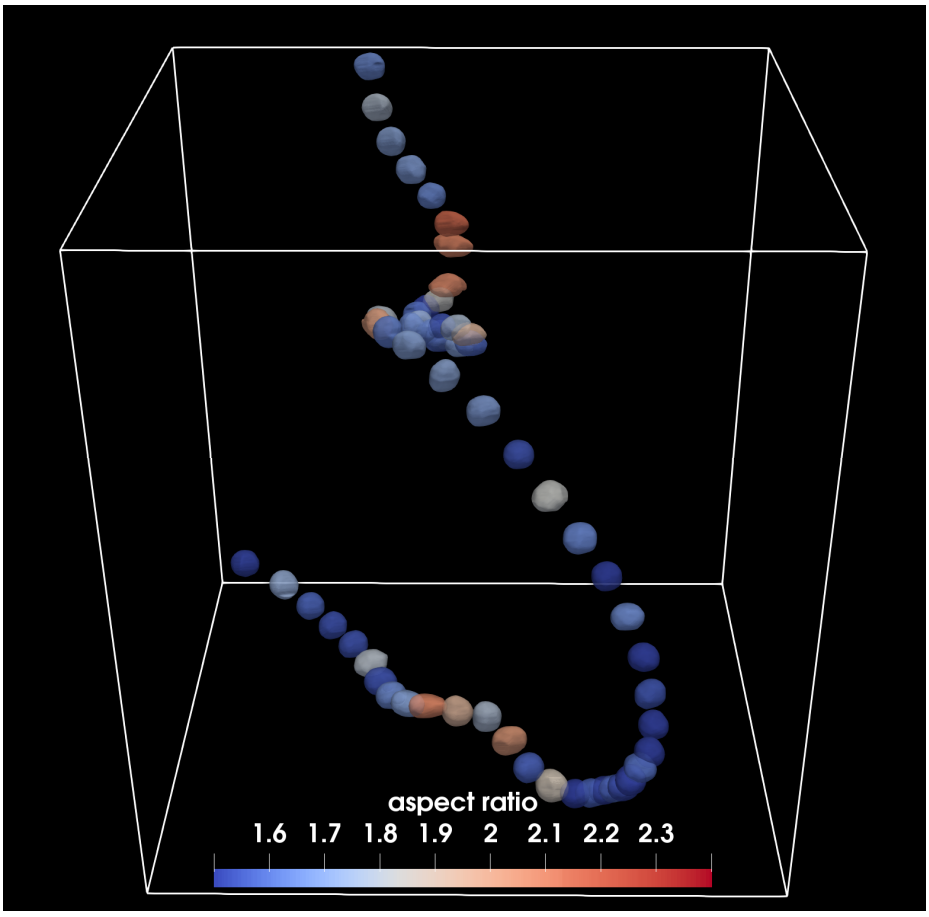

Figure 3.10: The reconstructed bubble trajectory from an experimental dataset; only one every 30 frames is shown here. For each bubble, the surface is color-coded with the instantaneous bubble aspect ratio.

algorithm requires. The outlines of bubbles were easily determined from the image contrast. The standard VH method is then employed to reconstruct the initial 3D geometries of all bubbles in the view. As shown in Fig. 3.9(a), even only using the VH method, the volume overestimation reduces by 21% when N_{cam} increases from 2 to 4 but only by 12% as N_{cam} increases from 4 to 6. For the highly deformed bubble, as shown in Fig. 3.9(b), the volume overestimation drops by 34% as N_{cam} increases from 2 to 4, showing a more significant improvement compared with the weakly-deformed case. Nevertheless, the benefit of including two extra cameras to get from 4 to 6 cameras only has 12% reduction in volume overestimation, similar to the number for the weakly-deformed case. The results underscore the importance of having at least four real cameras for the complex geometries. Note that the reported percentage changes are calculated by treating the six-real-camera reconstructed volume as the actual bubble volume. Since the six-real-camera reconstruction must also overestimate the actual volume, these percentage numbers should be larger than what are reported here.

After VH, the reconstructed shape of each bubble can be input into our VC method to continue refining the geometry. In Fig. 3.9, it is clear that the algorithm tends to underestimate the bubble volume for $N_{cam} = 2$ because very few constraints from two real cameras can stop the algorithm. In this case, the algorithm starts to smooth the actual tip of the elongated bubble. As N_{cam}

becomes large, the VC performs really well for the weakly-deformed case, but the improvement is limited for the highly-deformed one. This suggests that the level of improvement is case sensitive, depending on many parameters, such as the aspect ratio, orientation, and concavity of the bubble geometry.

Once the shape is determined, the center of mass for the bubble is obtained by averaging the 3D locations of all surface vertexes. The center of mass can then be tracked between frames to connect the 3D reconstructed shapes into a trajectory. Fig. 3.10 shows an example of such a trajectory with the reconstructed shape shown every 30 frames. The color of each geometry indicates the aspect ratio α. Note that the major and minor axes for a geometry that underwent the non-affine deformation do not have to be normal to each other. For our experiments, as we know every vertex of the entire surface, the ratio between the longest and the shortest vertex-center distance was used to quantify α.

The time trace of the bubble volume variation is shown in Fig. 3.11(a). This gas bubble did not merge with another one or break over the course of 0.5 s; Nor should it have significant mass transfer with the surrounding fluid at the given condition, which implies that the observed large volume fluctuation may be an artifact due to the reconstruction uncertainty. In addition, the entire curve of 3-real-camera configuration is systematically higher than that of the 6-real-camera case, which is consistent with what we expect that the six cameras

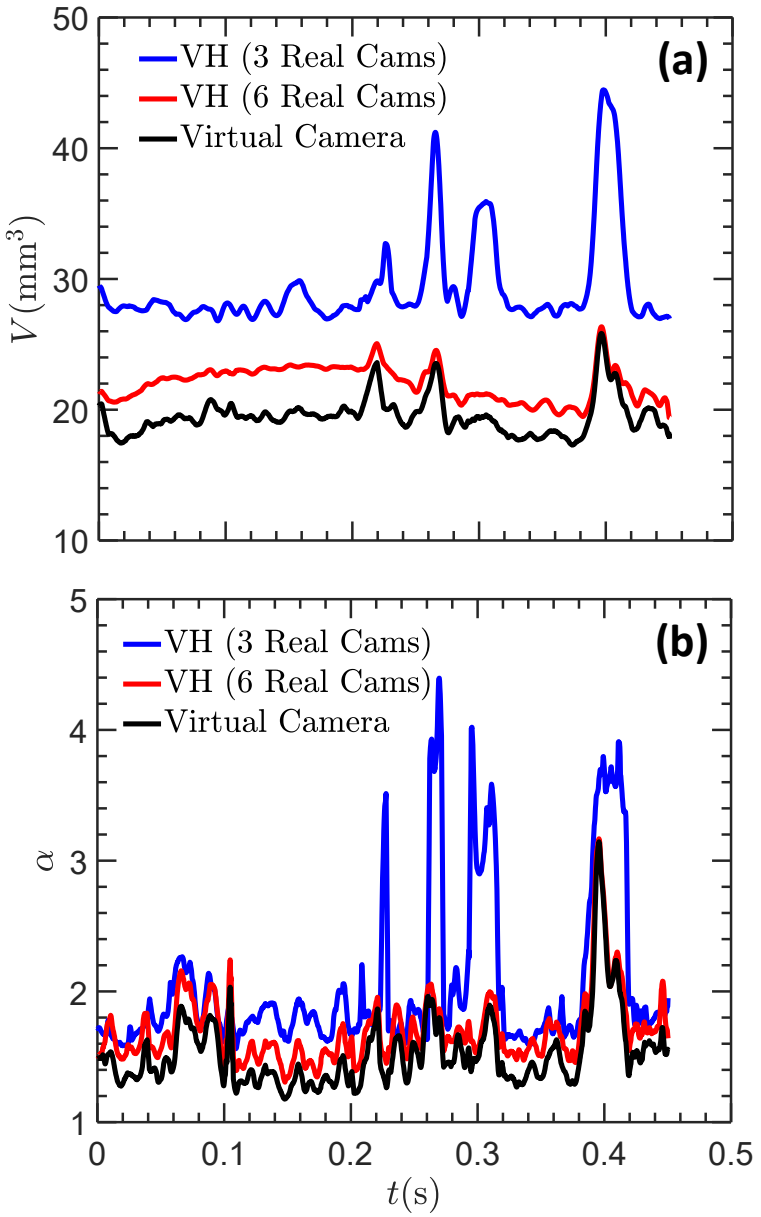

Figure 3.11: Time trace of (a) the volume V and (b) the aspect ratio α of a trajectory as shown in Fig. 3.10. Three different lines show the reconstructed results using VH with 3 real cameras (blue), 6 real cameras (red), as well as 6 real cameras plus applying our VC method (black).

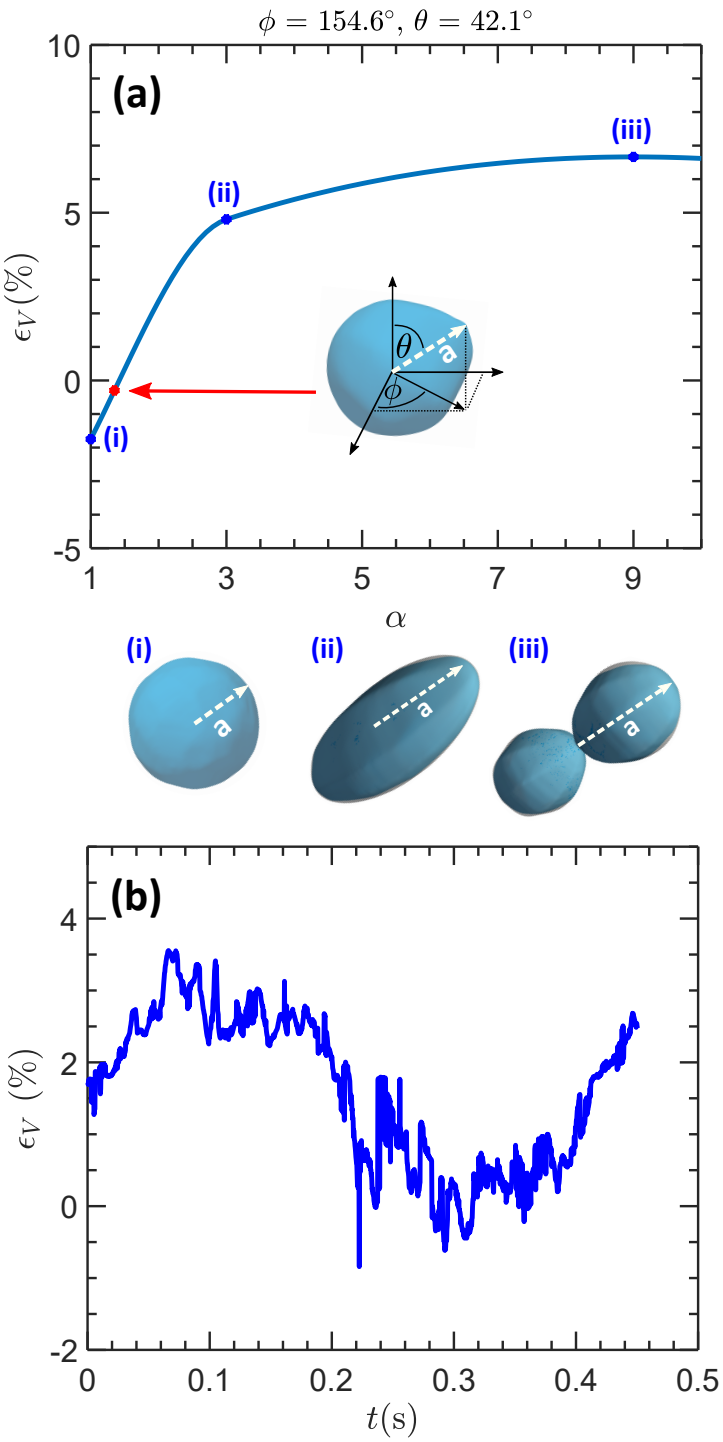

Figure 3.12: (a) The uncertainty of volume reconstruction ϵ_V versus aspect ratio α for three cases: (i) sphere ($\alpha = 1$), (ii) ellipsoid ($\alpha = 3$), (iii) dumbbell ($\alpha = 9$). The inset shows the reconstructed geometry of an actual bubble with $\alpha = 1.5$ and Euler angles at (154.6, 42.1, 0). ϵ_V of such a reconstruction is shown as the red dot by interpolation. (b) ϵ_V of the entire trajectory as shown in Fig. 3.10

provide more constraints. But this difference is not very small, nearly 27% if we treat the 6-real-camera reconstructed volume as the actual volume. In addition, there are four peaks from 0.2 s to 0.45 s, with the first peak slightly lower than the other three. For all four peaks, the image of this bubble overlaps with that of another one in at least one of the real cameras.The third peak falls back to normal as N_{cam} grows from 3 to 6 because this bubble and its neighbor appear to be two distinct entities in the extra 3 cameras added.

When the VC method is applied, it helps to remove more extra materials and brings the red curve systematically down by another 21% (the overall improvement from blue line to black line is 55%). In addition, it appears that the non-physical variation in the red curve with bubble volume from 0–0.2 s systematically higher than that from 0.25–0.35 s is gone after implementing the VC method. On the other hand, the improvement for the three peaks after implementing the VC method is small. As we mentioned before, this is inevitable as the geometrical constraint is lost in real cameras when the bubble image starts to overlap with another one nearby. Nevertheless, these events can be identified and removed during the post-processing step by relying on several key signatures: (i) the estimated volume is typically much larger than the mean of that trajectory, (ii) when a 3D geometry is projected onto 2D camera images, the bubble outline is attached to another bubble. Note that there is no solution to save these cases, the only thing that one can do is to remove

them from the statistics. Segmenting images is often unreliable because two bubbles touching each other can be easily confused with a bubble that is close to breakup.

The time trace of the aspect ratio α is shown in Fig. 3.11(b). α exhibits many small fluctuations that are not seen in volume as taking the ratio between the major and minor axes amplifies noise. The systematical reduction of α from 3-real-camera with VH to 6-real-camera with VC is clear, and the benefit of increasing N_{cam} from 3 to 6 is also obvious as three major peaks that have abnormally-large $\alpha > 3.5$ are removed. Note that these four peaks correspond to the same four peaks in the time trace of volume. This test case demonstrates the importance of not only having as many real cameras as one can afford but also using VC for complex deformable bubbles/droplets.

Finally, the reconstruction uncertainty of an experimental data needs to be assessed so we can be more selective in the post-processing step to calculate statistics. Since the actual volume of the bubble in an experimental dataset is not known, we cannot estimate ϵ_V as we did for synthetic datasets. However, we proposed another way to indirectly estimate ϵ_V based on the geometry and orientation for a given bubble. ϵ_V for sphere, ellipsoid, and dumbbell for different orientations have been obtained in Sec. 3.4. Since they represent different states of bubble deformation, ϵ_V is plotted as a function of aspect ratio α from 1 to 9 (1 for sphere, 3 for ellipsoid, and 9 for dumbbell). Note that the α is not

well defined for a dumbbell since the minor axis of a dumbbell is close to zero and α is close to infinity. We decide to set its aspect ratio to 9, as there is a high probability for the neck to emerge and bubble to break at this aspect ratio.

For each frame, after the reconstruction, the direction of the major axis can be acquired and denoted as $\vec{a}$, from which the Euler angle can be determined. For the particular example used in Fig. 3.12(a) inset, its Euler angle is (154.6, 42.1, 0). ϵ_V for three basic geometries with a range of Euler angles have been shown in Fig. 3.6 and 3.7. From these two figures, ϵ_V can be acquired for this specific Euler angle, and the results are shown as blue dots in Fig. 3.12. ϵ_V for the actual bubble at its $\alpha = 1.5$ (red dot) is estimated through a shape preserving piecewise cubic interpolation (blue line) from three basic geometries.

The same calculation was repeated for all frames in one trajectory and the time trace of ϵ_V is acquired and shown in Fig. 3.12(b), it implies that the volume for the first 0.2 s is probably more overestimated than the rest. This is consistent with the black curve shown in Fig. 3.11(a) that the volume of the reconstructed geometry is indeed slightly higher in the first 0.2 s. Another observation is that this uncertainty quantification did not capture those large peaks in volume estimation because this method only takes the geometry and orientation into account without knowing the presence of overlapping bubble images.

3.7 Conclusion and remarks

This chapter introduces a new virtual-camera method to improve the reconstruction accuracy of bubbles or droplets undergoing non-affine deformation in turbulence. This new method translates the physical constraint of minimal surface area to the image refinement on virtual cameras. The extra material due to the limited-angle reconstruction manifests as sharp corners on virtual camera planes, which can be smoothed and removed. The algorithm was first tested on three simple synthetic objects, including sphere, ellipsoid, and dumbbell. They represent three basic states of bubble deformation: undeformed, weakly-deformed, and severely-deformed. The reconstruction uncertainty appears to depend on both the geometry (convex or concave) and the orientation with respect to the camera configuration. Our method works well for simple and convex geometries for as few as two real cameras. More real cameras are required for either complex shapes or for geometries with concave features. In addition to these simple geometries, a DNS dataset of bubble deforming in a turbulent channel flow is used to quantify the uncertainty, and it turns out that the VC method reduces the volume overestimation from 20% to 10%. Finally, the reconstruction has also been tested on the experimental data of non-affine bubble deformation in strong turbulence. The volume overestimation drops from about 55% using 3 real cameras with classical VH method to about 4% using 6 real cameras and the VC method. In addition, the method also utilizes

the estimated geometrical aspect ratio and orientation to estimate the reconstruction uncertainty of each bubble in each frame, which can be leveraged to select the best reconstruction for statistics. In summary, this method provides a robust way to incorporate the physical constraints to improve the 3D reconstruction accuracy of bubbles and droplets in turbulent multiphase flow and it also paves the foundation for the future development of uncertainty quantification for strongly coupled gas-liquid and liquid-liquid multiphase flow.

Chapter 4

Simultaneous measurements of deforming Hinze-scale bubbles with surrounding turbulence

We experimentally investigate the breakup mechanisms and probability of Hinze-scale bubbles in turbulence. The Hinze scale is defined as the critical bubble size based on the critical mean Weber number, across which the bubble breakup probability was believed to have an abrupt transition from being dominated by turbulence stresses to being suppressed completely by the surface tension. In this work, to quantify the breakup probability of bubbles with sizes close to the Hinze scale and to examine different breakup mechanisms, both 3D bubble geometry and the locations of surrounding tracer particles were simultaneously reconstructed and tracked. From the experimental results, two

Weber numbers, one calculated from the slip velocity between two phases and the other one acquired from local velocity gradients, are separated and fitted with models that can be linked back to turbulence characteristics. Moreover, we also provide an empirical model to link bubble deformation to two Weber numbers by extending the relationship obtained from the potential flow theory. The proposed relationship between bubble aspect ratio and Weber numbers seems to work consistently well for a range of bubble sizes. Furthermore, the time traces of bubble aspect ratio and the two Weber numbers are connected using the linear forced oscillator model. Finally, having access to the distribution of these two Weber numbers provides a unique way to extract the breakup probability of bubbles with sizes close to the Hinze scale.

4.1 Introduction

The process by which finite-sized gas bubbles and liquid droplets break in a turbulent environment constitutes one of the most fundamental and practically important phenomena in multiphase flows. Details of how this takes place have significant impact in various industrial and natural processes, such as chemical reactors (Jakobsen, 2014), bioreactors (Kawase and Moo-Young, 1990), air-sea gas transfer (Liss and Merlivat, 1986), drag reduction (Lohse, 2018; Verschoof et al., 2016), and two-phase heat transfer (Lu and Tryggvason, 2008; Lu, Fer-

nandez, and Tryggvason, 2005; Dabiri, Lu, and Tryggvason, 2013). Bubbles in strong turbulence can deform, break, and coalesce with each other. The presence of deformation adds to a problem that is already complicated even for the dispersed two-phase flow with rigid, non-deformable particles (Balachandar and Eaton, 2010). Moreover, most works on bubble deformation have been limited to simulations (Elghobashi (2019) and the references within) with very few experimental works that can resolve both phases in 3D. It is thus the main objective of this paper to overcome this technical challenge and provide new experimental results to study bubble deformation and breakup in turbulence.

The earliest studies on bubble breakup in turbulence were conducted by Kolmogorov (1949) and Hinze (1955). In particular, Hinze unified the results of numerous preceding investigations. In his seminal work, he argued that only two dimensionless numbers are needed: one is the Weber number We (also used by Kolmogorov (1949)) and the other one is the viscosity group, $N = \mu_d/\sqrt{\rho_d \sigma D/2}$, in which ρ_d and μ_d are the density and the dynamic viscosity of the dispersed phase, respectively. σ is the surface tension, and D is the bubble diameter. This is the first time that the critical Weber number was introduced, and Hinze argued that the critical Weber number must depend only on N following $We_{crit} = c(1 + f(N))$, where $f(N)$ is a function of N. For bubbles with vanishing inner viscosity, the critical Weber number should just be a constant c. A critical Weber number of 0.59 was extrapolated from an

earlier experiment conducted by Clay (1940). In this work, the Weber number is defined based on external stresses τ applied on the bubble surface $We = \tau D/\sigma$. τ is related to the energy dissipation rate (ϵ) in the form of $\tau = C_2(\epsilon D)^{2/3}$ based on the Kolmogorov theory, in which $C_2 \approx 2.13$ is the Kolmogorov constant. This formulation should be, strictly speaking, only applied to homogeneous and isotropic turbulence, yet it has been used in many other flow configurations, including chemical reactors with impellers and jets based on the assumption of local isotropy.

Hinze's framework was constructed primarily for liquid droplets. But he noted that the critical Weber number is not universal; instead, it depends on the density difference between two phases. Sevik and Park (1973) extended this framework to bubbles splitting in turbulence, in which case a large density difference between the two phases was present. A slightly larger critical Weber number of 1.26 was observed. By assuming bubbles break once they start to resonate with surrounding turbulent eddies, the critical Weber number can be calculated analytically by equating the natural frequency of bubbles (Lamb, 1932) with the reciprocal of the eddy turnover time. The predicted value seems to agree with their measured results.

Introducing We_{crit} also comes with a critical length scale. For a given mean turbulence energy dissipation rate $\langle\epsilon\rangle$, the critical bubble size is often referred to as the Hinze scale D_H, and it is related to We_{crit} in the form of $We_{crit} =$

$\rho C_2(\langle\epsilon\rangle D_H)^{2/3} D_H/\sigma$. It is important to introduce the idea of energy-abundant/super-Hinze ($We \gg We_{crit}$ and $D \gg D_H$) versus energy-limited/sub-Hinze ($We < We_{crit}$ and $D < D_H$) breakups. The former one has been studied much more extensively than the latter for a simple reason: super-Hinze breakup is much faster and more frequent so it is easier to observe in a finite volume and to collect enough statistics. Super-Hinze breakup is typically studied in several different flow configurations: pipe flow (Hesketh, Etchells, and Russell, 1991) and turbulent jets (Sevik and Park, 1973; Martínez-Bazán, Montanes, and Lasheras, 1999; Vejražka, Zedníková, and Stanovskỳ, 2018). In these cases, the energy contained in turbulent eddies is so abundant that each bubble is almost guaranteed to break–it is only a matter of *time*.

Breakup frequency is an important parameter in the population balance equation (Hulburt and Katz, 1964; Ramkrishna, 2000). This framework has one limitation—it assumes that all bubbles above the Hinze scale will eventually break and no bubbles below the scale will ever break (no matter how long one waits). This poses an important challenge to numerical simulations to account for sub-Hinze scale microbubbles, which are important to air-sea gas exchange (Deane and Stokes, 2002), as well as underwater acoustics as these small bubbles tend to remain in the waterside for an extended period of time.

The breakup mechanisms that have been proposed and assessed in the literature include (i) persistent stretching by straining flows (parallel flow, plane

hyperbolic, axisymmetric hyperbolic, Couette flow, or rotating flow) (Hinze, 1955); bubbles tend to exhibit regular affine deformation in these types of flows (lenticular or cigar-shaped). (ii) resonance mechanism that relies on bubble oscillation continuing to siphon energy until breakup (Sevik and Park, 1973; Risso and Fabre, 1998; Hesketh, Etchells, and Russell, 1991). It typically assumes that the surrounding eddy retains a similar frequency with bubbles' natural frequency. (iii) Inertial mechanism relies on bubbles suddenly being exposed to strong flows, which leads to an almost-immediate irregular breakup. This mechanism has been studied in many contexts in addition to turbulence-induced breakup, e.g. raindrop fragmentation (Villermaux and Bossa, 2009) and bag breakup in crossflows (Ng, Sankarakrishnan, and Sallam, 2008).

Applying only one mean Weber number to account for three different breakup mechanisms is questionable; it completely ignores the third breakup mechanism for bubbles being suddenly exposed to a strong flow. One may argue that, if there is no strong mean flow, this mechanism is not important. However, in turbulence, bubbles do not follow surrounding flows exactly; bubbles always drift away either due to the added mass force or simply their finite size. This drift could lead to a significant velocity differences between the two phases. Although it may not be as strong as what could be encountered in a crossflow (ibid.), it may still contribute to bubble deformation and breakup. In fact, although bubble-eddy collision remains the most dominant model to explain the

bubble breakup process, it has been shown before that it is the relative velocity between the two phases that controls bubble deformation and breakup (Mathai, Lohse, and Sun, 2020b).

In addition, as Risso and Fabre (1998) noted, the instantaneous and local Weber number, We, could be much larger than the mean value, $\langle We \rangle$. They proposed to use the time trace of We along each bubble trajectory to evaluate its breakup frequency. However, in their experiments, the instantaneous Weber number was not directly accessible. As a result, velocity signals from experiments of single-phase turbulence were used as a surrogate. This is a common practice in the community as the simultaneous measurements of both phases, either in 2D or 3D, remain a challenge.

To resolve deformation and breakup of the Hinze or sub-Hinze scale bubbles, in this paper, we will introduce an experiment that provides simultaneous measurements of both bubble deformation and surrounding flows thanks to the recent advancement of the 3D high-concentration particle shadow tracking (Tan et al., 2019b) and 3D virtual-camera visual-hull shape reconstruction (Masuk, Salibindla, and Ni, 2019). In §4.2, the experimental setup of the vertical tunnel system with a large section of homogeneous and isotropic turbulence will be introduced. In the same section, the optical system designed to provide simultaneous measurements of both the phases will also be discussed. In §4.4, based on the new datasets, we discuss how flow decomposition can be conducted

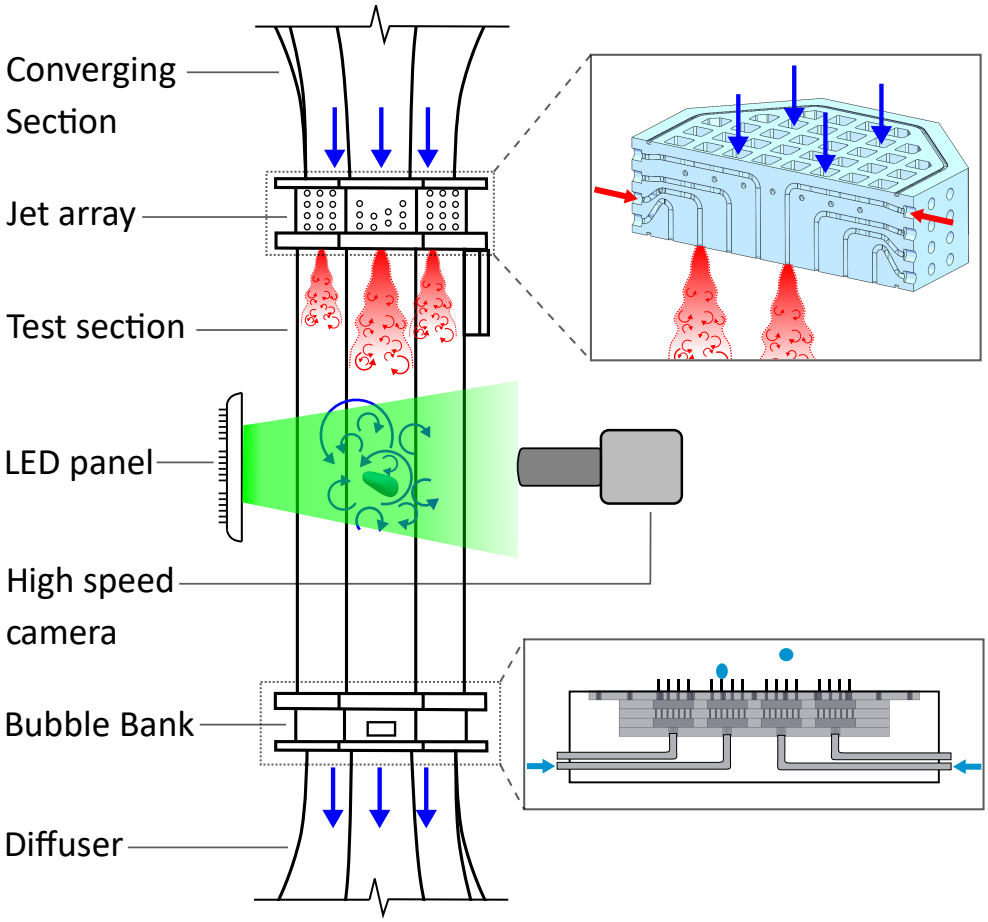

Figure 4.1: Schematic of the V-ONSET vertical water tunnel; two insets show the 3D model of the jet array used to fire high-speed water jets into the test section and a bubble bank to inject bubbles, respectively. Additional details concerning this facility can be found in Masuk et al. (2019)

to analyze the relative roles played by different mechanisms. In §4.4.5, we finally estimate the breakup probability of bubbles in turbulence with a limited energy dissipation rate.

4.2 Experimental Setup

A facility was designed to accomplish two main goals: (i) to maintain homogeneous and isotropic turbulence in a large volume to ensure that bubbles within this volume experience similar turbulence characteristics, and (ii) bubble deformation should be driven primarily by turbulence rather than buoyancy, and that bubble sizes remain close to the Hinze scale, so we can investigate the deformation and breakup of the Hinze-scale and sub-Hinze-scale bubbles. Satisfying both criteria is challenging. For example, many systems that feature a large region of homogeneous and isotropic turbulence tend to have a low energy dissipation rate (Variano, Bodenschatz, and Cowen, 2004) ($\langle\epsilon\rangle = O(10^{-5}\text{–}10^{-3})$ m^2/s^3), whereas facilities that use water jets to break bubbles and study their statistics can generate a large energy dissipation rate $\langle\epsilon\rangle = O(0.1\text{–}10^{3})$ m^2/s^3 at the cost of having strong flow inhomogeneity and anisotropy (Martínez-Bazán, Montanes, and Lasheras, 1999; Vejražka, Zedníková, and Stanovskỳ, 2018).

The experimental setup used for the current study is essentially a vertical water tunnel capable of generating turbulence with $\langle\epsilon\rangle$ roughly at $0.16 - 0.5$ m^2/s^3. To extend the residence time of a Hinze-scale bubble in the view area, the mean flow in the tunnel was configured to move downward in a vertically-oriented test section. The flow speed was adjusted to balance the rise velocity of bubbles with diameters at around 3 mm to increase the residence time of

these bubbles in the view area. Combined with $\langle \epsilon \rangle$ in this region, $\langle We \rangle$ was roughly at 1.19, indicating most bubbles in the interrogation volume would be close to the Hinze scale.

Turbulence in the test section was generated using 88 high-speed water jets (up to 12 m/s), each of which has a diameter d of 5 mm, firing co-axially downward into the test section along with the mean flow. The firing pattern of these momentum jets was randomized in a way similar to the work by Variano, Bodenschatz, and Cowen (2004) in order to ensure that no secondary flow structure would develop in the test section (Variano, Bodenschatz, and Cowen, 2004; De Silva and Fernando, 1994; Srdic, Fernando, and Montenegro, 1996). On average, 12.5% of the jets were kept on at a time as this was found to maximize the turbulence intensity. The test section was set much farther downstream of the jets (about $80d$) to ensure that the jets were well mixed and turbulence becomes homogeneous and isotropic with very little spatial variation. Additional details concerning this setup and its flow characteristics can be found in Masuk et al. (2019).

Bubbles were generated at the bottom of the test section using two different sizes of hypodermic needles. The size range of bubbles in the experiment was 2–7 mm in diameter. This bubble injection was far below the measurement volume to ensure that bubbles entering the measurement volume already lost memory of the injection.

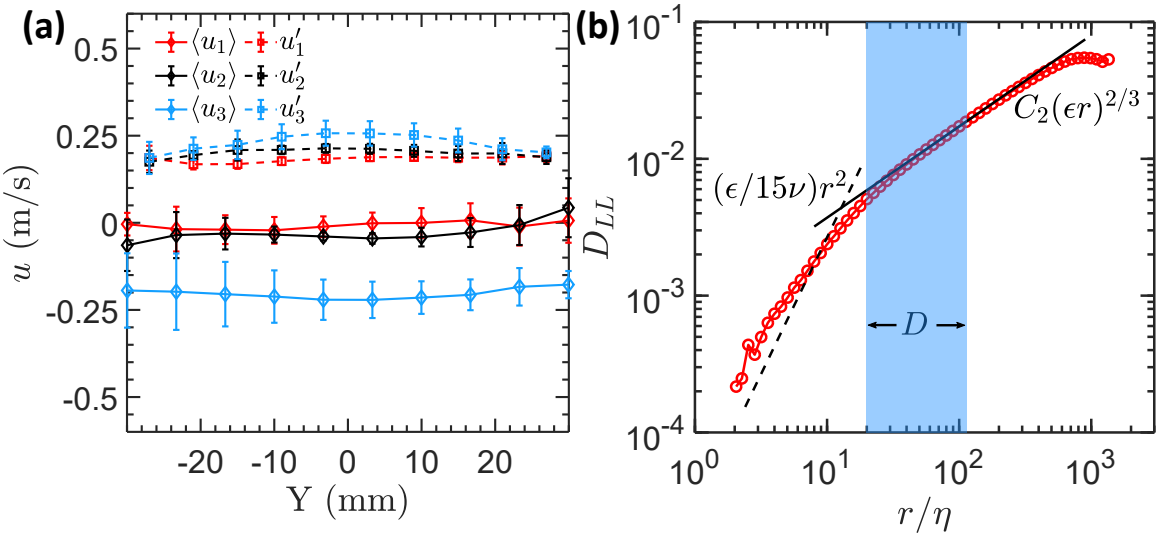

Figure 4.2: (a) The spatial distribution of the mean and fluctuation velocity of all three components along the horizontal Y axis; (b) The longitudinal structure function D_{LL} as a function of the scale separation r normalized by the Kolmogorov length scale η. The dashed and solid lines indicate the two limiting scaling laws predicted by the Kolmogorov theory in the dissipative and inertial ranges, respectively.

Both the bubble dynamics and turbulence statistics were collected using non-invasive optical measurements. Since Kolmogorov timescale $\tau_\eta = 2.5$ ms, six high-speed cameras with 4000 fps frame rate were used to ensure that about 10 frames of images were taken within one τ_η. These cameras were spatially distributed to cover the entire perimeter of the octagonal test section. Six LED panels were used to provide diffused backlighting to cast shadows of both particles and bubbles onto the imaging planes of all six cameras.

4.3 Flow characterization

The first step was to obtain some classical statistics of the single-phase turbulence without bubble injection to ensure that the design of the facility satisfies the two aforementioned requirements. The same setup described in §4.2 was used and tracer trajectories were processed to evaluate the velocity field. In figure 4.2(a), the spatial distribution of the velocity fluctuations along both the vertical and horizontal directions are shown. It is evident that there is very little, if at all, spatial gradient of both the mean velocity and the fluctuation velocity within the entire interrogation volume. This result confirms that the flow is close to homogeneous and isotropic. The details of other tests can be found in Masuk et al. (2019).

The second criterion regarding the turbulence-induced deformation relies on $\langle\epsilon\rangle$, which can be extracted from the second-order structure function, or just the longitudinal component of it, i.e. D_{LL}. D_{LL} obtained from single-phase turbulence without bubbles in our facility is shown in figure 4.2(b). It can be seen that our experiments were able to resolve length scales as small as 2η, with η being the Kolmogorov length scale $\eta = (\nu^3/\langle\epsilon\rangle)^{1/4}$. η is close to 50 μm, which is close to the pixel resolution in our setup. We can resolve such a small scale thanks to our in-house high-concentration particle tracking system that employs the Shake-The-Box method (Tan et al., 2019b).

The structure function should approach two limits: one in the dissipative

range ($r \ll \eta$) and the other in the inertial range ($\eta \ll r \ll L$). L is the integral scale, which is estimated based on $L \approx u'^3/\epsilon$, where u' is the fluctuation velocity. In the dissipative range, the structure function follows the relationship of $D_{LL} = (\epsilon/15\nu)r^2$. In the inertial range, the 2/3 - scaling law is based on the classical Kolmogorov theory. Although how long the inertial range is and if the Kolmogorov constant C_2 is affected by the finite-Reynolds number effect are subjected to further investigation (Ni, Xia, et al., 2013), using a standard number $C_2 = 2.13$ can provide a reasonable estimation of ϵ. The solid line shown in the figure is based on the calculated $\langle\epsilon\rangle = 0.16$ m^2/s^3. However, if ϵ obtained from the inertial range is used to predict the dissipative range D_{LL} (dashed line), it appears that the dashed line is systematically lower than the experimental results. In sum, the difference of $\langle\epsilon\rangle$ estimated from either dissipative or inertial range helps to quantify the experimental uncertainty of the mean energy dissipation rate: $\langle\epsilon\rangle$=0.22$\pm$0.07 m^2/s^3. Moreover, after bubbles get injected into the system, bubbles can actively modulate turbulence and increase the local energy dissipation rate to around 0.52 m^2/s^3.

The shaded area in figure 4.2(b) marks the size range of bubbles with respect to the Kolmogorov scale η. As one can see, most bubbles are within the inertial range of turbulence, indicating that their deformation and breakup are indeed driven by the velocity fluctuations that can be estimated by the inertial range scaling.

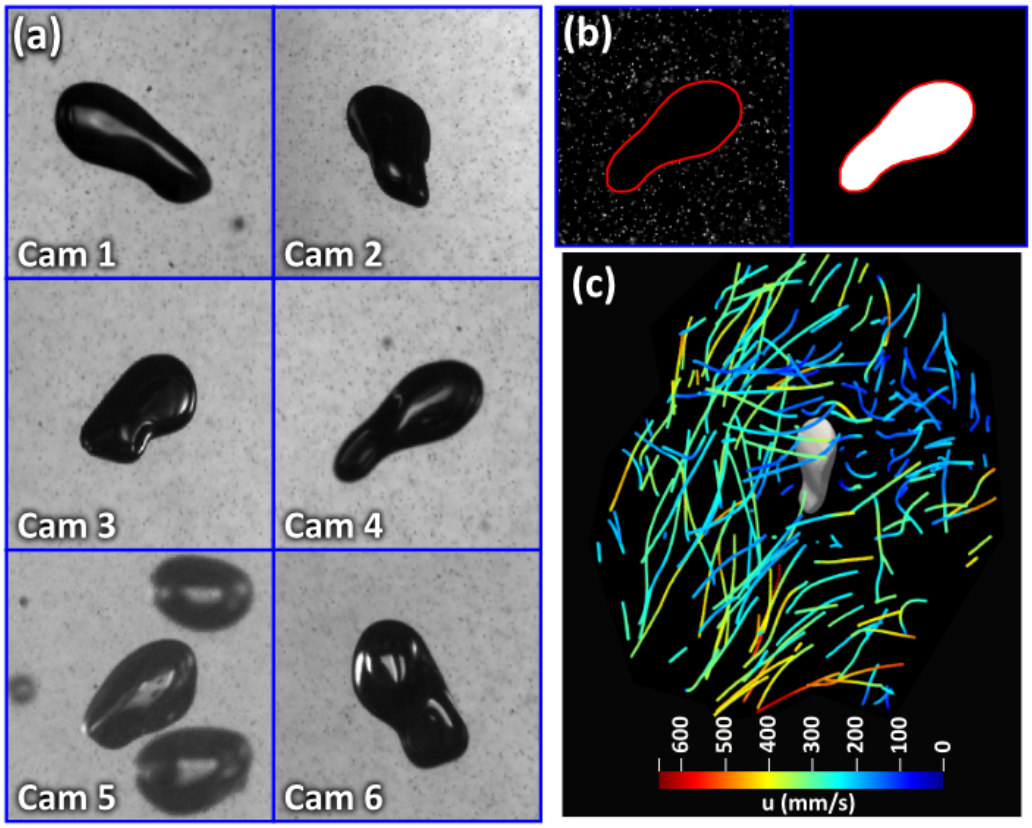

Figure 4.3: (a) Raw images of one highly-deformed bubble observed by six high-speed cameras simultaneously, (b) The outline and silhouette of the same bubble extracted from Cam 4, (c) 3D tracks of about 40 tracer particles within $4D$ (D is the bubble diameter) from the center of a bubble that is shown as a 3D reconstructed object.

4.4 Results and discussions

4.4.1 Simultaneous bubble and particle tracking

As shown in figure 4.3(a), shadows of both bubbles and particles were projected onto the imaging planes of cameras. It is straightforward to separate their images based on the size difference. An example of segmented images of

a bubble and surrounding tracer particles is shown in figure 4.3(b). The bubble silhouette was then input into a recently-developed virtual-camera visual hull method (Masuk, Salibindla, and Ni, 2019) for 3D shape reconstruction. Averaging surface points on the reconstructed geometry helps to determine the center of mass, which was then tracked in 3D to obtain a bubble trajectory. This procedure was repeated for all bubbles to acquire both the kinematic (from tracks) as well as geometrical information (from 3D shape reconstruction). On average, there were about 15 bubbles in the interrogation volume at each time instant and each bubble trajectory roughly lasts about 0.09 seconds (360 frames).

Separated images for tracer particles were input into our in-house OpenLPT (Tan et al., 2019b) to perform the shake-the-box calculation (OpenLPT has already been open-sourced and is available for the entire community to use @JHU-Ni-Lab on Github). Compared with bubbles, significantly more particles could be found in the interrogation volume. At each time instant, there were about 6,000 tracer particles, and the mean track length was about 200 for each tracer particle.

Figure 4.3(c) shows one example of about 40 tracer trajectories nearby a bubble that was reconstructed from silhouettes segmented from figure 4.3(a). In this case, trajectories of tracer particles within $4D$ away from the bubble center were included. These tracks would be used to estimate the flow condition around the bubble. Since a high-concentration of tracer particles were avail-

able nearby almost every bubble, this experiment provided access to almost all information—the Weber number, turbulence energy dissipation rate, and even the eigenvalues of the velocity gradient tensor—locally, instantaneously, and along each bubble trajectory. Additional information concerning the setup and measurement techniques can be found in works by Masuk, Salibindla, and Ni (2019), Masuk et al. (2019), and Tan et al. (2019b).

4.4.2 Flow velocity and velocity gradient

For a bubble at location $\mathbf{x_0}$, its surrounding flow velocity $\mathbf{u}^p$ can be found at a number of discrete points ($p = 1, 2, ..., n$) where n tracer particles are located. These tracer particles are sought within a radius of $D_s/2$ from the bubble center. The flow field within this range can be decomposed into leading terms by applying the Taylor expansion:

$$\begin{gathered} u_i^p(\mathbf{x_0} + \mathbf{x}^p) \approx \overline{u_i}(\mathbf{x_0}) + \widetilde{A}_{ij}(\mathbf{x_0})x_j^p + O\left(\frac{1}{2}x_j^p \widetilde{H}_{jik}(\mathbf{x_0})x_k^p\right) \\ \widetilde{A}_{ij}(\mathbf{x_0}) = \frac{\partial u_i^p}{\partial x_j^p} \quad \text{and} \quad \widetilde{H}_{jik}(\mathbf{x_0}) = \frac{\partial^2 u_i^p}{\partial x_j^p \partial x_k^p} \end{gathered} \tag{4.1}$$

where $\overline{u_i} = \sum_{p=1}^{n} u_i^p(\mathbf{x_0} + \mathbf{x}^p)/N$ represents the local mean flow. $\widetilde{A}_{ij}$ and $\widetilde{H}_{jik}$ indicate the velocity gradient tensor and the Hessian matrix, respectively, and the tilde represents coarse-graining at the bubble size. $\mathbf{x}^p$ is the separation

vector directed from the p_{th} tracer particle to the bubble center at $\mathbf{x_0}$. For small micro-bubbles with sizes in the dissipative range ($D \ll \eta$), the flow is linear so the velocity Hessian is negligibly small. This higher-order term grows as a function of bubble size and eventually becomes important for bubbles with sizes in the inertial range ($\eta \ll D \ll L$).

It has been shown before that the measurements of the velocity gradient tensor can be so accurate that it can be used to predict the dynamics of non-spherical particles in turbulence (Ni et al., 2015). The velocity Hessian, on the other hand, requires measuring the gradient of the velocity gradient (three 3×3 matrices), which requires a large number of tracer particles. Even if these many particles are possible to attain, the signals, after subtracting the contribution from $\overline{u_i}$ and $\widetilde{A}_{ij}(\mathbf{x_0})x_j^p$, becomes too weak to be measured accurately. As a result, we limit only to the first two orders, i.e. the mean flow velocity $\overline{u_i}$ and the velocity gradient $\widetilde{A}_{ij}(\mathbf{x_0})$, to capture the key mechanisms of deformation.

The velocity gradient tensor $\widetilde{A}_{ij}$ can be uniquely solved if we have four particles around a bubble. In practice, on average, 30–40 particles were used to perform least-squares fit by seeking the minimum value of the squared residuals $\sum_p [u_i^p - \widetilde{A}_{ij}x_j^p]^2$ (Ni et al., 2015; Pumir, Bodenschatz, and Xu, 2013). Although finite-sized bubbles typically come with a large search radius and abundant nearby tracer particles thanks to our tracking method (Tan et al., 2020), particles surrounding a bubble are still randomly distributed in space. If nearby

particles stay primarily within a quasi-2D plane, the estimation of the out-of-plane velocity gradient will have large uncertainty. Similar to previous studies (Ni et al., 2015; Xu, Pumir, and Bodenschatz, 2011), an inertia tensor $I = \sum_p x_i^p x_j^p / tr(\sum_p x_i^p x_j^p)$ was adopted to evaluate the shape factor of the particle cloud. If particles are uniformly distributed in 3D, three eigenvalues of this inertia tensor (γ_i) equal to 1/3. For a quasi-2D distribution, the smallest eigenvalue (γ_3) will be very close to zero, and the gradient along that direction cannot be calculated. In practice, events with γ_3/γ_1 smaller than 0.15 was therefore removed from the statistics. A more stringent criterion can be put forward by only selecting cases if they satisfy $tr(\widetilde{A}_{ij}) = 0$ (Ni et al., 2015; Lüthi, Tsinober, and Kinzelbach, 2005; Hoyer et al., 2005). However, for $\widetilde{A}_{ij}$ around a deformable bubble, the flow divergence may not be zero so this criterion was not enforced.

Based on $\widetilde{A}_{ij}$, the coarse-grained rate-of-strain tensor, $\widetilde{S}_{ij}$, and rotation tensor, $\widetilde{\Omega}_{ij}$ can be directly obtained: $\widetilde{S}_{ij} = \frac{1}{2}(\widetilde{A}_{ij} + \widetilde{A}_{ji})$, $\widetilde{\Omega}_{ij} = \frac{1}{2}(\widetilde{A}_{ij} - \widetilde{A}_{ji})$. Figure 4.4(a) shows the probability density function (PDF) of two eigenvalues of $\widetilde{S}_{ij}$ (the largest $\widetilde{\lambda}_1$ and the smallest $\widetilde{\lambda}_3$) based on different D_s. The PDFs of $|\widetilde{\lambda}_1|$ and $|\widetilde{\lambda}_3|$ overlap with each other for three D_s considered, indicating that the magnitude of flow stretching and compression near a bubble on average is similar. The PDF progressively shifts leftward as D_s becomes larger because coarse graining at a larger D_s works effectively as enlarging a low-pass filter,

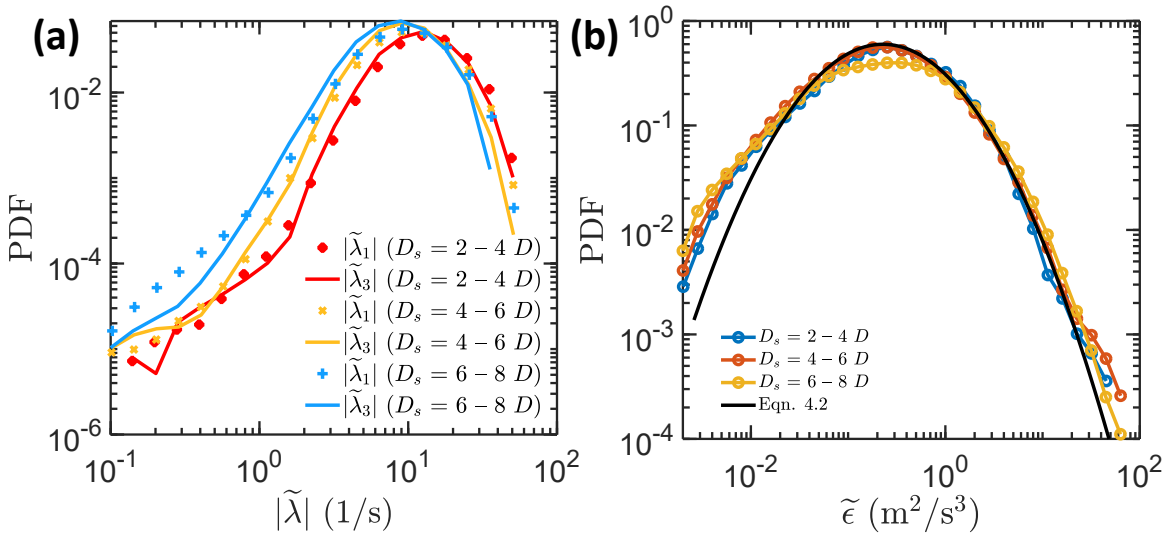

Figure 4.4: (a) The distribution of the two eigenvalues ($\widetilde{\lambda}_1$ and $\widetilde{\lambda}_3$) of the local rate-of-strain tensor coarsed-grained at the bubble scale D ($|\widetilde{\lambda}|$ is used here because $\widetilde{\lambda}_3 < 0$.); Three search diameters ranging from from 2–4D to 6–8D are denoted by different colors. (b) The distribution of the local coarsed-grained energy dissipation rate $\widetilde{\epsilon}$. The log-normal distribution from equation 4.2 is shown as solid line.

which will continue to reduce the gradient as D_s increases. Since $D_s > D$, calculating the velocity gradient tensor from tracers located $D_s/2$ away from the bubble center will always underestimate $\widetilde{A}_{ij}$ at the bubble scale D. Fortunately, both D_s and D are in the inertial range, and the eigenvalues of $\widetilde{A}_{ij}$ can be related to the local energy dissipation rate in the form of $C_2(\widetilde{\epsilon}D_s)^{2/3} = (\widetilde{\lambda}_3 D_s)^2$, where $C_2 = 2.13$ is the Kolmogorov constant (Ni, Xia, et al., 2013; Batchelor, 1953; Sreenivasan, 1995) and $\widetilde{\epsilon}$ is the coarse-grained energy dissipation rate. In figure 4.4(b), the PDFs of the estimated local $\widetilde{\epsilon}$ using three different search diameters D_s are shown. Despite their differences in $\widetilde{\lambda}_3$, once converted to $\widetilde{\epsilon}$, three curves from all three D_s fall right on top of each other, indicating that the

local $\widetilde{\epsilon}$ is roughly the same for the range of D_s considered. Therefore, although a $D_s > D$ is needed for selecting tracer particles, the statistics reported are insensitive to D_s thanks to the universal inertial range scaling in homogeneous and isotropic turbulence.

The coarse-grained energy dissipation rate can be described by the log-normal distribution based on the Kolmogorov refined theory in 1962 (Kolmogorov, 1962) and multi-fractal spectrum (Meneveau and Sreenivasan, 1991).

$$P\left(\frac{\epsilon_r}{\langle\epsilon\rangle}\right) = \frac{1}{\epsilon_r/\langle\epsilon\rangle}\frac{1}{\sqrt{2\pi(A+\mu\ln(L/r))}}\exp\left[-\frac{(\ln(\epsilon_r/\langle\epsilon\rangle)+1/2(A+\mu\ln(L/r)))^2}{2(A+\mu\ln(L/r))}\right] \tag{4.2}$$

where ϵ_r is the energy dissipation rate coarse-grained at a scale r. $\mu \approx 0.25$ is the intermittency exponent. $L = 3.2$–6 cm is the integral length scale. A is a parameter that needs to be fitted to the experimental data to determine the variance of $\widetilde{\epsilon}$ when $r = L$, which was found to be around one. Based on the definition, $\widetilde{\epsilon}$ measured from our experiments is equivalent to $\epsilon_r|_{r=D}$, which is shown as the black solid line in figure 4.4. The nice agreement between the experimental data and the log-normal distribution (equation 4.2) shows that the measured coarse-grained energy dissipation rate is consistent with the classical Kolmogorov theory.

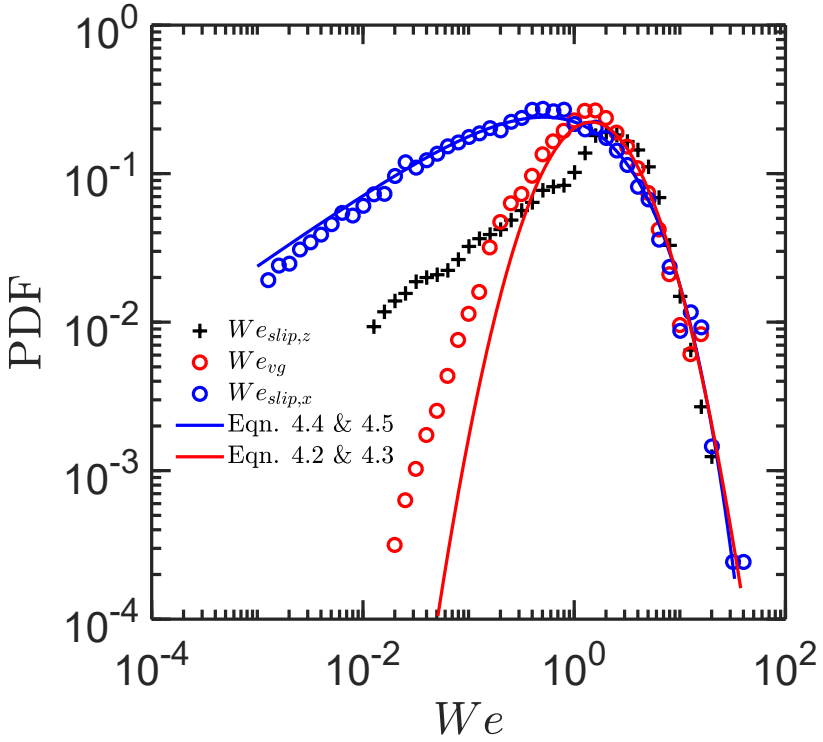

Figure 4.5: The distribution of the Weber number, based on the slip velocity, $We_{slip,x}$ and $We_{slip,z}$ and the velocity gradient, We_{vg}. Two lines represent the Weber number distributions obtained from the log-normal distribution of $\widetilde{\epsilon}$ (equation 4.2, red line) and the stretched exponential fit of the slip velocity (equation 4.4, blue line), respectively.

4.4.3 Different types of deformation

4.4.3.1 Bubble deformation by the velocity gradient We_{vg}

In turbulence, the difference of dynamic pressure across a bubble acts to push the bubble interface inward to drive bubble deformation. Based on this argument, $\widetilde{\lambda}_3$, which is associated with the direction that compresses the most, should be the more relevant eigenvalue of $\widetilde{A}_{ij}$. Following the argument, the

Weber number can be defined as

$$We_{vg} = \frac{\rho(\widetilde{\lambda}_3 D)^2 D}{\sigma} \sim \frac{C_2(\widetilde{\epsilon} D)^{2/3}}{\sigma} \tag{4.3}$$

This Weber number definition is based on the local coarse-grained $\widetilde{A}_{ij}$ and $\widetilde{\epsilon}$, which is different from the mean Weber number defined by Kolmogorov (1949) and Hinze (1955). Figure 4.5 shows the distribution of local We_{vg} based on the measurements of $\widetilde{A}_{ij}$ along each bubble track. The distribution peaks at around one, and all data points on the right side of the peak, which consists of a large portion of the total events, represent cases when bubbles deform under strong velocity gradients. On top of the experimental results, the model of We_{vg} based on equation 4.2 and 4.3 is also shown. Similar to figure 4.4(b), the log-normal distribution of the local $\widetilde{\epsilon}$ explains the observed shape of the PDF of We_{vg}, from which bubble breakup probability can be determined.

4.4.3.2 Slip-velocity induced deformation We_{slip}

As Hinze stated in his original seminal work (ibid.), employing the velocity gradient to evaluate the deformation and breakup of droplets should only be applied if there is no large density difference between the dispersed phase and the carrier phase. For bubbles in water, such a large density difference does exist, and it is not surprising that We_{vg} may not capture the total stress exerted

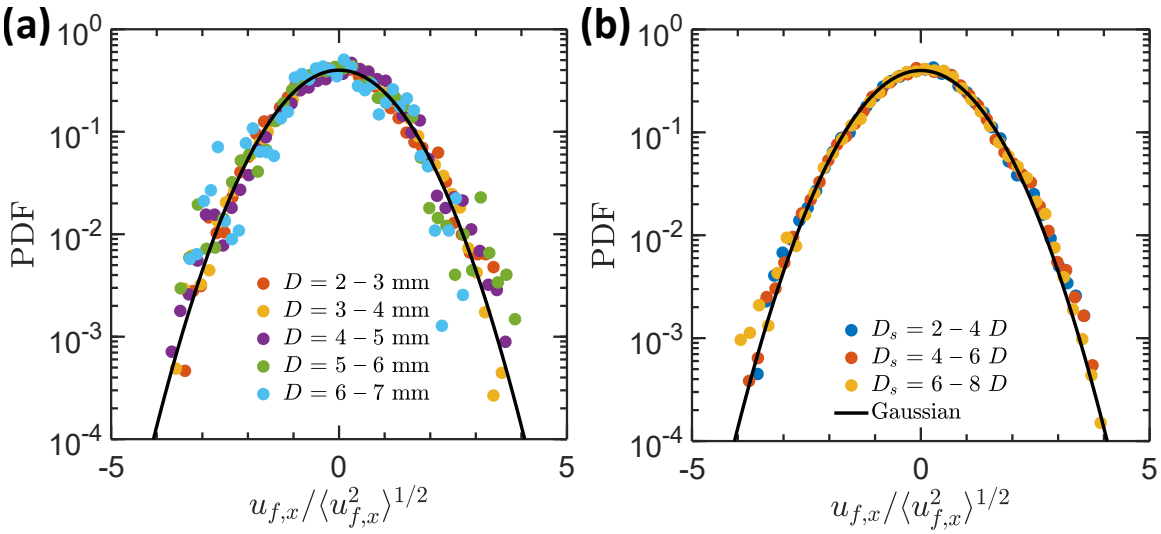

Figure 4.6: The distribution of the horizontal flow velocity $u_{f,x}$ (normalized by its own standard deviation) nearby bubbles of (a) different sizes D with (b) different search diameters D_s.

by turbulence. For example, the instantaneous velocity mismatch of two phases could also lead to significant dynamic stress that needs to be evaluated. This effect can be captured by the so-called slip velocity, $\mathbf{u}_{slip} = \mathbf{u}_b - \mathbf{u}_f$. As its name suggests, $\mathbf{u}_{slip}$ quantifies the drift of a bubble of velocity $\mathbf{u}_b$ away from the instantaneous local flow velocity $\mathbf{u}_f$.

$\mathbf{u}_f$ represents the continuous-phase fluid velocity at the center of a bubble which is the same as $\overline{u_i}$ used in equation 4.1. Figure 4.6(a) shows the PDF of only one horizontal component of $\mathbf{u}_f$ normalized by its own standard deviation. $\mathbf{u}_f$ can be calculated around bubbles of different sizes, which are shown in different symbols. The solid line indicates the standard normal distribution, which seems to fit well with the horizontal velocity distribution of bubbles of all sizes, at least for the range of bubble sizes considered. If we combine the PDF

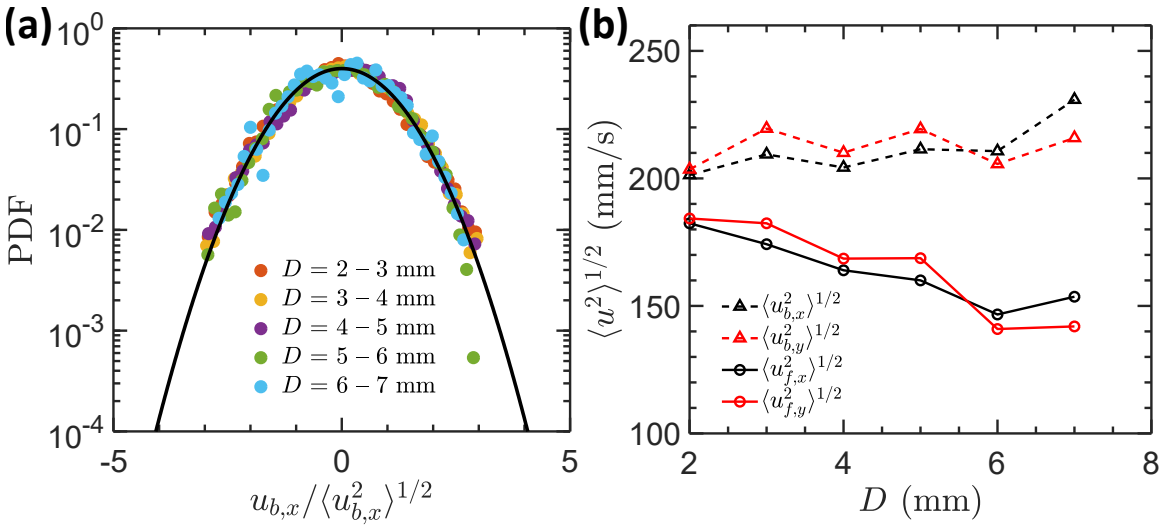

Figure 4.7: (a) The distribution of the horizontal velocity $u_{b,x}$ of bubbles (normalized by its own standard deviation) with different diameter D; (b) The fluctuation of mean flow velocity (solid) and bubble velocity (dashed lines) along two different directions versus bubble size D.

of all sizes together, the result is shown in figure 4.6(b). The scatter becomes weaker compared with the PDF for individual sizes in figure 4.6(a) simply because samples from different sizes are combined. To rule out the possible D_s effect, the same procedure was repeated for three different D_s =2–4D to 6–8D. As one can see in figure 4.6(b), no discernible difference is observed. This suggests that $\mathbf{u}_f$ is not sensitive to D_s either.

$\mathbf{u}_b$ denotes the velocity of a bubble extracted from its trajectory. The lateral component along the x-axis is $u_{b,x}$. Figure 4.7(a) shows the distribution of $u_{b,x}$ (normalized by its own standard deviation) for a wide range of bubble sizes, and the distribution for all bubble sizes seem to agree with a Gaussian distribution (solid line) very well. The standard deviation of $\mathbf{u}_b$ for both lateral

directions are shown as dashed lines in figure 4.7(b), and they exhibit a weak, if at all, dependence on D. Note that, in the other limit for bubbles rising in a quiescent medium with no turbulence, since the horizontal velocity is coupled with the size-dependent rise velocity (Ern et al., 2012), it is expected that $\langle u_{b,x}^2 \rangle^{1/2}$ should also depend on the bubble size. However, the observed nearly-constant $\langle u_{b,x}^2 \rangle^{1/2}$ clearly indicates that the buoyancy effect has been erased in the horizontal directions by the presence of intense turbulence. Figure 4.7(a) also displays the standard deviation of $\mathbf{u}_f$ along two lateral directions. In contrast to $\langle u_{b,x}^2 \rangle^{1/2}$, $\langle u_{f,x}^2 \rangle^{1/2}$ seems to decrease as D increases. This is expected as a bubble serves effectively as a large filter that reduces the fluctuation of the local mean flow velocity, i.e. $\mathbf{u}_f$. If the curves of both $\langle u_{b,x}^2 \rangle^{1/2}$ and $\langle u_{f,x}^2 \rangle^{1/2}$ were extrapolated to small bubble sizes, one can see that eventually $\langle u_{b,x}^2 \rangle^{1/2}$ and $\langle u_{f,x}^2 \rangle^{1/2}$ would cross over at around 200 mm/s for bubble size close to zero, which is the right limit that extremely-small bubbles should behave similarly to tracers $\langle u_{b,x}^2 \rangle^{1/2} \approx \langle u_{f,x}^2 \rangle^{1/2}$.

Although both u_f and u_b along the x-axis appear to follow the Gaussian distribution, the slip velocity $u_{slip} = u_f - u_b$ does not. As shown in figure 4.8(a), for bubbles of all sizes, the tails of the slip-velocity PDF ($u_{slip,x}$) are systematically higher than that of the Gaussian function (black solid line), indicating that the slip velocity is more intermittent than the velocity of either phase alone. Again, for the distribution of the normalized slip velocity, no obvious size dependence

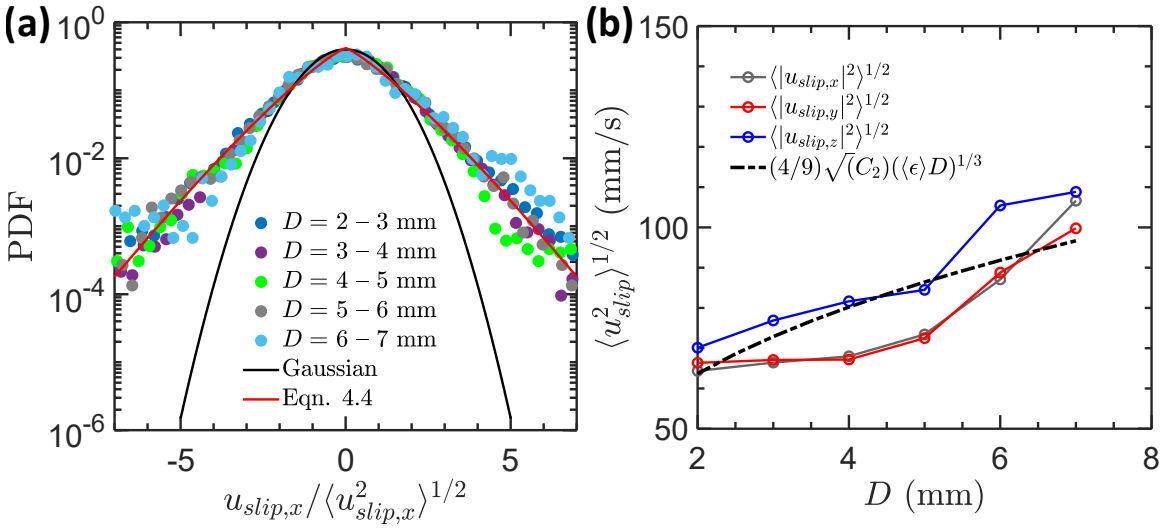

Figure 4.8: (a) The distribution of the normalized horizontal slip velocity between the two phases; Symbols denote bubbles of different sizes and the black solid line indicates the standard normal distribution. The red solid line shows the stretched exponential (equation 4.4) fit to the data. (b) The fluctuation slip velocity of all three components versus the bubble diameter D; The solid line indicates the estimation from the second-order structure function. The prefactor $4/9$ is chosen to minimize the offset between the solid line and the data.

is observed. Note that the PDF of u_{slip} resembles that of the velocity increment between two points in single-phase turbulence (Kailasnath, Sreenivasan, and Stolovitzky, 1992; Sreenivasan, 1999; Li and Meneveau, 2005). The PDF of the velocity increment has been fitted with a stretched exponential function (Kailasnath, Sreenivasan, and Stolovitzky, 1992), which is adopted here to describe the observed PDF of slip velocity.

$$P(u_{slip,x}) = C \exp\left[-Q\left(\frac{u_{slip,x}}{\langle u_{slip,x}^2\rangle^{1/2}}\right)^m\right] \tag{4.4}$$

$$We_{slip} = \frac{\rho u_{slip}^2 D}{\sigma} \tag{4.5}$$

where C is the normalization factor, and Q and m are fitting parameters in the stretched exponential function. For single-phase turbulence, the degree to which the tail of the PDF is stretched depends on the scale separation. If the velocity separation is close to the integral length scale, the PDF recovers the Gaussian distribution (m = 2). As the separation becomes smaller and smaller, the PDF becomes more and more intermittent; at $m = 1$, the PDF follows an exponential function that is symmetric about zero. If we take the bubble size 0.03 L to 0.12 L as the scale separation to calculate the velocity increment in single-phase turbulence, the scaling exponent m should vary between 0.8 to 1.05 based on the work by Kailasnath, Sreenivasan, and Stolovitzky (ibid.).

In our case, although the slip velocity distribution also follows the stretched exponential, the PDF preserves its shape (constant Q and m in equation 4.4) for all bubble sizes considered with no obvious scale dependence. m was found to be a constant close to 6/5, which is slightly larger than the range of m from 0.8 to 1.05 in single-phase turbulence. This observation suggests that the slip velocity between two phases is less intermittent compared with the velocity increment between two points in single-phase turbulence under the same scale separation, which is not surprising since bubbles could effectively filter out many intermittent small-scale fluctuations.

In addition, the fluctuation slip velocity ($\langle u_{slip}^2 \rangle^{1/2}$) increases as a function of bubble size D, suggesting that larger bubbles with larger inertia tend to deviate further away from the surrounding fluid velocity. On top of the data, the typical velocity scale of an eddy of the bubble scale D following the relationship of $\sqrt{C_2}(\langle \epsilon \rangle D)^{1/3}$ is also shown as the solid-dash line in figure 4.8(b). To compare with the data, the curve has been shifted downward by multiplying with a factor of 4/9 that is chosen to make sure the curve and the data have similar magnitude. It seems that the scaling of $\sim D^{1/3}$ agrees with the trend of the fluctuation slip velocity for the range of bubble sizes considered. This result may indicate that, as long as bubble size is in the inertial range, the distribution of u_{slip} can be predicted based on D and the mean energy dissipation rate $\langle \epsilon \rangle$ by following equation 4.4 with three key parameters: $Q = 3/4$, $m = 6/5$,

and $\langle u_{slip,x}^2 \rangle^{1/2} = (4/9)\sqrt{C_2}(\langle \epsilon \rangle D)^{1/3}$ ($C_2 = 2.13$).

Finally, the distribution of We_{slip}, calculated based on equation 4.4 and 4.5, is shown in figure 4.5. The blue solid line indicates the predicted We_{slip} based on the stretched exponential fit to the horizontal slip velocity $u_{slip,x}$ (equation 4.4). The distribution also peaks at around $We \approx 1$, which is slightly smaller than the most probable value of We_{vg}. However, it can be seen that the right tails of both PDFs (We_{vg} and $We_{slip,x}$), which are in the range of We that is important for deformation and breakup, are very close to each other. This may suggest that, for bubble deformation, slip velocity and velocity gradient may be equally important. In other words, completely relying on the velocity gradient may not account for all stresses that bubbles experience in turbulence.

4.4.3.3 Buoyancy-induced deformation

Although the turbulence energy dissipation rate has been set as high as possible in our facility, the buoyancy effect is not negligible. In figure 4.5, the PDF of We_{slip} in the vertical direction based on the z-axis slip velocity, i.e. $We_{slip,z}$ is also shown. This PDF has a bump near $We_{slip,z} \approx 3 - 4$ because of the buoyancy effect, but both the left and right tails seem to agree with those of $We_{slip,x}$. This suggests that the turbulence effect is still present in $We_{slip,z}$ and the effect of buoyancy is primarily limited to a small region near the peak of the PDF.

Note that $We_{slip,z}$ is similar to the Eötvös number: $Eo = \rho g D^2/\sigma$, as the terminal vertical slip velocity driven primarily by buoyancy should be proportional $u_{slip,z} \sim \sqrt{gD}$. Note that this relationship is approximate, as the buoyancy-driven terminal rise velocity is also sensitive to the bubble geometry, orientation, and the drag coefficient. In intense turbulence, these parameters could also be functions of ϵ. In a recent paper (Salibindla et al., 2020b), the drag coefficient of bubble with different sizes in intense turbulence was reported, and it follows $C_D = \max(24/Re_b(1+0.15Re_b^{0.687}), \min(f(Eo), f(Eo)/We^{1/3})$ where $f(Eo) = 8Eo/3(Eo+4)$. Based on this equation, the most probable slip velocity in the vertical direction can be calculated. For the size range of bubbles considered, $We_{slip,z}$ calculated based on C_D is about 3–4, which is consistent with the bump of $We_{slip,z}$ observed in the PDF.

In addition, it seems that the bump in the distribution of $We_{slip,z}$ is limited to a narrow range, and the right tail of $We_{slip,z}$ seems to be close to that of $We_{slip,x}$ and We_{vg}. This suggests that, at least for our parameters when $\langle\epsilon\rangle \approx 0.2$–0.5 m^2/s^3, the buoyancy-induced deformation is limited. If we keep increasing $\langle\epsilon\rangle$, the buoyancy effect will become even weaker.

4.4.4 Bubble aspect ratio vs. Weber numbers

So far, we have been focusing primarily on discussing the distribution of different definitions of Weber numbers and understand the connection between

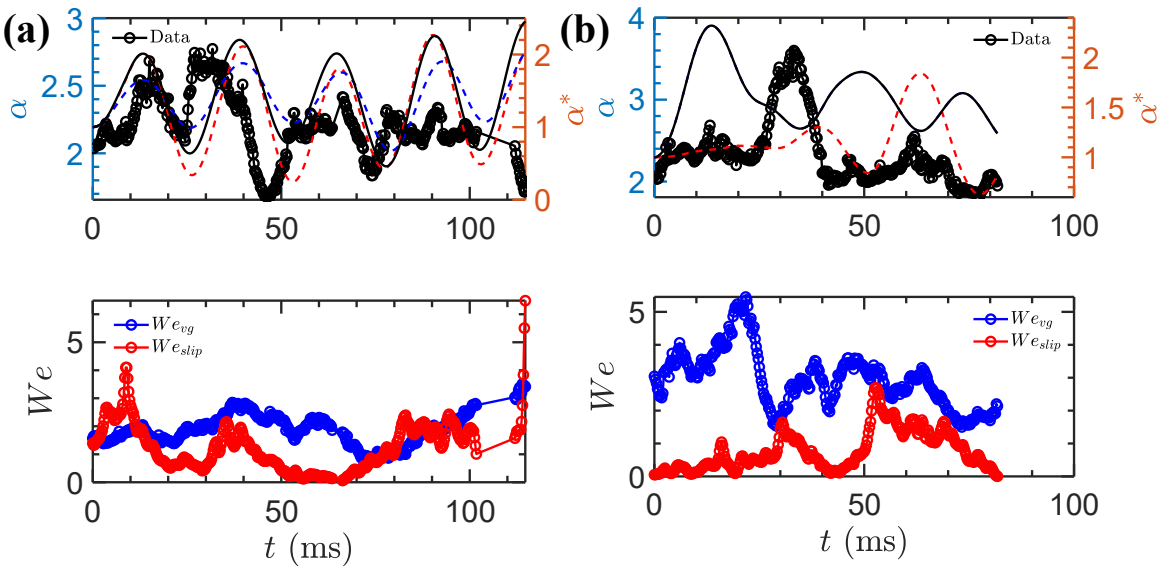

Figure 4.9: (a-b) Two example time traces of bubble aspect ratio and the Weber number; Symbols denote experimental data of bubble aspect ratio (black), We_{vg} (blue), and We_{slip} (red). In addition, α^* calculated from the linear forced-oscillation model (equation 4.6) by using $\max(We_{slip}, We_{vg})$ (black solid line), We_{slip} (red dashed line), and We_{vg} (blue dashed line) are also shown for comparison.

these Weber numbers and turbulence characteristics, such as the turbulent kinetic energy dissipation rate and velocity increments. In this section, the instantaneous Weber numbers along bubble trajectories will be used to study the mechanisms of bubble deformation and breakup in turbulence.

4.4.4.1 Simultaneous measurements of bubble geometry and We

Figure 4.9 shows two examples of simultaneous measurements of bubble aspect ratio (α) and Weber numbers (We_{vg} and We_{slip}). α was calculated based on

the ratio between the major and minor axes of the 3D reconstructed shape. As shown in figure 4.9(a), the reconstruction seems to successfully capture the oscillation of a bubble that undergoes small-amplitude deformation. We_{vg} and We_{slip} calculated based on tracer velocity around the same bubble are also shown. For this particular case, most instantaneous We are smaller than 5, and α is not similar to either We at first glance. The only evident correlation is probably at $t = 10$ – 20 ms, when a small peak observed in the time trace of α seems to be related to a similar peak found in the time trace of We_{slip} maybe 5 ms earlier. For $t = 50$ – 70 ms, despite We_{slip} drops close to zero, α continues to rise thanks to a relatively large value of We_{vg}. This indicates that bubbles probably respond to both Weber numbers, likely to be the maximum instantaneous Weber number, i.e. max(We_{vg},We_{slip}).

The simultaneous measurements also provide a framework to test models for bubble deformation and breakup. One such model has been proposed before by Risso and Fabre (1998) and Lalanne, Masbernat, and Risso (2019), which is essentially a forced oscillator model that connects bubble deformation directly to local We through a linear differential equation. This model is designed to follow the interaction between a bubble with surrounding turbulent eddies along its Lagrangian trajectory, exactly how our experiments were performed. The

dimensionless form of the equation is:

$$\frac{d^2\hat{a}}{d\hat{t}^2} + 2\xi\frac{d\hat{a}}{d\hat{t}} + \hat{a} = K'We(t) \tag{4.6}$$

where $\xi = 1/2\pi\tau_d f_2$ is the damping coefficient, τ_d is the damping time scale, and f_2 is the oscillation period of a bubble, which is the Lamb mode 2 bubble natural frequency (Lamb, 1932). The amplitude of the instantaneous $We(t)$ is controlled by the prefactor K'. $We(t)$ was not available before in other experiments, and it had to be estimated based on two-point velocity measurements from single-phase turbulence (Risso and Fabre, 1998). In this work, in addition to measuring $We(t)$ directly, the method also allows us to distinguish between We_{vg} and We_{slip}. But since the model did not explicitly account for individual We, here we apply three different inputs: $We(t) = We_{vg}$ (blue dashed line), $We(t) = We_{slip}$ (red dashed line), and $We(t) = \max(We_{vg}, We_{slip})$ (black solid line) to equation 4.6 to compare model predictions with directly-measured aspect ratio, and the results are shown in figure 4.9 and 4.10.

Note that $\hat{a}$ in equation 4.6 is defined as the ratio of the deformed radius ($a = R - D/2$) to D, where R is the major axis of the deformed bubble and D is the diameter of an equivalent sphere of the same volume. It has to be converted to $\alpha^* = 2(\hat{a}D + D/2)/D$ for comparisons with the measured α. However, despite our best efforts, $\alpha \neq \alpha^*$ because α^* does not contain information about the

minor axis, which has to be replaced with $D/2$. Nevertheless, α and α^* should share the same trend as bubbles deform. Indeed, similarities can be observed between α and α^* in figure 4.9. The magnitude of α^* is affected by the prefactor K' in equation 4.6, which is fixed at 0.1 for our experiments. Note that this value is smaller than the proposed order of unity by Risso and Fabre (1998). In figure 4.9, the model captures roughly four oscillation periods, which can also be seen from the experimental results. The phase lag of each period of α keeps changing in the experimental data, e.g. the second peak is much closer to the first one and further away from the third one. This varying phase lag is a feature that cannot be reproduced from the model as the model-predicted α^* seems to have a rather constant phase lag throughout the entire time trace.

Figure 4.9(b) shows another example to compare α with α^*. A large α observed at 32 ms seems to correlate with an event of large We_{vg} occurred at 20 ms, whereas a small bump of α at 60 ms seems to correspond to a sudden increase of We_{slip} at 50 ms. This observation is still consistent with the argument that bubble deformation tends to be driven by both Weber numbers. In this case, three model-predicted time traces of α^* differ from each other; We_{vg} is systematically larger than We_{slip} for the entire duration. Nevertheless, for this case, although the model-predicted time trace still embraces some oscillatory features, the measured results do not. Over a similar period of time compared with figure 4.9(a), only one distinct peak is observed in figure 4.9(b). This sug-

gests that the linear-oscillator model provided by Risso and Fabre (1998) can capture certain cases, but not for all bubbles. In some cases the bubble oscillation may be overruled by the surrounding flow dynamics. For these cases with a weak oscillation, the model tends to overpredict the bubble aspect ratio.

Since the model provided by Risso and Fabre (ibid.) is primarily designed to characterize the breakup process, figure 4.10 shows two examples of bubbles that eventually break. We for breaking bubbles is clearly much larger: one reaches close to 40 and the other one climbs up to almost 20, nearly a factor of 4 – 8 larger than the cases for small-amplitude deformation in figure 4.9. In figure 4.10(a), We_{slip} dominates, but a local event at $We_{slip} \approx 40$ did not break the bubble, even though it did successfully deform the bubble to a large $\alpha \approx 8$. Following a peak of We_{slip} at 85 ms, this bubble eventually broke at $t = 90$ ms, with the instantaneous We about 10 and local aspect ratio close to 2.

This example is actually very typical, representing many breakup events that do not occur at the moment when α reaches its peak. Instead, bubbles split at a later time as they attempt to retract back to sphere. During retraction, the excess surface energy stored on the bubble interface is transferred back to the surrounding flows in the form of the turbulent kinetic energy (Dodd and Ferrante, 2016). However, this process is unstable because of the large density difference between the two phases, and it eventually leads to breakup before bubbles return to a spherical shape.

For the first example, We_{slip} is intermittent with a large variation of magnitude in a short period of time, which seems to be consistent with the notion of eddy-bubble collision (Prince and Blanch, 1990; Risso and Fabre, 1998) that this bubble keeps encountering different eddies with varying intensity. For the second example shown in figure 4.10(b), both Weber numbers slowly increase with time until the bubble breaks. The aspect ratio does not vary much throughout the entire time trace. For the last 20 ms, the aspect ratio of this bubble is close to a constant. Rather than eddy-bubble collision, the results seem to suggest an alternative mechanism: bubbles entrained in an eddy slowly get pulled apart by this eddy as it grows in strength over time.

The model predictions are shown alongside with two examples. In both cases, oscillations clearly observed in α^* from the model calculation are not so obvious in experimental results. It is not entirely surprising as large deformation is expected to be nonlinear and should deviate from the linear equation 4.6.

4.4.4.2 Distribution of bubble aspect ratio

In addition to the response of individual bubbles to different Weber numbers, the distribution of α could also be connected to that of We to examine if the bubble aspect ratio can be solely determined by We in a statistical sense. This relationship between α and We was first derived by Moore (1965) for bub-

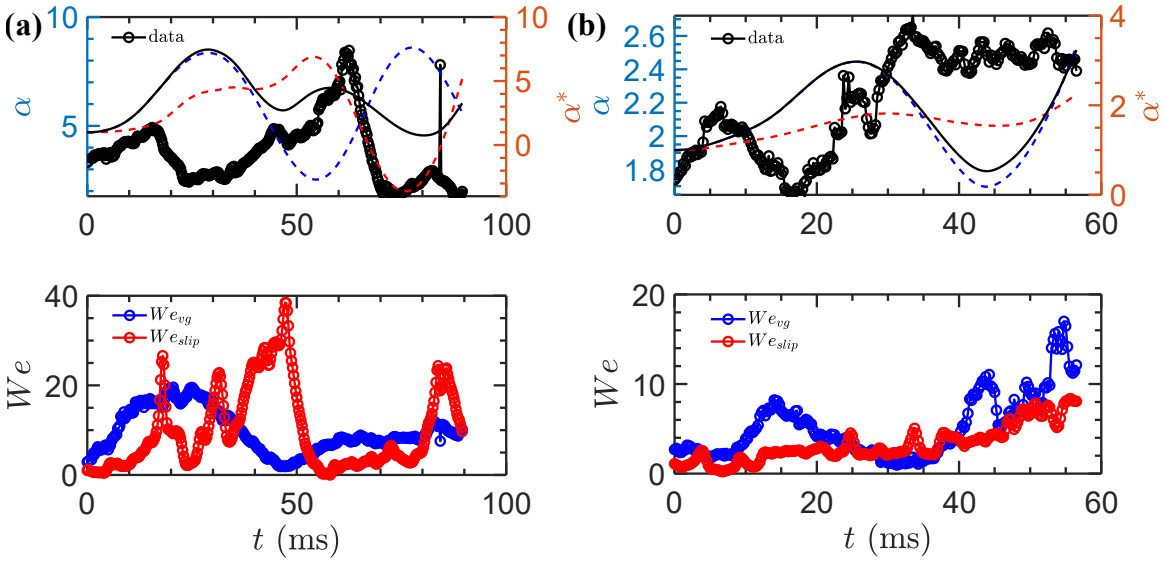

Figure 4.10: (a-b) Example time traces of two breakup events. Symbols and lines are the same as those in figure 4.9. The bubble breaks at 89.5 ms for (a) and at 56.5 ms for (b).

bles rising in a quiescent medium:

$$\alpha = 1 + \frac{9}{64} We + O(We^2) \tag{4.7}$$

where We here was defined to account for the dynamic pressure driven by the rising motion of bubbles, not by turbulence. In addition, the key assumption in this model is that $We \ll 1$ so that the departure from a spherical shape is so small that high-order terms associated with We^2 can be ignored.

For $We \approx 1$ or above, the potential flow theory applied to oblate ellipsoids with fore-aft symmetry yields:

$$We(\alpha) = 4\alpha^{-4/3}(\alpha^3 + \alpha - 2)[\alpha^2 sec^{-1}\alpha - (\alpha^2 - 1)^{1/2}]^2(\alpha^2 - 1)^{-3} \tag{4.8}$$

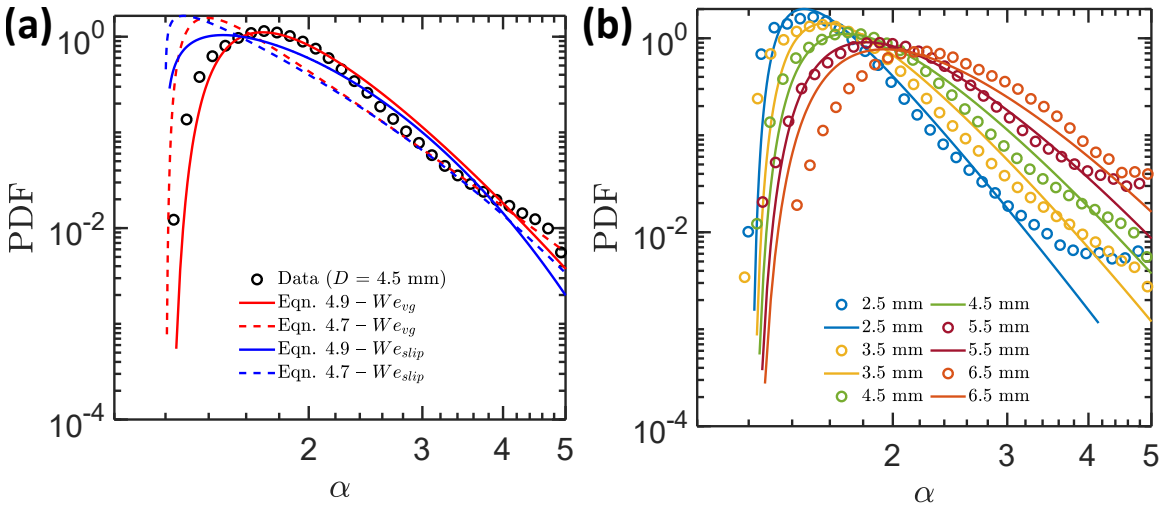

Figure 4.11: The distribution of bubble aspect ratio α for (a) one size $D = 4.5$ mm to test against different We vs. α relationship listed in two different equations 4.7 and 4.8 by using either We_{slip} (blue) and We_{vg} (red) and for (b) a range of sizes from 2.5 mm to 6.5 mm; solid lines are calculated from equation 4.9.

This equation has a maximum aspect ratio of 6 when the Weber number is close to 3.745, above which the symmetric shape is impossible to attain for a bubble. Although this formulation provides a better framework for our studies of bubbles with $\langle We \rangle \approx 1$, it cannot predict the relationship between α and instantaneous We for $We > 3.745$, which is about 21.5% of the total events in our experiments.

Figure 4.11(a) shows the PDF of α for bubble size $D = 4.5$ mm. The PDF peaks at $\alpha = 1.7$ and has a long tail that skews towards larger values of α. On top of the experimental results, the PDF of α calculated from equation 4.7 using $We = We_{vg}$ as the input is also plotted as the red dashed line. Although the peak location is slightly different from the experimental results, the overall

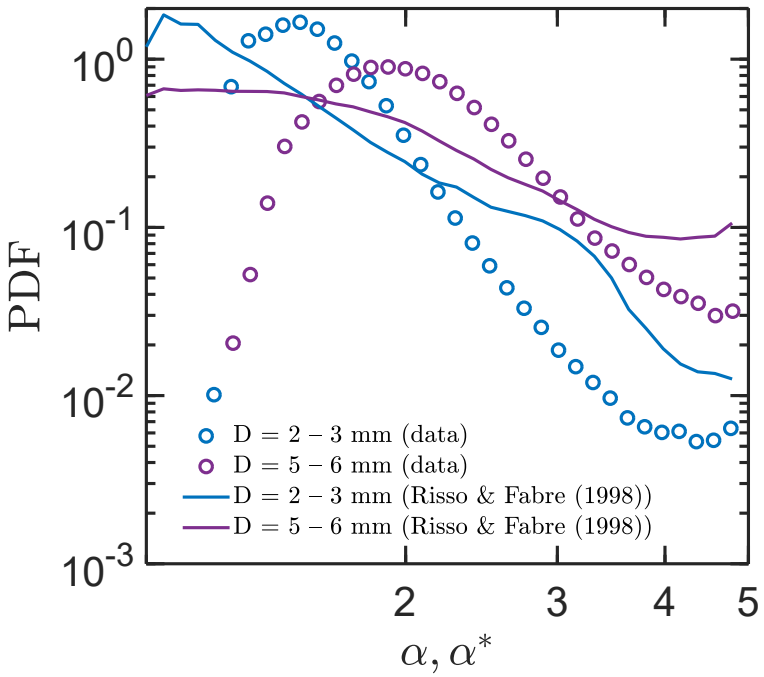

Figure 4.12: The distribution of bubble aspect ratio α for two different sizes ($D = 2$ – 3 mm and $D = 5$ – 6 mm) from experiments (circle) and linear forced-oscillation model (line, equation 4.6).

trend is close. Since the long tail in the PDF of We_{vg} comes from the log-normal distribution of $\widetilde{\epsilon}$, a large probability of strong deformation $\alpha > 2$ is likely to be contributed by intermittent events with a large $\widetilde{\epsilon}$. If α versus We_{vg} follows a linear relationship, the two PDFs should overlap with each other. To make the red dashed line closer to the experimental results, we have tried to add a second-order correction to equation 4.7, which does not provide a satisfactory result (not shown here). Finally, after adjusting the parameters in equation 4.7, we settle down to a simple new equation

$$\alpha = \frac{2}{5} We^{\frac{2}{3}} + 1.2 \tag{4.9}$$

to fit the data, which is shown as the red solid line in figure 4.11(a). This new fit shows an excellent agreement with the measured PDF of α. Moreover. the solid blue line in figure 4.11(a) shows the PDF of α by implementing $We = We_{slip}$ in equation 4.9. Similar trend of α can still be seen even with a different Weber number. But it tends to underpredict α, which is consistent with the observation in figure 4.5 that the peak of We_{slip} PDF is on the left side of We_{vg} PDF. Nevertheless, the right tail of α can be reproduced by the calculations using both We_{slip} and We_{vg}. This may imply that the dynamic stresses contributed by both velocity gradients and the slip velocity are equally important, but turbulent velocity gradients seem to work better and thus more important for mild deformation.

Figure 4.11(b) compiles the PDFs of α for five different bubble sizes, from 2.5 mm to 6.5 mm with an interval of 1 mm. The peaks of these PDFs progressively shift rightward towards a larger α as D grows, which is consistent with our intuition that large bubbles are more deformable and thus have a larger α on average. Moreover, the PDF becomes wider (the right tail of the PDF rises) as D increases, which implies that the probability of bubbles with α much larger than the mean also increases. To explain this, equation 4.9 is applied to all these cases with different D, and results are shown as solid lines with corresponding colors to compare with the PDF of measured α. The modeled PDF of α agrees with the measured results really well for most bubble sizes except for the largest bubbles where the buoyancy effect may deform bubbles even further. This agreement suggests that the observed trend of PDF as a function of bubble size is driven mostly by the change of We, but the relationship may not be linear.

An alternative method to predict the relationship between α and We is to use the model provided by equation 4.6. As discussed before, although the model-predicted time trace of α does not match with the measured one exactly, the model is still able to capture some key features of the time trace. Here, we want to extend the test to the PDF of α^*. The comparison is shown in figure 4.12 for only two sizes of 2.5 mm and 5.5 mm for simplicity. The model seems to reproduce the overall trend of the PDF. But the PDF of α^* calculated from the

model seems to be much more flat than that of the measured α, indicating a much higher probability of large α^* compared with the measured results. This observation is consistent with the time traces shown in figure 4.10 that the linear-oscillator model seems to overpredict the number of large deformation events because not all bubble deformation can be described by linear shape oscillation.

This observed difference can also be attributed to other possible reasons. For example, equation 4.6 is a linear one-dimensional model with both We and α^* being scalars. In our experiments, We_{vg} has an implicit direction that follows the largest compression direction of the rate-of-strain tensor, and We_{slip} should be aligned with the slip velocity direction. Their contribution to bubble deformation may not be as simple as max(We_{vg}, We_{slip}). In certain circumstances, they could potentially work against each other, which is not accounted for in the linear-oscillator model.

4.4.5 Breakup probability

One condition that is implicitly assumed in many breakup models (Martínez-Bazán, Montanes, and Lasheras, 1999) is that all bubbles will break, just a matter of time. This implies a breakup probability (p_b) close to 100%, which should be valid for large $We \gg 1$ and $D \gg D_H$. However, for bubbles with $We1$ and DD_H, p_b could be anywhere from 0 to 100%. This number has not

been reported before from previous experiments as it is challenging to estimate p_b given the limited residence time of bubbles within the view area. The data that has been generated in this work provides a unique way to evaluate p_b indirectly based on two assumptions: (i) turbulence remains close to homogeneous and isotropic so that the statistics collected from the entire view area can be compiled together to predict the breakup probability; and (ii) the local Weber number is the sole parameter that determines the status of bubble deformation and breakup. Introducing and measuring local We is one step further from the Hinze's seminal work, in which the ensemble-averaged $\langle We \rangle$ was adopted to quantify the breakup probability. The limitation of adopting $\langle We \rangle$ is that, based on $\langle We \rangle$ being larger or smaller than the critical We_{crit}, p_b is close to a step function ($p_b = 1$ if $\langle We \rangle > We_{crit}$; $p_b = 0$ if $\langle We \rangle < We_{crit}$). However, in turbulence, local flows could be orders of magnitude stronger than the mean; bubbles could break in response to the local We instead of the mean Weber number. To transfer this intuition to quantitative results, the main objective of this section is to determine p_b by linking local We to bubble deformation.

Before applying the PDF of local Weber numbers to estimate p_b, we would like to extend the PDF of We_{vg} and We_{slip} beyond our experiments to other turbulent flows with different $\langle \epsilon \rangle$ and bubble size D. Based on equations 4.2 and 4.4, the distribution of local We for three $\langle \epsilon \rangle$ from 0.1 m^2/s^3 to 10 m^2/s^3 are shown in figure 4.13(a). Both We_{slip} and We_{vg} shift rightward systematically

with a seemingly-identical shape. It is important to note that the shape remains the same on the logarithmic scale, which indicates that the distribution widens and the standard deviation of local We increases as $\langle\epsilon\rangle$ grows.

From the distribution, we can estimate p_b based on:

$$p_b(\langle We\rangle) = \int_{We_{crit}}^{+\infty} p(We)d(We) \tag{4.10}$$

where the local We could be either We_{vg} or We_{slip}, and $\langle We\rangle = \int_{-\infty}^{+\infty}[We \times p(We)]d(We)$. It can be seen that, as $\langle We\rangle$ increases, either due to a larger D or larger ϵ, p_b will grow.

Figure 4.13(b) shows p_b as a function of $\langle We\rangle$ to connect to other experiments that do not have access to the local Weber number. In most previous works, comparing $\langle We\rangle$ with We_{crit}, this figure should look like a step function as $p_b = 1$ for $\langle We\rangle \geq We_{crit}$ and $p_b = 0$ for $\langle We\rangle < We_{crit}$. The two limits still apply in figure 4.13(b), but the transition is much smoother, spanning over a few orders of magnitude of $\langle We\rangle$. Note that, although We_{crit} has to be selected like what has been done before, this choice does not affect the shape of the curve. As shown in figure 4.13(b), when we change We_{crit} from 1 to 4, it just shifts the transitional $\langle We\rangle$ towards the new We_{crit} without affecting the overall trend.

This framework applies to We_{vg} and We_{slip}, both of which contribute to bubble breakup. Since the right tail of their respective distribution is very close to

each other, an equal contribution from the two We to p_b was assumed. As the result, the curves of p_b for either We alone approach 0.5 for $\langle We \rangle$ much larger than We_{crit} to ensure that the sum of the two p_b equals to one. Moreover, even for the same We_{crit}, p_b of We_{slip} (blue lines) stays mostly above that of We_{vg} (red lines) until they cross at a location very close to the plateau near $p_b = 0.5$. This difference can be ascribed to the difference of the PDFs: the PDF of We_{vg} is closer to a log-normal distribution whereas the PDF of We_{slip} has a large probability of small We. This also suggests that bubbles close to the Hinze scale may be deformed more often by the slip velocity.

Finally, the total breakup probability p_b by summing the contribution from We_{vg} and We_{slip} and using $We_{crit} = 1$ to 4 are shown as three cyan lines in figure 4.13. These three lines are fitted with the same switch function:

$$p_b = [1 + (2.8We/We_{crit})^{-1.7}]^{-1} \tag{4.11}$$

which includes We_{crit} as the input. The fitted results are shown in figure 4.13(b) as three black solid lines. One may not see the cyan lines at all because the fit overlap perfectly with the calculated results over the entire $\langle We \rangle$ range for three We_{crit} considered. Equation 4.11 provides a method to estimate bubble breakup probability in turbulence, particularly for bubbles close to the Hinze scale and $\langle We \rangle \approx 1$.

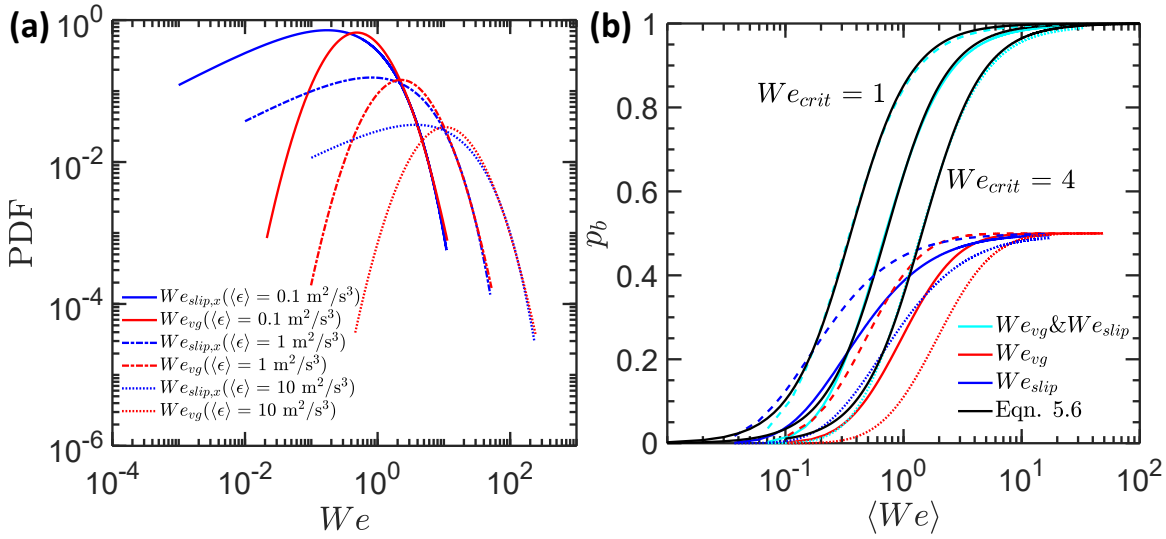

Figure 4.13: (a) The predicted distribution of both $We_{slip,x}$ and We_{vg} for different energy dissipation rates from ϵ=0.1 to 10 m^2/s^3. (b) Breakup probability p_b calculated based on different mean Weber number $\langle We\rangle$. Three sets of lines indicate three different We_{crit} from 1 to 4. Within each set, p_b based on the total Weber number (cyan), or either We_{vg} (red) or We_{slip} (blue) alone, are shown. The curves from the total We were fitted with equation 4.11 to predict p_b for any mean We and any selected We_{crit}.

4.5 Conclusion

Bubble deformation and breakup in intense turbulence is ubiquitous in many applications, but details of how this takes place for a bubble close to the Hinze scale remain elusive because of the lack of data to probe the interaction between small finite-sized bubbles and surrounding turbulence. In this study, both 3D bubble geometry and nearby 3D particle tracks were acquired simultaneously using our in-house virtual camera reconstruction and particle tracking algorithm, respectively. The experiments were performed in a system that can reach a high turbulent energy dissipation rate that can significantly deform and even break bubbles, while maintaining homogeneous and isotropic turbulence throughout the entire measurement volume. Since the 3D information of both phases is available, this unique dataset allows us to interrogate the coupling between the two phases, in particular the key mechanisms that drive bubble deformation and breakup. The flow velocity was decomposed into two components, the local flow velocity and velocity gradient, both coarse-grained at the bubble scale. Each component can be used to define its own Weber number as a way to quantify their relative contribution to bubble deformation.

In this study, in addition to directly measuring the Weber numbers, bubble deformation is also connected to the log-normal distribution of the local energy dissipation rate ϵ. The modeled distribution and the measured results of both ϵ and We_{vg} agree really well. Moreover, because of the density mismatch be-

tween the two phases and the finite bubble size effect, the slip velocity also plays an important role. Based on this observation, a different Weber number has been defined to measure deformation driven by the slip velocity, whose distribution can be fitted with a stretched exponential function. Based on this functional form, the distribution of the slip-velocity-based Weber number can be connected to $\langle\epsilon\rangle$ and bubble size.

The distribution of the Weber number was also connected to the reconstructed bubble geometry. It has been shown that the relationship that was developed for describing bubbles rising in a quiescent medium does not work well for the turbulent case. A new non-linear model was proposed to improve the fit and it seems to work well for a range of bubble sizes considered. In addition, the results were tested against a linear forced oscillator model that was proposed before. Although the model does seem to reproduce some key features of a few example time traces qualitatively, the distribution of the predicted aspect ratio does not match with the directly-measured results quantitatively.

Finally, based on the Weber number distribution, we generalized the distribution for different bubble sizes and energy dissipation rates in order to evaluate breakup probability, which was estimated based on the mean energy dissipation rate in many other works. In contrast to what has been proposed before that bubble breakup probability experiences a precipitous drop as bubble size decreases below the Hinze scale, accounting for the distribution of local

Weber number helps to smooth the curve near the Hinze scale. The final calculated relationship between breakup probability and the mean Weber numbers was fitted with a simple function that can help future works to estimate bubble breakup probability based on the mean Weber number.

Chapter 5

Orientation dynamics of finite-sized bubbles in intense turbulence during deformation and breakup

We present simultaneous three-dimensional measurements of deformable finite-sized bubbles and surrounding turbulent flows. The orientations of bubbles are linked to the representative directions of two key mechanisms that drive the bubble deformation: turbulent strain rate and the slip velocity between the two phases. Preferential alignment between bubbles and the slip velocity is the strongest, indicating a dominant role played by the slip velocity. We also compared our experimental results to simulations on the deformation of ideal material elements with no slip velocity or surface tension. Without these two effects, material elements show very different alignment with the

turbulent strain rate, further confirming the role played by the slip velocity. In addition to deformation, when bubbles start to break, it is surprising to find that the relative orientations of bubbles start to change significantly. The alignment of the strongly-deformed bubbles with the eigenvectors of turbulent strain rate becomes much stronger, whereas the bubble semi-major axis switches from being perpendicular to the slip velocity to being aligned with it, almost a 90° turn. This puzzling orientation change occurs because the slip velocity contains the contributions from both the bubble velocity and the flow velocity. As bubbles experience strong deformation, the fast elongation of the semi-major axis leads to a large bubble velocity, which dominates the slip velocity and forces it to be aligned with the semi-major axis of the bubble. Essentially, the slip velocity switches from a driving mechanism to a driven result as bubbles approach breakup.

5.1 Introduction

Finite-sized bubbles and droplets transported by turbulent flows in nature and industrial applications are constantly deformed by surrounding turbulent stresses. Their shapes and orientations are often neglected in simulations assuming point particles, even though it is well known that many forces in the equation of motion for bubbles. For instance, the added mass (Lamb, 1924;

Brennen, 1982; Brennen, 2005; Magnaudet and Eames, 2000), lift (Mathai, Lohse, and Sun, 2020a), and drag forces all depend on the relative orientation of bubbles with their surrounding flows. Deformation essentially adds to a problem that is already complex even for rigid spheres (Balachandar and Eaton, 2010) or non-spherical particles (Voth and Soldati, 2017). Thanks to the advance of numerical methods, the direct numerical simulation has made significant progress in tackling this problem (Elghobashi, 2019). However, it is often quite expensive to resolve the complex deformation of finite-sized bubbles/droplets in turbulence. As a result, the deformation of small sub-Kolmogorov-scale neutrally-buoyant droplets is often modeled using phenomenological models (Maffettone and Minale, 1998; Biferale, Meneveau, and Verzicco, 2014).

Most experimental investigations of the orientation of deformable bubbles are limited to simple flow configurations, e.g. shear flows. In these viscous flows, the orientation of bubbles was measured as a function of the capillary number, size (Rust and Manga, 2002; Kameda, Katsumata, and Ichihara, 2008), or the viscosity ratio (Müller-Fischer et al., 2008). Flows in these cases were in a quasi-steady state and the flow inertia could be neglected; consequently, a final steady orientation that depends only on the balance between the flow shear and the capillary stress could be reached (Huber et al., 2014). Compared with bubbles, significantly more attention has been paid to the deformation

and orientation of oil droplets in steady shear flows (Armandoost, Bayareh, and Nadooshan, 2018; Feigl et al., 2007; Guido and Greco, 2001; Guido, Greco, and Villone, 1999; Guido and Villone, 1998; Megías-Alguacil, Fischer, and Windhab, 2006).

The study of bubbles/droplets deformed by viscous flows can be extended to understand the orientation of the sub-Kolmogorov-scale bubbles in turbulence, as bubbles at this scale are still subject to viscous deformation. The additional complexity comes from the unsteady viscous stress driven by the local and instantaneous turbulent strain rate. By coupling a phenomenological model for viscous deformation (Maffettone and Minale, 1998) to a direct numerical simulation of turbulence, the orientation of sub-Kolmogorov-size neutrally buoyant droplets in homogeneous and isotropic turbulence was investigated by Biferale, Meneveau, and Verzicco (2014). It was observed that unlike small rigid non-spherical particles e.g. rods and fibers (Ni et al., 2015; Chevillard and Meneveau, 2013; Shin and Koch, 2005; Parsa et al., 2012), the semi-major axis of the deformed droplets align more preferentially with the maximum stretching direction of turbulent strain rate than with the vorticity vector, which could be attributed to the deformability of these droplets. The degree of this alignment decreases with an increasing Capillary number. A similar method was also applied to study the orientation dynamics of neutrally buoyant droplets in turbulent Taylor-Couette flows (Spandan, Lohse, and Verzicco, 2016). The

semi-major axis of these droplets also preferentially aligns with the maximum stretching direction, and the alignment is stronger near the wall as compared to that in the bulk region where the flow is more isotropic.

Finite-sized bubbles deforming in intense turbulence is in the opposite limit where the viscous effect becomes negligible (the capillary number is much smaller than one). Since works in this regime are limited, if not unavailable, we seek inspiration from another case where bubbles with a finite Reynolds number rise in an otherwise quiescent medium following non-rectilinear paths. In this case, large bubbles are deformed by the pressure gradient across the bubble induced by buoyancy. The semi-minor axis of the bubble typically aligns with its velocity (Legendre, Zenit, and Velez-Cordero, 2012; Riboux, Risso, and Legendre, 2010; Ellingsen and Risso, 2001; Lunde and Perkins, 1998) within less than 2° (Ern et al., 2012; Mougin and Magnaudet, 2001), while both of these two directions oscillate about the vertical axis within about 30° (Ern et al., 2012; Riboux, Risso, and Legendre, 2010; Ellingsen and Risso, 2001) for a wide range of bubble sizes (Luewisutthichat, Tsutsumi, and Yoshida, 1997). Moreover, the oscillating bubble orientation has also been connected to the wake oscillation, and these two signals are in anti-phase with each other (Tayler et al., 2012), suggesting a coupled process.

In high-Reynolds-number turbulent flows, bubbles were also observed to oscillate periodically within 45° about the vertical axis (Ravelet, Colin, and

Risso, 2011), consistent with but having slightly larger amplitude than the one reported in a quiescent medium. One plausible explanation for such a similar bubble behavior in both quiescent and turbulent media is that, in the experiment by Ravelet, Colin, and Risso (2011), turbulence was relatively weak in comparison with the dominant role played by buoyancy. As a result, bubbles would still be deformed preferentially by buoyancy, and their orientation still aligned with the vertical direction. As turbulence becomes stronger than the buoyancy, new phenomena may start to emerge. In a recent work, it was shown that finite-sized bubbles rising in intense turbulence experience different lift and drag forces thanks to the turbulence-induced deformation (Salibindla et al., 2020a).

In the current study, we performed careful experimental measurements of bubble orientation in intense turbulence where turbulent stresses, rather than buoyancy, become important in bubble deformation. Both the three-dimensional (3D) shape of bubbles and turbulent flows surrounding them were measured simultaneously. The experimental setup and measurement techniques used in this work has been introduced previously in chapter 2. The measurable quantities and their calculations will be summarized in §5.2.1. The acquired unique data set helps us to investigate the preferential alignment of bubble semi-major ($\hat{\boldsymbol{r}}_1$) and semi-minor axes ($\hat{\boldsymbol{r}}_3$) with the representative directions of two deformation mechanisms, i.e. the slip velocity and turbulent strain rate, which will

be discussed in §5.3.1. Finally, in §5.3.2, the evolution of bubble orientation with respect to the surrounding flow as they approach the extreme events of breakup will be introduced and explained.

5.2 Experimental Measurements and Deformation mechanisms

5.2.1 Flow measurements and characteristics

From the reconstructed geometry of a bubble, the semi-major and semi-minor axes ($\boldsymbol{r}_1$ and $\boldsymbol{r}_3$) can be determined by measuring the longest and shortest distance from surface vertices to the center-of-mass of the bubble, respectively. The ratio between them is the aspect ratio, i.e. $\alpha = |\boldsymbol{r}_1|/|\boldsymbol{r}_3|$. Note that this way of extracting bubble semi-axes does not force them to be orthogonal to each other, which is more accurate since not all bubbles follow affine deformation in turbulence. In addition to the geometrical information, the bubble trajectory can be directly acquired by linking the centers of the 3D reconstructed geometries over time, from which the bubble velocity $\boldsymbol{u}_b$ can be calculated.

From our in-house particle tracking results, velocity $\boldsymbol{u}^p$ and acceleration $\boldsymbol{a}^p$ of the p_{th} tracer particle at any time instant can be determined by applying a Gaussian kernel to the particle trajectory (Ni, Huang, and Xia, 2012; Mordant,

Crawford, and Bodenschatz, 2004). If this tracer particle is located within a search radius ($D_s/2$) around the center of a bubble, it can be used to quantify the flow characteristics nearby the bubble, including the local mean flow velocity $u_f = \sum_{p=1}^{n} u_i^p(\boldsymbol{x_0} + \boldsymbol{x}^p)/n$ and velocity gradients. Here, n is the total number of tracer particles that can be identified within the search radius. Note that, because this study focuses on finite-sized bubbles, their alignment and orientation should be associated with flows at the bubble scale. Therefore, the velocity gradients discussed hereafter will be referred to as $\widetilde{A}_{ij}$, where tilde represents the coarse-graining at the bubble size of D. The method used to calculate $\widetilde{A}_{ij}$ has been discussed in detail in chapter 4.

To ensure that the measured velocity gradient tensor is correct, the alignment of the coarse-grained vorticity vector $\hat{\boldsymbol{\omega}}$ with three eigenvectors of $\widetilde{S}_{ij}$, i.e. $\hat{\boldsymbol{e}}_i$ ($i = 1, 2, 3$) is shown in figure 5.1. Although this alignment is calculated based on the coarse-grained velocity gradient $\widetilde{A}_{ij}$, the results are consistent with what have been reported before (Ni, Ouellette, and Voth, 2014; Xu, Pumir, and Bodenschatz, 2011; Ashurst et al., 1987; Huang, 1996) for the local velocity gradient A_{ij}. In both cases, coarse-grained or not, the vorticity vector is preferentially aligned with the eigenvector corresponding to the intermediate eigenvalue of turbulent strain rate as both of these vectors are aligned with the maximum Lagrangian stretching direction during vortex stretching (Ni, Ouellette, and Voth, 2014). In addition, this relative orientation is not sensitive to

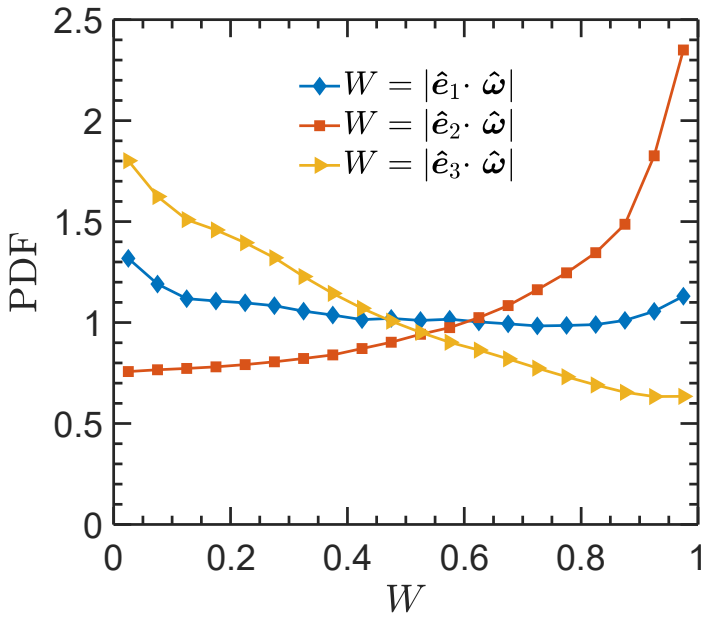

Figure 5.1: Probability density function of the cosine of the angle between vorticity $\hat{\omega}$ and eigenvectors of the strain-rate tensor $\hat{e}_i$.

the range of D or D_s considered in this work, which suggests that (i) the velocity gradient measurement is successful, and (ii) this preferential alignment does not depend on the selected search diameter.

5.2.2 Deformation mechanisms

Since a bubble can be simultaneously stretched along the maximum stretching direction i.e. $\hat{e}_1$ or compressed along the maximum compression direction, i.e. $\hat{e}_3$, the dimensionless Weber number that measures the ratio between the pressure that drives deformation and the relaxation due to the surface tension can be written as $We_{vg} = \rho(\lambda D)^2 D/\sigma$ with λ being either λ_1 and λ_3. Based on a previous study by (Masuk, Salibindla, and Ni, 2020b), the distribution of

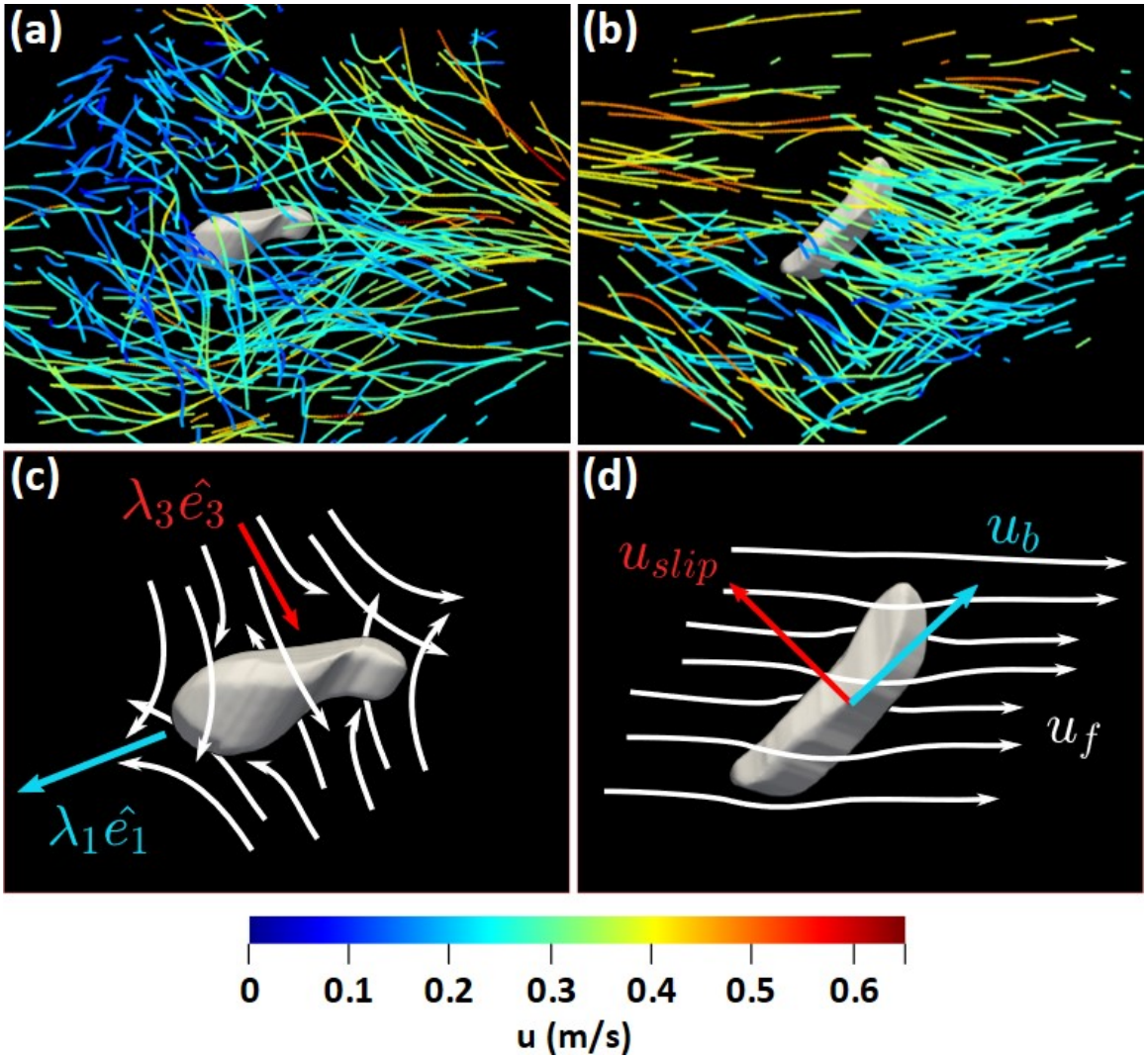

Figure 5.2: Reconstructed three-dimensional shape of deforming bubbles with surrounding tracer trajectories (the instantaneous velocity magnitude u of each particle is indicated by the color), including (a) a case that is primarily deformed by turbulent strain and (b) another case that is deformed mostly by the slip velocity. (c-d) show the schematic of the coarse-grained flow field around these two bubbles.

these two Weber numbers seems to be almost the same. In this paper, we intend to study the orientation dynamics of bubbles relative to $\hat{e}_1$ and $\hat{e}_3$ to test if we can distinguish the contribution of stretching from compression for bubble deformation.

Figure 5.2(a) shows an example of a bubble deformed by a strong turbulent strain rate that is illustrated by many tracer particles, whose trajectories are color-coded with their instantaneous velocity magnitude. Although the flow field is quite complicated and contains dynamics over multiple scales, the estimated $\widetilde{S}_{ij}$ coarse-grained at the bubble scale is sketched in Figure 5.2(c). Through this procedure, small-scale fluctuations are removed and the remaining flows correspond to stretching and compression at the bubble scale. For this case, it is clearly seen that $\hat{e}_3$ aligns with the bubble semi-minor axis $\hat{r}_3$, whereas $\hat{e}_1$ aligns with the bubble semi-major axis $\hat{r}_1$. The result is consistent with our intuition, but it is important to collect statistics of such relative orientation to ensure that the example showed is not an isolated case.

The other important driving mechanism for bubble deformation is the slip velocity $\boldsymbol{u}_{slip} = \boldsymbol{u_b} - \boldsymbol{u_f}$ between the two phases. Bubbles that are subject to $\boldsymbol{u}_{slip}$ will experience a strong gradient of dynamic pressure, which can be used to define another Weber number: $We_{slip} = \rho u_{slip}^2 D/\sigma$. We_{slip} can be defined either using the total slip velocity or one of its three components along the three principal directions. The slip velocity could arise due to multiple effects: (i)

the buoyancy effect; this effect is the strongest for bubbles rising in an otherwise quiescent medium, in which the bubble deformation is primarily driven by the slip velocity along the vertical direction; (ii) the added mass force, which is important for bubbles traveling in strong turbulence with large acceleration fluctuations; and (iii) the finite size effect; Even for density-matched two-phase flows, this finite-sized effect could still lead to the slip velocity between the two phases (Bellani and Variano, 2012; Cisse, Homann, and Bec, 2013). Figure 5.2(b) shows an example of a bubble that is subject to a strong slip velocity along the horizontal direction. After coarse-graining the flow field, figure 5.2(d) illustrates the mean flow around the bubble, which is primarily along the horizontal direction. At the same time, the bubble is sliding towards the direction marked by the cyan arrow. As a result, the slip velocity is pointing at a direction indicated by the red arrow, which aligns excellently with the direction of the semi-minor axis $\hat{\boldsymbol{r}}_3$ of the reconstructed bubble geometry.

5.3 Results and Discussion

5.3.1 Alignment and orientation of deforming bubbles

To collect the statistics of the relative orientation of bubbles with respect to the representative directions of different driving mechanisms, figure 5.3 shows the probability density function (PDF) of the cosine of the angle (W) between

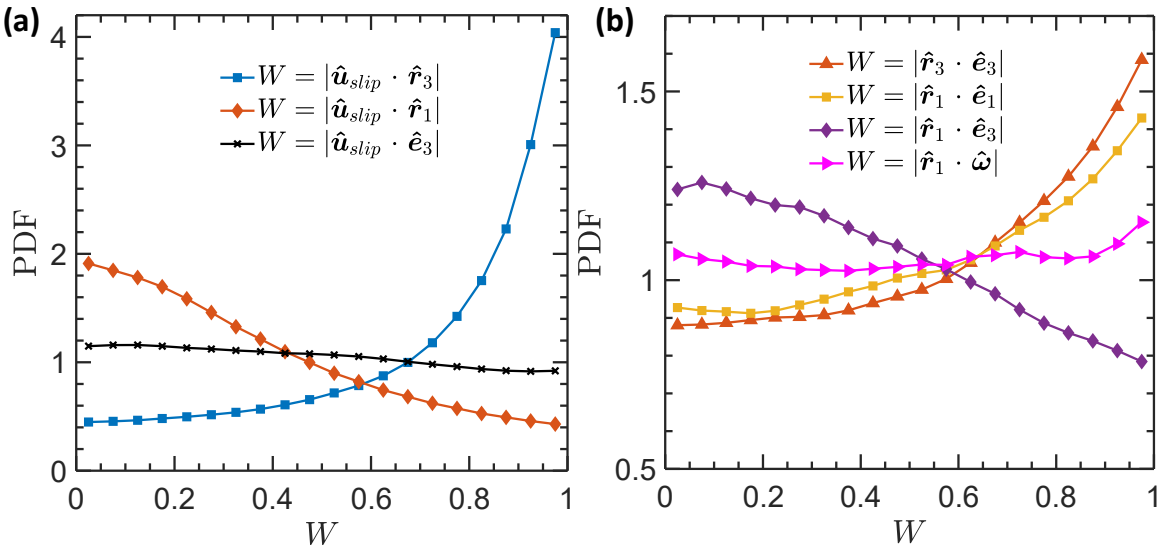

Figure 5.3: Probability density function of the cosine of the angle between bubble axes with (a) the slip velocity and (b) the turbulent strain rate.

two unit vectors. If two unit vectors are completely randomly oriented with each other, the PDF should be close to a uniform distribution ($p(W) = 1$ for all W, where $p(\cdots)$ represents the probability). A peak at $W = 1$ in the PDF would suggest a preferential alignment between the two vectors, whereas a peak near $W = 0$ would imply that the two vectors are perpendicular to each other. Figure 5.3(a) shows the orientation of the slip velocity $\hat{\boldsymbol{u}}_{slip}$ with respect to $\hat{\boldsymbol{r}}_1$ and $\hat{\boldsymbol{r}}_3$. It is evident that there is a clear preferential alignment between $\hat{\boldsymbol{u}}_{slip}$ and $\hat{\boldsymbol{r}}_3$, which suggests that the stagnation pressure induced by the slip velocity impinging on the bubble interface compresses the bubble along that direction.

Note that $\hat{\boldsymbol{r}}_1$ and $\hat{\boldsymbol{r}}_3$ were not forced to be orthogonal to each other during the 3D reconstruction so that any non-affine deformation can also be captured.

In addition to compression, bubbles also extend in other directions to conserve the volume. The relative orientation between $\hat{\boldsymbol{r}}_1$ and $\hat{\boldsymbol{u}}_{slip}$ is also shown in figure 5.3(a). The preference of $\hat{\boldsymbol{r}}_1$ being perpendicular to $\hat{\boldsymbol{u}}_{slip}$ is much weaker compared to that of $\hat{\boldsymbol{r}}_3$ being aligned with $\hat{\boldsymbol{u}}_{slip}$. Such a difference suggests that the orientation of a deformable bubble is primarily determined by the slip velocity compressing the bubble.

In addition to the slip velocity, contribution from the surrounding turbulent strain rate is also shown in figure 5.3(b). In this case, $\hat{\boldsymbol{r}}_1$ and $\hat{\boldsymbol{r}}_3$ preferentially align with $\hat{\boldsymbol{e}}_1$ and $\hat{\boldsymbol{e}}_3$, respectively. The alignment between $\hat{\boldsymbol{r}}_3$ and $\hat{\boldsymbol{e}}_3$ is slightly stronger, suggesting a more important role played by the flow compression. But the small difference suggests that both stretching and compression are important for bubble deformation induced by turbulent strain rate. We believe that finite-sized bubbles are primarily driven by compression, but due to volume conservation, bubbles have to be elongated along other directions. It just happens that $\hat{\boldsymbol{r}}_1$ is the preferred direction with the least resistance for bubble elongation.

The preferential alignment between bubble axes with the eigenvectors of turbulent strain rate is much weaker compared to that with the slip velocity, even though the Weber numbers based on the slip velocity and turbulent strain rate are similar (Masuk, Salibindla, and Ni, 2020b). One plausible reason is that the slip velocity is associated with large-scale flow motions, which can sus-

tain for a longer period of time compared with the turbulent strain rate. Therefore, although these two have similar overall magnitude, the bubble alignment may be dominated more by the slip velocity. In addition, the slip velocity and turbulent strain rate do not always work collaboratively. Figure 5.3(a) also shows the PDF of the relative orientation between $\hat{\boldsymbol{e}}_3$ and $\hat{\boldsymbol{u}}_{slip}$, which seems to be close to a random distribution and may slightly prefer a perpendicular orientation. It suggests that these two mechanisms are not correlated and may even compete with each other occasionally. So a preferential alignment with the slip velocity may lead to a weaker alignment with turbulent strain rate, and vice versa.

If we assume that the bubble shape is a triaxial ellipsoid, it should be described as a symmetric, positive definite, second-rank tensor $\boldsymbol{P}$. The phenomenological equation to describe the time evolution of $\boldsymbol{P}$ was provided by Maffettone and Minale (1998).

$$\frac{d\boldsymbol{P}}{dt} - (\boldsymbol{\Omega}\cdot\boldsymbol{P} - \boldsymbol{P}\cdot\boldsymbol{\Omega}) = -\frac{f_1}{\tau}\left(\boldsymbol{P} - g(\boldsymbol{P})\boldsymbol{I}\right) + f_2(\boldsymbol{S}\cdot\boldsymbol{P} + \boldsymbol{P}\cdot\boldsymbol{S}) \tag{5.1}$$

where $\boldsymbol{S}$ and $\boldsymbol{\Omega}$ represent the symmetric and anti-symmetric part of the velocity gradient tensor. $\tau = \mu D/2\sigma$ is the interfacial relaxation timescale. μ and σ are the dynamic viscosity and the surface tension of water, respectively. $\boldsymbol{I}$ is the second-rank unit tensor. The equation has two main contributions,

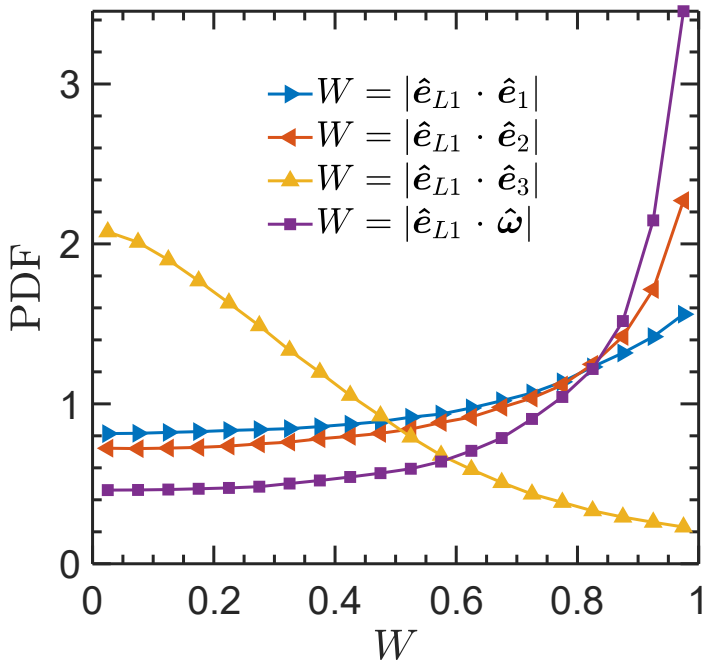

Figure 5.4: Probability density function of the cosine of the angle between the semi-major axis of material elements $\hat{e}_{L1}$ and both vorticity $\hat{\omega}$ and eigenvectors of the strain-rate tensor, $\hat{e}_i$.

deformation, and restoration (the first term on the right side). f_1 and f_2 are two coefficients associated with the viscosity ratio. $g(\boldsymbol{P})$ is introduced to preserve the volume of the bubble.

Strictly speaking, equation 5.1 should not work for finite-sized bubbles as it assumes a linear flow around the bubble, which applies only for bubbles with size $D \ll \eta$. Moreover, this equation does not account for the slip velocity or the buoyancy effect due to a large density mismatch between the two phases. Nevertheless, if we ignore the density mismatch and replace $\boldsymbol{S}$ and Ω with their coarse-grained counterparts, this equation may be used to estimate the alignment between a deforming neutrally-buoyant droplet with its surround-

ing coarse-grained turbulent strain rate.

To simplify the problem even further, if the restoring term led by the surface tension is also ignored, the equation restores to the deformation equation of a material element (Girimaji and Pope, 1990), $d\boldsymbol{F}/dt = \boldsymbol{A} \cdot \boldsymbol{F}$, in which $\boldsymbol{F}$ is the deformation tensor. $\boldsymbol{F}$ can be converted to left $\boldsymbol{C}^{(L)}$ or right $\boldsymbol{C}^{(R)}$ Cauchy-Green strain tensor by using $\boldsymbol{C}^{(L)} = \boldsymbol{F} \cdot \boldsymbol{F}^T$ and $\boldsymbol{C}^{(R)} = \boldsymbol{F}^T \cdot \boldsymbol{F}$. One can easily prove that $\boldsymbol{C}^{(L)} \equiv \boldsymbol{P}$. This suggests that a bubble without surface tension will be deformed by turbulence similarly to the deformation process of a material element, whose three semi-major axes can be determined based on the eigenvectors of $\boldsymbol{C}^{(L)}$. The deformation equation can be numerically integrated to obtain $\boldsymbol{C}^{(L)}$ as reported in Ni et al. (2015) using the DNS results by Benzi et al. (2009). The same method was implemented in this work to elucidate the orientation dynamics of neutrally-buoyant bubbles/droplets in the limit of zero surface tension and zero slip velocity. Although the eigenvalues of $\boldsymbol{C}^{(L)}$ grow exponentially as the integration time increases, the eigenvectors of $\boldsymbol{C}^{(L)}$, $\hat{e}_{Li}$ do not vary too much and they can be used to represent the directions of neutrally-buoyant droplets with zero surface tension.

Figure 5.4 shows the relative orientation between the semi-major axis of the deformed material element $\hat{e}_{L1}$ with three eigenvectors, $\hat{e}_i$, of the strain rate tensor as well as with the vorticity vector $\hat{\omega}$. As it has been discussed before by Ni et al. (2015), the strongest alignment is observed between the

semi-major axis of the material element and the vorticity vector because vorticity is generated by the vortex stretching process. As a vortex is stretched by the Lagrangian stretching $\boldsymbol{C}^{(L)}$, it ends up aligning with $\hat{e}_{L1}$.

Comparing figure 5.3 with figure 5.4, the semi-major axis of a material element, $\hat{e}_{L1}$, shows strong alignment with $\hat{e}_2$ and $\hat{\omega}$, whereas the semi-major axis $\hat{r}_1$ of finite-sized bubbles show very weak alignment, if at all, with either of the two vectors. This finding is qualitatively consistent with the work conducted by Biferale, Meneveau, and Verzicco (2014). In their simulations, it was found that, for a small capillary number, the alignment between the semi-major axis of the neutrally buoyant droplets with $\hat{\omega}$ is relatively weak. As the capillary number increases, the alignment becomes stronger. It suggests that, despite the difference in Reynolds number and sizes, our results of the orientation dynamics of finite-sized bubbles share some similarities with the sub-Kolmogorov-scale neutrally-buoyant droplets at a small capillary number.

Nevertheless, it is evident that the alignment of finite-sized bubbles with the coarse-grained strain rate is much weaker than that for sub-Kolmogorov-scale droplets. The weaker alignment is mainly due to two reasons: (i) the competing effect from the slip velocity, and (ii) our shape reconstruction allows non-affine deformation, so the semi-major and semi-minor axes of bubbles are not necessarily orthogonal to each other, which should also weaken the alignment with the eigenvectors of the coarse-grained turbulent strain rate.

5.3.2 Breakup

In the previous section, the statistics of the alignment between the semi-major and semi-minor axes of deforming bubbles and representative directions of the slip velocity and velocity gradients have been discussed. To collect enough statistics, bubbles with different aspect ratios and sizes were all compiled together. The question arises as to if the alignment depends on how strong the bubble is deformed and will the roles played by different mechanisms change when bubbles experience strong deformation. In this section, we will turn to bubbles with strong deformation and breakup events to unveil the key mechanisms behind bubble breakup in turbulence.

Since both the slip velocity and turbulent strain rate can be tracked along each bubble trajectory, the temporal evolution of these quantities, as well as the bubble geometry, can be acquired. For all our experiments, 190 datasets were collected; total 480,329 bubbles were reconstructed and tracked over time. The majority of these bubbles did not break in the finite residence time that they spent in the view volume; only 195 breakup events were identified and reconstructed. Details concerning the reconstruction of the breakup events can be found in Masuk, Salibindla, and Ni (2019) and Qi et al. (2020).

For all these breakup events, the breakup moment is identified first, and the time traces of $We_{slip,x}$ and We_{vg} before breakup are compiled together to calculate the time evolution of the Weber numbers. Figure 5.5 shows the PDFs

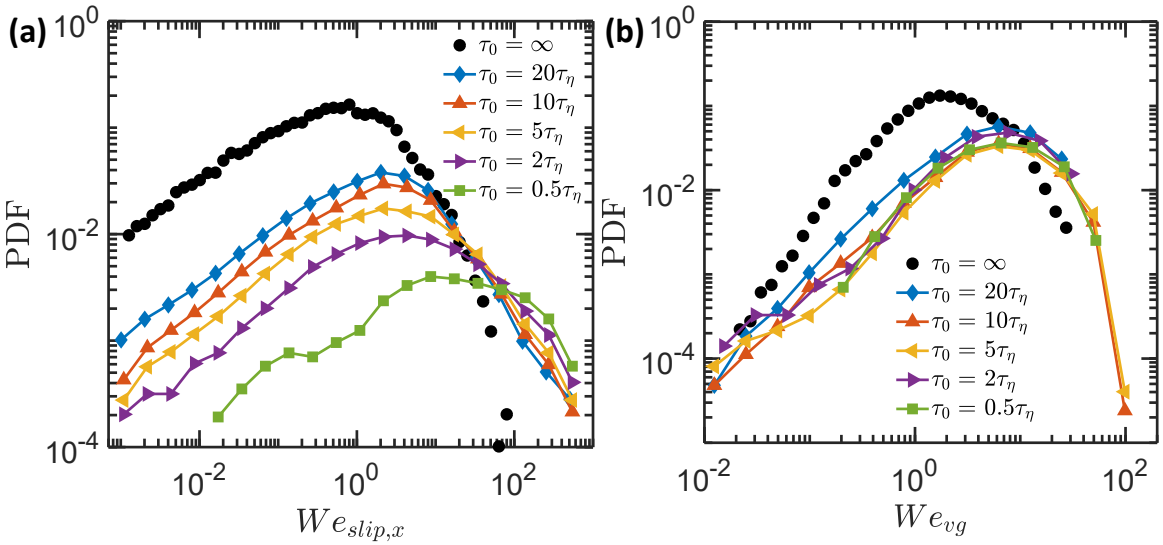

Figure 5.5: Probability density function of (a) the slip-velocity-based Weber number and (b) the strain-rate-based Weber number, for mild deformation case (black solid symbols) as well as different times (τ_0) before breakup.

of We_{slip} and We_{vg} as a function of different time periods before breakup. The closest and the farthest time that were tracked before the breakup was about 0.5 τ_η and 20 τ_η, respectively. We also plot the PDF of $We_{slip,x}$ and We_{vg} for all bubbles, including both weak and strong deformation cases, in figure 5.5(a) and (b) as black solid circles. It is obvious that the Weber numbers for bubbles that are about to break are systematically larger than that for all bubbles with a similar size. In addition, it can be seen that $We_{slip,x}$ continues to grow gradually from 20 τ_η to 5 τ_η. However, from 5 τ_η to the moment of breakup, the distribution leaps rightward over an order of magnitude to a larger $We_{slip,x}$. It indicates that the bubble breakup is associated with a timescale that is within $\sim$ 5 τ_η. Over this time, the slip velocity experiences a dramatic change. The same calculation was also performed for We_{vg} and the results are shown in fig-

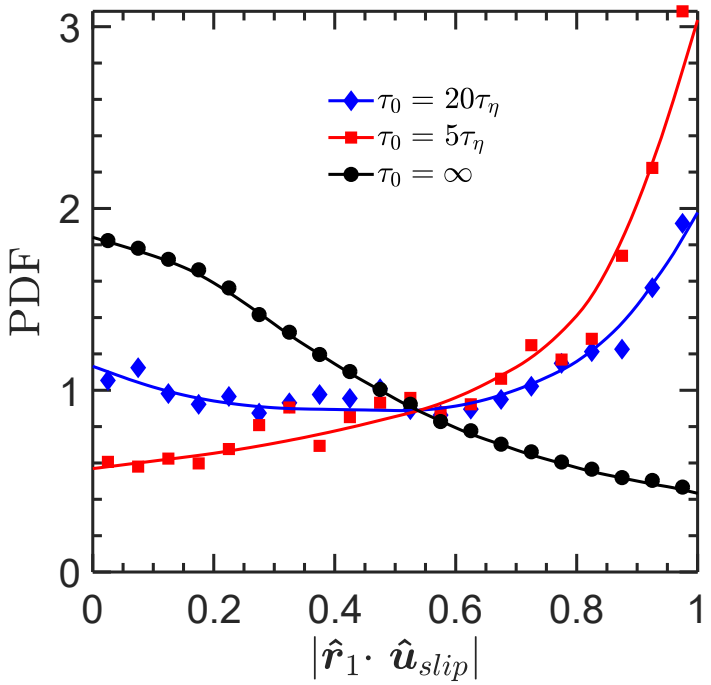

Figure 5.6: Probability density function of the cosine of the angle between the bubble semi-major axis $\hat{\boldsymbol{r}}_1$ and the slip velocity $\hat{\boldsymbol{u}}_{slip}$ for mild deformation and two different time (τ_0) before breakup.

ure 5.5(b). It is evident that We_{vg}, similar to $We_{slip,x}$, even at 20 τ_η prior to the breakup moment, is higher than that for all bubbles. But, unlike the case for $We_{slip,x}$, the distribution of We_{vg} does not seem to have a systematical shift over time. Nevertheless, the left tail for very small We_{vg} seems to shift rightward as bubbles approach breakup, indicating that the number of events with very small velocity gradients become fewer near breakup. In contrast to the distinct behaviors of the time evolution of $We_{slip,x}$ and We_{vg} for breaking bubbles, the distribution of these two Weber numbers, shown as black solid symbols in figure 5.5 (a) and (b), for all bubbles are quite close to each other, both of which peak at around $We \approx 1$.

In addition to the Weber numbers, figure 5.6 shows the alignment of the slip velocity with the semi-major axis of the bubble for (i) all bubbles, (ii) only the breaking bubbles (5 τ_η prior to the breakup), and (iii) only the breaking bubbles (20 τ_η prior to the breakup). There seems to be a consistent trend of the bubble semi-major axis flipping from a perpendicular to a parallel orientation relative to the direction of the slip velocity, which is opposite to the discussion in §5.3.1 that slip velocity should act to flatten, instead of elongating, the bubble along its direction.

This surprising behavior can only be understood once the discussion of the relative orientation of the bubble semi-major axis with the eigenvectors of turbulent strain rate tensor is completed. Figure 5.7(a) shows the distribution of the alignment of the bubble semi-major axis with $\hat{e}_3$, similar to figure 5.3(b). Here, the distribution is shown as a function of the time prior to the breakup event. For all bubbles, as we discussed in §5.3.1, the bubble semi-major axis slightly prefers a perpendicular orientation with respect to the strongest compression direction $\hat{e}_3$. Unlike the case for the slip velocity, this preference becomes even stronger as bubbles approach breakup over time, which can be clearly seen in figure 5.7(a).

Although the distribution of We_{vg} that measures the magnitude of the driving force does not change much over time (figure 5.5), turbulent strain rate seem to compress the bubble more effectively as $\hat{e}_3$ becomes more perpendic-

ular to $\hat{r}_1$ and aligns better with $\hat{r}_3$ over time. However, as one can see that, although the trend over time is obvious, the PDFs of the relative orientation are quite noisy because of the limited number of breakup events. To ensure that this observed trend is true, figure 5.7(b) shows the PDF for the same relative orientation but only for cases when bubbles experienced large deformation (α >2.5) but did not break. The PDF shows a very similar trend to what has been observed for breaking bubbles close to the breakup moment. This provides a consistent picture that the flow compression around bubbles does not become larger but more effective as it aligns better with bubbles as they approach breakup or strong deformation.

Based on the observation of the relative orientation between $\hat{\boldsymbol{r}}_1$ with the slip velocity ($\hat{\boldsymbol{u}}_{slip}$) and turbulent strain rate ($\hat{\boldsymbol{e}}_3$), it is clear that, before the breakup, the slip velocity becomes stronger in magnitude and the velocity gradient aligns better with bubbles and consequently breaks the bubble more effectively. It seems that each of these two mechanisms adjusts in a different way to assist the breakup. The puzzling observation of almost 90° rotation of the relative orientation between the slip velocity and $\hat{\boldsymbol{r}}_1$ turns out to be due to the definition of the slip velocity that contains contributions from both the flow and bubble velocities. For weak deformation, both velocities are important and the slip velocity drives the bubble deformation. As bubbles approach breakup, the bubble velocity increases dramatically, overtaking the entire slip

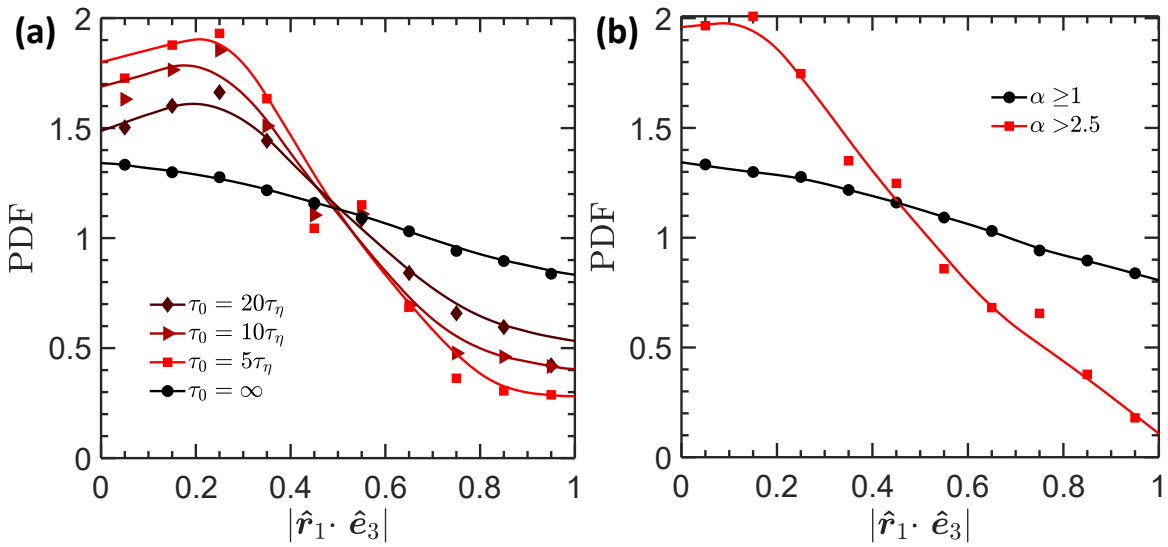

Figure 5.7: Probability density function of the cosine of the angle between the bubble semi-major axis $\hat{r}_1$ and the smallest eigenvector of the strain-rate tensor $\hat{e}_3$ for (a) different times (τ_0) before breakup and (b) all strongly-deformed (aspect ratio $\alpha > 2.5$) cases.

velocity direction. Since the bubble velocity during strong deformation aligns with $\hat{r}_1$, the slip velocity ends up being aligned with the semi-major axis. In other words, the slip velocity switches from being the driving mechanism to the driven result of bubble deformation because it has contributions from both of the two phases.

5.4 Conclusion

The orientation dynamics of deformed finite-sized bubbles in homogeneous and isotropic turbulence with a large energy dissipation rate has been studied experimentally. Both the bubble geometry and many surrounding tracer par-

ticles are simultaneously reconstructed and tracked in 3D. From this unique data set, we are able to study the relative orientation between bubbles and the representative directions of two different deformation driving mechanisms, including turbulent strain rate and the slip velocity between the two phases.

For mild deformation, the strongest alignment is observed between the bubble semi-minor axis and the slip velocity, suggesting that bubbles are predominately compressed by the slip velocity. At the same time, the bubble semi-major and semi-minor axes are aligned with the strongest stretching and compression directions of turbulent strain rate, respectively. Compared with the relative orientation of bubbles with the slip velocity, the alignment of bubbles with turbulent strain rate is weaker and could be affected by the competition between deformation driven by turbulent strain rate and by the slip velocity.

The orientation dynamics of deformable bubbles are also compared to that of neutrally-buoyant sub-Kolmogorov-scale material elements with no surface tension or slip velocity. Their orientations show strong alignments with the vorticity vector and the intermediate eigenvector of the turbulent strain rate. But such an alignment is completely missing for finite-sized bubbles based on our experimental results. This observed difference qualitatively agrees with a previous simulation on sub-Kolmogorov-scale droplets with different capillary numbers, indicating that the restoring force from the surface tension could strongly affect their orientation.

Finally, the orientation dynamics of bubbles are studied for strongly-deformed bubbles, in particular the events close to breakup. As bubbles approach a breakup, the preference for a perpendicular orientation between $\hat{e}_3$ and $\hat{r}_1$ grows, leading to a more effective strain-induced deformation. The alignment between $\hat{u}_{slip}$ and the bubble semi-major axis ($\hat{r}_1$) switches from being perpendicular to being aligned with each other. This transition was explained by the possible switch of the role played by the slip velocity from the driving mechanism to the driven results because of the sudden increase in bubble velocity due to deformation.

Chapter 6

Towards a simple model for the deformation and orientation dynamics of finite-sized bubbles in both quiescent and turbulent media

We present a new phenomenological model that describes both the deformation and orientation dynamics of finite-sized bubbles in both quiescent and turbulent media by constraining different terms against the 3D simultaneous measurements of two phases, i.e. bubbles and surrounding flows. The model extends the equation proposed by Maffettone and Minale (*J. Non-Newtonian Fluid Mech.,* vol. 78, 1998, pp. 227-241) by including two new terms, pseudo-strain-rate and pseudo-rotation terms, that account for the slip-velocity in-

duced deformation and the wake-induced rotation. With these new terms, the new model covers two key governing mechanisms for describing the deformation dynamics of finite-sized bubbles, including the local strains at the bubble scale and the slip velocity between the two phases. The model also introduces three dimensionless coefficients that measure the relative importance of each driving mechanism. The advantage of this framework is that each coefficient affects one particular statistics from our experimental results, which helps to isolate and evaluate the value of each coefficient one by one and avoid any questionable multi-variable fitting procedures. The model was tested against the measured deformation and orientation dynamics, and excellent agreements are observed for a number of statistics from both quiescent and turbulent cases, thereby confirming the validity of the new model. Finally, we discuss how to possibly extend the proposed framework to describe the deformation and orientation dynamics of finite-sized drops with arbitrary density and viscosity, which remains to be tested by future experiments.

6.1 Introduction

Deformation and breakup of gas bubbles and oil droplets in turbulent water are ubiquitous in nature, from bubble-mediated gas transfer in the ocean (Wanninkhof and McGillis, 1999) to the fragmentation and dispersion of an oil spill

(Delvigne and Sweeney, 1988; Yang et al., 2015). Despite advances made in the field of multiphase flows and droplet-laden turbulence (Elghobashi, 2019; Mathai, Lohse, and Sun, 2020b; Risso, 2018), our understanding of these problems are still limited because of the complex nonlinear interactions between two phases across a deformable interface and the manifestation of these interactions across multiple length and time scales in turbulence. Unlike rigid objects, the geometries of deformable objects have almost infinite degrees of freedom. To simplify the problem, the key parameters with the first-order effects include the shape of bubbles as well as their orientation with respect to the surrounding flows.

The deformation of the dispersed phase is sensitive to many parameters. Other than the size, it is mostly determined by the competition between the intensity of local inertial/viscous driving forces and the surface tension restoring forces (Stone, 1994). In a regime where the viscous stress dominates, Taylor (1932) and Taylor (1934) showed that the droplet deformation is determined by the viscosity ratio between two fluids and the capillary number $Ca = \mu_c G D/\sigma$, where μ_c is the viscosity of the carrier fluid, G is the local shear rate around the droplet, D is the droplet diameter, and σ is the surface tension. Ca essentially measures the ratio between viscous shear stresses and the restoring stress due to the surface tension. The larger Ca, the more intense the flow shear rate; if Ca surpasses a critical value (Ca_{cr}), the drop breaks. In addition to the drop

deformation, the orientation dynamics of drops is also closely associated with the local shear rate.

To capture both the deformation and orientation dynamics of drops in viscous shear flows, Maffettone and Minale (1998) developed a model (MnM model hereafter) for characterizing the dynamics of a single neutrally-buoyant drop immersed in an infinite medium with a generic flow field. In particular, this model assumes that drops follow ellipsoidal shapes based on experimental observations (Guido and Villone, 1998) and numerical simulations (Kennedy, Pozrikidis, and Skalak, 1994). The MnM model works well for simple shear (Guido and Villone, 1998), planar and uniaxial elongational flows, as well as the linear combinations of these canonical flows (Bentley and Leal, 1986). The agreement can be extended to Ca that is not far from Ca_{cr}, even though the drop shape starts to deviate from an ellipsoid and the non-linear effects start to become important.

For drops deforming in viscous shear flows, there are two main assumptions: (i) the relative motion between the center of mass of drops with surrounding flow is negligible compared with the drop deformation. This can be accomplished by matching the density of both phases or selecting a high-viscosity fluid for the carrier phase. (ii) The viscous shear stress on the drop interface is much larger than the dynamic pressure exerted by the surrounding moving fluid. For both assumptions to hold, one only needs to make sure that

the drop Reynolds number $Re_b = u^s D/\nu_c$ is smaller than one, in which ν_c is the kinematic viscosity of the carrier phase and u^s is the magnitude of the drop slip velocity with respect to the surrounding flow.

Unlike drops, gas bubbles tend to have a large density difference with the surrounding liquid. One canonical problem is related to the rise motion of finite-sized bubbles in water at rest. In this case, Re_b could range from $O(10^2)$ to $O(10^3)$ (Magnaudet and Eames, 2000). Therefore, the viscous stress ($\mu_c G$) becomes less important than the dynamic pressure exerted on the bubble interface due to their buoyant rising motion ($\Delta\rho g D$), and consequently Ca is much smaller than the Eötvös number $Eo = \Delta\rho g D^2/\sigma$, where $\Delta\rho = \rho_c - \rho_d$ is the density difference between the dispersed phase (ρ_d) and the carrier phase (ρ_c). When Eo is larger than one, the bubble aspect ratio can be determined based on Eo. Moore (1965) developed a simple model to link the bubble aspect ratio α to Eo for small Eo close to one, and extended it to larger Eo by using the potential flow method. It was found that a maximum α of 6 can be achieved for Eo close to 3.745, beyond which a symmetric deformation cannot be attained.

Note that, in many papers discussing the bubble deformation due to their rise motion, the dimensionless number that was often used is the Weber number: $We = \rho_c u^2 D/\sigma$. One can see that $We \approx Eo$ if the bubble rise velocity $u \approx \sqrt{gD}$. But in turbulence, when the slip velocity between bubbles and surrounding flows is not entirely controlled by the bubble rise velocity, these two

dimensionless numbers are not the same anymore. To make a clear distinction, Eo will be used only for representing the bubble deformation by buoyancy, whereas We is reserved for characterizing the deformation driven by the surrounding turbulence in this paper.

In turbulence, the problem can be roughly categorized based on the droplet/bubble size, either in the dissipative range ($D \ll \eta$) or in the inertial range ($\eta \ll D \ll L$), where η and L are the Kolmogorov and integral length scales respectively. For small sizes, if the object is neutrally-buoyant and only responds to the local and instantaneous flow field, its center-of-mass motion can be integrated based on the local velocity. The drop shape, if assumed to be an ellipsoid, can be solved based on simple models, such as the MnM model (Maffettone and Minale, 1998). Although MnM model was originally proposed to describe the drop deformation in viscous shear flows, it is still valid to be used in turbulence as long as the drop size is so small that the surrounding flow is still dominated by the linear viscous shear stress. Such an approach helps to couple the simulation of background turbulence with a phenomenological model, which enabled the simultaneous simulations of the deformation of around 10^4 to 10^5 drops. This framework has been utilized to study the drop deformation in homogeneous and isotropic turbulence by Biferale, Meneveau, and Verzicco (2014) and in a Taylor-Couette system by Spandan, Lohse, and Verzicco (2016). Similar frameworks of coupling carrier-phase simulation with simple models

for the dispersed phase has also been utilized for studying the tumbling motion of non-spherical particles (Challabotla, Zhao, and Andersson, 2015; Marchioli, Fantoni, and Soldati, 2010), stretching and buckling of flexible rods (Allende, Henry, and Bec, 2018), as well as the breakup of ductile aggregates (Marchioli and Soldati, 2015).

The study of finite-sized bubble deformation in turbulence is much more complicated. As detailed by Elghobashi (2019) in a recent review, there are three main DNS approaches to study finite-sized bubbles and droplets in turbulence: (i) tracking individual points on the bubble interface, e.g. front tracking (Unverdi and Tryggvason, 1992; Tryggvason et al., 2001);(ii) tracking a scalar function, e.g. volume of fluid (VOF) (Scardovelli and Zaleski, 1999; Dodd and Ferrante, 2016), Level-set (Sussman, Smereka, and Osher, 1994; Osher and Fedkiw, 2001), Lattice-Boltzmann method (LBM) (Shan and Chen, 1993), or phase field method (PFM); (iii) a more recently developed hybrid method that couples the immerse boundary method (IBM) with a phenomenological interaction potential method (IPM). All these sophisticated models are extremely valuable tools to investigate finite-sized bubble/droplet deformation in turbulence. However, they are very expensive to perform for a large number of bubbles/droplets in a large system even with the most advanced computational methods.

The objective of this paper is to develop a phenomenological model for finite-

sized bubbles based on experimental measurements of bubble deformation in both quiescent and turbulent environments. Similar to MnM model, the proposed model takes the known flow conditions, including velocity gradients and the bubble slip velocity as inputs, and predicts the time evolution of the bubble shape and orientation by assuming ellipsoidal bubble shapes. In previous chapters (chapter 2, 3, and 4), we introduced the experimental setup and the measurement techniques that enable the simultaneous measurements of both phases, including the 3D shape of bubbles and their surrounding turbulence. In this chapter, a new phenomenological model accounting for the contribution of slip velocity to bubble deformation and orientation dynamics will be discussed and explained in §6.2. The model parameters will be calibrated against experimental results for bubbles deforming in a quiescent and turbulence media in §6.3. In the same section, we will also show how to extend the proposed new models to characterize the deformation of finite-sized droplets with different viscosity and density.

6.2 Finite-sized Bubble Deformation Model (FBD Model)

There are three main objectives of this paper. The first is to develop a model to capture the deformation dynamics of finite-sized bubbles with diameter D

($\eta < D < L$) in turbulence and in water at rest. Secondly, the developed model should correctly account for two deformation mechanisms driven by the local velocity gradients and the slip velocity between the two phases. For one extreme limit when bubbles rise in an otherwise quiescent medium, the bubble deformation is dominated by the slip velocity. In this case, Eo is much greater than one, and We driven by the velocity gradients is close to zero. In the other limit, the turbulent energy dissipation rate becomes so large that bubble deformation driven by the dynamic pressure gradient caused by velocity gradients ($We \geq 1$) becomes important. The third objective is to use our experimental results to validate the model and constrain different dimensionless coefficients in the model.

Before introducing our own model, we start with the MnM model originally proposed by [**?**] to describe the shape evolution of neutrally-buoyant droplets experiencing a linear velocity gradient by using a symmetric positive-definite second-order tensor P_{ij} to represent the droplet shape in the following equation.

$$\frac{dP_{ij}}{dt} = \Omega_{ik}P_{kj} - P_{ik}\Omega_{kj} + f_2(\mu)(S_{ik}P_{kj} + P_{ik}S_{kj}) - \frac{f_1(\mu)}{\tau}(P_{ij} - g(P)\delta_{ij}) \qquad (6.1)$$

where the three eigenvalues of P_{ij} represent the squared lengths of three semi-axes of an ellipsoid. S_{ij} and Ω_{ij} are the symmetric and anti-symmetric

parts of the velocity gradient tensor (A_{ij}) that the droplet is subject to, respectively. In particular, $S_{ij} = (A_{ij}+A_{ji})/2$ and $\Omega_{ij} = (A_{ij}-A_{ji})/2$. For a simple shear flow with a small Reynolds number, f_1 and f_2 are functions of the viscosity ratio $\mu = \mu_d/\mu_c$, where μ_d and μ_c represent the dynamic viscosity of inner fluid of bubbles/drops and their surrounding carrier fluid, respectively. The last term on the right side of equation 6.1 is the restoring term, in which $\tau = \mu_d D/2\sigma$ is the relaxation time scale of the droplet determined by μ_d and the coefficient of surface tension σ. D is the equivalent sphere diameter of the droplet. The volume conservation is ensured in the model with $g(P) = 3\mathrm{III}_P/\mathrm{II}_P$, where III_P and II_P are the invariants of P_{ij}:

$$\mathrm{I}_p = P_{ii},\ \mathrm{II}_P = -\frac{1}{2}(P_{ij}P_{ij} - \mathrm{I}_P^2),\ \mathrm{III}_P = \frac{1}{3}(P_{ik}P_{kj}P_{ji} - \mathrm{I}_P^3 + 3\mathrm{I}_P\mathrm{II}_P) \tag{6.2}$$

This model works well for describing the deformation of bubbles in simple flows, and it has been validated against several experimental results (Guido and Villone, 1998; Bentley and Leal, 1986; Torza, Cox, and Mason, 1972; Guido, Minale, and Maffettone, 2000). MnM model has also been used for characterizing the shape evolution of small neutrally-buoyant droplets in turbulence (Biferale, Meneveau, and Verzicco, 2014; Spandan, Lohse, and Verzicco, 2016). This works under two conditions: (i) D is in the dissipative range ($D \ll \eta$),

where the viscous stress still dominates; (ii) Drops are neutrally-buoyant with no significant slip velocity.

For finite-sized bubbles with D in the inertial range ($\eta \ll D \ll L$), these two assumptions no longer hold. Bubbles have significant density mismatch with surrounding flows and they will have nonlinear interactions with surrounding eddies of multiple length and time scales. At a first glance, it may appear that the MnM model simply cannot be used at all to describe the deformation of finite-sized bubbles. But a recent study by Masuk, Salibindla, and Ni (2020a) showed that bubbles' semi-major ($\hat{\mathrm{r}}_1$) and semi-minor ($\hat{\mathrm{r}}_3$) axes are preferentially aligned with two eigenvectors, i.e. $\hat{\mathrm{e}}_1$ (maximum stretching direction) and $\hat{\mathrm{e}}_3$ (maximum compression direction), of the turbulent strain rate tensor coarse-grained at the bubble size, respectively. This suggests that, among all the eddies with different sizes, it is the eddy with the size similar to D that plays the most important role in determining the bubble deformation and orientation.

To reflect the roles played by the large eddy with the size of D, we can simply replace the velocity gradients in MnM model with the coarse-grained velocity gradients:

$$\frac{dP_{ij}}{dt} = \widetilde{\Omega}_{ik}P_{kj} - P_{ik}\widetilde{\Omega}_{kj} + f_2'(\widetilde{S}_{ik}P_{kj} + P_{ik}\widetilde{S}_{kj}) - \frac{f_1'}{\tau_n}(P_{ij} - g(\mathrm{II}_P, \mathrm{III}_P)\delta_{ij}) \qquad (6.3)$$

where the coarse-grained velocity gradient ($\widetilde{A}_{ij}$) can be directly accessed from our experiments, and Ω_{ij}, and S_{ij} in the MnM model are replaced with the symmetric and anti-symmetric parts of $\widetilde{A}_{ij}$ ($\widetilde{S}_{ij} = (\widetilde{A}_{ij} + \widetilde{A}_{ji})/2$, and $\widetilde{\Omega}_{ij} = (\widetilde{A}_{ij} - \widetilde{A}_{ji})/2$). f_1' and f_2' are two dimensionless coefficients, and τ_n is the typical relaxation timescale of the bubble, which will be discussed in §6.3.1.

In addition to the coarse-grained velocity gradients, another effect brought in by finite-sized bubbles is the strong slip velocity, driven by the density mismatch and finite size effect (Bellani and Variano, 2012; Cisse, Homann, and Bec, 2013). The importance of the slip velocity was clearly highlighted in a recent work by Masuk, Salibindla, and Ni (2020a). In particular, the bubble semi-minor axis seems to preferentially align not only with the eigenvector ($\hat{e}_3$) associated with the the smallest eigenvalue (λ_3, strongest compression) of $\widetilde{S}_{ij}$ but also with the slip velocity $\boldsymbol{u}^s$. It indicates that the role played by the slip velocity cannot be ignored for finite-sized bubbles.

To include the contribution of the slip velocity, a new term that describes the bubble deformation subjected to the slip velocity needs to be added to the model. To appropriately formulate this term, experimental results on bubbles' responses to just the slip velocity are needed. In intense turbulence, based on our experimental results, the contributions from velocity gradients and the slip velocity, measured by their respective Weber numbers, have very similar distributions. So it is nearly impossible to have a clean separation of their

effects.

To solve this problem, we decide to seek a simpler case where the slip velocity is the only dominant mechanism for bubble deformation with nearly zero velocity gradients. Such an example is readily available for a bubble rising in an otherwise quiescent medium. We performed such an experiment in the same V-ONSET facility by simply turning all jets and the mean flow off to allow individual bubbles to rise in an undisturbed environment. The same diagnostic system was used to extract the bubble rise motion and their shapes in 3D. One such example is shown in figure 6.1. The blue line indicates the time trace of the bubble dimension along the semi-minor axis (r_3), and the red line shows the slip velocity projected onto the direction of $\hat{\mathrm{r}}_3$, i.e. ($|\boldsymbol{u}^s \cdot \hat{\boldsymbol{r}}_3|$). Both signals show some apparent oscillations in time because of the well-known path instability developed due to the wake-bubble interaction (Ern et al., 2012; Mougin and Magnaudet, 2001; Tayler et al., 2012; Mougin and Magnaudet, 2006). It seems that the time traces of r_3 and $|\boldsymbol{u}^s \cdot \hat{\boldsymbol{r}}_3|$ are out of phase with each other, indicating that an increase of the slip velocity results in a decrease in the bubble minor axis. It is consistent with our expectation that a stronger dynamic pressure from a larger slip velocity tends to compress the bubble along that direction. When the slip velocity weakens, the bubble can relax back towards a spherical geometry and results in an increase of r_3.

In this case, the background flow is almost stagnant and the velocity gra-

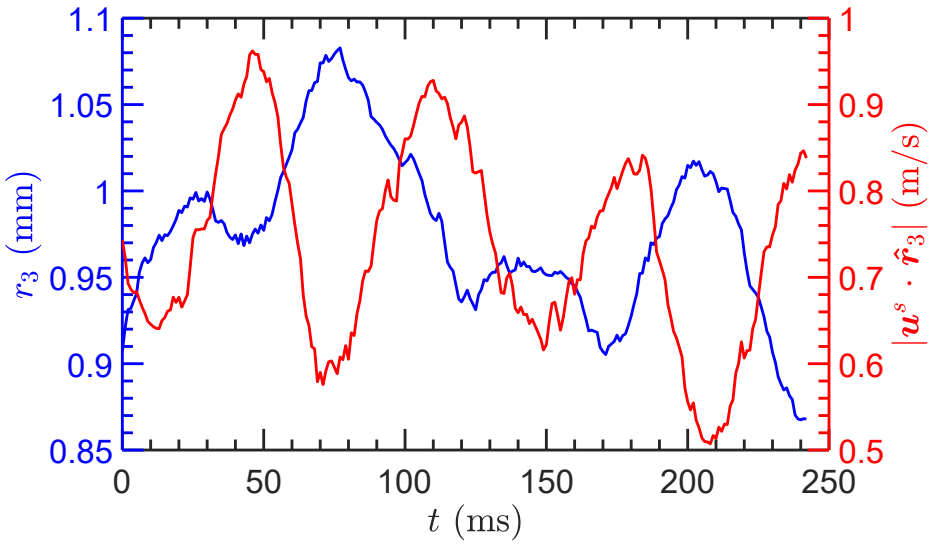

Figure 6.1: An example time trace of the semi-minor axis (r_3) and the bubble slip velocity projected onto the direction of r_3 for an air bubble rising in an otherwise quiescent water medium

dient around the bubble is negligible if we do not consider the bubble-induced flows. Following this argument, the terms associated with $\widetilde{S}_{ij}$ and $\widetilde{\Omega}_{ij}$ in equation 6.3 become close to zero. It is evident that, without these two terms, there is no other driving force in the current equation 6.3 that can deform a bubble. So the roles played by the slip velocity has to be added.

In figure 6.1, it is clear that the slip velocity primarily compresses bubbles along its direction. Based on this observation, a pseudo-strain-rate tensor S'_{ij} is formulated by borrowing the concept of stress-strain relationship for isotropic materials in continuum mechanics (Ugural and Fenster, 2003). The stress tensor γ_{ij} has to be aligned with the slip velocity $\boldsymbol{u}^s$ following: $\gamma_{ij} = -\rho_c u_i^s u_j^s$. This allows us to define a pseudo-strain-rate tensor S'_{ij}:

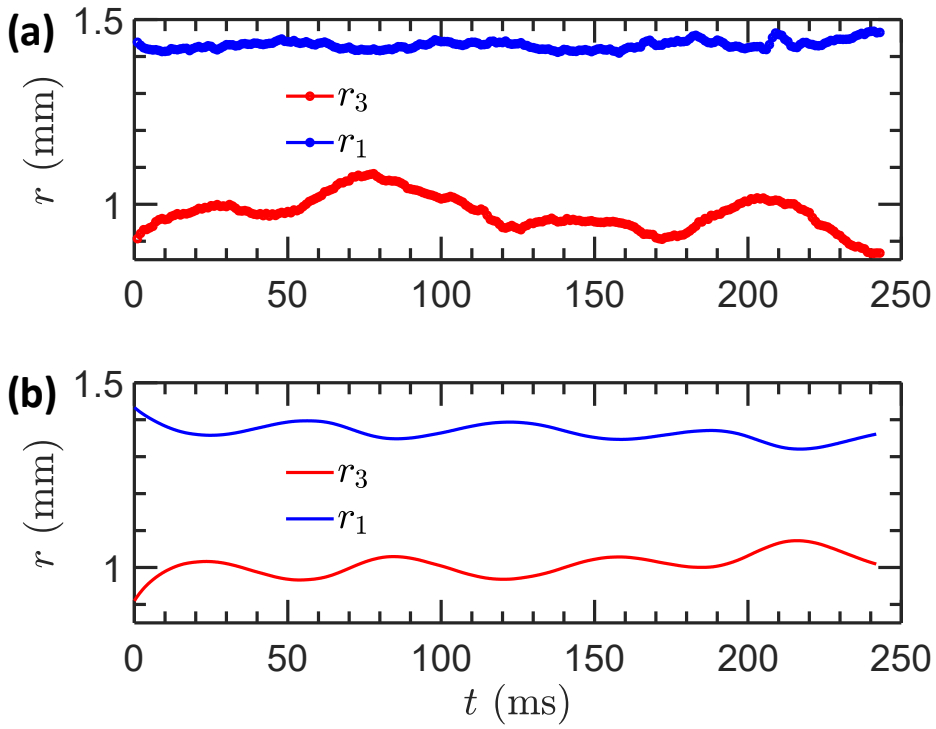

Figure 6.2: Example time traces of the semi-major (blue) and semi-minor (red) axes of an air bubble rising in water at rest from (a) direct experimental measurements and (b) the model calculation by using the pseudo-strain-rate term based on the slip velocity.

$$S'_{ij} = \frac{1}{E\tau_n}[(1+\nu)\gamma_{ij} - \nu\gamma_{kk}\delta_{ij}] \tag{6.4}$$

where E is a constant related to the restoring stress of the bubble. Since the restoring force for bubbles comes from the surface tension (σ), E can be related to σ as $E = \sigma/D$. Another constant in equation 6.4 is ν, similar to the Poission's ratio used in solid mechanics. For incompressible materials, ν is 0.5, which is also used in our case. Since bubbles used in our experiments are gas bubbles rather than vapor bubbles, this assumption should hold.

The advantage of this pseudo-strain-rate term is that it can be added to equation 6.3 similar to the formulation of the strain-rate term, i.e. $K_s(S'_{ik}P_{kj} + P_{ik}S'_{kj})$, with a new coefficient K_s that measures its relative importance. To validate the new model, we numerically integrate equation 6.3 after adding equation 6.4 and setting $\widetilde{S}_{ij} = 0$ and $\widetilde{\Omega}_{ij} = 0$. The time series of $\boldsymbol{u}^s$ for many bubbles were fed into equation 6.4 to calculate the time series of S'_{ij}. The integration was performed using the fourth-order Runge-Kutta method. The initial condition for P_{ij} was set such that the semi-minor axis of P_{ij} is identical to that of the measured bubble. The dimensions along the other two axes were assumed to be the same, and the total volume of the modelled and measured geometries were also kept the same. This initial condition essentially fits the measured bubble geometry with an oblate spheroidal shape. Similar initial conditions and integration methods will be used for the rest of this paper.

Both the semi-major and semi-minor axes integrated from the new model with the pseudo-strain-rate term is shown in figure 6.2(b) along with the experimental result shown in figure 6.2(a) for comparison. In this case, $f'_1 = 1$ and $K_s = 0.14$ were used. The reasons for selecting these values will be discussed in §6.3.1. It can be seen that the model successfully reproduces the oscillation of both r_3 and r_1 simply based on the oscillation of the slip velocity. In addition, the oscillation amplitude is slightly different between the experimental results and the model prediction because the modelled oblate spheroidal geometry is

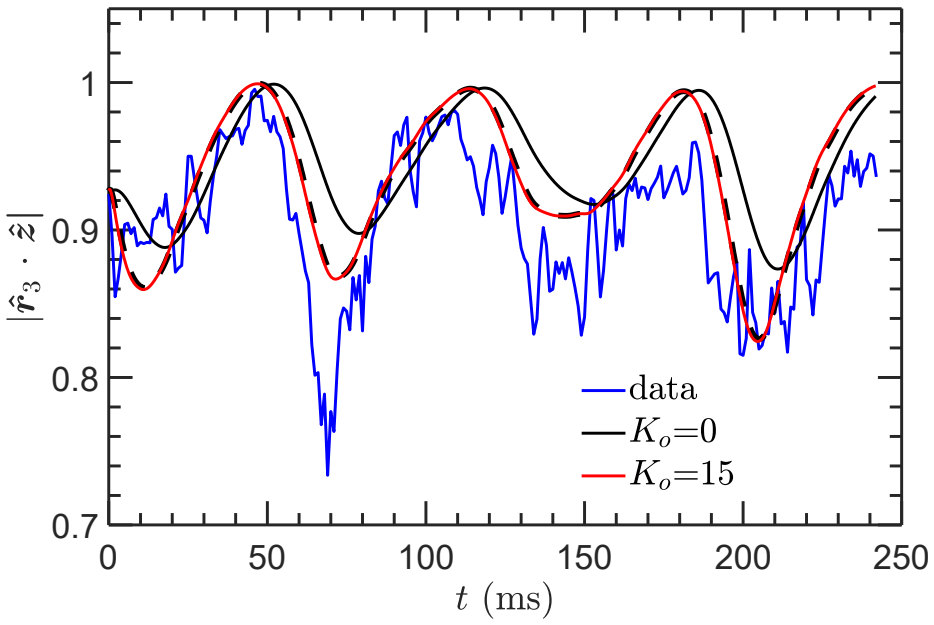

Figure 6.3: Time evolution of the cosine of the angle between the semi-minor axis of a bubble and the vertical direction $\hat{z}$, including the direct experimental measurements (blue) as well as the model predictions with $K_o = 0$ (black solid line), $K_o = 30$ (red solid line), and $f_2' = 0$ and $K_s = 0$ (rigid-particle limit, black dashed line).

an approximation and the actual bubble will always show some deviation.

In addition to the shape oscillation, decades of works have revealed the following essential picture of the dynamics of finite-sized air bubbles rising in purified water with no contaminants or surfactants. The bubble first rises along a straight line, followed by a zigzag motion and subsequent spiral circular motion. During this process, its orientation also oscillates along with its slip velocity. It has been shown by many previous works that the semi-minor axis of a bubble oscillates between 0° to 30° (Mougin and Magnaudet, 2001) with respect to the vertical direction. Such an oscillation arises from the wake dynamics (Ern et al., 2012; Mougin and Magnaudet, 2001; Tayler et al.,

2012; Mougin and Magnaudet, 2006). The wake vortices break and reform with reversed rotation near the inflection point of the zigzag motion (Mougin and Magnaudet, 2001), whereas the wake is continuously generataed during the spiral motion.

Figure 6.3 shows a time trace of the relative orientation between $\hat{\boldsymbol{r}}_3$ and the vertical direction $\hat{\boldsymbol{z}}$. The orientation oscillation can be clearly captured by the 3D shape reconstruction. The black line shows the prediction based on the modified MnM model with the addition of the pseudo-strain-rate term. It is clear that the modeled results seem to capture the orientation oscillation. But for each oscillation period, as the relative orientation reaches the peak and starts to drop, the predicted time trace consistently lags behind the experimental one. We found that the lag is linked to the fact that the predicted bubble semi-minor axis does not rotate away from the vertical axis as fast as the slip velocity does.

To illustrate the underlying mechanism, figure 6.4 shows a schematic of the possible processes of a bubble following the re-orientation of the slip velocity. In this case, the bubble is shown as an oblate spheroid geometry at t_0 as if it was compressed due to a slip velocity aligned with the vertical z axis prior to t_0. At t_0, $\boldsymbol{u}^s$ switches to a new direction along with the y axis. There are two possible ways that a bubble can adjust its orientation to the new $\boldsymbol{u}^s$. The first way is through deformation without changing the bubble axes. The pseudo-

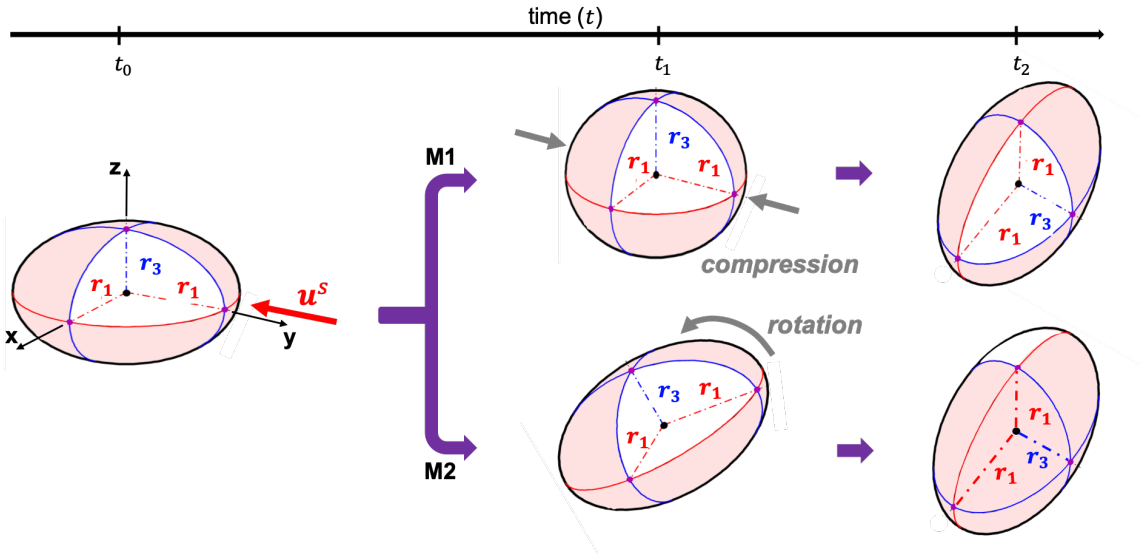

Figure 6.4: Schematic of two possible bubble-reorientation mechanisms as the slip velocity changes it direction, including (M1) deformation along a different direction, or (M2) simple rotation while maintaining the original geometry.

strain-rate in this case acts to first assist the restoring force to help the bubble to return back to a sphere and then continue compressing the bubble along the new $\boldsymbol{u}^s$ direction. In this case, the bubble axes did not change their orientations, only their lengths. But as a result, the semi-minor axis seems to switch from the z axis to the y axis.

Alternatively, bubble could simply rotate towards a new direction while maintaining its original oblate spheroidal geometry. The evidence to support such a mechanism can be drawn from decades of research on the path instability observed both for bubbles (Magnaudet and Eames, 2000; Mougin and Magnaudet, 2001, 2006) and rigid non-spherical particles rising/settling in an otherwise quiescent medium (Ern et al., 2012). It has been shown that rigid oblate

spheroidal particles can exhibit similar orientation oscillation as deformable bubbles (Mougin and Magnaudet, 2006; Fernandes et al., 2008; Cano-Lozano et al., 2016). This observation has led to a conclusion that the deformability effect is not important for path instability, and it also implies that the oscillation of the bubble orientation is likely connected to rotation rather than deformation. Following this argument, the pseudo-strain-rate term may not be enough to account for all effects introduced by the slip velocity because it does not contain an anti-symmetric component to describe the bubble rotation due to wake-bubble interaction.

The rigorous way of modelling this interaction and the resulting torque to rotate the bubble is through the Kevin-Kirchhoff equation (Kirchhoff, 1870; Mougin and Magnaudet, 2002):

$$(m\mathbb{I} + \mathbb{A}) \cdot \frac{\mathrm{d}\boldsymbol{u^s}}{\mathrm{d}t} + m\boldsymbol{\omega} \times \boldsymbol{u^s} = \boldsymbol{F} + (m - \rho_c V)\boldsymbol{g} \tag{6.5}$$

$$(\mathbb{J} + \mathbb{D}) \cdot \frac{\mathrm{d}\boldsymbol{\omega}}{\mathrm{d}t} + \boldsymbol{\omega} \times (\mathbb{J} \cdot \boldsymbol{\omega}) = \boldsymbol{\Gamma} \tag{6.6}$$

where $\boldsymbol{u^s}$ and $\boldsymbol{\omega}$ indicate body translational and rotational velocities with their main axes aligning with the principal axes of the body. To be consistent with the rest of the paper, the translational velocity is denoted the same as the slip velocity since the background flow velocity is close to zero. $\mathbb{A}$ and

$\mathbb{D}$ are the translational and rotational added-mass tensors, respectively. For bubbles with negligible inertia, both mass m and inertial tensor $\mathbb{J}$ should be close to zero. $\boldsymbol{F}$ and Γ are the instantaneous hydrodynamic force and torque obtained by integrating local stresses and moments over the bubble interface. There have been many attempts to solve the Kevin-Kirchhoff equations by coupling them with the Navier-Stokes equation (Mougin and Magnaudet, 2002), potential flow approximation (Fernandes et al., 2008), and subcritical bifurcation model of the lateral lift force (Shew and Pinton, 2006). Through these models and simplifications, the importance of the wake dynamics as well as the added mass effects have been established. Note that, in this framework, bubbles are considered as rigid spheroids without the deformation oscillation, which suggests that the deformation and orientation oscillation can be separately modelled.

Therefore, to model the orientation oscillation, a new pseudo-rotation tensor Ω'_{ij} is introduced to characterize the bubble rotation induced by the wake dynamics:

$$\Omega'_{ij} = -\frac{1}{2}\epsilon_{ijk}\omega'_k \tag{6.7}$$

where $\boldsymbol{\omega}'$ is the pseudo-vorticity vector. This equation connects to the Kevin-Kirchhoff equation (6.6) based on the relationship between vorticity and the object angular velocity: $\boldsymbol{\omega}' = 2\boldsymbol{\omega}$. Although it may appear that $\boldsymbol{\omega}'$ is readily

available after solving equation 6.5 and equation 6.6 together, the inputs to these equations, i.e. $\boldsymbol{F}$ and $\boldsymbol{\Gamma}$, can only be acquired by integrating hydrodynamic forces over the entire bubble interface, which requires having access to the entire flow field nearby a bubble. Since the goal of the proposed framework is to model the bubble dynamics based on simplified flow information, we cannot rely on the Kevin-Kirchhoff equation directly, at least not in its complete form without a simple but realistic model for $\boldsymbol{F}$ and $\boldsymbol{\Gamma}$. In the current framework, we turn to a simple experimental observation that $\hat{\boldsymbol{r}}_3$ always tries to align with the direction of $\boldsymbol{u}_i^s$, which is consistent with what has also been reported in previous works (Mougin and Magnaudet, 2001). Based on this observation, we propose that $\omega_i' = \phi\epsilon_{ijk}(\hat{r}_3)_j\hat{u}_k^s$ with a magnitude of $|\boldsymbol{\omega'}| = \phi$. The variable ϕ is the angle between two unit vectors: $\hat{\boldsymbol{r}}_3$ and $\hat{\boldsymbol{u}}^s$. This pseudo-vorticity vector $\boldsymbol{\omega}'$ points at a direction that is perpendicular to both $\hat{\boldsymbol{r}}_3$ and $\hat{\boldsymbol{u}}^s$. ϵ_{ijk} is the Levi-Civita tensor. In this way, $\boldsymbol{\omega}'$ is designed such that the pseudo-rotation tensor Ω_{ij}' rotates the semi-minor axis of the bubble towards the direction of the slip velocity at a rate linearly proportional to ϕ.

Finally, adding both the pseudo-strain-rate (S_{ij}') and pseudo-rotation (Ω_{ij}') terms to equation 6.3 leads to a new model (Finite-sized bubble deformation model, or FBD model hereafter) to describe the affine deformation of finite-sized bubbles in both linear flows and turbulence.

$$\frac{dP_{ij}}{dt} = \widetilde{\Omega}_{ik}P_{kj} - P_{ik}\widetilde{\Omega}_{kj} + f_2'(\widetilde{S}_{ik}P_{kj} + P_{ik}\widetilde{S}_{kj}) - \frac{f_1'}{\tau_n}(P_{ij} - g(\mathbf{II}_P, \mathbf{III}_P)\delta_{ij}) + K_o(\Omega_{ik}'P_{kj} - P_{ik}\Omega_{kj}') + K_s(S_{ik}'P_{kj} + P_{ik}S_{kj}') \quad (6.8)$$

The coefficients K_o and K_s are constants that set the relative roles played by these two new terms, respectively. These two new coefficients have to be constrained through comprehensive experimental results that will be introduced in §6.3.1. Here, to demonstrate that they can capture the observed oscillations for bubbles rising in an otherwise quiescent medium, we fix them at $K_s = 0.14$ and $K_o = 15$.

The red line in figure 6.3 shows the predicted relative orientation of the semi-minor axis of the bubble, which seems to agree with the measured results better than the black line obtained using the pseudo-strain-rate term alone, capturing not only the overall trend but also the shape of each peak. In addition, the lag between the blue line and black line at the trailing edge of each peak is reduced by the addition of the pseudo-rotation term.

Furthermore, in order to ensure that the model can reproduce the key observation that the bubble deformation does not affect the orientation oscillation, we performed another test of the model by setting $f_2' = 0$ and $K_s = 0$, which essentially forces the bubble to retain its initial geometry throughout the en-

tire time trace without any deformation. The results are shown as the black dashed line in figure 6.3. The line falls right on top of the red line, suggesting that the orientation oscillation can be reproduced even for rigid particles without deformation.

Similar tests were also performed to repeat the calculation of the shape oscillation in figure 6.2(b) for cases with or without the pseudo-rotation term. The results are almost identical, suggesting that the deformation dynamics is mostly dominated by the pseudo-strain-rate term. Combining this test with the previous one on the deformation oscillation, we conclude that both the pseudo-rotation and pseudo-strain-rate terms are important to characterize the bubble deformation and orientation in flows, and their coefficients, i.e. K_o and K_s, can be separately evaluated based on the deformation oscillation and orientation oscillation. In addition, FBD model, in its essence, is a first-order linear model that cannot capture the free oscillation of a bubble. The emergence of the oscillation in both deformation and orientation dynamics arises from the oscillation in the slip velocity due to the path instability.

6.3 Results and Discussion

In equation 6.8, there are four dimensionless coefficients: f_1', f_2', K_o, and K_s. Other than f_1' for the relaxation term, each driving mechanism has a coefficient

that needs to be determined from experimental results. The advantage of our experimental results is that we have a rather unique dataset with simultaneous measurements of the two phases. P_{ij} can be either determined from the 3D bubble shape reconstruction or from the integration of the FBD model based on the flow information. Since the measurements of these two phases are independent, the comparison between them will provide a way to constrain these coefficients and validate our model. In this section, we intend to link different coefficients to different statistics so we can constrain them one by one to avoid multi-variable fitting.

6.3.1 Quiescent rising

The time traces of both bubble geometry and orientation have already been used in the previous section to introduce the additional terms. It is clear that the new model works well for this configuration. In this section, the focus is shifted to the discussion of different coefficients. Special attention has to be paid to two new coefficients f_1' and f_2' that replace $f_1(\mu)$ and $f_2(\mu)$ in the MnM model. $f_1(\mu)$ and $f_2(\mu)$ were introduced as non-dimensional and non-negative terms that quantify the relative roles played by the relaxation and shear stresses in linear shear flows, both of which are related to the viscosity ratio μ. For finite-sized bubbles in turbulence, the capillary number is negligible and the turbulence Weber number becomes large so bubbles are deformed

by inertial forces. In this case, the gradient of the dynamic pressure is more important than shear stresses. Therefore, the flow viscosity becomes secondary, and $f_1(\mu)$ and $f_2(\mu)$ are replaced with f_1' and f_2', both of which are independent of the viscosity ratio.

Note that $f_1(\mu)$ enters the MnM model along with the relaxation timescale τ, which is also a function of μ. For the same aforementioned reason, τ should not depend on μ for finite-sized bubbles. Therefore, the relaxation frequency $f_1(\mu)/\tau$ is replaced with the natural frequency of a bubble, which is $1/\tau_n = \sqrt{(96\sigma)/(\rho_c D^3)}/2\pi$ based on Lamb's mode 2 frequency. Following this argument, f_1' should be of order unity and τ_n should follow the $2\pi/\sqrt{(96\sigma)/(\rho_c D^3)}$ for all cases discussed in this paper. For convenience, f_1' is fixed at one.

Once f_1' is fixed, the two remaining coefficients are K_s and K_o that are related to the pseudo-strain-rate and pseudo-rotation terms, respectively. As we have shown before in figure 6.2 and 6.3, not all statistics depend on both coefficients at the same time: the deformation oscillation is not sensitive to K_o, whereas the orientation oscillation does not have to rely on K_s.

The symbols in figure 6.5 show the probability distribution function (PDF) of the bubble aspect ratio $\alpha = r_1/r_3$ from our experiments, i.e. $p(\alpha_e)$. In this particular case, the bubble size D is around 2.5 mm. The majority of bubbles have small aspect ratios, but the tail of $p(\alpha_e)$ extends to a large α close to 3. In addition to $p(\alpha_e)$, the distribution of α can also be determined by integrating

the FBD model ($p(\alpha_m)$) using equation 6.8 with a selected K_s. For each bubble trajectory, the initial condition of P_{ij} is set the same as the oblate fit of the bubble 3D reconstructed geometry; P_{ij} for the rest of the trajectory is numerically integrated based on the time trace of the slip velocity.

A non-linear search for K_s was performed to minimize the difference between the two PDFs: $p(\alpha_m)$ and $p(\alpha_e)$. From this search, $K_s = 0.14$ was obtained, which is similar to the result if we minimize the difference between α_m and α_e for all bubble trajectories directly. The final PDF of α calculated from the FBD model using $K_s = 0.14$ is shown as the red line in figure 6.5. With only one fitting parameter, $p(\alpha_m)$ agrees well with the directly-measured PDF. In particular, $p(\alpha_m)$ captures the long right tail for large α and a steep drop for small α close to one nicely. The fact that these two PDFs agree with each other suggests that the model captures the essential physics of the deformation dynamics.

The average α calculated from both PDFs only differ by 3.5%. This small difference comes from the lower left tail from the model prediction. This difference can also be seen in the example track shown in figure. 6.2. The predicted track seems to have a larger amplitude because the modeled oscillation can reach a lower valley for both r_1 and r_3 compared with the experimental results.

Such a difference may potentially be attributed to the experimental uncertainty of the 3D shape reconstruction, which has been discussed systematically

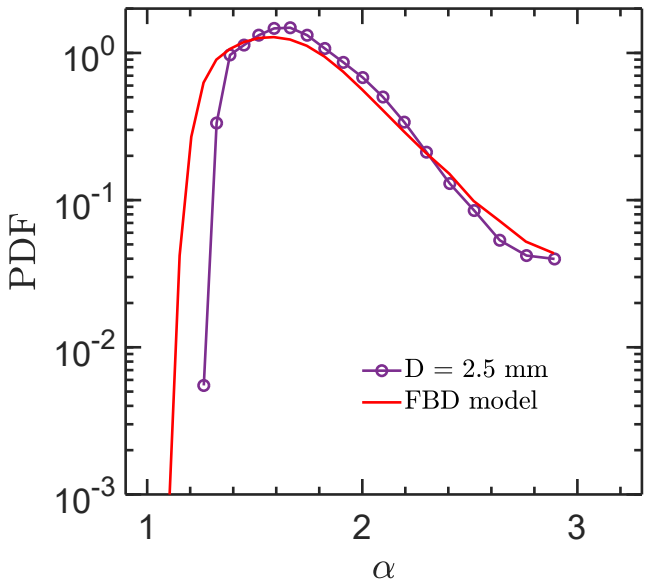

Figure 6.5: The probability density distribution of aspect ratio α for bubbles with diameter of D =2–3 mm rising in an otherwise quiescent medium, including direct measurements (open circles) and model predictions (red solid line).

in another paper (Masuk et al., 2019). The key point is that the uncertainty is larger when the shape is close to a sphere because any reconstruction artifacts could result in an overestimation of α. In other words, we have more confidence in large α than those close to one. So when we fit K_s, more weight was put on the right tail of α than the left.

Once K_s and f_1' are fixed, the only remaining coefficient for the quiescent rising case is K_o, which can be constrained by the bubble orientation. Note that the distribution of the alignment between $\hat{r_3}$ and $\hat{z}$ is very close to one. As shown in figure 6.3, the oscillation of $|\hat{r_3} \cdot \hat{z}|$ is from 0.8 to 1. So rather than fitting K_o based on the PDF, we directly fit K_o based on all the instantaneous trajectories, which are all quite similar to what has been shown in figure 6.3

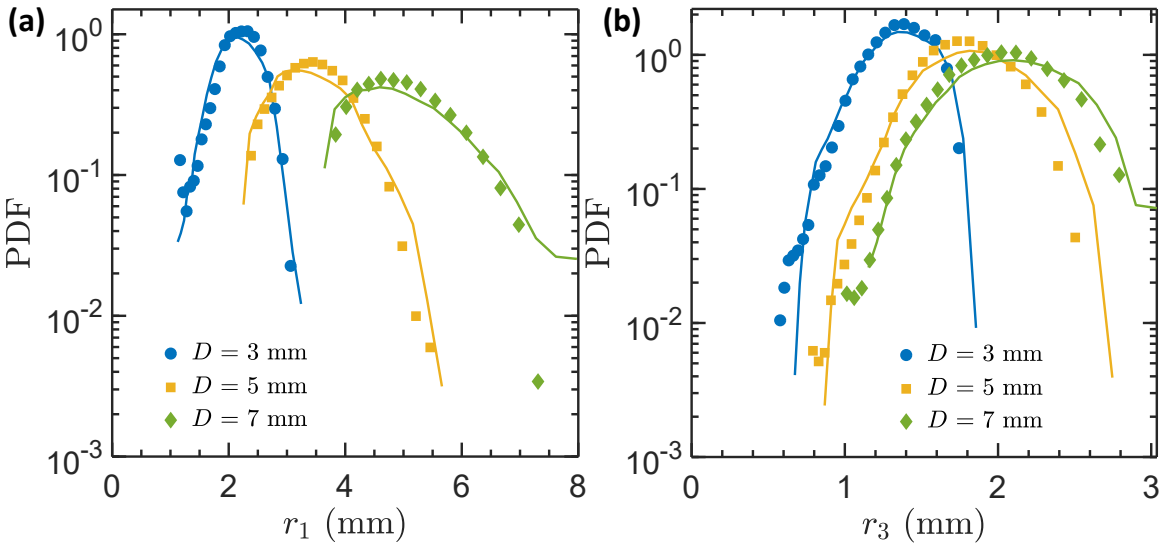

Figure 6.6: The probability density distributions of (a) the semi-major axis (r_1) and (b) the semi-minor axis (r_3) of bubbles with three different sizes from $D =$ 2–4 mm to $D =$ 6–8 mm in turbulence. Symbols show experimental results and solid lines with the same color indicate the corresponding model predictions.

because bubbles rising in a quiescent medium are very reproducible. This fit yields K_o = 15.

6.3.2 Turbulence

We assume that the three coefficients: f_1', K_o, and K_s, determined from the quiescent case, can be directly applied to describe the bubble deformation in turbulence because the key underlying physics that bubbles are deformed by the competition between the gradient of the dynamic pressure across the interface and the restoring stress due to the surface tension does not change for bubbles moving in either a quiescent or a turbulent medium.

The key differences between the quiescent and the turbulent cases include:

(i) the slip velocity comes not only from buoyancy but also from the random fluctuations of the surrounding turbulent flows; (ii) the local velocity gradients are not zero and has to be measured along with the bubble trajectory. Their contributions to the bubble deformation introduce the additional coefficient f_2'. In our experiments, both the slip velocity and the local coarse-grained velocity gradient can be measured accurately. More details can be found in a recent paper by Masuk, Salibindla, and Ni (2020b). Here, the same dataset is used for evaluating the new model.

In order to constrain f_2', the statistics of the measured bubble 3D shape is used. In particular, figure 6.6(a) and (b) present the PDFs of the semi-major and semi-minor axes for a range of bubble sizes (D= 3 – 7 mm), respectively. For both cases, symbols represent the measured results, whereas the solid lines of the same color show the model predictions by integrating equation 6.8 using the slip velocity and velocity gradients along the bubble trajectories.

As D grows, the PDFs of both r_1 and r_3 shift monotonically rightward. At the same time, the PDF becomes wider because the distribution of the Weber numbers based on the slip velocity and velocity gradients expand (this result has been shown elsewhere by Masuk, Salibindla, and Ni (ibid.)), which indicates that large bubbles are more susceptible to stronger deformation. It can be seen that both features can be successfully captured by the new FBD model almost perfectly.

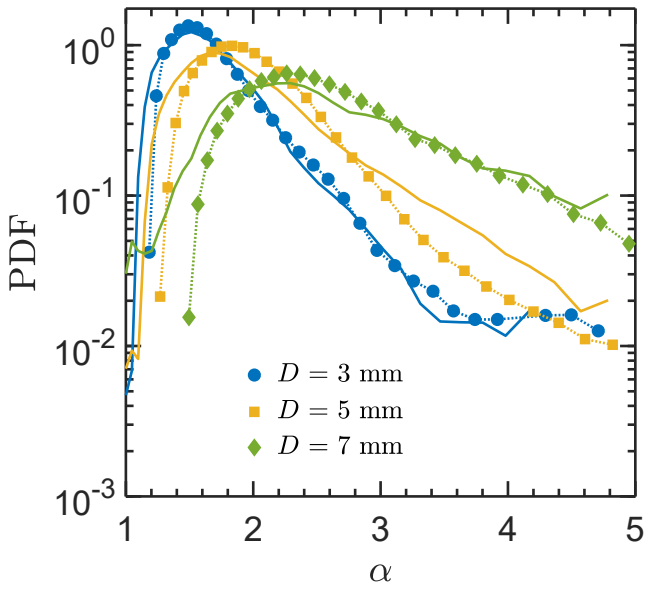

Figure 6.7: The probability density distribution of aspect ratio α of bubbles with different sizes in turbulence. Symbols show experimental results, and solid lines with the same color indicate the model predictions.

Note that the overall shape of the PDF is controlled by both the slip velocity and velocity gradients. But the role played by the slip velocity, controlled by K_s, has already been fixed at 0.14 based on the discussions in §6.3.1 so the only unknown here is f_2' that controls the contribution of the turbulent strain rate. When f_2' increases, the PDF becomes wider and the peak shifts towards right. To some degree, f_2' is overconstrained because only one parameter is needed to capture two features (peak location and width) of the distribution of r_1 and r_3 for a range of bubble sizes. In practice, the optimization was performed for r_1 of one size at $D = 3$ mm, from which $f_2' = 0.5$ was obtained. In figure 6.6, it is evident that, although f_2' is fitted based on one size, it helps to match the PDFs of both r_1 and r_3 for all three sizes, which confirms that the model provides an

excellent prediction of the bubble geometry with a range of sizes.

Further tests are performed to reproduce the aspect ratio $\alpha = r_1/r_3$. The distribution of α for three different sizes of bubbles are shown in figure 6.7. The shape and overall changes of PDF as a function of D are similar to the discussions for r_1 and r_3. For the smallest size of bubble (D = 3 mm), the model prediction seems to agree with the measured PDF of α very well because this is the size that we used to fit f_2'. For D = 5 mm and D = 7 mm, the agreement is still very good, capturing the overall trend, including the steep drop at small α and long tail at large α. But a small deviation can be seen: the peak location shifts towards smaller α and the long right tail seems to drop at a slower rate as α increases. This small difference can be attributed to two reasons: (i) the definition of α; the reconstructed 3D surface consists of many vertices. r_1 and r_3, from the experiments, are defined as the longest and shortest center-to-vertex distances. For experimental results that also contain non-affine bubble deformation, $\hat{\boldsymbol{r}}_1$ and $\hat{\boldsymbol{r}}_3$ do not have to be perpendicular to each other. But in the model prediction, the bubble shape is assumed to follow the ellipsoidal shape. α is calculated as the ratio between the semi-major and semi-minor axes of the ellipsoid that are always perpendicular to each other. For bubbles deforming in turbulence, any concave areas on the bubble interface could result in a smaller semi-minor axis and thus a large aspect ratio. Such a process can never be captured by the model which consequently results in an underprediction of

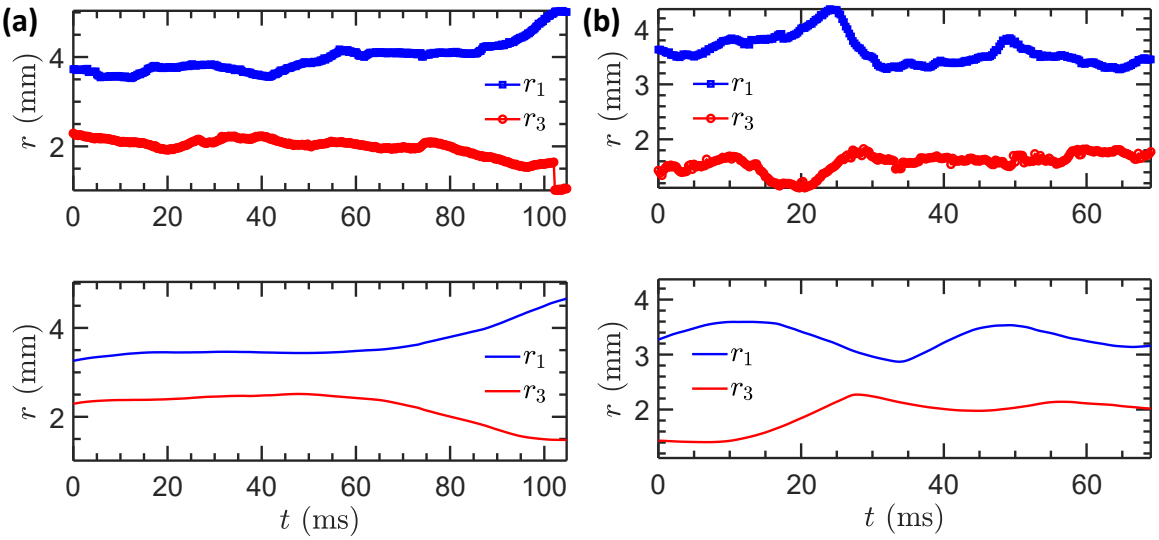

Figure 6.8: Two example time traces of the semi-major (r_1) and semi-minor (r_3) axes of bubbles deforming in intense turbulence, with both directly measured results (top panels) and model predictions (bottom panels).

α. (ii) Nonlinear deformation contributed by eddies with size smaller than the bubble size; This effect was not accounted for in the linear FBD model (equation 6.8). But for the Weber number range considered in this paper, the linear model works almost perfectly, indicating this non-linear deformation is probably small for the range of Weber numbers and bubble sizes considered.

In addition to distributions, in figure 6.8, two example time traces of both experimental measurements and model predictions for semi-axes of two different bubbles deforming in turbulence are shown. Top two panels show the experimental measurements of r_1 and r_3, whereas the bottom panels show the corresponding model prediction. It is evident that the model manages to predict the overall trend of the temporal fluctuations of the bubble deformation for both cases. It is important to admit that not all measured time traces of r_1

and r_3 agree with their calculated counterparts. Even for the two cases shown in figure 6.8, although the model captures the overall trend, it clearly misses the small-scale fluctuations, which are likely driven by eddies smaller than the bubble size. In addition, the measured peaks of r_1 seem to lag behind the calculated results. This phase lag is expected. In the FBD model, the bubble response frequency is fixed at its natural frequency obtained by assuming small-amplitude oscillation. Although it provides a good overall estimation, it does not necessarily work well for large-amplitude deformation that is likely to be non-linear. As a result, one can see phase lags between the measured and calculated r_1. Ideally, τ_n in the FBD model should also be a function of $\alpha(t)$. For simplicity, this more-complicated correction is not modeled in the current framework.

Once all four coefficients f_1', f_2', K_o, and K_s are fixed, we can evaluate the performance of the FBD model in predicting the bubble orientational dynamics. Given that the bubble deformation is controlled both by the slip velocity and the velocity gradients, the bubble orientation is shown as the cosine of the angle (W) between the bubble semi-minor axis ($\hat{\boldsymbol{r}}_3$) either with $\hat{\boldsymbol{u}}^s$ (figure 6.9(a)) or with one of the eigenvectors of the coarse-grained velocity gradients, i.e $\hat{\boldsymbol{e}}_3$ (figure 6.9(b)) . If the bubble orientation is completely random, the PDF of W should follow a uniform distribution at one for the entire range of W. If the distribution peaks at one, it indicates that $\hat{\boldsymbol{r}}_3$ preferentially aligns with that

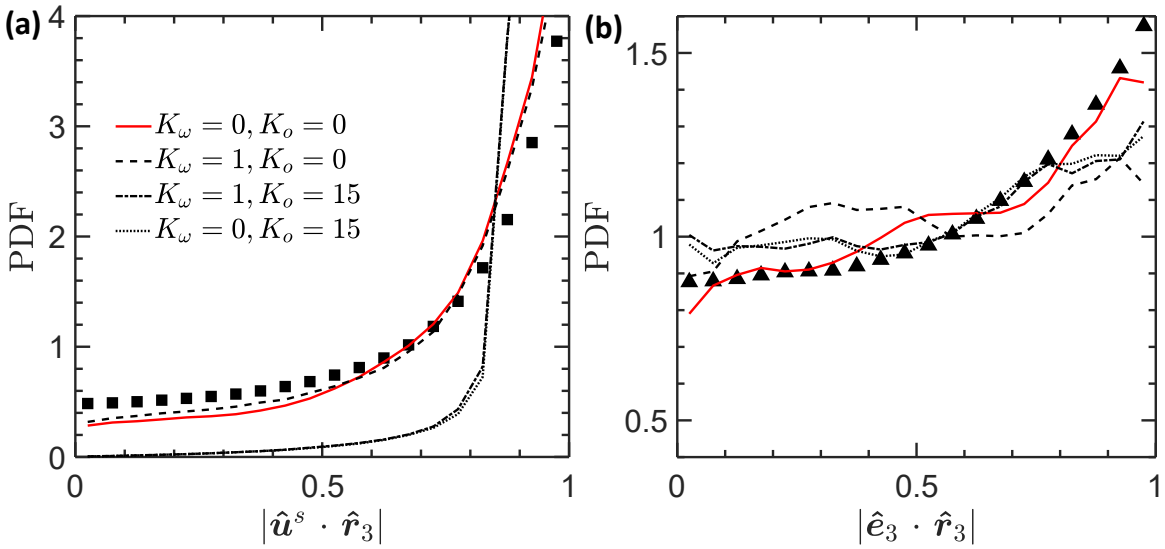

Figure 6.9: The probability density distribution of the alignment between (a) the bubble semi-minor axis ($\hat{r}_3$) and the slip velocity ($\hat{u}^s$), (b) the bubble semi-minor axis ($\hat{r}_3$) and the compression ($\hat{e}_3$) directions of their surrounding coarse-grained strain-rate tensor. Symbols show directly-measured results, and the lines indicate the model prediction using different combinations of coefficients.

vector. In figure 6.9(a), it is evident that $\hat{r}_3$ shows the strongest alignment with the slip velocity. In figure 6.9(b), the preferential orientation of $\hat{r}_3$ with $\hat{e}_3$ confirms that bubbles are compressed along $\hat{e}_3$ and therefore aligns its semi-minor axis $\hat{r}_3$ with it.

In addition to the measured distribution, we also integrate the FBD model (equation 6.8) to obtain the PDFs of the alignment using the slip velocity and velocity gradients along the bubble trajectories as inputs. Since all coefficients have already been determined from other tests, we start by calculating the bubble orientation by using the same set of coefficients ($f_1' = 1$, $f_2' = 0.5$, $K_s = 0.14$, $K_o = 15$) similar to the deformation dynamics. The resulting orientation is shown as dash-dotted line in figure 6.9(a) and (b). Although the relative

orientation between $\hat{\boldsymbol{r}}_3$ with $\hat{e}_3$ in (b) seems to reproduce a similar trend to the measured results, the model-predicted $\hat{\boldsymbol{r}}_3$ shows a much stronger alignment with $\boldsymbol{u}^s$.

We realize that the strong alignment between $\hat{\boldsymbol{r}}_3$ and $\boldsymbol{u}^s$ is contributed by the fact that the coefficient for the pseudo-rotation term (K_o) is too large, which essentially forces $\hat{\boldsymbol{r}}_3$ to always immediately adjust to the direction of the new $\boldsymbol{u}^s$ at every time step. The fact that K_o may be smaller in turbulence than that in a quiescent medium is not surprising because the pseudo-rotation term is linked to the wake-induced bubble rotation. For a bubble rising in water at rest, there is a persistent wake formed behind the bubble. In this case, K_o is large and the pseudo-rotation term is important. In turbulence, particularly in intense turbulence with a large energy dissipation rate, the wake, even it forms, may not sustain long enough behind the bubble before it is perturbed by the pre-existing background turbulence. Therefore, it is possible that the importance of the pseudo-rotation term becomes smaller in intense turbulence. To test this conjecture, we calculate the bubble orientation by setting $K_o = 0$ (dashed line), and the results become very close to the measured alignment between $\hat{\boldsymbol{r}}_3$ and $\boldsymbol{u}^s$.

But even the wake effect becomes smaller, it should still exist for finite-sized bubbles with large enough slip velocity. The fact that setting $K_o = 0$ does not affect the bubble orientation suggests that the reorientation of bubbles in

turbulence may not be driven by rotation at all, and it is the deformation that controls the bubble orientation (M1 rather than M2 in figure 6.4). Continuing this logic leads to the next argument: If the bubble rotation is not important, we hypothesize that even the flow vorticity from the ambient turbulence does not play an role. Note that the coarse-grained rotation term ($\widetilde{\Omega}_{ij}$) does not have a coefficient based on the original MnM model. Here, to quantify its importance, we introduce a new coefficient K_ω, which is supposed to be one for the FBD model. Here, to test the hypothesis of bubble rotation, K_ω is also set as zero. The result is shown as the red solid line in both figures. Consistent with our expectation, removing the contribution of both rotational terms provides the best prediction of bubble orientation, which implies that the bubble reorientation in turbulence is mostly due to deformation along another direction rather than rotating to a new direction. This is distinct from, nearly opposite to, the bubble reorientation in a quiescent medium, where the wake-induced rotation could be as important, if not more.

6.3.3 Possible extensions to finite-sized droplets in turbulence

As we have shown in the previous two sections, the FBD model captures the deformation and orientation dynamics of deformable bubbles in both a quiescent and a turbulent medium. The advantage of this model is that it can de-

scribe the dynamics of finite-sized bubbles with significant density mismatch from surrounding flows. But if the inner fluid is changed from gas to other liquids, e.g. light oil, will this model still work? Since we do not have experimental data on oil deformation in turbulence yet, it is difficult to draw a conclusion now. In this section, we will try to provide some suggestions to the possible extension of the FBD model for finite-sized droplets with different density and viscosity.

First of all, it is safe to assume that the contributions from both the velocity gradients and the slip velocity will probably remain the same even for finite-sized drops. Following this argument, we expect that the flow strain rate and rotation terms will stay as they are for drops. Since the dimensionless coefficients measure the driving forces, they may also remain the same as no changes have been made to the carrier phase. Given the similarities between the flow strain rate and the pseudo-strain-rate, the dimensionless coefficients in front of the pseudo-strain-rate term will also stay the same.

The only force that will be modified when we change the inner fluid to oil or other liquids is the relaxation term. This leads naturally to the discussion of the natural frequency of droplets that undergo small oscillations about the spherical form. The natural frequency does not depend on the dissipative term, implying that the viscosity ratio will not enter the equation even if the inner fluid viscosity becomes significantly higher than that of air. Nevertheless, the

density of the fluid will become important because the general formulation for the natural frequency of a sphere of liquid of density ρ_d surrounded by an infinite mass of other liquid of density ρ_c can be written as:

$$(2\pi/\tau_n)^2 = 8n(n+1)(n-1)(n+2)\frac{\sigma}{[(n+1)\rho_d + n\rho_c]\, D^3} \tag{6.9}$$

As one can see, this general formulation is a function of the density of both phases, ρ_c and ρ_d. For bubbles, one can assume $\rho_d \approx 0$, the equation is then simplified as $\tau_n = 2\pi/\sqrt{(96\sigma)/(\rho_c D^3)}$, which recovers the formulation used in the FBD model. For other liquids, we can simply use the full equation $\tau_n = 2\pi/\sqrt{(192\sigma)/[(3\rho_d + 2\rho_c)D^3)}$.

6.4 Conclusion

This work focuses on developing a model capable of capturing the key deformation and orientation dynamics of finite-sized bubbles in both a quiescent and a turbulent medium. The model takes simplified surrounding flow information as inputs and outputs the bubble geometry and orientation. Such a model can only be developed from and evaluated by experiments that have access to both the flow information and the bubble geometry simultaneously in 3D and in both a quiescent and a turbulent medium.

Such a simultaneous measurement was made possible through our experi-

mental effort. Six high-speed cameras were used to reconstruct the 3D shape of bubbles with their surrounding 3D tracer particle trajectories in a vertical water tunnel, which creates intense turbulence with a large energy dissipation rate to deform finite-sized bubbles. In this facility, it has been recently found that the deformation of finite-sized bubbles are mainly governed by two key mechanisms: (i) local velocity gradients, and (ii) the slip velocity between a bubble and the carrier phase.

Based on the observation, a new finite-sized bubble deformation model is proposed in this work. The FBD model is a linear phenomenological model that aims to capture the affine deformation of bubbles in both a quiescent and a turbulent medium. The FBD model builds upon a model developed for describing the deformation of neutrally-buoyant drops in viscous shear flows by Maffettone and Minale (1998), which was limited to small sub-Kolmogorov-scale drops. The FBD model makes a few additions: (i) extending from small drops to finite-sized bubbles by replacing the local velocity gradients with the velocity gradients coarse-grained at the bubble size; (ii) accounting for the bubble deformation responding to the local slip velocity by using the a pseudo-strain-rate tensor; (iii) modeling the wake-induced bubble rotation by adding the a pseudo-rotation tensor.

In order to test the performance of the FBD model, the time series of the coarse-grained velocity gradient and the slip velocity from the direct experi-

mental measurements, following each bubble trajectory, in both a quiescent and a turbulent medium are input into the model. The output from the model is the time evolution of the bubble geometry and orientation, which can also be directly and independently measured from the 3D bubble shape reconstruction. The difference between the calculated and measured geometries and orientations provides a unique way of calibrating and validating the proposed FBD model.

In the FBD model, there are four new coefficients. The coefficient for bubble relaxation can be fixed based on the bubble natural frequency. The remaining three coefficients can be isolated and calibrated by connecting each one of them to an individual statistics. In particular, the coefficients associated with the pseudo-strain-rate, pseudo-rotation, and flow strain rate can be constrained based on the bubble deformation in quiescent water, bubble orientation in quiescent water, and bubble deformation in turbulence, respectively. Finally, from the statistics of the bubble orientation, we determine that both the flow rotation and the pseudo-rotation terms are negligible in controlling the bubble orientation in turbulence because, in strong turbulence, the rotation of bubble is driven by the deformation from another direction due to the re-orientation of the strain rate and slip velocity rather than from rotation. Finally, by appropriately adjusting the fluid properties, we propose possible extensions of the FBD model to describe the deformation dynamics of finite-sized drops in turbulence.

Chapter 7

Summary and Future Work

7.1 Summary

Considering numerous applications in both natural and industrial multiphase flows, as mentioned in section 1.1 of Chapter 1, the physical understanding on the mechanisms of turbulence induced deformation and breakup of bubbles are of great interest. Such knowledge are crucial in developing high fidelity physics based phenomenological models for the interaction between different phases in turbulent multiphase flows as direct numerical simulations of such flows are not always very feasible.

In this dissertation, we have presented our experimental investigation on the bubble dynamics in a strong turbulent flow. One of the major challenges in such experimental investigations is that, owing to large density difference between bubbles and water, the buoyancy induced bubble deformation can be very

large. In natural and industrial turbulent multiphase flow turbulence is much stronger than buoyancy however it is non-trivial to create such strong turbulent flows in a laboratory scale. Consequently, often the experimental studies on bubbles in turbulence the bubble dynamics is dominated by the buoyancy forces rather than the forces induced by turbulence. Seeking inspiration from these challenges we designed and built a new vertical water tunnel, V-ONSET, that can generate very strong homogeneous and isotropic turbulence with an energy dissipation rate of $O(0.1)$ m^2/s^3. This ensures that the finite-size bubbles in the tunnel experience significant deformation due to turbulent stresses. These bubble are injected into the tunnel test section using hypodermic needles and a controlled air flow. The tunnel also facilitates non-invasive simultaneous optical measurements of both bubbles and the turbulent carrier phase using six high-speed cameras with high spatio-temporal resolution in 3D. The spatial resolution of measurement is close to Kolmogorov length scale η and the temporal resolution is about 10 times faster than the Kolmogorov time scale τ_η. The turbulent flows generated in V-ONSET exhibit excellent homogeneity and isotropy as discussed in (Masuk et al., 2019) and in chapter 1.

The images obtained with the high-speed cameras of V-ONSET contains bubble shadows as well as the shadows of the 50 μm size density matched tracer particles added to visualize the carrier turbulent phase. Digital image processing was used to separate tracer particles and bubbles in these images

which were then fed into separate codes for 3D reconstruction of both phases. The Lagrangian trajectories of the tracer particles are reconstructed in 3D using an in-house particle tracking code based on the Shake-The-Box algorithm (Tan et al., 2020). From these trajectories flow characteristics of the turbulent water phase such as velocity, acceleration, and coarse-grained velocity gradient surrounding a bubble were calculated. On the other hand, a new algorithm based on the visual hull reconstruction technique in computer vision was developed to obtain the 3D geometries of the bubbles in our experiments. In this new algorithm called the virtual-camera method, additional physical constrain of surface tension was introduced to minimize reconstruction uncertainty. The center of mass of these 3D reconstructed bubbles were then tracked over time. Velocity and acceleration of the bubbles could then be calculated from these bubble trajectories. The detail of the new algorithm, its performance, and uncertainty quantification has been discussed in detain in chapter 3.

The simultaneous 3D measurements of bubbles and their surrounding turbulent flow provided us with unique experimental data to investigate the mechanisms responsible for bubble deformation and breakup in a homogeneous isotropic turbulent flow (chapter 4). To quantify the mechanism of turbulent velocity gradient we calculated a Weber number based on the eigenvalues of coarse-grained turbulent velocity gradient We_{vg}. The distribution of We_{vg} was also modeled with the log-normal distribution of the energy dissipation rate ϵ

which showed excellent agreement with the measured We_{vg} distribution. Another equally important mechanism for bubble deformation in turbulence is the slip velocity between the two phases due to the bubble finite-size effect and the density difference between bubbles and the carrier water phase. Therefore, we defined another Weber number based on the slip velocity We_{slip} and showed that the distribution of We_{slip} is comparable with the distribution of We_{vg} further affirming the importance of slip velocity in bubble deformation in turbulence. We found out that the experimentally measured distribution of the slip velocity could be fitted with a stretch exponential function which eventually allowed us to connect the distribution of We_{slip} to the mean energy dissipation rate $\langle\epsilon\rangle$, and the bubble size D. Based on the modeled distributions of We_{vg}, and We_{slip} the distribution of bubble deformation defined by aspect ratio α was also predicted, which agreed very well with the experimental measurements. Finally in chapter 4, we evaluated the breakup probability of bubbles in turbulence based on $\langle\epsilon\rangle$ and the modeled distributions of We_{vg}, and We_{slip}. Moreover, we provided a functional form for such breakup probability which is a function of the mean Weber number $\langle We\rangle$ and any chosen value for the critical Weber number We_{crit}. Traditionally, the breakup probability of bubbles are considered to precipitously change from zero to one across a We_{crit} like a step function; the model for breakup probability presented in this works help to smoothen this transition near the Hinze scale.

Complementary to identifying and evaluating different mechanism that control bubble dynamics in turbulent, another important question is that how are the bubbles oriented in a turbulent flow with respect to the turbulent flow structures; because, the orientation of bubble in the flow essentially regulates different forces that they are subject to. From our unique experimental measurements we studied such orientation dynamics of bubbles in turbulence with respect to the representative direction of the aforementioned deformation mechanisms. In particular, as discussed in chapter 5, we investigated the alignment of the directions of semi-major ($\hat{\boldsymbol{r}}_1$) and semi-minor ($\hat{\boldsymbol{r}}_3$) axes of bubbles along with the eigenvectors of coarse-grained velocity gradient (maximum stretching: $\hat{e}_1$, and maximum compression: $\hat{e}_3$), and the direction of slip velocity ($\hat{\boldsymbol{u}}_{slip}$). To discuss the orientation dynamics of bubbles, we divided bubble deformation into two groups (i) mild-deformation in which case bubbles deform in the turbulent flow but do not experience breakup; (ii) strong-deformation where the bubbles eventually breakup in turbulence. We found that for mild-deformation cases the strongest alignment was exhibited between $\hat{\boldsymbol{r}}_3$ and $\hat{\boldsymbol{u}}_{slip}$ while $\hat{\boldsymbol{r}}_1$, and $\hat{\boldsymbol{r}}_3$ also aligns with $\hat{e}_1$, and $\hat{e}_3$, respectively. This suggests that in turbulence the slip velocity mechanism predominantly compresses and deforms the bubbles which could also weaken the alignment between bubble semi-axes and the eigenvectors of coarse-grained velocity gradient. Such orientation of bubbles in turbulence is very different as compared to the orien-

tation of neutrally-buoyant sub-Kolmogorov-scale material elements with no surface tension or slip velocity indicating an important role played by the surface tension induced restoration stress and slip velocity on bubble orientation dynamics in homogeneous isotropic turbulence. The orientation of bubbles in turbulence evolves as they approach a breakup event. The alignment between $\hat{\boldsymbol{r}}_1$ and $\hat{\boldsymbol{e}}_1$ was observed to get stronger close to a breakup event which resulted in more effective deformation by the coarse-grained velocity gradient. Interestingly, close to a breakup event the alignment between bubble semi-major axis $\hat{\boldsymbol{r}}_1$ and the slip velocity direction $\hat{\boldsymbol{u}}_{slip}$ switches to be aligned with each other from being perpendicular to each other which occurs due to possible switch in roles of the slip velocity from being a deformation-driving mechanism to being an outcome owing to the sudden increase in deformation induced bubble velocity.

Finally, in chapter 6, we present a 3D phenomenological model (FBD model) capable of capturing the key deformation characteristics in homogeneous isotropic turbulence. As the goal of this model is to predict the affine deformation of bubbles in turbulence, the bubble shape is assumed to be an ellipsoid which is defined by a symmetric positive-definite second-order tensor in our model. The model predicts the time evolution of the shape of a bubble taking inputs from both the aforementioned deformation mechanisms of coarse-grained velocity gradient and the slip velocity. In order to test the performance of this model

as well as to determine the values for the coefficient in the model we took advantage of our unique simultaneous experimental measurements of bubble geometry and the surrounding turbulent flow. The measurements of the coarse-grained velocity gradient and the slip velocity obtained by following a bubble in our experiment was fed into the model to predict the shape evolution of the bubble. By repeating the process for many bubble from our experiments using V-ONSET, statistics of the model prediction such as distributions of the bubble semi-axes, and aspect ratio was obtained which exhibited an excellent agreement with our experimental measurement given the simplicity of the model. A few cases of the model prediction for the temporal evolution of bubble semi-axes was also compared with our experimental measurements to demonstrate that even temporally the model could capture some key features of bubble deformation in turbulence.

7.2 Future work

Turbulence and multiphase flows have been studied for over a century at this point; however, owing to their inherent complexity, vastness, and applications in technological advancement there are still numerous open questions in these subjects. Our understanding has advanced significantly but, there is still more to learn. Specially, the dynamics of finite-size buoyant deformable parti-

cles in a background turbulent flow i.e. bubbles in turbulence is a topic that we started to learn about very recently about three decades or so. Also, this might be the most complicated form of multiphase flow that consists of large density and viscosity ratios, deformability, surface tension, complex anisotropic shapes, and additional length and time scales in an already multi-scale problem of turbulence. Each of these characteristics add more complexity to the problem. The framework presented in this dissertation to study the one-to-one interaction between bubbles and turbulence through simultaneous measurements contain excellent potential to advance our fundamental understanding on the physics of in this subject. These types of frameworks should be extended in terms of experimental apparatus, measurement techniques, and of course regarding thoughtful data analysis to complement the process of understanding turbulent multiphase flows. Some of these certainly need long time, process and effort to improve on. However, obviously there are still a lot of questions that can be investigated with our current capabilities and data. For instance, the data obtained from V-ONSET can be used to explores topics such as (i) particle pair dispersion in turbulence which is crucial to advance our understanding on the numerous oceanic, atmospheric, as well as industrial turbulent mixing process; (ii) pair dispersion of similar size bubbles, bubbles of different sizes are also imperative in the aforementioned turbulent mixing processes; (iii) daughter bubble size distribution in violent turbulent breakup that is relevant to heat

and mass transfer in various industrial reactor as well as in ocean-atmosphere gas exchange; and (iv) bubble-induced turbulence modulation, a topic that has been studied rather extensively. However, our understanding on the fundamentals of the process still needs a lot more studies. These are only a few of many possible future work directions that my colleagues in the Fluid Transport Lab are working on. With more advanced measurement techniques and specially designed experiments for turbulent multiphase flows in the future, the opportunities are endless.

References

Deane, Grant B and M Dale Stokes (2002). “Scale dependence of bubble creation mechanisms in breaking waves”. In: *Nature* 418.6900, pp. 839–844.

Wanninkhof, Rik and Wade R McGillis (1999). “A cubic relationship between air-sea CO2 exchange and wind speed”. In: *Geophysical Research Letters* 26.13, pp. 1889–1892.

Wilson, L (1976). “Explosive volcanic eruptions—III. Plinian eruption columns”. In: *Geophysical Journal International* 45.3, pp. 543–556.

JDoorschot, Judith J, Michael Lehning, and Anouck Vrouwe (2004). “Field measurements of snow-drift threshold and mass fluxes, and related model simulations”. In: *Boundary-Layer Meteorology* 113.3, pp. 347–368.

Lu, Hua and Yaping Shao (2001). “Toward quantitative prediction of dust storms: an integrated wind erosion modelling system and its applications”. In: *Environmental Modelling & Software* 16.3, pp. 233–249.

REFERENCES

Bourouiba, Lydia, Eline Dehandschoewercker, and John WM Bush (2014). "Violent expiratory events: on coughing and sneezing". In: *Journal of Fluid Mechanics* 745, pp. 537–563.

Kantarci, Nigar, Fahir Borak, and Kutlu O Ulgen (2005). "Bubble column reactors". In: *Process Biochemistry* 40.7, pp. 2263–2283.

Minale, Mario (2010). "Models for the deformation of a single ellipsoidal drop: a review". In: *Rheologica acta* 49.8, pp. 789–806.

Maffettone, PL and Mario Minale (1998). "Equation of change for ellipsoidal drops in viscous flow". In: *Journal of Non-Newtonian Fluid Mechanics* 78.2-3, pp. 227–241.

Degaleesan, S, M Dudukovic, and Y Pan (2001). "Experimental study of gas-induced liquid-flow structures in bubble columns". In: *AIChE journal* 47.9, pp. 1913–1931.

Afshar Ghotli, Reza, Abdul AA Raman, Shaliza Ibrahim, and Saeid Baroutian (2013). "Liquid-liquid mixing in stirred vessels: a review". In: *Chemical Engineering Communications* 200.5, pp. 595–627.

Foka, M, J Chaouki, C Guy, and D Klvana (1996). "Gas phase hydrodynamics of a gas-solid turbulent fluidized bed reactor". In: *Chemical Engineering Science* 51.5, pp. 713–723.

Ishii, Mamoru and Takashi Hibiki (2010). *Thermo-fluid dynamics of two-phase flow*. Springer Science & Business Media.

REFERENCES

Balachandar, S and John K Eaton (2010). “Turbulent dispersed multiphase flow”. In: *Annual Review of Fluid Mechanics* 42, pp. 111–133.

Elghobashi, Said (2019). “Direct numerical simulation of turbulent flows laden with droplets or bubbles”. In: *Annual Review of Fluid Mechanics* 51, pp. 217–244.

Tennekes, Hendrik and John Leask Lumley (1972). *A first course in turbulence*. MIT press.

Pope, Stephen B (2000). *Turbulent flows*. Cambridge university press.

Kundu, Pijush K and Ira M Cohen (2008). *Fluid Mechanics 4th*.

Richardson, Lewis Fry (1922). *Weather prediction by numerical process*. Cambridge university press.

Ishii, Mamoru (1975). “Thermo-fluid dynamic theory of two-phase flow”. In: *STIA* 75, p. 29657.

Voth, Greg A and Alfredo Soldati (2017). “Anisotropic particles in turbulence”. In: *Annual Review of Fluid Mechanics* 49, pp. 249–276.

Elghobashi, S (1991). “Particle-laden turbulent flows: direct simulation and closure models”. In: *Applied Scientific Research* 48.3-4, pp. 301–314.

Unverdi, Salih Ozen and Grétar Tryggvason (1992). “A front-tracking method for viscous, incompressible, multi-fluid flows”. In:

Tryggvason, Grétar, Bernard Bunner, Asghar Esmaeeli, Damir Juric, N Al-Rawahi, W Tauber, J Han, S Nas, and Y-J Jan (2001). “A front-tracking

method for the computations of multiphase flow". In: *Journal of computational physics* 169.2, pp. 708–759.

Scardovelli, Ruben and Stéphane Zaleski (1999). "Direct numerical simulation of free-surface and interfacial flow". In: *Annual review of fluid mechanics* 31.1, pp. 567–603.

Dodd, Michael S and Antonino Ferrante (2016). "On the interaction of Taylor length scale size droplets and isotropic turbulence". In: *Journal of Fluid Mechanics* 806, pp. 356–412.

Sussman, Mark, Peter Smereka, and Stanley Osher (1994). "A level set approach for computing solutions to incompressible two-phase flow". In: *Journal of Computational physics* 114.1, pp. 146–159.

Osher, Stanley and Ronald P Fedkiw (2001). "Level set methods: an overview and some recent results". In: *Journal of Computational physics* 169.2, pp. 463–502.

Enwald, Hans, Eric Peirano, and A-E Almstedt (1996). "Eulerian two-phase flow theory applied to fluidization". In: *International Journal of Multiphase Flow* 22, pp. 21–66.

Fox, Rodney O (2012). "Large-eddy-simulation tools for multiphase flows". In: *Annual Review of Fluid Mechanics* 44, pp. 47–76.

Chen, Shiyi and Gary D Doolen (1998). "Lattice Boltzmann method for fluid flows". In: *Annual review of fluid mechanics* 30.1, pp. 329–364.

REFERENCES

Manninen, Mikko, Veikko Taivassalo, Sirpa Kallio, et al. (1996). *On the mixture model for multiphase flow*.

Delhaye, Jean-Marc (1974). “Jump conditions and entropy sources in two-phase systems. Local instant formulation”. In: *International Journal of Multiphase Flow* 1.3, pp. 395–409.

Delhaye, Jean-Marc, Michel Giot, and ML Riethmuller (1981). *Thermohydraulics of two-phase systems for industrial design and nuclear engineering*. Hemisphere Pub.

Boure, JA and JM Delhaye (1982). *General equations and two-phase flow modeling*.

Chang, Yu-Chung, TY Hou, B Merriman, and Stanley Osher (1996). “A level set formulation of Eulerian interface capturing methods for incompressible fluid flows”. In: *Journal of computational Physics* 124.2, pp. 449–464.

Nobari, MR, Y-J Jan, and G Tryggvason (1996). “Head-on collision of drops—A numerical investigation”. In: *Physics of Fluids (1994-present)* 8.1, pp. 29–42.

Lapin, A and A Lübbert (1994). “Numerical simulation of the dynamics of two-phase gas—liquid flows in bubble columns”. In: *Chemical Engineering Science* 49.21, pp. 3661–3674.

Sokolichin, A and G Eigenberger (1994). “Gas - liquid flow in bubble columns and loop reactors: Part I. Detailed modelling and numerical simulation”. In: *Chemical Engineering Science* 49.24, pp. 5735–5746.

REFERENCES

Jakobsen, Hugo A, Bente H Sannæs, Sverre Grevskott, and Hallvard F Svendsen (1997). “Modeling of vertical bubble-driven flows”. In: *Industrial & Engineering Chemistry Research* 36.10, pp. 4052–4074.

Johansen, ST (1990). “On the Modelling of Disperse Two Phase Flows. Dr. Techn”. PhD thesis. Thesis, NTH, Trondheim.

Squires, Kyle D and John K Eaton (1991). “Preferential concentration of particles by turbulence”. In: *Physics of Fluids A: Fluid Dynamics* 3.5, pp. 1169–1178.

Biferale, Luca, Charles Meneveau, and Roberto Verzicco (2014). “Deformation statistics of sub-Kolmogorov-scale ellipsoidal neutrally buoyant drops in isotropic turbulence”. In: *Journal of fluid mechanics* 754, pp. 184–207.

Spandan, Vamsi, Detlef Lohse, and Roberto Verzicco (2016). “Deformation and orientation statistics of neutrally buoyant sub-Kolmogorov ellipsoidal droplets in turbulent Taylor–Couette flow”. In: *Journal of fluid mechanics* 809, pp. 480–501.

Mathai, Varghese, Detlef Lohse, and Chao Sun (2020b). “Bubbly and Buoyant Particle–Laden Turbulent Flows”. In: *Annual Review of Condensed Matter Physics* 11, pp. 529–559.

Lohse, Detlef (2018). “Bubble puzzles: From fundamentals to applications”. In: *Physical review fluids* 3.11, p. 110504.

REFERENCES

Lance, M and J Bataille (1991). “Turbulence in the liquid phase of a uniform bubbly air–water flow”. In: *Journal of Fluid Mechanics* 222, pp. 95–118.

Kurian, Thomas and Jens HM Fransson (2009). “Grid-generated turbulence revisited”. In: *Fluid dynamics research* 41.2, p. 021403.

Poorte, REG and A Biesheuvel (2002). “Experiments on the motion of gas bubbles in turbulence generated by an active grid”. In: *Journal of Fluid Mechanics* 461, p. 127.

Rensen, Judith, Stefan Luther, and Detlef Lohse (2005). “The effect of bubbles on developed turbulence”. In: *Journal of Fluid Mechanics* 538.1, pp. 153–187.

Goepfert, Charles, Jean-Louis Marié, Delphine Chareyron, and Michel Lance (2010). “Characterization of a system generating a homogeneous isotropic turbulence field by free synthetic jets”. In: *Experiments in fluids* 48.5, pp. 809–822.

Zimmermann, Robert, Haitao Xu, Yoann Gasteuil, Mickaël Bourgoin, Romain Volk, Jean-François Pinton, Eberhard Bodenschatz, and International Collaboration for Turbulence Research (2010). “The Lagrangian exploration module: An apparatus for the study of statistically homogeneous and isotropic turbulence”. In: *Review of Scientific Instruments* 81.5, p. 055112.

Bellani, Gabriele and Evan A Variano (2014). “Homogeneity and isotropy in a laboratory turbulent flow”. In: *Experiments in fluids* 55.1, pp. 1–12.

REFERENCES

Variano, Evan A, Eberhard Bodenschatz, and Edwin A Cowen (2004). “A random synthetic jet array driven turbulence tank”. In: *Experiments in fluids* 37.4, pp. 613–615.

Loewenberg, M (1993). “Stokes resistance, added mass, and Basset force for arbitrarily oriented, finite-length cylinders”. In: *Physics of Fluids A: Fluid Dynamics (1989-1993)* 5.3, pp. 765–767.

Albråten, Per J (1981). *Two-phase Flow Dynamics in ECC*. Tech. rep. Chalmers Tekniska Hoegskola.

Risso, Frédéric (2018). “Agitation, mixing, and transfers induced by bubbles”. In: *Annual Review of Fluid Mechanics* 50, pp. 25–48.

Prakash, Vivek N, J Martínez Mercado, Leen van Wijngaarden, Ernesto Mancilla, Yoshiyuki Tagawa, Detlef Lohse, and Chao Sun (2016). “Energy spectra in turbulent bubbly flows”. In: *Journal of fluid mechanics* 791, pp. 174–190.

Kolmogorov, AN (1949). “On the breakage of drops in a turbulent flow”. In: *Dokl. Akad. Navk. SSSR*. Vol. 66. 5, pp. 825–828.

Hinze, JO (1955). “Fundamentals of the hydrodynamic mechanism of splitting in dispersion processes”. In: *AIChE Journal* 1.3, pp. 289–295.

Sevik, M and SH Park (1973). “The splitting of drops and bubbles by turbulent fluid flow”. In:

Prince, Michael J and Harvey W Blanch (1990). “Bubble coalescence and break-up in air-sparged bubble columns”. In: *AIChE Journal* 36.10, pp. 1485–1499.

Martínez-Bazán, Carlos (1999). “On the breakup of an air bubble injected into a fully developed turbulent flow. Part 1. Breakup frequency”. In: *Journal of Fluid Mechanics* 401, pp. 157–182.

Risso, Frédéric and Jean Fabre (1998). “Oscillations and breakup of a bubble immersed in a turbulent field”. In: *Journal of Fluid Mechanics* 372, pp. 323–355.

Ravelet, Florent, Catherine Colin, and Frédéric Risso (2011). “On the dynamics and breakup of a bubble rising in a turbulent flow”. In: *Physics of Fluids* 23.10, p. 103301.

König, Franziska, El-Sayed Zanoun, Emir Öngüner, and Christoph Egbers (2014). “The CoLaPipe—the new Cottbus large pipe test facility at Brandenburg University of Technology Cottbus-Senftenberg”. In: *Review of Scientific Instruments* 85.7, p. 075115.

La Porta, Arthur, Greg A Voth, Alice M Crawford, Jim Alexander, and Eberhard Bodenschatz (2001). “Fluid particle accelerations in fully developed turbulence”. In: *Nature* 409.6823, p. 1017.

Gils, Dennis PM van, Gert-Wim Bruggert, Daniel P Lathrop, Chao Sun, and Detlef Lohse (2011). “The Twente turbulent Taylor–Couette (T^3C) facility:

strongly turbulent (multiphase) flow between two independently rotating cylinders". In: *Review of scientific instruments* 82.2, p. 025105.

Lathrop, Daniel P, Jay Fineberg, and Harry L Swinney (1992). "Turbulent flow between concentric rotating cylinders at large Reynolds number". In: *Physical review letters* 68.10, p. 1515.

Ravelet, Florent, Rene Delfos, and Jerry Westerweel (2010). "Influence of global rotation and Reynolds number on the large-scale features of a turbulent Taylor–Couette flow". In: *Physics of Fluids* 22.5, p. 055103.

Hultmark, Marcus, Margit Vallikivi, SCC Bailey, and AJ Smits (2012). "Turbulent pipe flow at extreme Reynolds numbers". In: *Physical review letters* 108.9, p. 094501.

Bodenschatz, Eberhard, Gregory P Bewley, Holger Nobach, Michael Sinhuber, and Haitao Xu (2014). "Variable density turbulence tunnel facility". In: *Review of Scientific Instruments* 85.9, p. 093908.

King, Eric M and Jonathan M Aurnou (2013). "Turbulent convection in liquid metal with and without rotation". In: *Proceedings of the National Academy of Sciences*, p. 201217553.

White, Christopher M, Adonios N Karpetis, and Katepalli R Sreenivasan (2002). "High-Reynolds-number turbulence in small apparatus: grid turbulence in cryogenic liquids". In: *Journal of Fluid Mechanics* 452, pp. 189–197.

REFERENCES

Kolmogorov, Andrei N (1941). “The local structure of turbulence in incompressible viscous fluid for very large Reynolds numbers”. In: *Dokl. Akad. Nauk SSSR*. Vol. 30. 4. JSTOR, pp. 301–305.

Maaß, Sebastian, Florian Metz, Torsten Rehm, and Matthias Kraume (2010). “Prediction of drop sizes for liquid–liquid systems in stirred slim reactors, Part I: Single stage impellers”. In: *Chemical Engineering Journal* 162.2, pp. 792–801.

Zhou, Genwen and Suzanne M Kresta (1996). “Impact of tank geometry on the maximum turbulence energy dissipation rate for impellers”. In: *AIChE journal* 42.9, pp. 2476–2490.

Mercado, Julian Martinez, Vivek N Prakash, Yoshiyuki Tagawa, Chao Sun, Detlef Lohse, and (International Collaboration for Turbulence Research) (2012). “Lagrangian statistics of light particles in turbulence”. In: *Physics of fluids* 24.5, p. 055106.

Gils, Dennis PM van, Daniela Narezo Guzman, Chao Sun, and Detlef Lohse (2013). “The importance of bubble deformability for strong drag reduction in bubbly turbulent Taylor–Couette flow”. In: *Journal of fluid mechanics* 722, pp. 317–347.

Ezeta, Rodrigo, Sander G Huisman, Chao Sun, and Detlef Lohse (2018). “Turbulence strength in ultimate Taylor–Couette turbulence”. In: *Journal of fluid mechanics* 836, pp. 397–412.

REFERENCES

De Silva, IPD and HJS Fernando (1994). “Oscillating grids as a source of nearly isotropic turbulence”. In: *Physics of Fluids* 6.7, pp. 2455–2464.

Villermaux, E, B Sixou, and Y Gagne (1995). “Intense vortical structures in grid-generated turbulence”. In: *Physics of fluids* 7.8, pp. 2008–2013.

Srdic, A, HJS Fernando, and L Montenegro (1996). “Generation of nearly isotropic turbulence using two oscillating grids”. In: *Experiments in Fluids* 20.5, pp. 395–397.

Birouk, Madjid, Brahim Sarh, and Iskender Gökalp (2003). “An attempt to realize experimental isotropic turbulence at low Reynolds number”. In: *Flow, turbulence and combustion* 70.1-4, pp. 325–348.

Hwang, W and JK Eaton (2004). “Creating homogeneous and isotropic turbulence without a mean flow”. In: *Experiments in Fluids* 36.3, pp. 444–454.

Carter, Douglas, Alec Petersen, Omid Amili, and Filippo Coletti (2016). “Generating and controlling homogeneous air turbulence using random jet arrays”. In: *Experiments in Fluids* 57.12, p. 189.

Oguz, Hasan N and Andrea Prosperetti (1993). “Dynamics of bubble growth and detachment from a needle”. In: *Journal of Fluid Mechanics* 257, pp. 111–145.

Wu, Mingming and Morteza Gharib (2002). “Experimental studies on the shape and path of small air bubbles rising in clean water”. In: *Physics of fluids* 14.7, pp. L49–L52.

REFERENCES

Talaia, Mário AR (2007). “Terminal velocity of a bubble rise in a liquid column”. In: *World Academy of Science, Engineering and Technology* 28, pp. 264–268.

Ern, Patricia, Frédéric Risso, David Fabre, and Jacques Magnaudet (2012). “Wake-induced oscillatory paths of bodies freely rising or falling in fluids”. In: *Annual Review of Fluid Mechanics* 44, pp. 97–121.

Variano, Evan A and Edwin A Cowen (2008). “A random-jet-stirred turbulence tank”. In: *Journal of Fluid Mechanics* 604, pp. 1–32.

Smith, Barton L and Ari Glezer (1998). “The formation and evolution of synthetic jets”. In: *Physics of fluids* 10.9, pp. 2281–2297.

Glezer, Ari and Michael Amitay (2002). “Synthetic jets”. In: *Annual review of fluid mechanics* 34.1, pp. 503–529.

Malmstr oem, Tor G, Allan T Kirkpatrick, Brian Christensen, and Kevin D Knappmiller (1997). “Centreline velocity decay measurements in low-velocity axisymmetric jets”. In: *Journal of Fluid mechanics* 346, pp. 363–377.

Martínez-Bazán, Carlos, JL Montanes, and Juan C Lasheras (1999). “On the breakup of an air bubble injected into a fully developed turbulent flow. Part 1. Breakup frequency”. In: *Journal of Fluid Mechanics* 401, pp. 157–182.

Hak, Mohamed Gad-el and Stanley Corrsin (1974). “Measurements of the nearly isotropic turbulence behind a uniform jet grid”. In: *Journal of Fluid Mechanics* 62.1, pp. 115–143.

REFERENCES

Jordt, Anne, Claudius Zelenka, Jens Schneider von Deimling, Reinhard Koch, and Kevin Köser (2015). “The Bubble Box: Towards an Automated Visual Sensor for 3D Analysis and Characterization of Marine Gas Release Sites”. In: *Sensors* 15.12, pp. 30716–30735.

Ni, Rui, Stefan Kramel, Nicholas T Ouellette, and Greg A Voth (2015). “Measurements of the coupling between the tumbling of rods and the velocity gradient tensor in turbulence”. In: *Journal of Fluid Mechanics* 766, pp. 202–225.

Raffel, Markus, Christian E Willert, Fulvio Scarano, Christian J Kähler, Steve T Wereley, and Jürgen Kompenhans (2018). *Particle image velocimetry: a practical guide*. Springer.

Lindken, R and W Merzkirch (2000). “Velocity measurements of liquid and gaseous phase for a system of bubbles rising in water”. In: *Experiments in fluids* 29.1, S194–S201.

Lindken, R and W Merzkirch (2002). “A novel PIV technique for measurements in multiphase flows and its application to two-phase bubbly flows”. In: *Experiments in fluids* 33.6, pp. 814–825.

Tan, S., A. Salibindla, A. U. M. Masuk, and R. Ni (2019a). “An open-source Shake-the-Box method and its performance evaluation”. In: *13th International Symposium on Particle Image Velocimetry*.

REFERENCES

Ni, Rui, Shi-Di Huang, and Ke-Qing Xia (2011). “Local energy dissipation rate balances local heat flux in the center of turbulent thermal convection”. In: *Physical review letters* 107.17, p. 174503.

De Karman, Theodore and Leslie Howarth (1938). “On the statistical theory of isotropic turbulence”. In: *Proceedings of the Royal Society of London. Series A-Mathematical and Physical Sciences* 164.917, pp. 192–215.

Ni, Rui, Nicholas T Ouellette, and Greg A Voth (2014). “Alignment of vorticity and rods with Lagrangian fluid stretching in turbulence”. In: *Journal of Fluid Mechanics* 743, R3.

White, BR (1982). “Two-phase measurements of saltating turbulent boundary layer flow”. In: *International Journal of Multiphase Flow* 8.5, pp. 459–473.

Woolf, DAVID K (1997). “Bubbles and their role in gas exchange”. In: *The sea surface and global change*.

Sun, Xiaodong, Todd R Smith, Seungjin Kim, Mamoru Ishii, and Jennifer Uhle (2002). “Interfacial area of bubbly flow in a relatively large diameter pipe”. In: *Experimental thermal and fluid science* 27.1, pp. 97–109.

Galindo, Enrique, Andrzej W Pacek, and Alvin W Nienow (2000). “Study of drop and bubble sizes in a simulated mycelial fermentation broth of up to four phases”. In: *Biotechnology and bioengineering* 69.2, pp. 213–221.

REFERENCES

Besagni, Giorgio and Fabio Inzoli (2016). “Bubble size distributions and shapes in annular gap bubble column”. In: *Experimental Thermal and Fluid Science* 74, pp. 27–48.

Giovannettone, JP, E Tsai, and John S Gulliver (2009). “Gas void ratio and bubble diameter inside a deep airlift reactor”. In: *Chemical Engineering Journal* 149.1-3, pp. 301–310.

Maldonado, M, JJ Quinn, CO Gomez, and JA Finch (2013). “An experimental study examining the relationship between bubble shape and rise velocity”. In: *Chemical Engineering Science* 98, pp. 7–11.

Fujiwara, A, Y Danmoto, Koichi Hishida, and Masanobu Maeda (2004). “Bubble deformation and flow structure measured by double shadow images and PIV/LIF”. In: *Experiments in fluids* 36.1, pp. 157–165.

Honkanen, M (2009). “Reconstruction of three-dimensional bubble surface from high-speed orthogonal imaging of dilute bubbly flow”. In: *Proceedings of computational methods in multiphase flow V, New Forest, UK*, pp. 469–480.

Fu, Yucheng and Yang Liu (2018). “3D bubble reconstruction using multiple cameras and space carving method”. In: *Measurement Science and Technology* 29.7, p. 075206.

Mulayim, Adem Yasar, Ulas Yilmaz, and Volkan Atalay (2003). “Silhouette-based 3-D model reconstruction from multiple images”. In: *IEEE Transac-*

tions on Systems, Man, and Cybernetics, Part B (Cybernetics) 33.4, pp. 582–591.

Matusik, Wojciech, Chris Buehler, Ramesh Raskar, Steven J Gortler, and Leonard McMillan (2000). "Image-based visual hulls". In: *Proceedings of the 27th annual conference on Computer graphics and interactive techniques*. ACM Press/Addison-Wesley Publishing Co., pp. 369–374.

Laurentini, A. (1994). "The visual hull concept for silhouette-based image understanding". In: *IEEE Transactions on Pattern Analysis and Machine Intelligence* 16.2, pp. 150–162. ISSN: 01628828.

Kutulakos, Kiriakos N and Steven M Seitz (2000). "A theory of shape by space carving". In: *International journal of computer vision* 38.3, pp. 199–218.

Sidky, Emil Y and Xiaochuan Pan (2008). "Image reconstruction in circular cone-beam computed tomography by constrained, total-variation minimization". In: *Physics in Medicine & Biology* 53.17, p. 4777.

Medoff, Barry P, William R Brody, Menahem Nassi, and Albert Macovski (1983). "Iterative convolution backprojection algorithms for image reconstruction from limited data". In: *JOSA* 73.11, pp. 1493–1500.

Sidky, Emil Y, Chien-Min Kao, and Xiaochuan Pan (2006). "Accurate image reconstruction from few-views and limited-angle data in divergent-beam CT". In: *Journal of X-ray Science and Technology* 14.2, pp. 119–139.

REFERENCES

Rau, Matthew J, Pavlos P Vlachos, and Suresh V Garimella (2016). “A tomographic-PIV investigation of vapor-induced flow structures in confined jet impingement boiling”. In: *International Journal of Multiphase Flow* 84, pp. 86–97.

Adhikari, D and EK Longmire (2012). “Visual hull method for tomographic PIV measurement of flow around moving objects”. In: *Experiments in fluids* 53.4, pp. 943–964.

Ristroph, Leif, Gordon J Berman, Attila J Bergou, Z Jane Wang, and Itai Cohen (2009). “Automated hull reconstruction motion tracking (HRMT) applied to sideways maneuvers of free-flying insects”. In: *Journal of Experimental Biology* 212.9, pp. 1324–1335.

Isidoro, John and Stan Sclaroff (2003). “Stochastic Refinement of the Visual Hull to Satisfy Photometric and Silhouette Consistency Constraints.” In: *ICCV*. Vol. 3, p. 1335.

Furukawa, Yasutaka and Jean Ponce (2009). “Carved visual hulls for image-based modeling”. In: *International Journal of Computer Vision* 81.1, pp. 53–67.

Kanatani, Ken-ichi and Tsai-Chia Chou (1989). “Shape from texture: General principle”. In: *Artificial Intelligence* 38.1, pp. 1–48.

Ouellette, Nicholas T, Haitao Xu, and Eberhard Bodenschatz (2006). “A quantitative study of three-dimensional Lagrangian particle tracking algorithms”. In: *Experiments in Fluids* 40.2, pp. 301–313.

Ni, Rui, Shi-Di Huang, and Ke-Qing Xia (2012). “Lagrangian acceleration measurements in convective thermal turbulence”. In: *Journal of Fluid Mechanics* 692, pp. 395–419.

Tsai, Roger Y (1986). “An efficient and accurate camera calibration technique for 3D machine vision”. In: *Proc. of Comp. Vis. Patt. Recog.*, pp. 364–374.

Wieneke, B (2008). “Volume self-calibration for 3D particle image velocimetry”. In: *Experiments in fluids* 45.4, pp. 549–556.

Lu, Jiacai and Gretar Tryggvason (2008). “Effect of bubble deformability in turbulent bubbly upflow in a vertical channel”. In: *Physics of Fluids (1994-present)* 20.4, p. 040701.

Fu, Yucheng and Yang Liu (2016). “Development of a robust image processing technique for bubbly flow measurement in a narrow rectangular channel”. In: *International Journal of Multiphase Flow* 84, pp. 217–228.

Jakobsen, Hugo A (2014). *Chemical reactor modeling*. Springer.

Kawase, Y and M Moo-Young (1990). “Mathematical models for design of bioreactors: Applications of: Kolmogoroff’s theory of isotropic turbulence”. In: *The Chemical Engineering Journal* 43.1, B19–B41.

Liss, Peter S and Liliane Merlivat (1986). “Air-sea gas exchange rates: Introduction and synthesis”. In: *The role of air-sea exchange in geochemical cycling*. Springer, pp. 113–127.

Verschoof, Ruben A, Roeland CA Van Der Veen, Chao Sun, and Detlef Lohse (2016). “Bubble drag reduction requires large bubbles”. In: *Physical review letters* 117.10, p. 104502.

Lu, JC, A Fernandez, and G Tryggvason (2005). “Drag reduction in a turbulent channel due to bubble injection”. In: *Phys. Fluids* 17, p. 095102.

Dabiri, Sadegh, Jiacai Lu, and Gretar Tryggvason (2013). “Transition between regimes of a vertical channel bubbly upflow due to bubble deformability”. In: *Physics of Fluids* 25.10, p. 102110.

Clay, PH (1940). “The mechanism of emulsion formation in turbulent flow”. In: *Proceedings of the Section of Sciences* 43, pp. 852–965.

Lamb, H. (1932). *Hydrodynamics*. Dover Books on Physics. Dover publications. ISBN: 9780486602561. URL: https://books.google.com/books?id=237xDg7T0RkC.

Hesketh, Robert P, Arthur W Etchells, and TW Fraser Russell (1991). “Experimental observations of bubble breakage in turbulent flow”. In: *Industrial & Engineering Chemistry Research* 30.5, pp. 835–841.

Vejražka, Jiří, Mária Zedníková, and Petr Stanovskỳ (2018). “Experiments on breakup of bubbles in a turbulent flow”. In: *AIChE Journal* 64.2, pp. 740–757.

REFERENCES

Hulburt, Ho M and Stanley Katz (1964). “Some problems in particle technology: A statistical mechanical formulation”. In: *Chemical engineering science* 19.8, pp. 555–574.

Ramkrishna, Doraiswami (2000). *Population balances: Theory and applications to particulate systems in engineering*. Elsevier.

Villermaux, Emmanuel and Benjamin Bossa (2009). “Single-drop fragmentation determines size distribution of raindrops”. In: *Nature Physics* 5.9, pp. 697–702.

Ng, C-L, R Sankarakrishnan, and KA Sallam (2008). “Bag breakup of nonturbulent liquid jets in crossflow”. In: *International Journal of Multiphase Flow* 34.3, pp. 241–259.

Tan, S, A Salibindla, AUM Masuk, and R Ni (2019b). “An open-source shake-the-box method and its performance evaluation”. In: *13th International Symposium on Particle Image Velocimetry*.

Masuk, Ashik Ullah Mohammad, Ashwanth Salibindla, and Rui Ni (2019). “A robust virtual-camera 3D shape reconstruction of deforming bubbles/droplets with additional physical constraints”. In: *International Journal of Multiphase Flow*, p. 103088.

Masuk, Ashik Ullah Mohammad, Ashwanth Salibindla, Shiyong Tan, and Rui Ni (2019). “V-ONSET (Vertical Octagonal Noncorrosive Stirred Energetic Turbulence): A vertical water tunnel with a large energy dissipation rate

to study bubble/droplet deformation and breakup in strong turbulence". In: *Review of Scientific Instruments* 90.8, p. 085105.

Ni, Rui, Ke-Qing Xia, et al. (2013). "Kolmogorov constants for the second-order structure function and the energy spectrum". In: *Physical Review E* 87.2, p. 023002.

Pumir, Alain, Eberhard Bodenschatz, and Haitao Xu (2013). "Tetrahedron deformation and alignment of perceived vorticity and strain in a turbulent flow". In: *Physics of Fluids* 25.3, p. 035101.

Tan, Shiyong, Ashwanth Salibindla, Ashik Ullah Mohammad Masuk, and Rui Ni (2020). "Introducing OpenLPT: new method of removing ghost particles and high-concentration particle shadow tracking". In: *Experiments in Fluids* 61.2, p. 47.

Xu, Haitao, Alain Pumir, and Eberhard Bodenschatz (2011). "The pirouette effect in turbulent flows". In: *Nature Physics* 7.9, pp. 709–712.

Lüthi, Beat, Arkady Tsinober, and Wolfgang Kinzelbach (2005). "Lagrangian measurement of vorticity dynamics in turbulent flow". In: *Journal of Fluid mechanics* 528, pp. 87–118.

Hoyer, Klaus, Markus Holzner, Beat Lüthi, Michele Guala, Alexander Liberzon, and Wolfgang Kinzelbach (2005). "3D scanning particle tracking velocimetry". In: *Experiments in Fluids* 39.5, pp. 923–934.

REFERENCES

Batchelor, George Keith (1953). *The theory of homogeneous turbulence*. Cambridge university press.

Sreenivasan, Katepalli R (1995). "On the universality of the Kolmogorov constant". In: *Physics of Fluids* 7.11, pp. 2778–2784.

Kolmogorov, Andrey Nikolaevich (1962). "A refinement of previous hypotheses concerning the local structure of turbulence in a viscous incompressible fluid at high Reynolds number". In: *Journal of Fluid Mechanics* 13.1, pp. 82–85.

Meneveau, Charles and KR Sreenivasan (1991). "The multifractal nature of turbulent energy dissipation". In: *Journal of Fluid Mechanics* 224, pp. 429–484.

Kailasnath, P, KR Sreenivasan, and G Stolovitzky (1992). "Probability density of velocity increments in turbulent flows". In: *Physical review letters* 68.18, p. 2766.

Sreenivasan, Katepalli R (1999). "Fluid turbulence". In: *Reviews of Modern Physics* 71.2, S383.

Li, Yi and Charles Meneveau (2005). "Origin of non-Gaussian statistics in hydrodynamic turbulence". In: *Physical review letters* 95.16, p. 164502.

Salibindla, Ashwanth KR, Ashik UM Masuk, Shiyong Tan, and Rui Ni (2020b). "Lift and drag coefficients of deformable bubbles in intense turbulence determined from bubble rise velocity". In: *Journal of Fluid Mechanics*.

REFERENCES

Lalanne, Benjamin, Olivier Masbernat, and Frédéric Risso (2019). “A model for drop and bubble breakup frequency based on turbulence spectra”. In: *AIChE Journal* 65.1, pp. 347–359.

Moore, DW (1965). “The velocity of rise of distorted gas bubbles in a liquid of small viscosity”. In: *Journal of Fluid Mechanics* 23.04, pp. 749–766.

Lamb, Horace (1924). *Hydrodynamics*. University Press.

Brennen, CE (1982). *A Review of Added Mass and Fluid Inertial Forces*. Tech. rep.

Brennen, Christopher Earls (2005). *Fundamentals of multiphase flow*. Cambridge university press.

Magnaudet, Jacques and I Eames (2000). “The motion of high-Reynolds-number bubbles in inhomogeneous flows”. In: *Annual Review of Fluid Mechanics* 32.1, pp. 659–708.

Mathai, Varghese, Detlef Lohse, and Chao Sun (2020a). “Bubble and buoyant particle laden turbulent flows”. In: *Annu. Rev. Condens. Matter Phys* 11.

Rust, AC and Michael Manga (2002). “Bubble shapes and orientations in low Re simple shear flow”. In: *Journal of colloid and interface science* 249.2, pp. 476–480.

Kameda, M, T Katsumata, and M Ichihara (2008). “Deformation of bubbles in a highly viscous pipe flow”. In: *Fluid dynamics research* 40.7-8, p. 576.

REFERENCES

Müller-Fischer, Nadina, Philip Tobler, Marco Dressler, Peter Fischer, and Erich J Windhab (2008). “Single bubble deformation and breakup in simple shear flow”. In: *Experiments in fluids* 45.5, pp. 917–926.

Huber, C, Y Su, CT Nguyen, Andrea Parmigiani, Helge M Gonnermann, and J Dufek (2014). “A new bubble dynamics model to study bubble growth, deformation, and coalescence”. In: *Journal of Geophysical Research: Solid Earth* 119.1, pp. 216–239.

Armandoost, Parisa, Morteza Bayareh, and Afshin Ahmadi Nadooshan (2018). “Study of the motion of a spheroidal drop in a linear shear flow”. In: *Journal of Mechanical Science and Technology* 32.5, pp. 2059–2067.

Feigl, Kathleen, David Megias-Alguacil, Peter Fischer, and Erich J Windhab (2007). “Simulation and experiments of droplet deformation and orientation in simple shear flow with surfactants”. In: *Chemical engineering science* 62.12, pp. 3242–3258.

Guido, Stefano and Francesco Greco (2001). “Drop shape under slow steady shear flow and during relaxation. Experimental results and comparison with theory”. In: *Rheologica acta* 40.2, pp. 176–184.

Guido, S, F Greco, and M Villone (1999). “Experimental determination of drop shape in slow steady shear flow”. In: *Journal of colloid and interface science* 219.2, pp. 298–309.

REFERENCES

Guido, Stefano and Marco Villone (1998). “Three-dimensional shape of a drop under simple shear flow”. In: *Journal of rheology* 42.2, pp. 395–415.

Megías-Alguacil, David, Peter Fischer, and Erich J Windhab (2006). “Determination of the interfacial tension of low density difference liquid–liquid systems containing surfactants by droplet deformation methods”. In: *Chemical engineering science* 61.5, pp. 1386–1394.

Chevillard, Laurent and Charles Meneveau (2013). “Orientation dynamics of small, triaxial–ellipsoidal particles in isotropic turbulence”. In: *Journal of fluid mechanics* 737, pp. 571–596.

Shin, Mansoo and Donald L Koch (2005). “Rotational and translational dispersion of fibres in isotropic turbulent flows”. In: *Journal of Fluid Mechanics* 540, pp. 143–173.

Parsa, Shima, Enrico Calzavarini, Federico Toschi, and Greg A Voth (2012). “Rotation rate of rods in turbulent fluid flow”. In: *Physical review letters* 109.13, p. 134501.

Legendre, Dominique, Roberto Zenit, and J Rodrigo Velez-Cordero (2012). “On the deformation of gas bubbles in liquids”. In: *Physics of Fluids* 24.4, p. 043303.

Riboux, Guillaume, Frédéric Risso, and Dominique Legendre (2010). “Experimental characterization of the agitation generated by bubbles rising at high Reynolds number”. In: *Journal of Fluid Mechanics* 643, pp. 509–539.

REFERENCES

Ellingsen, Kjetil and Frederic Risso (2001). “On the rise of an ellipsoidal bubble in water: oscillatory paths and liquid-induced velocity”. In: *Journal of Fluid Mechanics* 440, pp. 235–268.

Lunde, Knud and Richard J Perkins (1998). “Shape oscillations of rising bubbles”. In: *In Fascination of Fluid Dynamics*. Springer, pp. 387–408.

Mougin, Guillaume and Jacques Magnaudet (2001). “Path instability of a rising bubble”. In: *Physical review letters* 88.1, p. 014502.

Luewisutthichat, Wilai, Atsushi Tsutsumi, and Kunio Yoshida (1997). “Chaotic hydrodynamics of continuous single-bubble flow systems”. In: *Chemical Engineering Science* 52.21-22, pp. 3685–3691.

Tayler, Alexander B, Daniel J Holland, Andrew J Sederman, and Lynn F Gladden (2012). “Exploring the origins of turbulence in multiphase flow using compressed sensing MRI”. In: *Physical review letters* 108.26, p. 264505.

Salibindla, Ashwanth KR, Ashik Ullah Mohammad Masuk, Shiyong Tan, and Rui Ni (2020a). “Lift and drag coefficients of deformable bubbles in intense turbulence determined from bubble rise velocity”. In: *Journal of Fluid Mechanics* 894.

Mordant, Nicolas, Alice M Crawford, and Eberhard Bodenschatz (2004). “Experimental Lagrangian acceleration probability density function measurement”. In: *Physica D: Nonlinear Phenomena* 193.1-4, pp. 245–251.

REFERENCES

Ashurst, Wm T, AR Kerstein, RM Kerr, and CH Gibson (1987). “Alignment of vorticity and scalar gradient with strain rate in simulated Navier–Stokes turbulence”. In: *The Physics of fluids* 30.8, pp. 2343–2353.

Huang, Mei-Jiau (1996). “Correlations of vorticity and material line elements with strain in decaying turbulence”. In: *Physics of Fluids* 8.8, pp. 2203–2214.

Masuk, AUM, AKR Salibindla, and R Ni (2020b). “Simultaneous measurements of deforming Hinze-scale bubbles with surrounding turbulence”. In: *Journal of Fluid Mechanics* submitted.

Bellani, Gabriele and Evan A Variano (2012). “Slip velocity of large neutrally buoyant particles in turbulent flows”. In: *New Journal of Physics* 14.12, p. 125009.

Cisse, Mamadou, Holger Homann, and Jérémie Bec (2013). “Slipping motion of large neutrally buoyant particles in turbulence”. In: *Journal of Fluid Mechanics* 735.

Girimaji, SS and SB Pope (1990). “Material-element deformation in isotropic turbulence”. In: *Journal of fluid mechanics* 220, pp. 427–458.

Benzi, Roberto, Luca Biferale, Enrico Calzavarini, Detlef Lohse, and Federico Toschi (2009). “Velocity-gradient statistics along particle trajectories in turbulent flows: The refined similarity hypothesis in the Lagrangian frame”. In: *Physical Review E* 80.6, p. 066318.

Qi, Y, AUM Masuk, and R Ni (2020). “Towards a model of bubble breakup in turbulence through experimental constraints”. In: *International Journal of Multiphase Flow* submitted.

Delvigne, Gerardus Athenasius Leonardus and C_E Sweeney (1988). “Natural dispersion of oil”. In: *Oil and Chemical Pollution* 4.4, pp. 281–310.

Yang, Di, Bicheng Chen, Marcelo Chamecki, and Charles Meneveau (2015). “Oil plumes and dispersion in L angmuir, upper-ocean turbulence: Large-eddy simulations and K-profile parameterization”. In: *Journal of Geophysical Research: Oceans* 120.7, pp. 4729–4759.

Stone, Howard A (1994). “Dynamics of drop deformation and breakup in viscous fluids”. In: *Annual Review of Fluid Mechanics* 26.1, pp. 65–102.

Taylor, Geoffrey Ingram (1932). “The viscosity of a fluid containing small drops of another fluid”. In: *Proceedings of the Royal Society of London. Series A, Containing Papers of a Mathematical and Physical Character* 138.834, pp. 41–48.

Taylor, Geoffrey Ingram (1934). “The formation of emulsions in definable fields of flow”. In: *Proceedings of the Royal Society of London. Series A, containing papers of a mathematical and physical character* 146.858, pp. 501–523.

Kennedy, Mark Robert, C Pozrikidis, and R Skalak (1994). “Motion and deformation of liquid drops, and the rheology of dilute emulsions in simple shear flow”. In: *Computers & fluids* 23.2, pp. 251–278.

REFERENCES

Bentley, BJ and L Gary Leal (1986). “An experimental investigation of drop deformation and breakup in steady, two-dimensional linear flows”. In: *Journal of Fluid Mechanics* 167, pp. 241–283.

Challabotla, Niranjan Reddy, Lihao Zhao, and Helge I Andersson (2015). “Orientation and rotation of inertial disk particles in wall turbulence”. In: *Journal of Fluid Mechanics* 766.

Marchioli, Cristian, Marco Fantoni, and Alfredo Soldati (2010). “Orientation, distribution, and deposition of elongated, inertial fibers in turbulent channel flow”. In: *Physics of fluids* 22.3, p. 033301.

Allende, Sofía, Christophe Henry, and Jérémie Bec (2018). “Stretching and buckling of small elastic fibers in turbulence”. In: *Physical review letters* 121.15, p. 154501.

Marchioli, Cristian and Alfredo Soldati (2015). “Turbulent breakage of ductile aggregates”. In: *Physical Review E* 91.5, p. 053003.

Shan, Xiaowen and Hudong Chen (1993). “Lattice Boltzmann model for simulating flows with multiple phases and components”. In: *Physical review E* 47.3, p. 1815.

Torza, S, RG Cox, and SG Mason (1972). “Particle motions in sheared suspensions XXVII. Transient and steady deformation and burst of liquid drops”. In: *Journal of colloid and interface science* 38.2, pp. 395–411.

REFERENCES

Guido, Stefano, Mario Minale, and Pier Luca Maffettone (2000). “Drop shape dynamics under shear-flow reversal”. In: *Journal of Rheology* 44.6, pp. 1385–1399.

Masuk, AUM, AKR Salibindla, and R Ni (2020a). “Orientation dynamics of finite-sized bubbles in intense turbulence during deformation and breakup”. In: *Journal of Fluid Mechanics* submitted.

Mougin, Guillaume and Jacques Magnaudet (2006). “Wake-induced forces and torques on a zigzagging/spiralling bubble”. In: *Journal of Fluid Mechanics* 567, p. 185.

Ugural, Ansel C and Saul K Fenster (2003). *Advanced strength and applied elasticity*. Pearson education.

Fernandes, Pedro C., Patricia Ern, Frédéric Risso, and Jacques Magnaudet (2008). “Dynamics of axisymmetric bodies rising along a zigzag path”. In: *Journal of Fluid Mechanics* 606, pp. 209–223. DOI: 10.1017/S0022112008001663. URL: https://doi.org/10.1017/S0022112008001663.

Cano-Lozano, José Carlos, Carlos Martínez-Bazán, Jacques Magnaudet, and Joël Tchoufag (2016). “Paths and wakes of deformable nearly spheroidal rising bubbles close to the transition to path instability”. In: *Physical Review Fluids* 1.5, p. 053604.

REFERENCES

Kirchhoff, Gustav (1870). “Ueber die Bewegung eines Rotationskörpers in einer Flüssigkeit.” In: *Journal für die reine und angewandte Mathematik* 1870.71, pp. 237–262.

Mougin, G and Jacques Magnaudet (2002). “The generalized Kirchhoff equations and their application to the interaction between a rigid body and an arbitrary time-dependent viscous flow”. In: *International journal of multiphase flow* 28.11, pp. 1837–1851.

Shew, Woodrow L and Jean-François Pinton (2006). “Dynamical model of bubble path instability”. In: *Physical review letters* 97.14, p. 144508.

Vita

Ashik Ullah Mohammad Masuk

Education

Ph.D. in Mechanical Engineering Johns Hopkins University Baltimore, MD	Fall 2020
M.Sc. in Mechanical Engineering The Pennsylvania State University University Park, PA	Spring 2017
B.Sc. in Mechanical Engineering Islamic University of Technology Bangladesh	Fall 2012

VITA

Technical Skills

Mechanical Design | Fluid Dynamics | Turbulent Flows | Multiphase Flows | Designing and Building Large-Scale Experimental Facilities | 3D Printing | Machine Shop | Synchronized Data Acquisition | Laser Diagnostics | High-speed Imaging | Shadowgraphy | Computerized Flow Controls | Lab Equipment Management | Experimental Data Analysis and Modeling | Signal Processing | Virtual 3D Reconstruction of Complex Shaped Objects | Digital Image Processing | Algorithm Development | Computer vision | Lagrangian Particle Tracking | Statistical Analysis | Physics Based Modeling | Mentoring and Teaching

Programming Languages: Matlab, C, C++, Python

Software: ANSYS (Fluent, Mechanical APDL), LabVIEW, Simulink, SolidWorks, AutoCAD, Illustrator, Blender, Inkscape, LaTeX, Minitab

Peer Reviewed Journal Publications

- **Masuk, A.U.M.**, Salibindla, A., and Ni, R. (2019). "V-ONSET (Vertical Octagonal Noncorrosive Stirred Energetic Turbulence): A vertical water tunnel with a large energy dissipation rate to study bubble/droplet deformation and breakup in strong turbulence". Review of Scientific Instruments, 90(8), p.085105.

- **Masuk, A.U.M.**, Salibindla, A., and Ni, R. (2019). "A robust virtual-

camera 3D shape reconstruction of deforming bubbles/droplets with additional physical constraints". International Journal of Multiphase Flow, p.103088.

- **Masuk, A.U.M.**, Salibindla, A., and Ni, R. (2020). "Simultaneous measurements of deforming Hinze-scale bubbles with surrounding turbulence". Journal of Fluid Mechanics – *under review*

- **Masuk, A.U.M.**, Salibindla, A., and Ni, R. (2020). "Orientation dynamics of finite-sized bubbles in intense turbulence during deformation and breakup". Journal of Fluid Mechanics – *under review*

- **Masuk, A.U.M.**, Salibindla, A., and Ni, R. (2020). "A phenomenological model on the deformation and orientation dynamics of finite-sized bubbles in both quiescent and turbulent media". Journal of Fluid Mechanics – *under review*

- Salibindla, A., **Masuk, A.U.M.**, Tan, S., and Ni, R. (2020)."Extract lift and drag coefficients of bubbles in turbulence from experimental measurements of bubble rise velocity". Journal of Fluid Mechanics, 894

- Salibindla, A., **Masuk, A.U.M.**, and Ni, R. (2020)."Experimental investigations of the added mass force of deformable bubbles in intense turbulence". Journal of Fluid Mechanics – *under review*

- Qi, Y., **Masuk, A.U.M.**, and Ni, R. (2020). "Towards a model of bubble breakup in turbulence through experimental constraints". International Journal of Multiphase Flow – *in press*

- Salibindla, A.K., Subedi, R., Shen, V.C., **Masuk, A.U.M.**, and Ni, R. (2018). "Dissolution-driven convection in a heterogeneous porous medium". Journal of Fluid Mechanics, 857, pp.61-79.

- Tan, S., Salibindla, A., **Masuk, A.U.M.**, and Ni, R. (2020). "Introducing OpenLPT: new method of removing ghost particles and high-concentration particle shadow tracking". Experiments in Fluids, 61(2), 47

Selected Conference Presentations

- **Masuk, A.U.M.**, Salibindla, A., Tan S., and Ni, R., (2019). On the Mechanisms of Hinze-Scale Bubble Deformation and Breakup in Strong Turbulence. NETL Multiphase Flow Science Workshop

- **Masuk, A.U.M.**, Salibindla, A., Tan S., and Ni, R., (2018). Experimental studies of deformation and breakup of bubbles under strong turbulence. American Physical Society-Division of Fluid Dynamics.

- **Masuk, A.U.M.**, Salibindla, A., and Ni, R., (2017). Lagrangian evolution of deformation of finite-size bubbles in turbulent multiphase flow. Ameri-

can Physical Society-Division of Fluid Dynamics.

- **Masuk, A.U.M.**, Salibindla, A., and Ni, R., (2017). V-ONSET: A new Penn State multiphase flow facility to probe Lagrangian interfacial transfer dynamics. Paper presented at 17th International Topical Meeting on Nuclear Reactor Thermal Hydraulics, NURETH 2017, Xi'an, Shaanxi, China.

Awards & Honors

- **Featured Research**: New water tunnel provides nearly oceanic levels of turbulence,
  American Institute of Physics Scilight, (August 16, 2019)
- Scholarship and 3 years' tuition waiver for undergraduate studies at IUT from OIC
- Board scholarship from Bangladesh government for excellent performance in HSC examination (2009-2012)